BILINGUAL PUBLISHING GROUP

Journal of Atmospheric Science Research

Volume 7 • Issue 1 • January 2024 ISSN 2630-5119(Online)

Volume 7 Issue 1 • January 2024 • ISSN 2630-5119 (Online)

Journal of Atmospheric Science Research

BILINGUAL PUBLISHING GROUP

BILINGUAL PUBLISHING GROUP

Volume 7 | Issue 1 | January 2024 | Page1-117

Journal of Atmospheric Science Research

Contents

Articles

BILINGUAL PUBLISHING GROUP

Journal of Atmospheric Science Research

https://journals.bilpubgroup.com/index.php/jasr/index

ARTICLE

Some Features of Black Carbon Aerosols Connected with Regional Climate Over Pristine Environment

***Saurabh Yadav*[1], *Panuganti C. S. Devara*[1*], *S. M. Sonbawne*[2], *B. S. Murthy*[2], *S. Tiwari*[1], *S. Wadhwa*[1], *A. Kumar*[1]**

[1] *Amity Centre of Excellence in Ocean-Atmosphere Science and Technology (ACOAST), Amity University Haryana (AUH), Gurugram, 122413, India*

[2] *Indian Institute of Tropical Meteorology (IITM), Pashan, Pune, 411008, India*

ABSTRACT

The authors report the results of aethalometer black carbon (BC) aerosol measurements carried out over a rural (pristine) site, Panchgaon, Haryana State, India during the winter months of 2021–2022 and 2022–2023. They are compared with collocated and concurrent observations from the Air Quality Monitoring Station (AQMS), which provides synchronous air pollution and surface meteorological parameters. Secular variations in BC mass concentration are studied and explained with variations in local meteorological parameters. The biomass burning fire count retrievals from NASA-NOAA VIIRS satellite, and backward airmass trajectories from NOAA-ERL HYSPLIT Model analysis have also been utilized to explain the findings. They reveal that the north-west Indian region contributes maximum to the BC mass concentration over the study site during the study period. Moreover, the observed BC mass concentrations corroborate the synchronous fire count, primary and secondary pollutant concentrations. The results were found to aid the development of mitigation methods to achieve a sustainable climate system.

Keywords: Carbonaceous aerosols; Dual-spot technique; Temporal variations; Primary and secondary pollutants; Stubble burning; Long-range transport; Satellite products

1. Introduction

Black carbon (BC) is regarded as a gas tracer of combustion inefficiency, and a precursor of carbon dioxide and tropospheric ozone [1]. It has a negative effect on health because it is a key structural part of

*CORRESPONDING AUTHOR:
Panuganti C.S. Devara, Amity Centre of Excellence in Ocean-Atmosphere Science and Technology (ACOAST), Amity University Haryana (AUH), Gurugram, 122413, India; Email: pcsdevara@ggn.amity.edu

ARTICLE INFO
Received: 26 October 2023 | Revised: 27 November 2023 | Accepted: 5 December 2023 | Published Online: 12 December 2023
DOI: https://doi.org/10.30564/jasr.v7i1.6040

CITATION
Yadav, S., Devara, P.C.S., Sonbawne, S.M., et al., 2023. Some Features of Black Carbon Aerosols Connected with Regional Climate Over Pristine Environment. Journal of Atmospheric Science Research. 7(1): 1–18. DOI: https://doi.org/10.30564/jasr.v7i1.6040

fine particulate matter, which transports numerous other chemical components [2] and is a major contributor to aerosol-induced air pollution [3–5]. BC is abundant in the environment, including soils, ice, sediments, and the air. BC was discovered to make up 12–31% of the sedimentary organic components at two deep ocean locations that are thousands of years old [6]. During the industrial era, the consumption of fossil fuels and biofuels increased significantly, resulting in a considerable increase in atmospheric BC emissions [7–14]. Approximately 20% of BC is emitted by the combustion of biofuels, 40% by the combustion of fossil fuels, and 40% by the combustion of open biomass [3,15]. India is the world's second largest BC emitter after Africa [3,16] with emissions expected to climb substantially in the future decades [17]. This is mostly because low-efficiency home fuel combustion accounts for 47% of Indian BC emissions, followed by industry emissions (22%), transportation (17%), and open burning (12%) [18]. In Indo Gangetic Plains (IGP), wintertime BC concentrations are large (around 60%), caused by emissions from biofuel combustion for cooking and heating in the residential home sector [19]. Because of the level of industrialisation, transportation density, and fuel usage for electricity generation and in households, the BC concentrations will inevitably be very area dependent and seasonally fluctuating [20].

With a lifespan of a few days to weeks, BC is a transient air contaminant, unlike other potent greenhouse gases, (carbon dioxide and methane with life cycles of more than 100 and 12 years respectively). The longevity of BC in the atmosphere, its impact on clouds, and its optical qualities are all affected by interactions with other aerosol components. BC is produced in conjunction with several aerosols and aerosol precursor gases. BC readily combines with other aerosol components in the atmosphere. This mixing enhances BC's light absorption, improves its ability to form liquid-cloud droplets, changes its ability to form ice nuclei, and modifies its atmospheric removal rate [21]. During its brief atmospheric lifetime, BC is transported regionally and across continents. Precipitation and surface contact remove atmospheric pollutants within a few days to weeks. As a result, BC concentrations in remote regions of the atmosphere are substantially lower than in source regions [22]. BC has a climate forcing of 1.1 W/m^2, it warms the Earth by absorbing sunlight, heating the atmosphere, reducing albedo when it settles on snow and ice (direct effect), and indirectly interacting with clouds [3]. Through a variety of extremely intricate processes, BC influences the features of ice clouds and liquid clouds. These mechanisms include increasing the number of liquid cloud droplets, increasing precipitation in mixed-phase clouds, and affecting the number of ice particles and cloud extent. The ensuing radiative changes in the atmosphere are regarded as BC's indirect climatic consequences [23]. Due to its light-absorbing qualities, BC also contributes significantly to low visibility [24]. It has the highest ability to absorb light per unit mass in the atmosphere. Because of its high absorption over a wide wavelength range, it has the potential to considerably neutralise or even reverse the "white house" effect caused by aerosol scattering [25,26].

The atmospheric BC poses a significant hazard to human health both directly through exposure to toxic chemicals and indirectly through climate change and their impact on life-supporting systems on Earth because of long-range transport and growing population [27]. During its short period of residence, it causes various health problems like cardiovascular disease, respiratory problems, cancer and even birth defects. Recent studies on the health effects of airborne particles demonstrate a clear link between combustion-derived particles, notably BC, and cardiovascular disease and mortality (CVD and CVM) [28,29]. Population exposure to BC is significant, with over 60 million people recognized as living in BC concentration hotspots (wintertime mean, > 20 ug/m^3) [19]. The megacity's attributable proportion of overall cardiovascular disease mortality (CVM) burden to BC exposures is 62%. The semiurban area accounted for approximately 49% of the overall BC-attributable CVM burden across the IGP. More than 400,000 lives might be saved each year from CVM by prioritising emission reductions from the combustion of

domestic biofuel in semi-urban areas, diesel oil in transportation, and coal in megacities' thermal power plants and brick kiln industries [19]. It was concluded that BC, rather than PM, could be an effective supplemental air quality indicator for assessing air quality health concerns [30]. Reducing BC has been suggested as one of the simplest strategies to slow down short-term global warming by the IPCC and other climate researchers [31]. Because BC is readily taken from the atmosphere by deposition, concentrations respond swiftly to reductions in emissions. Thus, reducing BC emissions represents a viable mitigation technique that could lower anthropogenic global climate forcing in the short term while also slowing the corresponding rate of climate change [32].

To analyse the problem of air pollution, it is critical to understand its sources, the impact of various meteorological elements on dispersion, and the topography of a city [33]. Due to its short residence time, complicated interactions with other atmospheric pollutants, inadequate monitoring (especially in India), and significant effects on the environment and human health, BC is a threat to everyone and needs to be mitigated. In this study, BC mass concentrations were reported during the winter period at a rural site in North India. The basic objectives were to determine temporal variations in BC concentration (diurnal, day to night, weekdays to weekends), its interactions with other air pollutants (PM2.5, PM10, CO, Ozone, C_6H_6) meteorology, influence of other parameters like fire events and wind dispersion patterns.

2. Material and methodology

The BC measurements in the present study were made with a Magee Scientific, USA Next-Generation Aethalometer Model AE33 (**Figure 1D**). It provides a real-time readout of the BC mass concentration at each data point at the specified time basis [34–37]. Once-a-minute BC data was obtained from aethalometer which was then averaged depending upon plot type (variation). For diurnal variation and weekday to weekend studies, full data was used (without any average), while for day to night contrast studies, daily mean data was used. For correlation purposes, daily averaged values of BC and other variables were used. It detects optical attenuation by measuring the attenuation of the light beam passed through the sample location. This equipment continually collects and examines aerosol particles. An aerosol-rich air stream is passed through the filter strip at a measured flow rate. At the same time, the strip is illuminated by light-sensitive detectors, which measure the intensity of light passing through the unilluminated part of the strip, which serves as a reference point, compared to the collection point. As the optically absorbing material accumulates, the intensity of the light passing through it gradually decreases. A decrease in light intensity from one measurement to the next is interpreted as an increase in the material being collected. That increased amount is divided by the known airflow to calculate the concentration. Moreover, the instrument used in the present study collects two sample points of the same intake airflow at different collection rates and analyses them simultaneously. These two results are mathematically combined to eliminate the "Filter Loading Effect" nonlinearity and accurately measure the aerosol concentration. In addition, the analysis is performed at 7 optical wavelengths covering the spectrum from 370 nm to 950 nm. More details are available in Sonbawne et al. (2021) [38]. The mass concentration of BC is estimated by using the following formula available in the User Manual [39].

$$BC = S*(DATN/100) / [(1-G) *\sigma_{air} * C * (1-K*ATN) *AT] \quad (1)$$

where S is spot area (sq. cm), ATN is optical attenuation, F is flowrate (LPM), T is time (sec), σ_{air} is mass absorption cross-section (m^2/g), C is multiple scattering parameters, K is compensation parameter and G is leakage parameter.

The increase in optical absorption at shorter wavelengths can be interpreted as the presence of so-called "brown" carbonaceous material, which is usually an indicator of emissions from biomass burning [40].

A Hybrid Single-Particle Lagrangian Integrated Trajectory (HYSPLIT) model was utilized to create backward trajectory plots. It replicates the dispersion

and trajectory of substances carried and diffused through the atmosphere at various ranges ranging from local to global. It also computes pollutant dispersion, chemical transformation, and deposition in the atmosphere. In this study vertical trajectory model was used in obtaining backward trajectories at a height of 100 m and a duration of 96 hours. The whole month's trajectories were averaged for the monthly frequency trajectory plot (with a new trajectory starting every 6th hour) [41,42].

The region's fire count data was taken from the Fire Information for Resource Management System (FIRMS). It disseminates almost real-time active fire data from the MODIS and the VIIRS, with the latter's data being used due to its significantly higher resolution. The VIIRS was onboard the Suomi National Polar-orbiting Partnership (Suomi NPP) and NOAA-20 satellites, which were jointly operated by NASA and NOAA. VIIRS gathers visible and infrared pictures, as well as worldwide studies of the Earth's surface, atmosphere, cryosphere, and ocean. VIIRS expands on observations made by similar sensors aboard previously deployed satellites, such as NASA's MODIS and NOAA's Advanced Very High-Resolution Radiometer (AVHRR). VIIRS snow cover and sea ice algorithms have been optimized for compatibility with MODIS snow cover and sea ice datasets, ensuring continuity between MODIS and VIIRS data products and allowing for comparison of snow and sea ice data across MODIS, VIIRS, and beyond to simplify long-term climate data records [43].

For the present study, a rural station, Panchgaon (28.317°N, 76.916°E, 285 m above mean sea level) in Haryana State was chosen, which is situated around 50 km away from Delhi, India. **Figure 1A** displays a schematic diagram of the experimental site and the location of observations. It can be seen from the figure that in the northeast direction, two industrial hubs, namely, Manesar and Gurugram are present. Every time the northeasterly wind blows, pollutants are transported to the study site [44]. The site is located approximately five kilometres south of the Delhi-Jaipur National Highway (NH48) and is surrounded by Aravalli hillocks with an average altitude of around 200 m. Moreover, the Aethalometer, as depicted in the figure, was set up on the Institute Building's terrace (roughly 15 m AGL) free of surrounding terrain such as tall buildings and trees that would disrupt the flow patterns of BC particles in the air. The site is polluted by distant stationary sources such as brick kilns and mobile sources such as nighttime traffic, especially when heavy vehicles circulate on NH48. Open burning is also taken into consideration as one of the local sources of BC aerosols because of the rural setting around the study site.

Figure 1. A photograph depicting [A] Geography around the Amity University Haryana (AUH), [B] Areal view of the University Complex, [C] Four-stored Academic Block 'A' and its terrace where a suit of sensing instruments is installed, and [D] Multi-wavelength Aethalometer used for continuous measurements of simultaneous BC mass concentration (ng/m^3) and Biomass Burning (%).

3. Results and discussion

The results of the analysis of the observations made in the winter months of 2021–2022 and 2022–2023 are presented and discussed, and salient features are summarized in the following sub-sections. The mean diurnal change in BC mass concentration during the study period is illustrated in **Figure 2**. The last two weeks of December and the first week of January showed the highest BC aerosol pollution throughout the day at the study site, during this time the temperature at the sites plummets to a minimum. A high concentration during morning hours and early night hours is also apparent from the contour map (**Figure 2**). Such variations are further explained in the sub-section 3.1. The reduction in BC concentra-

tion with the progression of the season is apparent (December > January > February). As it is a rural site, BC concentrations are moderate throughout the study period.

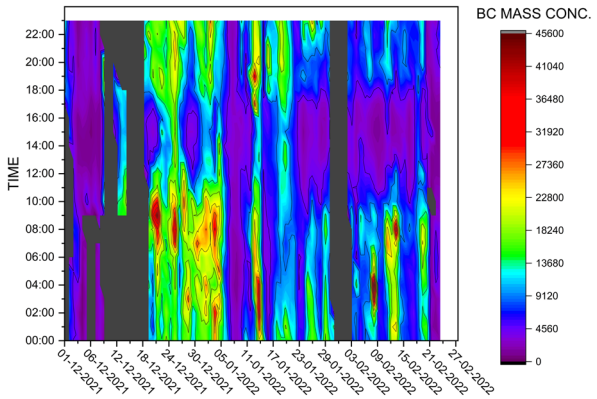

Figure 2. Composite diagram of BC concentration (ngm^{-3}) over Panchgaon during the winter period of 2021–2022.

3.1 Diurnal variation in BC aerosol mass concentration

Some notable diurnal variations were observed during the study period at the site. Diurnal variations can be utilized to understand the effect of meteorology and human activities, and PBL which influence the pollution levels in the atmosphere. Such variations help in the assessment of the relative air quality throughout the day. **Figure 3** depicts diurnal variations during December 2021, January, and February 2022. There is a distinct bi-modal distribution in the diurnal variation in BC mass concentration, with a major peak occurring in the morning and a secondary peak occurring in the evening hours (early night). The morning peak is ascribed to be due to the influence of transit associated with school-going children, office-going employees/workers, and the start of stores, among other things. As the day progresses, greater solar heating causes a deeper and more turbulent boundary layer, resulting in faster dispersion and hence dilution of BC near the surface [45]. A minimum diurnal concentration of BC is apparent during late afternoon hours (around 16:00 h). This late afternoon minimum is owing to the renowned effect of local boundary layer thickness and dynamics. The secondary peak is caused by the fumigation effect. The increase in BC concentration during the night could be attributed to the frequent instances of burning activities in the location, mostly to provide warmth against the cold during the winter months, which is rather usual in rural areas. Low-level inversion-like conditions lead to the formation of a boundary layer or mixing height during the study period [5,46], which predominates for a longer time during the night and early morning hours, resulting in reduced diffusion of submicron size aerosols [47–49]. This is consistent with the results reported by other investigators [50–53].

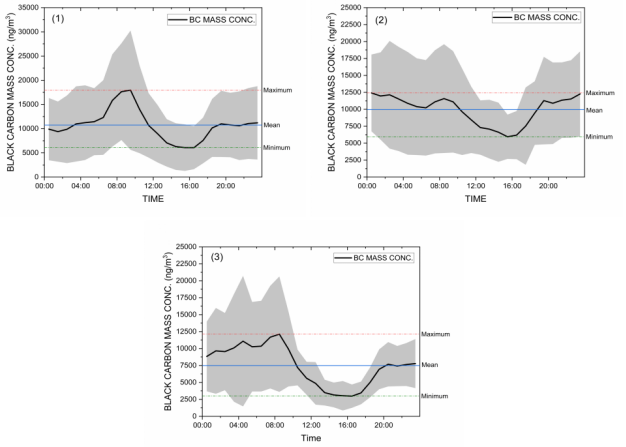

Figure 3. Monthly mean diurnal variations [(1) December 2021, (2) January 2022, (3) February 2022] observed during the study period of winter 2021–2022. The grey shaded portion around the mean curve in each frame indicates the variability in each data point. The range of BC mass concentration (maximum, average and minimum) observed in each month is also indicated in the figure.

Table 1 depicts the maximum, minimum, and mean diurnal values of BC mass concentration for each month. December exhibited maximum mean concentration, and the pollution level was mostly consistent. January exhibited middling concentration values, with an unequal distribution of high and low BC concentration days. For February the lowest BC pollution was observed, with a moderate spread of daily values from the mean value. The decrease in BC aerosols with winter progresses is possibly due to the seasonal meteorology change, and utilization of some inefficient (polluting) heating sources in the houses during wintertime.

Table 1. Percentage deviation of BC mass concentration against its mean value during the study period.

Month	Maximum (ng/m^3)	Minimum (ng/m^3)	Mean (ng/m^3)	Above mean (percentage)	Below mean (percentage)
December	17953.61	6076.94	10750.20	20.45%	20.45%
January	12414.95	5949.72	9949.95	14.30%	23.84%
February	12118.22	2975.34	7492.09	30.05%	35.49%

3.2 Day-night variations in BC aerosols

This sub-section addresses the aspect of how BC aerosols vary during daytime and nighttime. As nighttime weather circumstances differ greatly from daytime weather conditions, notably the planetary boundary layer (PBL) height, ambient temperature, and wind speed would impact the presence of pollutants in the air. **Figure 4** shows day to nighttime contrast. The BC nighttime concentration nearly invariably prevails as compared to the daytime concentration [54]. The high BC concentrations observed during December month are most likely due to the impact of regional meteorological variables (such as temperature, wind speed, direction, humidity, and so on) and these are modulated by stubble-burning activity in and around the study region [55]. The level of BC in the land air rises at night when there is a predominant land breeze. The ventilation coefficient rapidly decreases at night because the nocturnal boundary layer is shallower than the daytime counterpart and the wind speeds are lower [56]. The dates with high peaks during daytime as well as nighttime are majorly due to the local meteorology, long-range transport, and inversion conditions [57,58], as there could not have been a major difference in the local pollution sources in such a short duration.

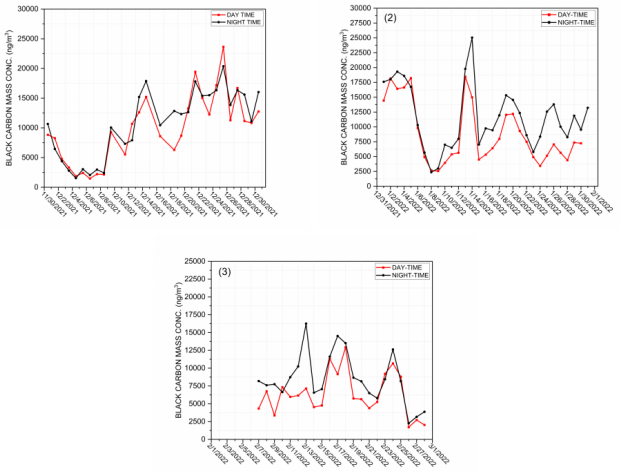

Figure 4. Monthly mean day and night variations in BC aerosols observed during the investigation period of winter 2021–2022. [(1) December 2021, (2) January 2022, (3) February 2022]

3.3 Weekdays and weekends variations in BC aerosols

The impact of anthropogenic activities and associated meteorological processes on BC aerosols during weekdays and weekends are studied in this sub-section. This variation mostly signifies the influence of anthropogenic activities on pollutant concentrations.

Figure 5 shows that BC mass concentrations are higher during the weekdays than on weekends [59], which corresponds to higher human activity during the weekdays [60]. Vehicles are a key source of BC aerosols, which are more prevalent during the weekdays than on weekends (and higher concentration during weekdays strengthens this presumption). Since most anthropogenic activities (industries, biomass burning etc.), apart from transportation, are ongoing throughout the week, it might be possible to estimate the contribution of vehicles in the BC concentration in an area by comparing the BC concentration on weekdays and weekends (especially between 8 and 9 a.m.). Even in this variance, the occurrence of a bimodal distribution demonstrates the importance of meteorology over anthropogenic activities. The higher concentrations during evening time on weekends can be attributed to the weekend effect (increased tendencies of hanging out, shopping, cinema, village house visits etc. on weekends). This effect is most dominant during December month, although high human activities, as well as

the compressed boundary layer, can be the reason for this pollution peaking [61,62]. During January month, weekdays dominated weekends by a considerable margin and the difference between weekdays and weekends aerosol concentration during the midnight got maximum, which was completely opposite of what we observed during rest two months. The marginal increase in BC mass concentration during weekends in the early hours of February could be due to additional sources of small gatherings with waste burning for warmness in the vicinity of the study site.

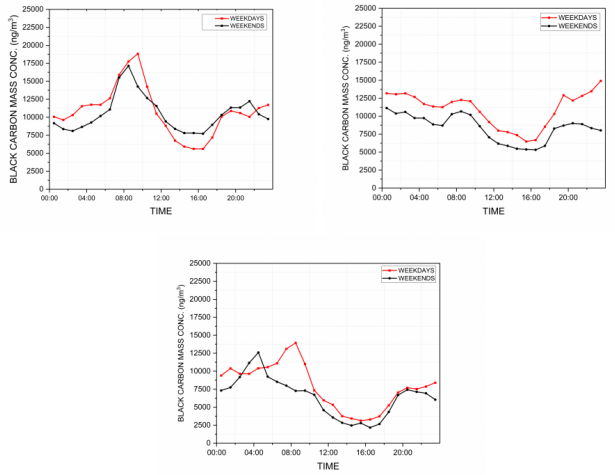

Figure 5. Monthly mean diurnal variation of BC on weekdays and weekends during the study period. [(1) December 2021, (2) January 2022, (3) February 2022]

3.4 Interaction between BC aerosols and meteorological parameters

The unexpected trends observed over three months indicate that there must be some factor(s) influencing the quantity of BC aerosols in the air. To have a better understanding of this, the concurrent time fluctuations in BC mass concentration and key meteorological parameters (humidity, temperature, and wind speed) were examined, and the findings are described in this section.

Association between relative humidity (RH) and BC aerosols

The graphs in **Figure 6** show the association between RH with BC mass concentration. Such relationships between BC concentration and relative humidity can be made use of to examine the nature of the aerosols (hydrophilic or hydrophobic) at the study site, and any hindrance by humidity can affect their residence time. **Figure 6** shows the trend in daily average values of BC and RH (in steps of 10%) for the three months. Even though no sharp positive or negative relation is visible, there are multiple instances where a decreasing trend is apparent, and some peaks and troughs are visible (at the same time or with some lag). Higher RH values associated with lower BC concentration were noticed in January and February months. The negative relationship between RH and BC aerosols was also reported by various researchers [63,64]. The negative relation might implicate towards the abundance of absorbing type aerosols over this region, and possible scavenging of aerosols under high humid conditions. This negative interaction is not totally consistent throughout the study period, demonstrating the complexity of these pollutants (hydrophilic versus hydrophobic, interaction with other parameters) and the potential influence of other meteorological conditions.

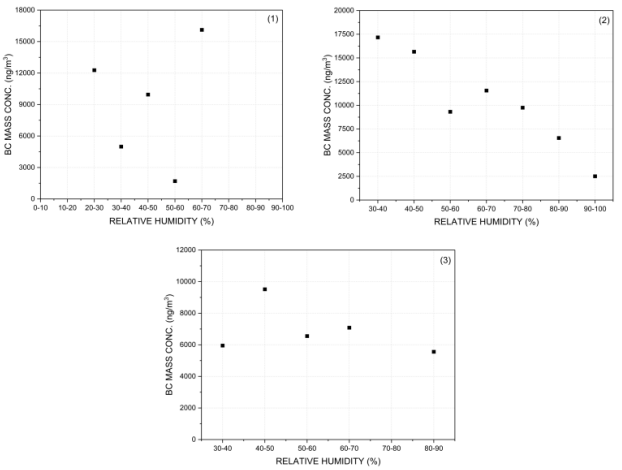

Figure 6. Relationship between BC mass concentration and RH in (1) December 2021, (2) January 2022, and (3) February 2022.

Interaction between temperature and BC mass concentration

Figure 7 depicts the daily mean variation of BC mass concentration with temperature (in a 2-degree interval). It is clear from the figure that there is no systematic relationship between BC mass concentration and temperature. During December and January

(winter) months, BC mass concentration initially increased with an increase in temperature up to about 18 degrees, and subsequently, this trend decreased at the higher temperature of around 20 degrees. This relationship was found to be inverse i.e. initially decrease in BC mass concentration up to about 20 degrees and increased up to 22 degrees at the end of winter season (February 2022). This could be due to limited data size, variability in the local boundary layer height and source strength of BC aerosols in the study region.

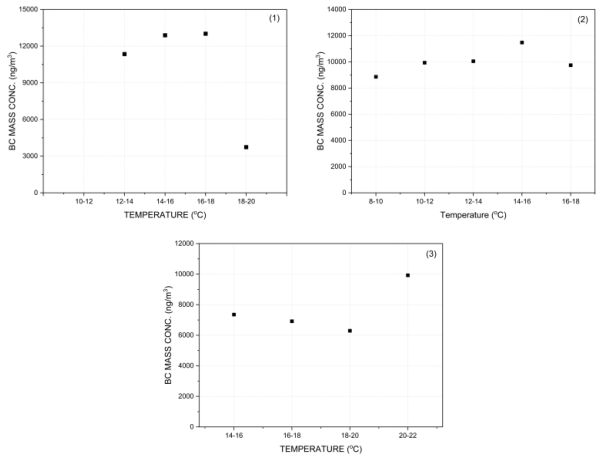

Figure 7. Relationship between BC mass concentration and temperature (1) December 2021, (2) January 2022, and (3) February 2022.

Most of the time, it is clear from the figure that higher temperature values are associated with lower BC concentration. The relationship between BC and temperature can be bidirectional, like temperature can influence BC and vice versa. BC aerosols have light absorbing properties [24], so they can lead to an increase in ambient temperature. When temperature rises, more convective activity leads to the dispersion of aerosols in an enlarged boundary layer [65].

Wind speed and BC mass concentration

The relationship between BC mass concentration and wind speed during the study period is depicted in **Figure 8**. Here daily averages of BC concentrations are plotted with daily averages of wind speed.

It is apparent from **Figure 8** that the relationship between wind speed and BC aerosols in the air is negative [66]. When wind speed increases BC mass concentration at the site decreases, because BC aerosols have a very small size (less than 2.5 microns), wind plays an important role in the dispersion of these microscopic aerosols in the air. Wind direction, wind speed, and proximity and direction of aerosol sources to the monitored site are crucial because the dispersion of aerosols due to wind occurs in two directions: wind disperses pollutants from a site to surroundings as well as from the surrounding to that site. The wind also has an impact on the BC mass concentration, like the other two parameters (temperature and relative humidity) under examination. All three graphs show this negative connection, however, there are some inconsistencies in the trend of these two parameters, but the concentration of BC was always low during high wind speeds however the opposite wasn't always true, showing mixed outcomes at low wind speeds. Other studies among researchers also showed mixed results depending on wind speed, direction, and lengths of wind period [67]. Local wind and long-range air mass trajectories influence the aerosol concentrations, the latter one is depicted in section 3.6.

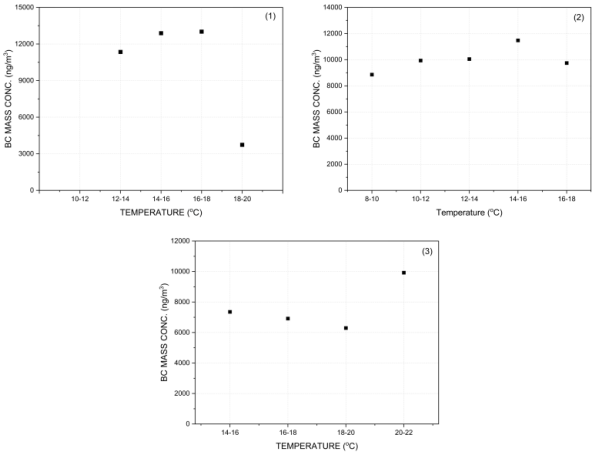

Figure 8. Same as Figure 6, but for wind speed intervals for the three months, (1) December 2021, (2) January 2022, (3) February 2022.

Correlation analysis between BC mass concentration and meteorological parameters

Pearson correlation coefficient between BC and meteorological parameters was calculated to determine the linear correlation. Its value is in the –1.0 to 1.0 range. A perfect negative correlation is shown by a correlation of –1.0, and a perfect positive cor-

relation is shown by a correlation of +1.0. No linear relationship exists between the two variables, as indicated by a correlation of 0.

We can infer from **Table 2** that the wind speed and BC mass concentration, as well as the daily minimum temperature, are always negatively correlated. The association between relative humidity, on the other hand, is negative for two months and positive for the remaining one, like maximum temperature association, but for opposite months. This variation in trend over the course of the three months demonstrates the presence of another parameter that was regulating BC mass concentrations during that time, and these might be associated with time lag/lead.

Table 2. Correlation coefficients were calculated between BC mass concentration and meteorological parameters.

	Temperature (Max.)	Temperature (Min.)	Wind speed	Relative humidity
December 2021	–0.37	–0.44	–0.23	0.26
January 2022	0.34	–0.45	–0.44	–0.58
February 2022	0.48	–0.06	–0.53	–0.11

3.5 Affinity between BC aerosols and other air pollutants

In this section, the associations between BC aerosols and other air pollutants are discussed. Air pollutants focussed on this section are PM2.5, PM10, CO, Ozone, and Benzene. Because of the certain common sources (combustion based) and types (BC-PM) between these parameters some kind of interaction can be expected. For the correlation plots, daily average values of variables are taken. And, due to data irregularities, data for 2022–2023 winter is taken for charting (of all variables).

Relationship between BC aerosol and PM2.5 concentration

For the months of December, January, and February, a regression analysis was performed between BC aerosols and PM2.5, which is depicted in **Figure 9**. BC is a part of particulate matter, which means it will make some proportion of PM at the study site, to check its extent, a correlation coefficient was calculated.

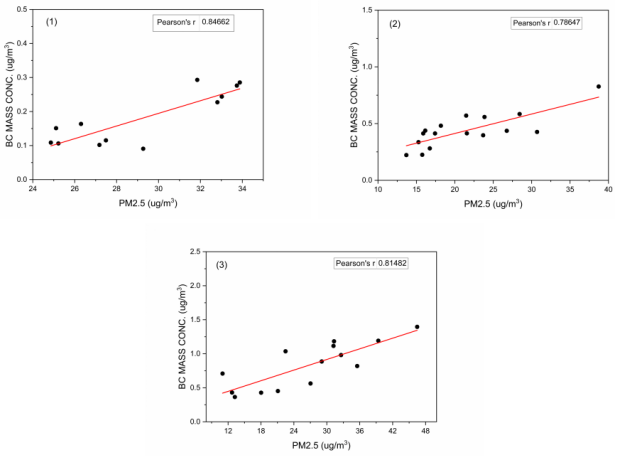

Figure 9. Association between BC aerosols and PM2.5. [(1) December 2021, (2) January 2022, (3) February 2022]

The correlation coefficient between BC mass concentration and PM2.5 was positive, with values of 0.84, 0.78, and 0.81 for December, January, and February respectively. This positive correlation indicates a significant and steady proportion of BC aerosols in PM2.5 [68] throughout the three months at the study site. The modest associations could be attributed to differences in the sources of BC and PM2.5 (and PM2.5 is a secondary pollutant too) [69]. These findings are congruent with those published in the literature by other researchers [5].

BC aerosol and PM10 concentration

The following plots (**Figure 10**) depict the correlation between BC aerosols and PM10 during the December, January, and February months.

The correlation coefficient between BC and PM10 was low with values of 0.48 for December, 0.08 and 0.001 for the January and February months, respectively. PM10 is made up of course (soil-derived dust particles, pollens) as well as fine particles (PM2.5), while BC aerosols are very fine particles (part of PM2.5), so moderately poor correlation for PM10 than PM2.5 is inherent, but in this case, the coherence between PM10 and BC was too low. The residence time of PM10 (coarser) particles is usually shorter than its fine particle subpart. The ambiguous relationship between PM and BC may be explained by the fact that when coupled with the stagnant atmosphere at low temperatures in

winter [70], PM and BC concentrations are potentially influenced by both autochthonous and input particles (source difference) [68].

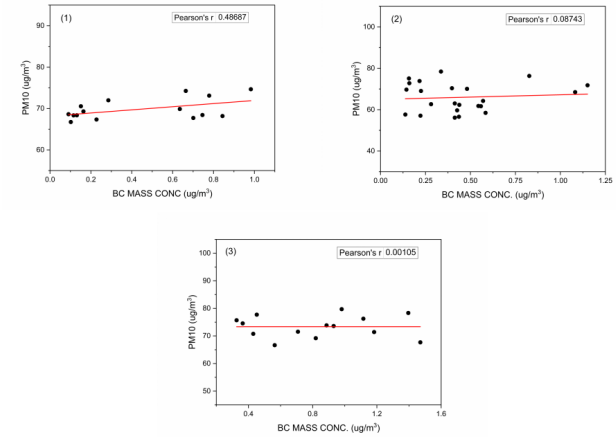

Figure 10. Same as Figure 9, but for PM10.

BC aerosols and CO

The following plots (**Figure 11**) show the regression analysis of BC aerosols and carbon monoxide during the December, January, and February months.

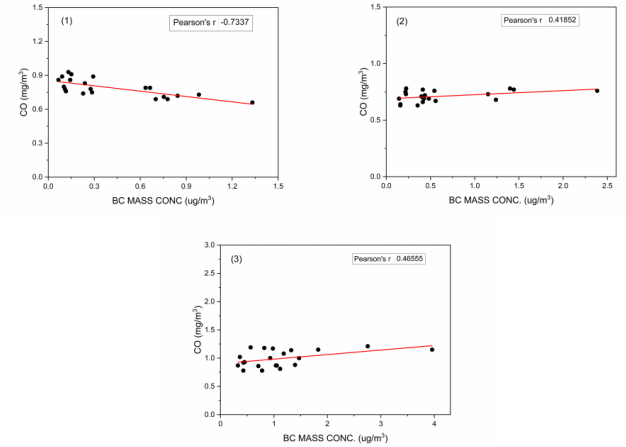

Figure 11. Same as Figure 9, but for CO.

The obtained correlation of BC aerosol and carbon monoxide was ambiguous throughout the three months, significantly negative for the December month (–0.73) while positive for the January and February months (0.41 and 0.46 respectively). Other studies have also reported a similar positive correlation between CO and BC, where both share common sources [70]. As both BC aerosols and CO are by-products of incomplete combustion, some positive correlation between the two is expected, but in this case, it was not significant. Such ambiguity could be a result of data limitations, different composition, and nature of variables in the atmosphere as well as differences in combustion processes (types) at the sources, even meteorology, but their extent is unknown.

BC aerosols and O_3

The following plots (**Figure 12**) depict the regression analysis of BC aerosols and ozone during December, January, and February 2022.

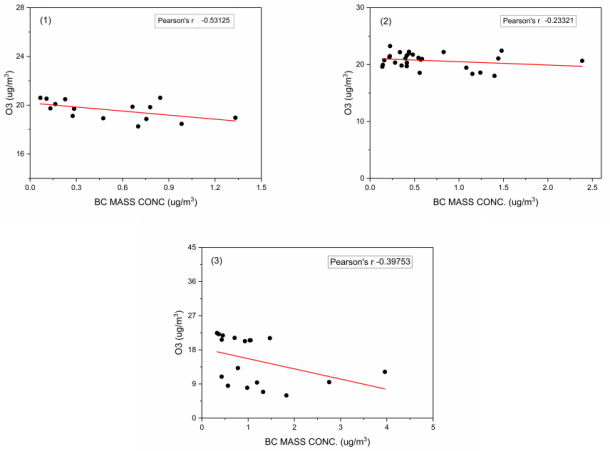

Figure 12. Same as Figure 9, but for ozone.

A negative association between BC aerosols and surface ozone was observed, with correlation coefficient values of –0.53 for December, –0.23 for January, and –0.39 for February, which matched with other studies [71,72]. These two parameters show opposite characteristics, e.g., BC peaks during the morning and early night hours and plummets during the afternoon (diurnal variations) while ozone peaks during the afternoon (high temperature). The hindrance in ozone formation reaction is possibly the major reason for the antagonist relationship. Research works have shown that by absorbing solar energy, BC lowers the photolysis coefficient, influencing the quantity of ozone near the ground [73]. The absorbing impact of BC heats the air above the BL, suppressing and delaying the growth of the BL, finally leading to a shift in surface ozone through an alteration in the contributions from chemical and physical processes (photochemistry, vertical mixing, and advection) [74].

BC aerosols and benzene

The following plots (**Figure 13**) depict the regression analysis of BC aerosols and benzene, for

the December, January, and February months.

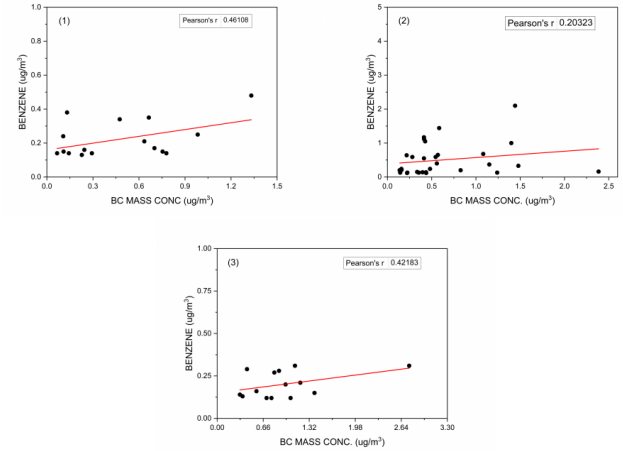

Figure 13. Same as Figure 9, but for Benzene.

A moderately positive correlation can be observed between BC and benzene for three months (0.46, 0.20, and 0.42 for December, January, and February, respectively) (**Table 3**). Benzene emissions are more concentrated towards chemical processes (chemical industry, brick kiln, smoking etc.). A positive correlation between the two can signify the possible contribution from surrounding chemical industries/brick kilns to the BC mass concentration [75]. Mostly brick kilns are in proximity to the study sites. There hasn't been much research into the interaction of BC with benzene.

Table 3. Correlation coefficient between BC aerosols and various air pollutants.

	PM2.5	PM10	O_3	CO	C_6H_6
December	0.84	0.48	–0.53	–0.73	0.46
January	0.78	0.09	–0.23	0.41	0.20
February	0.81	0	–0.39	0.46	0.42

3.6 Long-range transport of BC aerosols

Back trajectory maps were created using the HYSPLIT dispersion model to analyse the long-range transport of BC mass concentration to this site. Long-range transport is depicted using properly colour coded Trajectory Frequency and Cluster Means plots. Trajectory frequency has an average of hundreds of backward trajectories during a month, run for 96 hours at a height of 100 m at the study site.

Airmass characteristics during December 2021, January, and February 2022

The airmass back trajectory analysis shows that pollutants in the northwest direction contribute the most pollution (approximately 69%). This significant contribution is primarily the result of stubble burning events in Punjab State and the north-west districts of Haryana. Although stubble burning events are lower in December than in November (peak season), they are still sufficient to raise pollution levels at the study site. During January 2022, pollution dispersion is more widespread in the site's surrounding areas. The most came from the northwest (43%) direction. Wind is the most important factor in pollutant dispersion, and it correlated well with BC concentrations in January. The pollution outbreak during February appears to be dominated (78%) by the regions lying in the northwest direction. Wind speed during this month was found to be weak.

Relationship between fire count and BC mass concentration

The fire events, mostly from open burning and associated combustion processes (one of the principal sources of BC aerosols), are likely to have an impact on the BC mass concentration at the site. The analysis of data for December 2021, January, and February 2022 indicates no significant relationship between fire count and BC mass concentration. The reasons could be either a large separation between the fire locations and the aerosol monitoring site or unfavourable wind conditions. There were some overlapping peaks in both, but they were not consistent across the study period. Although there appear to be some similarity, nevertheless open burning is one of the major sources of BC aerosols in these regions. Studies have indicated a direct relationship between surface BC levels and biomass burning [76], and BC is an excellent aerosol indicator of wildfires and biomass burning [77,78].

4. Summary and conclusions

The motivation of the present study was to better understand the undulations in BC mass concentration and their relationship with natural/anthropogenic activities and variations in surface-level meteoro-

logical parameters during winters 2021–2022 and 2022–2023.

The key findings from the study are listed below:

● The mass concentration of BC aerosols was found to be lower and well within the safety range as compared to any urban site.

● The diurnal variation of BC mass concentration exhibited two maxima, one in the morning and the other in the late evening hours.

● The night-time BC concentrations are low as compared to those during the daytime, possibly due to less human activity, low temperature, and strong winds at night. This clearly demonstrates the significance of meteorological parameters in modulating BC concentrations over Panchgaon. Importantly, the influence of transport processes (both local and long-range) on BC variations over Panchgaon caused by surrounding Aravalli hillocks (valley-like) and resulting katabatic wind-flow patterns should not be ignored.

● Weekday BC concentrations were found to be higher than the weekend BC concentrations. Additionally, midday concentrations of BC are higher than nighttime ones. This might be a result of the high daytime convective activity, which aids in lifting more BC aerosols from the study site's surface and the vicinity.

● BC mass concentrations at the study site are found to be significantly influenced by both local and long-range sources.

● Relative humidity exhibits a negative relationship with BC mass concentration, indicating that the BC aerosols above the study area are predominantly absorbing (hydrophobic), leading to local warming.

● Although no substantial relationship was found between changes in temperature and BC mass concentration it may have an indirect role via local convective boundary layer dynamics.

● Throughout the study, there was a significant negative relationship between wind speed and BC mass concentration. The obvious reasons for this are the dispersion, dilution, and ventilation processes involved in the BC particle transformations.

● BC had a strong positive relationship with PM2.5 and a weak association with PM10 mass values, indicating some common source.

● A negative correlation between BC and O_3 indicates that BC may inhibit O_3 formation.

● A moderate positive correlation was found between BC and Benzene mass concentration, which might be due to nearby brick kilns located close to the study site.

● Trajectory analysis of long-range transport indicates that BC aerosols in the northwest (NW) direction contribute the most (50–60%). This is attributed mainly to stubble-burning activity in that direction.

● Fire emissions (count) from stubble-burning activity had a limited correlation with BC mass concentration, which may be attributed to the low number, poor brightness of the fire, low winds, and greater separation between the source (fire site) and the study location.

Authors' Contribution

Saurabh Yadav: Data downloading, analysis, plotting, table compilation and draft preparation. **Panuganti C.S. Devara** (Corresponding Author): Research idea, conceptualization, methodology, review, and editing. **S. M. Sonbawne:** Data analysis and plotting. **B. S. Murthy:** Data retrieval and analysis. **S. Tiwari**: Data analysis. **S. Wadhwa**: Data curation. **A. Kumar:** Data analysis and plotting. All authors read and approved the final manuscript.

Conflicts of Interest

The authors reported no potential conflicts of interest.

Data Availability Statement

The datasets used in this study are available on request by contacting the Corresponding Author of the paper.

Funding

This research received no external funding.

Acknowledgments

The research work reported in this paper was carried out under a Collaborative Research Program between IITM and AUH. The authors express their sincere gratitude to Hon'ble Founder President, Chancellor, Vice Chancellor, Pro Vice Chancellor, and all authorities of Amity University Haryana (AUH), Gurugram, India. The authors are also grateful to the Director, Indian Institute of Tropical Meteorology (IITM-MoES, GoI), Pune, India. Thanks, are also due to the Editor and anonymous Reviewers for their critical comments and valuable suggestions which helped to improve the original manuscript in terms of scientific content and clarity.

References

[1] Seiler, W., Fishman, J., 1981. The distribution of carbon monoxide and ozone in the free troposphere. Journal of Geophysical Research. 86(C8), 7255–7265.
DOI: https://doi.org/10.1029/jc086ic08p07255

[2] Rohr, A., McDonald, J., 2016. Health effects of carbon-containing particulate matter: Focus on sources and recent research program results. Critical Reviews in Toxicology. 46(2), 97–137.
DOI: https://doi.org/10.3109/10408444.2015.1107024

[3] Bond, T.C., Doherty, S.J., Fahey, D.W., et al., 2013. Bounding the role of BC in the climate system: A scientific assessment. Journal of Geophysical Research Atmospheres. 118(11), 5380–5552.
DOI: https://doi.org/10.1002/jgrd.50171

[4] Stocker, T.F., Qin, D., Plattner, G.K., et al., 2014. Climate change 2013: The physical science basis. Cambridge University Press: Cambridge.

[5] Safai, P.D., Raju, M.P., Budhavant, K.B., et al., 2013. Long term studies on characteristics of BC aerosols over a tropical urban station Pune, India. Atmospheric Research. 132–133, 173–184.
DOI: https://doi.org/10.1016/j.atmosres.2013.05.002

[6] Masiello, C.A., Druffel, E.R.M., 1998. BC in deep-sea sediments. Science. 280(5371), 1911–1913.
DOI: https://doi.org/10.1126/science.280.5371.1911

[7] Novakov, T., Ramanathan, V., Hansen, J.E., et al., 2003. Large historical changes of fossil-fuel black carbon aerosols. Geophysical Research Letters. 30(6).
DOI: https://doi.org/10.1029/2002GL016345

[8] Ito, A., Penner, J.E., 2005. Historical emissions of carbonaceous aerosols from biomass and fossil fuel burning for the period 1870–2000. Global Biogeochemical Cycles. 19(2), 1–14.
DOI: https://doi.org/10.1029/2004GB002374

[9] Dentener, F., Kinne, S., Bond, T., et al., 2006. Emissions of primary aerosol and precursor gases in the years 2000 and 1750 prescribed data-sets for AeroCom. Atmospheric Chemistry and Physics. 6(12), 4321–4344.
DOI: https://doi.org/10.5194/acp-6-4321-2006

[10] McConnell, J.R., Edwards, R., Kok, G.L., et al., 2007. 20th-century industrial black carbon emissions altered arctic climate forcing. Science. 317(5843), 1381–1384.
DOI: https://doi.org/10.1126/science.1144856

[11] He, Y., Zhang, G.L., 2009. Historical record of black carbon in urban soils and its environmental implications. Environmental Pollution. 157(10), 2684–2688.
DOI: https://doi.org/10.1016/j.envpol.2009.05.019

[12] Hirdman, D., Burkhart, J.F., Sodemann, H., et al., 2010. Long-term trends of black carbon and sulphate aerosol in the Arctic: Changes in atmospheric transport and source region emissions. Atmospheric Chemistry and Physics. 10(19), 9351–9368.
DOI: https://doi.org/10.5194/acp-10-9351-2010

[13] Skeie, R.B., Berntsen, T., Myhre, G., et al., 2011. Black carbon in the atmosphere and snow, from pre-industrial times until present. Atmospheric Chemistry and Physics. 11(14), 6809–6836.
DOI: https://doi.org/10.5194/acp-11-6809-2011

[14] Bond, T.C., Bhardwaj, E., Dong, R., et al., 2007. Historical emissions of black and organic carbon aerosol from energy-related combustion, 1850–2000. Global Biogeochemical Cycles. 21(2).
DOI: https://doi.org/10.1029/2006GB002840

[15] Ramanathan, V., Carmichael, G., 2008. Global and regional climate changes due to black carbon. Nature Geoscience. 1(4), 221–227.
DOI: https://doi.org/10.1038/ngeo156

[16] Brooks, J., Allan, J.D., Williams, P.I., et al., 2019. Vertical and horizontal distribution of submicron aerosol chemical composition and physical characteristics across northern India during pre-monsoon and monsoon seasons. Atmospheric Chemistry and Physics. 19(8), 5615–5634.
DOI: https://doi.org/10.5194/acp-19-5615-2019

[17] Rana, A., Jia, S., Sarkar, S., 2019. Black carbon aerosol in India: A comprehensive review of current status and future prospects. Atmospheric Research. 218, 207–230.
DOI: https://doi.org/10.1016/j.atmosres.2018.12.002

[18] Paliwal, U., Sharma, M., Burkhart, J.F., 2016. Monthly and spatially resolved black carbon emission inventory of India: Uncertainty analysis. Atmospheric Chemistry and Physics. 16(19), 12457–12476.
DOI: https://doi.org/10.5194/acp-16-12457-2016

[19] Verma, S., Ghosh, S., Boucher, O., et al., 2022. BC health impacts in the Indo-Gangetic plain: Exposures, risks, and mitigation. Science Advances. 8(31).
DOI: https://doi.org/10.1126/sciadv.abo4093

[20] Aruna, K., Kumar, T.V.L., Rao, D.N., et al., 2013. BC aerosols in a tropical semi-urban coastal environment: Effects of boundary layer dynamics and long range transport. Journal of Atmospheric and Solar-Terrestrial Physics. 104, 116–125.
DOI: https://doi.org/10.1016/j.jastp.2013.08.020

[21] Ackerman, T.P., Toon, O.B., 1982. Absorption of visible radiation in atmosphere containing mixtures of absorbing and non-absorbing particles: Erratum. Applied Optics. 21(5), 758.
DOI: https://doi.org/10.1364/AO.21.000758

[22] Akagi, S.K., Yokelson, R.J., Wiedinmyer, C., et al., 2011. Emission factors for open and domestic biomass burning for use in atmospheric models. Atmospheric Chemistry and Physics. 11(9), 4039–4072.
DOI: https://doi.org/10.5194/acp-11-4039-2011

[23] Andrews, E., Sheridan, P.J., Ogren, J.A., 2011. Seasonal differences in the vertical profiles of aerosol optical properties over rural Oklahoma. Atmospheric Chemistry and Physics. 11(20), 10661–10676.
DOI: https://doi.org/10.5194/acp-11-10661-2011

[24] Wolff, G.T., 1981. Particulate elemental carbon in the atmosphere. Journal of the Air Pollution Control Association. 31(9), 935–938.
DOI: https://doi.org/10.1080/00022470.1981.10465298

[25] Schwartz, S.E., 1996. The Whitehouse effect—Shortwave radiative forcing of climate by anthropogenic aerosols: An overview. Journal of Aerosol Science. 27(3), 359–382.
DOI: https://doi.org/10.1016/0021-8502(95)00533-1

[26] Haywood, J.M., Shine, K.P., 1997. Multi-spectral calculations of the direct radiative forcing of tropospheric sulphate and soot aerosols using a column model. Quarterly Journal of the Royal Meteorological Society. 123(543), 1907–1930.
DOI: https://doi.org/10.1002/qj.49712354307

[27] Raju, M.P., Safai, P.D., Sonbawne, S.M., et al., 2020. Black carbon aerosols over a high-altitude station, Mahabaleshwar: Radiative forcing and source apportionment. Atmospheric Pollution Research. 11(8), 1408–1417.
DOI: https://doi.org/10.1016/j.apr.2020.05.024

[28] Li, Y., Henze, D.K., Jack, D., et al., 2016. Assessing public health burden associated with exposure to ambient BC in the United States. Science of the Total Environment. 539, 515–525.
DOI: https://doi.org/10.1016/j.scitotenv.2015.08.129

[29] Cao, J., Xu, H., Xu, Q., et al., 2012. Fine

particulate matter constituents and cardiopulmonary mortality in a heavily polluted Chinese city. Environmental Health Perspectives. 120(3), 373–378.
DOI: https://doi.org/10.1289/ehp.1103671

[30] Janssen, N.A., Hoek, G., Simic-Lawson, M., et al., 2011. Black carbon as an additional indicator of the adverse health effects of airborne particles compared with PM10 and PM2.5. Environmental Health Perspectives. 119(12), 1691–1699.
DOI: https://doi.org/10.1289/ehp.1003369

[31] Elisabeth, R. Third-world stove soot is target in climate fight. New York Times, 2009 Apr 15. Available from: http://static1.1.sqspcdn.com/static/f/316880/5110141/1261163124307/NYT_black+carbon_15+April+09.pdf?token=-jY%2BN7vOjIBWiBwwpCmfeXyzbhuc%3D

[32] Abbatt, J.P.D., Benz, S., Czkzo, D.J., et al., 2006. Solid ammonium sulfate aerosols as ice nuclei: A pathway for cirrus cloud formation. Science. 313(5794), 1770–1773.
DOI: https://doi.org/10.1126/science.1129726

[33] Samad, A., Vogt, U., Panta, A., et al., 2020. Vertical distribution of particulate matter, BC and ultra-fine particles in Stuttgart, Germany. Atmospheric Pollution Research. 11(8), 1441–1450.
DOI: https://doi.org/10.1016/j.apr.2020.05.017

[34] Sandradewi, J., Prévôt, A.S.H., Szidat, S., et al., 2008. Using aerosol light abosrption measurements for the quantitative determination of wood burning and traffic emission contribution to particulate matter. Environmental Science and Technology. 42(9), 3316–3323.
DOI: https://doi.org/10.1021/es702253m

[35] Dutt, U., 2019. Application of the Aethalometer for Black Carbon Source Analysis [Internet]. Available from: https://www.researchgate.net/publication/332183185_Application_of_the_Aethalometer_for_black_carbon_source_analysis

[36] Laing, J.R., Jaffe, D.A., Sedlacek, A.J., 2020. Comparison of filter-based absorption measurements of biomass burning aerosol and background aerosol at the Mt. Bachelor observatory. Aerosol and Air Quality Research. 20(4), 663–678.
DOI: https://doi.org/10.4209/aaqr.2019.06.0298

[37] Duc, H.N., Shingles, K., White, S., et al., 2020. Spatial-temporal pattern of BC (BC) emission from biomass burning and anthropogenic sources in New South Wales and the greater metropolitan region of Sydney, Australia. Atmosphere. 11(6).
DOI: https://doi.org/10.3390/atmos11060570

[38] Sonbawne, S.M., Devara, P.C.S., Bhoyar, P.D., 2021. Multisite characterization of concurrent BC and biomass burning around COVID-19 lockdown period. Urban Climate. 39.
DOI: https://doi.org/10.1016/j.uclim.2021.100929

[39] Magee Scientific Aethalometer® Model AE33 [Internet]. Available from: https://mageesci.com/mproducts/magee-scientific-aethalometer/

[40] Weingartner, E., Saathoff, H., Schnaiter, M., et al., 2003. Absorption of light by soot particles: Determination of the absorption coefficient by means of aethalometers. Journal of Aerosol Science. 34(10), 1445–1463.
DOI: https://doi.org/10.1016/S0021-8502(03)00359-8

[41] Stein, A.F., Draxler, R.R., Rolph, G.D., et al., 2015. NOAA's HYSPLIT atmospheric transport and dispersion modeling system. Bulletin of the American Meteorological Society. 96(12), 2059–2077.
DOI: https://doi.org/10.1175/BAMS-D-14-00110.1

[42] Moya-Álvarez, A.S., Estevan, R., Martínez-Castro, D., et al., 2023. Spatial and temporal distribution of BC in Peru from the analysis of biomass burning sources and the use of numerical models. Earth Systems and Environment. 7(2), 411–430.
DOI: https://doi.org/10.1007/s41748-023-00342-4

[43] Earth Science Data Systems, N., 2016. Visible Infrared Imaging Radiometer Suite (VIIRS) [Internet]. Earthdata. Available from: https://www.earthdata.nasa.gov/learn/find-data/near-

real-time/viirs

[44] Devara, P., Munshi, P., Dumka, U., et al., 2018. Anomalous features of BC and particulate matter observed over rural station during Diwali Festival of 2015. Environmental pollution. Springer: Singapore. pp. 293–308. DOI: https://doi.org/10.1007/978-981-10-5792-2_24

[45] Babu, S.S., Moorthy, K.K., 2002. Aerosol BC over a tropical coastal station in India. Geophysical Research Letters. 29(23). DOI: https://doi.org/10.1029/2002GL015662

[46] Kompalli, S.K., Babu, S.S., Moorthy, K.K., et al., 2014. Aerosol BC characteristics over Central India: Temporal variation and its dependence on mixed layer height. Atmospheric Research. 147–148, 27–37. DOI: https://doi.org/10.1016/j.atmosres.2014.04.015

[47] Devara, P.C.S., Maheskumar, R.S., Raj, P.E., et al., 2002. Recent trends in aerosol climatology and air pollution as inferred from multi-year lidar observations over a tropical urban station. International Journal of Climatology. 22(4), 435–449. DOI: https://doi.org/10.1002/joc.745

[48] Dani, K.K., Ernest Raj, P., Devara, P.C.S., et al., 2012. Long-term trends and variability in measured multi-spectral aerosol optical depth over a tropical urban station in India. International Journal of Climatology. 32(1), 153–160. DOI: https://doi.org/10.1002/joc.2250

[49] Liu, B., Ma, Y., Gong, W., et al., 2019. The relationship between BC and atmospheric boundary layer height. Atmospheric Pollution Research. 10(1), 65–72. DOI: https://doi.org/10.1016/j.apr.2018.06.007

[50] Babu, S.S., Moorthy, K.K., 2001. Anthropogenic impact on aerosol BC mass concentration at a tropical coastal station: A case study. Current Science. 81(9), 1208–1214.

[51] Stull, R.B., 1988. An introduction to boundary layer meteorology. An introduction to boundary layer meteorology. Springer Science & Business Media: Berlin.

[52] Beegum, S.N., Moorthy, K.K., Babu, S.S., et al., 2009. Spatial distribution of aerosol BC over India during pre-monsoon season. Atmospheric Environment. 43(5), 1071–1078. DOI: https://doi.org/10.1016/j.atmosenv.2008.11.042

[53] Slater, J., Coe, H., McFiggans, G., et al., 2022. The effect of BC on aerosol-boundary layer feedback: Potential implications for urban pollution episodes. Atmospheric Chemistry and Physics. 22(4), 2937–2953. DOI: https://doi.org/10.5194/acp-22-2937-2022

[54] Rajeevan, K., Sumesh, R.K., Resmi, E.A., et al., 2019. An observational study on the variation of BC aerosol and source identification over a tropical station in south India. Atmospheric Pollution Research. 10(1), 30–44. DOI: https://doi.org/10.1016/j.apr.2018.06.009

[55] Kumar, V., Devara, P.C.S., Soni, V.K., 2023. Multisite scenarios of BC and biomass burning aerosol characteristics in India. Aerosol and Air Quality Research. 23(6). DOI: https://doi.org/10.4209/aaqr.220435

[56] Kunhikrishnan, P.K., Gupta, K.S., Ramachandran, R., et al., 1993. Study on thermal internal boundary layer structure over Thumba, India. Annales Geophysicae. 11, 52–60.

[57] Mallik, C., Venkataramani, S., Lal, S., 2012. Study of a high SO_2 event observed over an urban site in western India. Asia-Pacific Journal of Atmospheric Sciences. 48(2), 171–180. DOI: https://doi.org/10.1007/s13143-012-0017-3

[58] Hans, S., Samuel, M., Christel, F., et al., 2011. Does air pollution trigger infant mortality in western Europe? A case-crossover study. Environmental Health Perspectives. 119(7), 1017–1022. DOI: https://ehp.niehs.nih.gov/doi/10.1289/ehp.1002913

[59] Zhang, L., Shen, F., Gao, J., et al., 2020. Characteristics and potential sources of BC particles in suburban Nanjing, China. Atmospheric Pollution Research. 11(5), 981–991. DOI: https://doi.org/10.1016/j.apr.2020.02.011

[60] Lee, J., Yun, J., Kim, K.J., 2016. Monitoring of BC concentration at an inland rural area including fixed sources in Korea. Chemosphere. 143, 3–9.
DOI: https://doi.org/10.1016/j.chemosphere.2015.04.003

[61] Alappattu, D.P., Kunhikrishnan, P.K., Aloysius, M., et al., 2009. A case study of atmospheric boundary layer features during winter over a tropical inland station—Kharagpur (22.32°N, 87.32°E). Journal of Earth System Science. 118(4), 281–293.
DOI: https://doi.org/10.1007/s12040-009-0028-3

[62] Swamy, Y.V., Venkanna, R., Nikhil, G.N., et al., 2012. Impact of nitrogen oxides, volatile organic compounds and BC on atmospheric ozone levels at a semi arid urban site in Hyderabad. Aerosol and Air Quality Research. 12(4), 662–671.
DOI: https://doi.org/10.4209/aaqr.2012.01.0019

[63] Järvi, L., Junninen, H., Karppinen, A., et al., 2008. Temporal variations in BC concentrations with different time scales in Helsinki during 1996–2005. Atmospheric Chemistry and Physics. 8(4), 1017–1027.
DOI: https://doi.org/10.5194/acp-8-1017-2008

[64] Tiwari, S., Srivastava, A.K., Bisht, D.S., et al., 2013. Diurnal and seasonal variations of black carbon and PM2.5 over New Delhi, India: Influence of meteorology. Atmospheric Research. 125–126, 50–62.
DOI: https://doi.org/10.1016/j.atmosres.2013.01.011

[65] Mahapatra, P.S., Panda, S., Das, N., et al., 2013. Variation in BC mass concentration over an urban site in the eastern coastal plains of the Indian sub-continent. Theoretical and Applied Climatology. 117(1), 133–147.
DOI: https://doi.org/10.1007/s00704-013-0984-z

[66] Spalding, C., Hsu, S., Patel, M.M., et al., 2011. The effect of wind direction and speed on BC concentrations in northern Manhattan and the Bronx. Journal of Allergy and Clinical Immunology. 127(2), AB96.
DOI: https://doi.org/10.1016/j.jaci.2010.12.387

[67] Jereb, B., Gajšek, B., Šipek, G., et al., 2021. Traffic density-related BC distribution: Impact of wind in a basin town. International Journal of Environmental Research and Public Health. 18(12).
DOI: https://doi.org/10.3390/ijerph18126490

[68] Gong, W., Zhang, T., Zhu, Z., et al., 2015. Characteristics of PM1.0, PM2.5, and PM10, and their relation to black carbon in Wuhan, Central China. Atmosphere. 6(9), 1377–1387.
DOI: https://doi.org/10.3390/atmos6091377

[69] Choi, Y., Kanaya, Y., Park, S.M., et al., 2020. Regional variability in BC and carbon monoxide ratio from long-term observations over East Asia: Assessment of representativeness for BC (BC) and carbon monoxide (CO) emission inventories. Atmospheric Chemistry and Physics. 20(1), 83–98.
DOI: https://doi.org/10.5194/acp-20-83-2020

[70] Gupta, T., Mandariya, A., 2013. Sources of submicron aerosol during fog-dominated wintertime at Kanpur. Environmental Science and Pollution Research. 20(8), 5615–5629.
DOI: https://doi.org/10.1007/s11356-013-1580-6

[71] Tan, Y., Zhao, D., Wang, H., et al., 2021. Impact of BC on surface ozone in the yangtze river delta from 2015 to 2018. Atmosphere. 12(5).
DOI: https://doi.org/10.3390/atmos12050626

[72] Latha, K.M., Badarinath, K.V.S., 2004. Correlation between BC aerosols, carbon monoxide and tropospheric ozone over a tropical urban site. Atmospheric Research. 71(4), 265–274.
DOI: https://doi.org/10.1016/j.atmosres.2004.06.004

[73] An, J., Lv, H., Xue, M., et al., 2021. Analysis of the effect of optical properties of BC on ozone in an urban environment at the Yangtze River Delta, China. Advances in Atmospheric Sciences. 38(7), 1153–1164.
DOI: https://doi.org/10.1007/s00376-021-0367-9

[74] Gao, J., Zhu, B., Xiao, H., et al., 2018. Effects of BC and boundary layer interaction on surface ozone in Nanjing, China. Atmospheric Chemistry and Physics. 18(10), 7081–7094. DOI: https://doi.org/10.5194/acp-18-7081-2018

[75] Wang, F., Xu, J., Huang, Y., et al., 2021. Characterization of BC and its correlations with VOCs in the northern region of Hangzhou Bay in Shanghai, China. Atmosphere. 12(7). DOI: https://doi.org/10.3390/atmos12070870

[76] Majumdar, D., 2023. Spatial distribution and temporal variation of biomass burning and surface BC concentrations during summer (2015–2021) in India. Air Quality, Atmosphere and Health. 16(3), 459–476. DOI: https://doi.org/10.1007/s11869-022-01284-y

[77] Cheng, M.D., 2014. Geolocating Russian sources for Arctic BC. Atmospheric Environment. 92, 398–410. DOI: https://doi.org/10.1016/j.atmosenv.2014.04.031

[78] Dumka, U.C., Kaskaoutis, D.G., Tiwari, S., et al., 2018. Assessment of biomass burning and fossil fuel contribution to BC concentrations in Delhi during winter. Atmospheric Environment. 194, 93–109. DOI: https://doi.org/10.1016/j.atmosenv.2018.09.033

BILINGUAL PUBLISHING GROUP

Journal of Atmospheric Science Research

https://journals.bilpubgroup.com/index.php/jasr/index

ARTICLE

Control of the Dust Vertical Distribution over Western Africa by Convection and Scavenging

H. Senghor[1*], R. Pilon[3], B. Diallo[3], J. Escribano[4], F. Hourdin[3], J. Y. Grandpeix[3], O. Boucher[3], M. Gueye[6], A. T. Gaye[2], E. Machu[5]

[1] *National Agency of Civil Aviation and Meteorology, PO BOX 8184, Senegal*
[2] *Laboratory for Atmospheric-Oceanic Physics-Simeon Fongang, Cheikh Anta Diop University, Dakar, 10700, Senegal*
[3] *Laboratory of Dynamic Meteorology (LMD), CNRS/IPSL/UMPC, Paris, 75231, France*
[4] *Atmospheric Composition Group, Barcelona Supercomputing Center (BSC), Barcelona, 08034, Spain*
[5] *Spatial and Physical Oceanography Laboratory (LOPS), Brest University, CNRS, IRD, Plouzane, 29280, France*
[6] *Department of Mathematics and Computer Science, University of Sine Saloum El Hadj Ibrahima Niasse, PO BOX 55, Kaolack, Senegal*

ABSTRACT

Saharan dust represents more than 50% of the total desert dust emitted around the globe and its radiative effect significantly affects the atmospheric circulation at a continental scale. Previous studies on dust vertical distribution and the Saharan Air Layer (SAL) showed some shortcomings that could be attributed to imperfect representation of the effects of deep convection and scavenging. The authors investigate here the role of deep convective transport and scavenging on the vertical distribution of mineral dust over Western Africa. Using multi-year (2006–2010) simulations performed with the variable-resolution (zoomed) version of the LMDZ climate model. Simulations are compared with aerosol amounts recorded by the Aerosol Robotic Network (AERONET) and with vertical profiles of the Cloud-Aerosol Lidar with Orthogonal Polarization (CALIOP) measurements. LMDZ allows a thorough examination of the respective roles of deep convective transport, convective and stratiform scavenging, boundary layer transport, and advection processes on the vertical mineral dust distribution over Western Africa. The comparison of simulated dust Aerosol Optical Depth (AOD) and distribution with measurements suggest that scavenging in deep convection and subsequent re-evaporation of dusty rainfall in the lower troposphere are critical processes for explaining the vertical distribution of desert dust. These processes play a key role in maintaining a well-defined dust layer with a sharp transition at the top of the SAL and in establishing the seasonal cycle of dust distribution. This vertical distribution is further reshaped offshore in the Inter-Tropical Convergence Zone (ITCZ) over the Atlantic Ocean by marine boundary layer turbulent and convective transport and wet deposition at the surface.

Keywords: Dust; Vertical distribution; Sahara; Sahel; West Africa; Climate model; Convection; Scavenging; ITCZ

*CORRESPONDING AUTHOR:
Habib Senghor, National Agency of Civil Aviation and Meteorology, PO BOX 8184, Senegal; Email: habib.senghor@ucad.edu.sn

ARTICLE INFO
Received: 10 October 2023 | Revised: 21 December 2023 | Accepted: 26 December 2023 | Published Online: 8 January 2024
DOI: https://doi.org/10.30564/jasr.v7i1.6009

CITATION
Senghor, H., Pilon, R., Diallo, B., et al., 2024. Control of the Dust Vertical Distribution over Western Africa by Convection and Scavenging. Journal of Atmospheric Science Research. 7(1): 19–39. DOI: https://doi.org/10.30564/jasr.v7i1.6009

1. Introduction

North Africa is the world's largest source of dust with more than 55% of global dust emissions [1] and approximately 60% of this dust is transported from these arid and semi-arid emission areas across the Atlantic Ocean [2,3]. Mineral dust is known to negatively impact the West African economy [4] and human health in the Sahelian region [5]. It has been associated with mortality during warmer months in Mediterranean cities [6]. Long-range transport of Saharan dust is widely known as reported by Zanobetti and Schwartz (2009) for the United States: Saharan dust can intrude into the Caribbean Basin and the northern American continent after being lifted into the atmosphere by winds over West Africa and then transported across the Atlantic Ocean within the Saharan Air Layer [7]. Dust affects the local energy balance and modifies the hydrological cycle [8] through aerosol-radiation and aerosol-clouds interactions [3,9], but also through changes in atmospheric stability by absorption of solar radiation and surface thermal radiation [10]. Seasonal dust emission variability is highly driven by the variability of surface winds and in particular by variations in the low-level jet responsible for the maximum surface wind that occurs when momentum is transported downward to the surface by boundary layer convection [11,12]. In early summer, turbulence and high winds surface can raise heavy dust loading especially at the leading edge of the cold pool outflows from downdrafts of moist convection when the evaporating rainfall cools the air in the subcloud layer [13]. Dust storms induced by cold pool outflows are called "haboob" (a violent dust storm or sandstorm). This mechanism allows air mass to sink to the surface, particularly if the environment is dry adiabatic [14]. Furthermore, deep convection impacts the aerosol vertical distribution, which is also controlled by atmospheric transport and scavenging [15–17]. Considerable efforts have been made to study the role of aerosols in the Earth system [18] and more specifically over West Africa [19–21].

Recent modeling studies have shown that the dust cycle (defined as the emission, transport, and deposition of dust) depends on weather conditions and is highly sensitive to the removal by atmospheric hydrometeors [22]. Modeling has helped to narrow uncertainties in the spatial distribution of aerosols at the global scale [12,23–25]. Given the size of the domain involved in dust propagation, General Circulation Models (GCMs) are often used to tackle the dust problem and are used for a full description of all stages of its atmospheric lifecycle [26].

Nonetheless, models need to be improved to represent the vertical transport of dust to better explain the mechanisms controlling the aerosol vertical redistribution of dust over the Sahelo-Saharan region. For dry deposition, it is a common practice to choose a constant deposition velocity of aerosol in the first layers of the model for fine particles. The sedimentation or gravitational settling is usually estimated from simple parameterizations that can lead to the large spread in aerosol residence time shown in model intercomparison studies [27]. The sensitivity of the representation of aerosol vertical profiles and their physical processes is, to our knowledge, poorly studied in the literature. Additionally, particle size distribution, optical properties, and dust shape and composition are still poorly represented in models [28,29].

Representing the effects of transport and clouds is even more challenging. To address this problem, some authors have used terragenic (^{210}Pb) and cosmogenic (^{7}Be) aerosol tracers to estimate the impact of the removal of aerosol in the atmosphere by the convective and stratiform precipitations in GCMs [17,30–32].

We build on the inspiring effort by Pilon et al. (2015) to better represent the transport of dust and scavenging in the deep convective scheme in the LMDZ model in order to show the vertical structure of dust distribution in the SAL, over the Western Africa region, and its control by convective transport and scavenging.

This study provides additional insights into the convective transport and scavenging of Saharan dust through quantitative diagnostics of dust distribution and through the assessment of the contribution of

each physical process involved in this distribution. For this purpose, we use the new configuration of the LMDZ model coupled online with the Simplified Aerosol Model [12,24].

Section 2 introduces the model and describes the contribution of physical processes of dust transport in the LMDZ model. The methodology and the validation dataset are presented also in this section. Section 3 is devoted to the analysis of the results and the effects of the transport and scavenging of dust by convective processes. Finally, we discuss results in Section 4 and draw general conclusions in Section 5.

2. Experimental design

2.1 Climate modeling

The work presented here relies on the Laboratoire de Météorologie Dynamique GCM LMDZ version 6A [33], and more specifically the version used for the sixth Coupled Model Intercomparison Project (CMIP6) simulations. This model version includes a new set of physical parameterizations called "New Physics" addressing particular convective clouds. The parameterization of deep convection uses a modified version [34] of Emanuel's mass-flux scheme [35] coupled to a specific parameterization of cold pools [36,37] and to a stochastic triggering designed to make the frequency of occurrence of new convective systems within a mesh aware of the grid cell size [38]. The boundary layer convection is represented by the thermal plume model. It is described in Hourdin et al. (2019) [39] and now accounts for stratocumulus clouds. Large-scale condensation processes follow the work of Le Treut and Li (1991) [40]. This model version also includes the introduction of the latent heat release associated with water freezing and a new parameterization of non-orographic gravity waves targeting the representation of the Quasi-Biennial Oscillation (QBO). LMDZ has the particular ability to allow the deformation of its horizontal grid to focus on a region of interest [41,42].

LMDZ also allows the transport of an arbitrary number of tracers such as dust here. In this work, dust is considered as a tracer and is dealt with as any other tracer. An overview of tracer transport in the LMDZ climate model is provided by Heinrich and Jamelot (2011). A more detailed description is given in Section 2.3. Specific work was dedicated to the introduction of convective transport and scavenging in the Emanuel convective scheme and the modification of the large-scale condensation scavenging [17].

The LMDZ model is run here at a resolution of 1° × 1° over the domain 70°W–70°E; 0°N–40°N (the zoom is centered at 5°W, 19°N), with 39 hybrid sigma coordinate levels. The Simplified Aerosol Model (detailed in the next subsection) is embedded in LMDZ and provides the capability to represent different dust bins, their emission, lifting, and deposition.

Two five-year simulations have been performed after 10 years of spin-up as in Wang et al. (2018) [43] to reach groundwater table stability in the Organising Carbon and Hydrology in Dynamic Ecosystems (ORCHIDEE) land surface model coupled to LMDZ6A [44,45]. Both simulations only differ by the activation of large-scale and convective scavenging. These simulations are here in after referred to as NOSCAV and SCAV, respectively (**Table 1**). The Simulation with Scavenging (SCAV) serves as a control case. The time step for the computation of physic parameterization is 15 minutes in both simulations.

Owing to the constraints of computer time and the project timeline, only one LMDZ simulation has been performed for each configuration. The two simulations cover the period 2006–2010 when the observational measurements from African Monsoon Multidisciplinary Analysis (AMMA) were fully operational [46]. Horizontal winds were relaxed towards the European Centre for Medium-Range Weather Forecasts (ECMWF) ERA-Interim reanalysis [47], with a 48 h time relaxation in the zoom area and 3 h outside the grid-box as in Hourdin et al. (2015) [12]. Although ERA-Interim has been discontinued and replaced by ERA-5 reanalysis [48], the latter was not

available at the time the simulation was made. Test runs were performed using ERA-5 reanalysis wind but no significant difference was seen.

Table 1. LMDZ model with simulations period and NP package with and without scavenging, respectively.

Simulations	Configurations	Period (years)
SCAV	NP + Scavenging	2006–2010
NOSCAV	NP + No scavenging	

2.2 Aerosol model

We use the Simplified Aerosol Model (SPLA), originally developed by Huneeus et al. (2009) SPLA is an aerosol model of intermediate complexity that is fully embedded in the LMDZ model and has been used to estimate global aerosol emissions [49].

Escribano et al. (2016) have made the original version of SPLA compatible with LMDZ6A used in this research work. Thus, the aerosol model includes surface emissions and dust particles released by the evaporation cloud process, dry deposition, scavenging, convective transport, boundary layer mixing, transport from subgrid-scale thermals [12], and sedimentation for coarse mode aerosols [24].

The configuration of SPLA used here represents aerosols with five tracers: aerosol precursors (lumped together as a single species), fine aerosols, coarse sea salt aerosols with diameters ranging from 1–40 μm, and two coarse modes of desert dust. Dust thus contributes to three different bins: The Super Coarse Dust (SCDU) corresponds to diameters ranging from 6–30 μm, the Coarse or Intermediate Dust (CODU) to diameters ranging between 1 and 6 μm, and the Fine Particles (FINE) include to dust particles with diameters smaller than 1 μm [24]. They are listed in **Table 2**. In this study, emissions of aerosols other than dust are set to null. Fine aerosol thus consists only of dust fine mode. The emission scheme is adapted from the CHIMERE-Dust air quality model [50]. The dust production model is composed essentially of a saltation flux scheme from Marticorena and Bergametti 1995 [51] and a sandblasting model from Alfaro and Gomes (2001) [52]. Threshold friction velocities are estimated following Shao and Lu (2000) [53] and corrected by a drag efficiency coefficient [54]. SPLA contains the different coefficients for aerosol types.

The SPLA model relies on the land surface model to compute the stocks of water and carbon in the different soil and plant reservoirs, which the emission scheme depends upon.

Large-scale scavenging is composed of in-cloud (nucleation), below-cloud (impaction), and evaporation. The efficiency of in-cloud scavenging for dust aerosols is set to a value of 0.7 as in LMDZ, meaning that 30% of the dust aerosols are assumed to remain interstitial in the cloud. No distinction is made between hydrophilic and hydrophobic aerosols [55]. Below-cloud impaction efficiency is set to 0.5 [17,56].

Table 2. Dust size bins in the SPLA model.

Mineral dust	FINE	CODU	SCDU
Size (μm)	< 1	1–6	6–30

2.3 Representation of atmospheric transport

We recap here the treatment of LMDZ (and also the SPLA model) with dust transport, scavenging and the decomposition of tracer transport in its various contributions.

At each model time step, the tracer concentration in one grid cell is affected by the effects of the large-scale advection (computed with a second-order finite-volume; see Hourdin and Armengaud, 1999 [57] and of the various physical parameterizations that can affect tracers. The total tracer q tendency reads,

$$(\partial_t q)_{total} = (\partial_t q)_{adv} + (\partial_t q)_{phy} \quad (1)$$

where $(\partial_t q)_{adv}$ is the effect of large-scale advection and $(\partial_t q)_{phy}$ is the total effect of the physical parameterization. This physical tendency can be further decomposed as:

$$(\partial_t q)_{phy} = (\partial_t q)_{turbl} + (\partial_t q)_{therm} + (\partial_t q)_{cv} + (\partial_t q)_{lsscav} + (\partial_t q)_{sed} \quad (2)$$

where $(\partial_t q)_{turbl}$ denotes the transport induced by the turbulent diffusion in the atmospheric boundary layer, $(\partial_t q)_{therm}$ is the tendency induced by the ther-

mal plume model, $(\partial_t q)_{cv}$ denotes the transport and the scavenging by the Emanuel convection scheme, $(\partial_t q)_{lsscav}$ is the tendency induced by the large-scale scavenging, and finally, $(\partial_t q)_{sed}$ denotes the effect of tracer sedimentation. Each temporal variation of tracer concentration in the model physics is detailed below.

The turbulent transport in the planetary boundary layer is treated as a vertical diffusion with an eddy diffusivity *Kz* computed from the turbulent kinetic energy prognostic equation that follows Yamada (1983) [58].

The effect of large-scale scavenging is as follows:

$$(\partial_t q)_{lsscav} = (\partial_t q)_{ls,nucleation} + (\partial_t q)_{ls,impaction} + (\partial_t q)_{ls,evap} \quad (3)$$

where $(\partial_t q)_{ls,nucleation}$ is proportional to the conversion rate of cloud water into precipitation and the cloud fraction. The nucleation model is a modification from Reddy and Boucher (2004) [56] and aims to follow closely the large-scale condensation parameterization; $(\partial_t q)_{ls,impaction}$ is proportional to the precipitation flux and takes into account the impaction efficiency of raindrops and snowflakes;0 $(\partial_t q)_{ls,evap}$ depends on the precipitation flux. Each of these three tendencies is detailed in the appendix of Pilon et al. (2015) [17].

Dry deposition flux to the ground is assumed to be proportional to the aerosol concentration in the lowest model layer and to a prescribed velocity respectively of 0.1 cm. s^{-1} for FINE dust mode and 1.2 cm.s^{-1} for coarse dust [55].

Finally, deep convection affects the tracer distribution through both transport and scavenging in both the saturated and unsaturated drafts (which are separated by (1) precipitating water and (2) the air flowing down in the draft) constituting the mass fluxes of Emanuel's scheme. For analysis and in contrast to the study of Pilon et al. (2015) [17], we split the effect of deep convection on the tracer distribution into three tendencies reflecting the scavenging in saturated drafts $(\partial_t q)_{cvsscav}$, the scavenging in unsaturated drafts $(\partial_t q)_{cvunscav}$, and the deep convective transport by both drafts $(\partial_t q)_{cvtrsp}$.

$$(\partial_t q)_{cv} = (\partial_t q)_{cvtrsp} + (\partial_t q)_{cvsscav} + (\partial_t q)_{cvunscav} \quad (4)$$

2.4 Validation data

We compare simulated monthly mean AOD computed from the daytime averaged AOD between 2006 and 2010 to the observed AOD from AERONET sun photometers [59,60] (**Figure 1**). We also use the Level 2 product of Cloud-Aerosol Lidar and Infrared Pathfinder Satellite Observations (CALIPSO) launched on 28 April 2006 [61,62]. CALIPSO flies as part of the International Afternoon Constellation (A-Train) and provides global coverage of clouds and aerosol properties [63]. The latter are optical and physical properties obtained from the CALIOP onboard CALIPSO. The Vertical Feature Mask (VFM) algorithm is used to discriminate clouds and aerosol types [64,65]. We use CALIOP data from June 2006 to December 2010. We then compute the Dust Occurrence Frequency (DOF) using the same method found as in Adams et al. (2012) and Senghor et al. (2017) [65,66]:

$$DOF(x,y,z) = \frac{\sum_{n=0}^{N} p_n(x,y,z)}{\sum_{n=0}^{N} s_n(x,y,z)} \forall x,y,z \quad (5)$$

where p is the occurrence probability of dust at a grid point of longitude x, latitude y, and altitude z. s is the total number of valid satellite tracks in the grid-box, and N is the total number of grid points. The occurrences in the longitude (x) are summed and normalized by the total valid satellite tracks in the range 35°W–10°E using Equation (5). A horizontal grid spacing of 0.5° × 0.5° is used for grid data. The vertical resolution is 30 m for 290 vertical levels between –0.5 and 8 km above sea level. For the retrieval of the extinction coefficient from CALIOP, a Lidar ratio is required to be used for the aerosol type. Schuster et al. (2012) emphasized that the Lidar ratio shows a significant variability within the Sahara region [67]. Gasteiger et al. (2011) have shown that the Lidar ratio may also strongly depend on the shape and size of particles [28]. To avoid this dependency, we use qualitative information with the VFM for the estimation of the DOF as in Tsamalis et al. (2013) [68]. We are using the dust mass concentrations for the size bins with diameters ranging from 0.01–30 μm [24] to calculate the mineral dust occurrence for latitudinal cross-sections 12°–21°N in the model. We

use mass concentrations from the model outputs to compute the probability of DOF in the LMDZ model at each grid point when CALIPSO overpasses our domain between 10:00 and 15:00 UTC like all satellites in the Afternoon constellation (A-Train). For each valid satellite track, the dust occurrence is defined by the number concentration at each grid point if the mass concentration is larger than the threshold of 2.65 $g.cm^{-3}$ and 0 otherwise [69]. The probability is obtained when this number is divided by the sum of the number concentration in the grid box [65,67,68]. We have calculated the vertical coordinate of the model in km as in Wallace and Hobbs (2006) [70].

3. Results

We present here the assessment of the LMDZ/SPLA model in terms of AOD and vertical distribution of dust. We show the effect of the activation of scavenging by comparing two simulations: A control simulation where the scavenging is activated, and another one without activation of the scavenging (see **Table 1**). We also discuss the importance of the various components of the large-scale and parameterized vertical transport by decomposing this transport according to Equation (4).

3.1 Comparison of simulated and observed AOD

To assess the column-integrated aerosol amount simulated by the model, we made a comparison of the AOD at 550 nm between SCAV/NOSCAV simulations, and AERONET measurements [59]. As discriminated in Senghor et al. 2017 observed that AOD for dust is defined by using the Angstrom Exponent (AE) [65]. Only mineral dust is considered in the calculation of AOD from the SCAV and NOSCAV simulations. The comparison is made at different stations of the AERONET network in the Sahel region: Banizoumbou [13.54°N, 2.66°E] (**Figure 1b**), Agoufou [15.34°N, 1.47°W] (**Figure 1a**), Cinzana [13.27°N, 5.93°W] (**Figure 1c**) and Dakar [14.39°N, 16.95°W] (**Figure 1d**). The AERONET data show a clear annual cycle over the Sahel with a bimodal structure. The highest values of AOD are 0.6 and 0.7 for March and June in Dakar and Cinzana, respectively. Over Agoufou and Banizoumbou, the maximum is obtained respectively in June and April with a slightly higher value of AOD (0.8). The SCAV simulation reproduces a seasonal cycle of AOD in agreement with observations in West Africa with a maximum atmospheric aerosol loading in the dry season and a minimum AOD in the rainy season. The model underestimates slightly the AOD over Banizoumbou, Cinzana, and Agoufou in the dry season when the contribution of the biomass burning is maximum over Guinea Golf countries [71] and overestimates AOD over Dakar all along the year. The AOD from the SCAV simulation is similar to the observation during the summer and autumn seasons. By comparison, the NOSCAV strongly overestimates the atmospheric dust loading (AOD of 2 to 2.5) and shows a maximum in July–August. In July, the largest values of observed AOD (**Figure 1**) are also simulated in the model as well as the intensification of the westward dust transport in the SAL. Overall, **Figure 1** shows that the model is able to detect and reproduce the most active dust sources established from field campaigns over West Africa [71].

To further assess the spatial distribution of modeled dust aerosols (**Figures 2a, 2b, 2e and 2f**), Deep Blue AOD at 550 nm from Modis/Terra product (**Figures 2c and 2d**) is used for quantitative validation. In January, the transport of dust plume observed by the satellite between 0° and 20°N is well reproduced by the model as well as the active source located southwest of Mauritania close to the border with Senegal (**Figures 2a, 2c, and 2e**). The detection of these sources is missed by the satellite, but field campaigns, such as the Saharan Aerosol Long-Range Transport and Aerosol-Cloud-Interaction Experiment [71]; **Figure 5** shows that this location contains one of the most active dust sources in Western Africa. The model is in reasonable agreement with CALIPSO observation which shows a reinforcement of the dust layer on both sides, i.e. land and ocean (**Figure 3a**). In July, heavy atmospheric dust loading is observed by Modis (**Figure 2d**) between 10° and 25°N. **Figures 2b and 2f** show that, both models reproduce the strong seasonal change in the airborne

dust over Sahel as observed by satellites.

3.2 Vertical structure of the Saharan air layer

The vertical distribution of observed and simulated mineral dust in West Africa (band of latitude 12°–21°N) is marked by a strong seasonal variability (**Figure 3**). More dust is suspended in the atmosphere during boreal summer than during winter over the whole LMDZ domain. This seasonal cycle is shown by observations (**Figures 3a and 3c**) and is well captured by the model (**Figures 3b and 3d**). The larger dust occurrence obtained in summer is due to the stronger activity of the North African dust sources as shown by satellite observations and different field campaigns [71–73]. In winter, the vertical distribution of dust in the longitude band 12°–17°W is limited between the surface and 3 km and shows a maximum of dust occurrence between the surface and 2 km (**Figure 3a**). The experiment SCAV exhibits a maximum occurrence of dust in the same longitudinal cross-sections, but at a lower altitude and over a thinner atmospheric boundary layer less than the observations (**Figure 3b**). At the transition zone between the continent and the Atlantic Ocean (17°W; black dashed line in **Figure 3**), the dust layer is in contact with the ocean surface and the model can reproduce this structure of the dust layer. In summer, observations show that mineral dust is vertically distributed between the surface and 6 km, with a significant dust occurrence between 2 and 5 km (**Figure 3c**) within the SAL [65,68,74]. For both seasons, the NOSCAV simulation shows heavier atmospheric dust loading than model SCAV and observations (**Figures 3f and 3e**). At the transition zone (17°W), the Lidar measurements show a vertical discontinuity of dust layers between land and ocean surfaces. The dust in the model extends less in altitude and the occurrences are slightly higher but the vertical structure is well preserved. The model is also capable of reproducing the structure of the dust layer at the transition zone between land and ocean. In the following section, we will explain the mechanisms that control the elevation of dust layers over the ocean [65,66,68] and the westward dust transport away from the main dust sources and at the transition zone.

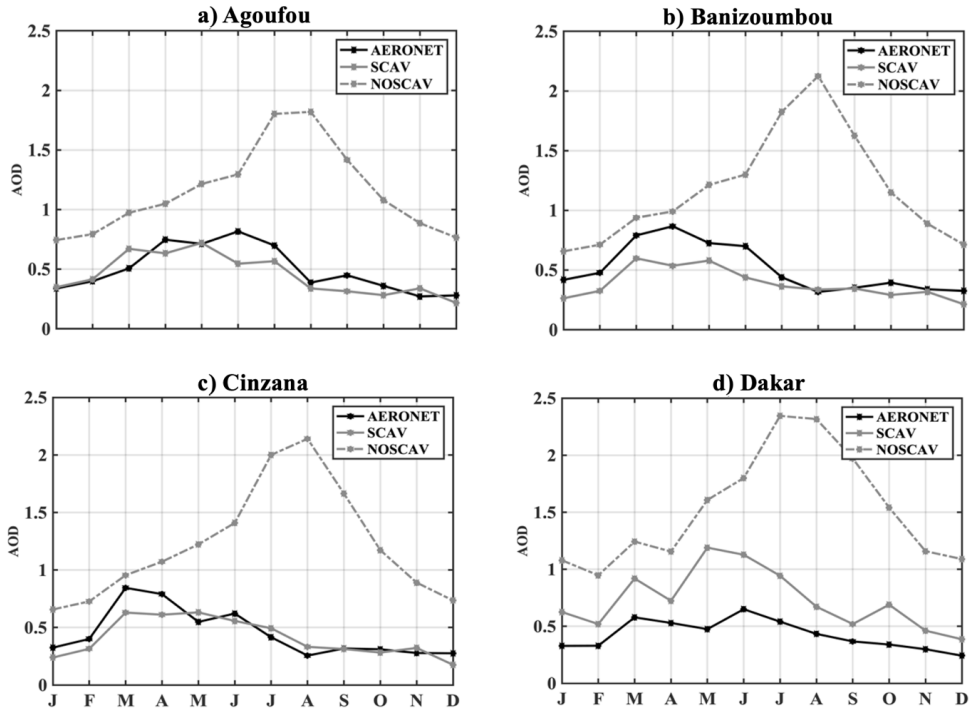

Figure 1. Modeled and observed monthly averaged AOD at 550 nm at four AERONET stations in the Sahel region (Agoufou (a), Banizoumbou (b), Cinzana (c) and Dakar (d)) during the period 2006–2010. The dashed gray line represents the AOD from the NOSCAV simulation, the solid gray line represents the SCAV simulation, and the black line is for AERONET data.

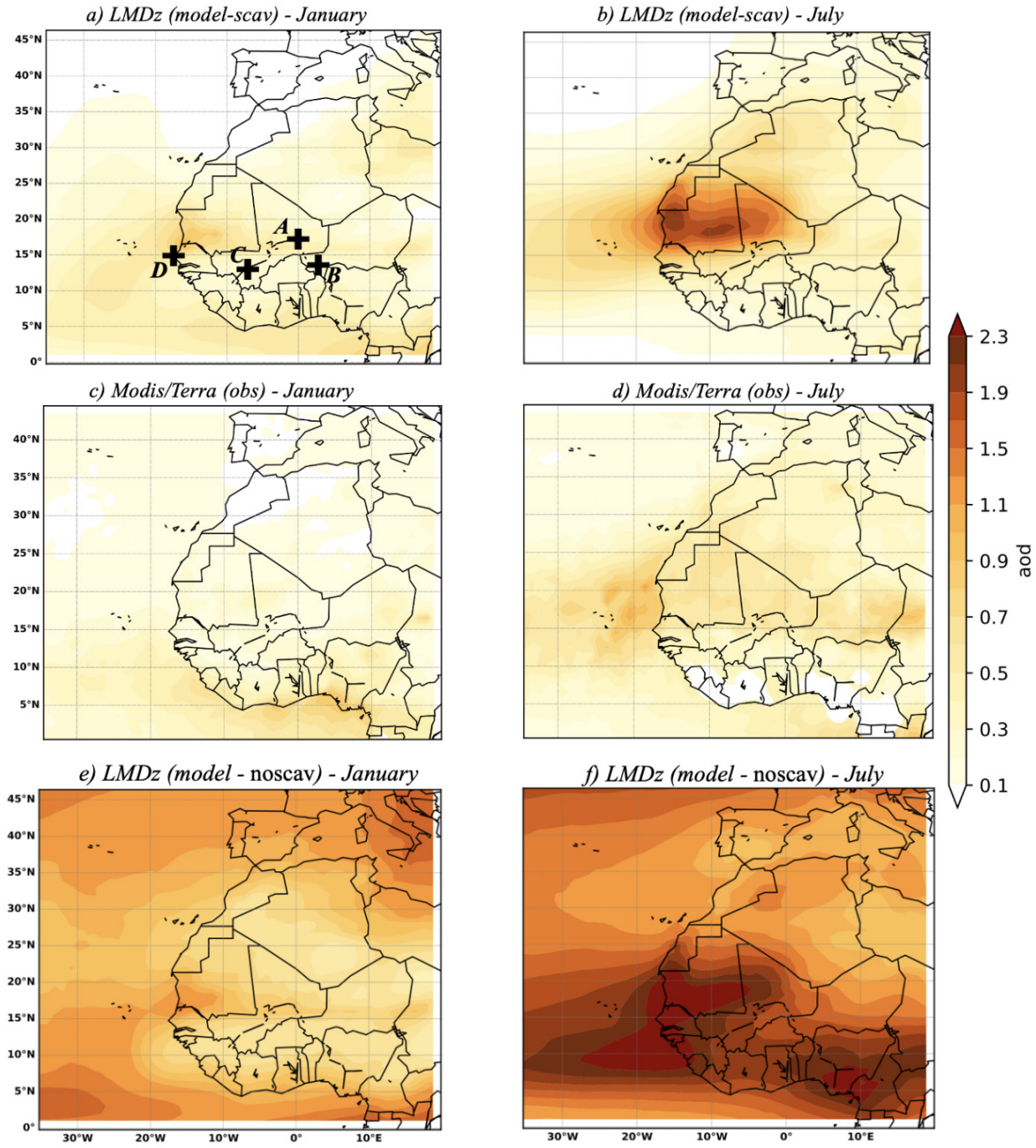

Figure 2. Monthly averaged spatial distributions of AOD at 550 nm, from 2006 to 2010 for January (left panels) and for July (right panels), in LMDZ simulations (a and b for SCAV; e and f for NOSCAV). c) and d) AOD retrievals from MODIS/Terra product and mapped onto the model grid. The A, B, C and D labels correspond to the AERONET stations in Agoufou, Banizoumbou, Cinzana and Dakar, respectively, all located in the Sahel region.

3.3 Control by the large-scale circulation

Figure 4 illustrates the seasonal variation of the vertical distribution of dust concentration over Western Africa. We averaged the two dust bins SCDU and FINE in the latitude range 16°W–10°E where the dust emission and transport occur in summer [46,71]. In January and over continents (**Figure 4**), the simulated wind field shows the Harmattan flux near the surface and a strong mass flux subsidence around 20°N, which blocks the vertical uplift of dust at 850 hPa. All sizes of dust are lifted over the Intertropical discontinuity by dry convection, but only the FINE mode is elevated in higher layers, up to 600 hPa at 0°N. The large-scale circulation is responsible for dust vertical transport over the continent in winter when the convergence of air masses from the Harmattan and the monsoon flux occurs, as described by Hamilton et al. (1945) and Stuut et al. (2005) [75,76]. South of 10°N, the vertical distribution of dust over West Africa is dominated by the convective updrafts in the ITCZ (**Figure 4a**). This strong vertical transport brings aerosols up to 600 hPa at the Equator. The Hadley cell plays an important role in controlling the dust vertical distribution by stopping the dust elevation at 850 hPa in the latitudinal range 20°–30°N. The westward transport of dust over the Atlantic Ocean induces an important dry deposition along the way with 90% of SCDU removed between land and Ocean (**Figures 4c and 3c**). The FINE concentration decreased by about 50% during their westward transport between 10°E and 35°W. The air subsidence associated with the Azores anticyclone blocks the elevation of the aerosol layers between 10° and 20°N but there is an important vertical transport of FINE between 0° and 10°S and 18°–35°W (**Figure 4c**) in agreement with observations [65,77,78]. As shown in **Figures 3a, 3b, and 3f**, a clear homogeneous transition of the vertical distribution of aerosols is seen between land and ocean with a dust layer in contact with the ocean surface (**Figure 4c**). In July, overland (**Figure 4b**), the maximum dust concentrations reach about 105 $\mu g.m^{-3}$ for the SCDU, 56 $\mu g.m^{-3}$ for CODU, and 5 $\mu g.m^{-3}$ for FINE. During summer, the effect of the Hadley cell on the dust vertical distribution is not as strong as in winter. The ITCZ signal is clear and intense in summer as shown by the strong wind of 0°–20°N (**Figure 4b**). The divergence of the air masses is located at 100 hPa in summer, whereas it occurs at 500 hPa in winter (**Figures 4b and 4a**). Above the dry convection in North Africa, the descending branch of the Hadley cell limits the vertical transport of desert dust at 500 hPa between 10° and 20°N in the model (**Figure 4b**). This is in agreement with previous studies based on observations [79–82]. The CODU and FINE concentrations decrease during their westward transport but less than for the SCDU particles (see Sections 3.4 and 3.5). The elevation of the dust layer located in the latitudinal cross-section 12°–20°N is similar to CALIOP observations (**Figures 3c–3d**). In the tropical eastern Atlantic basin (35°W–18°W), the maximum dust concentrations in the layer 2–5 km induce a weak dry deposition over the Ocean in both models as already underlined in Chiapello et al. (1995); Liu et al. (2012); Tsamalis et al. (2013) or Senghor et al. (2017) [65,68,83,84].

To further assess the vertical distribution of dust, vertical profiles of the simulated DOF are compared with observations in **Figure 5**. Both simulations can reproduce the altitude of the maximum DOF located around 3.5 km, but underestimate the redistribution of dust in the troposphere (from the surface to 3 km) overland, particularly in the SCAV simulation (**Figure 5a**). The NOSCAV simulation catches a maximum value similar to the observation of around 3.5 km. Both simulations are able to capture the inversion of DOF below 1 km and above 5 km overland (**Figure 5a**) as well as over the ocean (**Figure 5b**). Over the ocean, the two simulated DOF profiles show a distinct behavior compared to observations. The SCAV simulation appears to better simulate the DOF profile between 1.5 and 3.5 km where the maximum dust is observed (**Figure 5b**). However, both simulations underestimate the dust distribution above 4.5 km and from the surface to around 1 km.

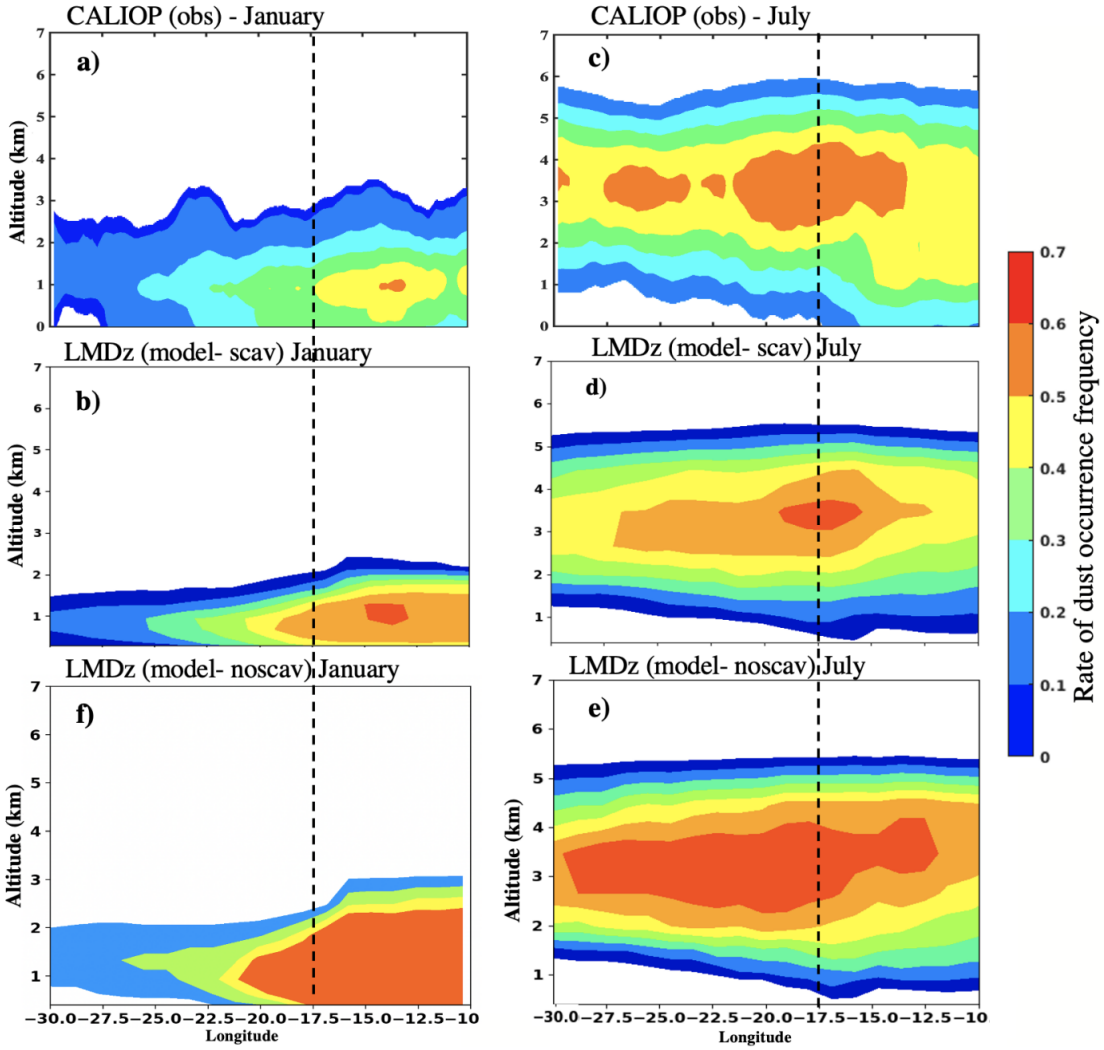

Figure 3. Vertical distribution of the dust aerosol occurrence frequency averaged over West Africa between latitudes 12°–21°N during January ((a) observations, (b) model (SCAV), and (f) model (NOSCAV)) and July ((c) observations, (d) model (SCAV), and (e) model (NOSCAV)). e) represents the vertical distribution of the dust occurrence with the NOSCAV simulation in July during the rainy season. The dust aerosol occurrence is averaged respectively for 5 years CALIPSO observations (2006–2010) and 5 years LMDZ model (2006–2010). The black dashed line represents the transitional zone between land and ocean.

3.4 Control of the vertical structure by physical processes

In this section, we focus our analysis on the processes impacting the dust vertical distribution in the troposphere. **Figure 6** shows the vertical profiles of the tendency of each model process (Equations (2), (3), and (4)) involved in the evolution of dust concentrations. In January, the boundary layer turbulence diffusion and thermal plume transport are the main processes enriching the lower atmosphere over the continent from 850 hPa to the surface (below 2 km). SCDU dust particles are removed by sedimentation which dominates the dry deposition below 850 hPa (**Figure 6a**). Dust is then transported westward over the ocean by advection (**Figure 6c**) between the surface level and 900 hPa (below 1 km). Note that the advection flux has a magnitude reaching approximatively 0.1 $g.kg^{-1}.day^{-1}$. Above the ocean, the large-scale scavenging redistributes the dust from 850 hPa (1.5 km) to the lower layers between 900 hPa and the surface (below 1km), and the thermal plume redistributes dust between 800 and 900 hPa (**Figure 6c**). Sedimentation and turbulence seem to withdraw dust from the lower atmosphere together with thermal plumes that slightly

enrich the surface layer (**Figure 6c**) in agreement with Friese et al., 2016 [85]. In January and above the coast (**Figure 6e**), the processes affect the dust distribution in a similar manner as over the ocean except for the thermal plumes above 500 m. Another subtle difference with the oceanic region is that the tendencies from advection, sedimentation, and thermals peak slightly lower.

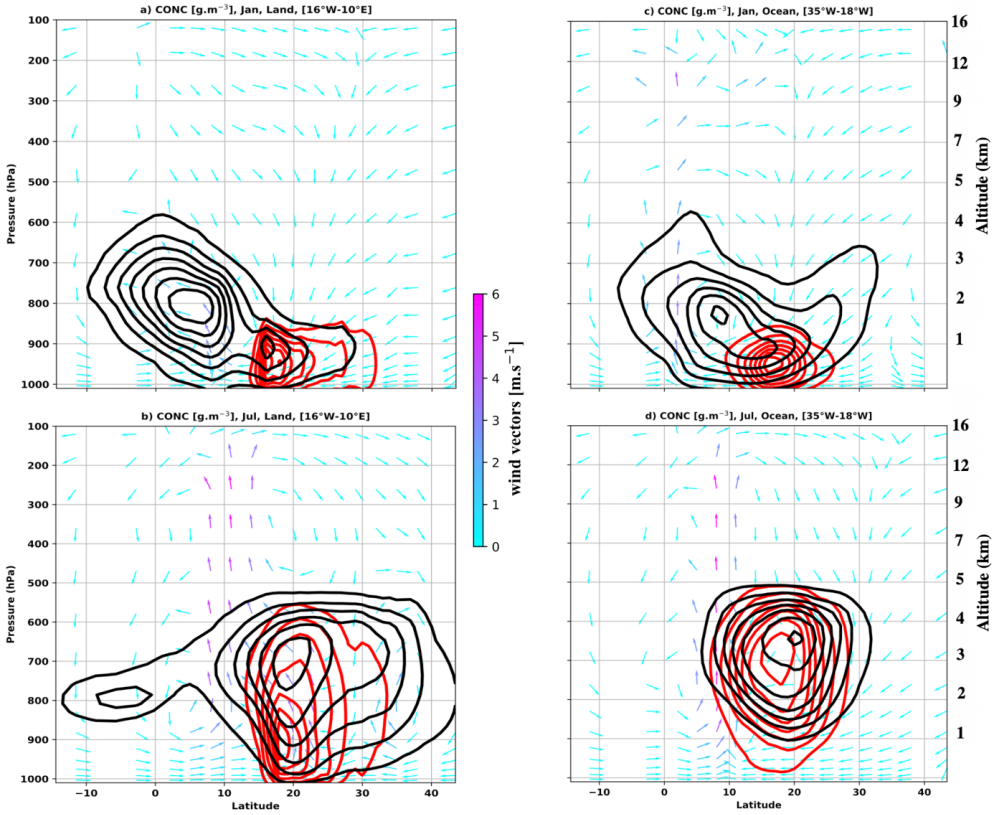

Figure 4. Vertical cross-sections (16°W–10°E) of aerosol concentration from SCAV, for the SCDU (red lines) and FINE (black lines) dust modes over West Africa and meridional wind (arrows; m/s) averaged over [16°W–10°E] for January (a, c) and July (b, d) between 2006 and 2010; Land (left; a, b) and Ocean (right; c, d). Dust concentrations (contours) are expressed in µg.m^{-3}. For the FINE mode, the black contour lines go from 0.5 to 5 µg.m^{-3} with a 0.5 µg.m^{-3} interval. For the SCDU mode red solid contour lines show values ranging from 15 to 105 µg.m^{-3} with a 25 µg.m^{-3} inter

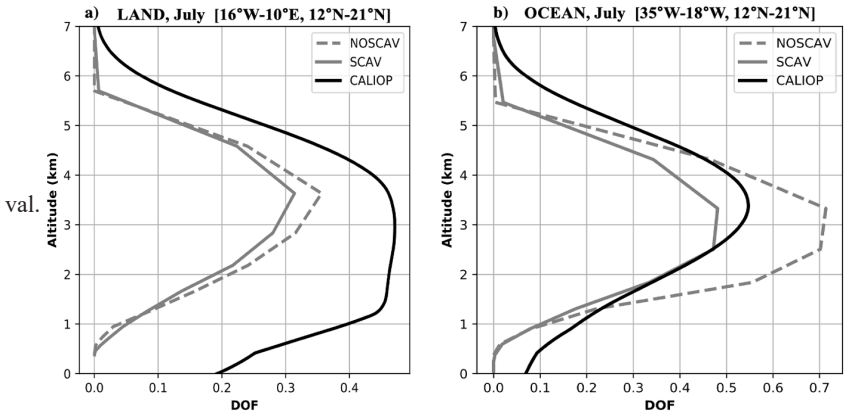

val.

Figure 5. Comparison of July vertical distribution of dust vertical frequency obtained from CALIOP observations (black lines), SCAV (gray lines), and NOSCAV (gray dashed lines) experiments for 2006–2010: (a) over the land (16°W–10°E) and (b) over the ocean (35°W–18°W).

In July, CODU is transported upward up to 600 hPa (4 km) overland by boundary layer turbulence and dry convection, represented in the model by the turbulent diffusion and the thermal plumes (not shown). The turbulent diffusion of the boundary layer raises the dust emitted at the surface up to 950 hPa, while the vertical transport to 800 hPa (2 km) is made by the thermal plumes (not shown). In the simulations, the effect of the monsoon flux on the dust vertical distribution is clearly shown by the negative advection tendency between the surface and 900 hPa (below 1 km), which is consistent with previous studies [68,80,86]. In higher levels of the atmosphere, the deep convective tendencies dominate the vertical transport. It will be detailed in the next section.

Larger size particles are redistributed in the atmosphere from the SAL (around 700 hPa) before being deposited at the surface by the sedimentation process. The latter is more important than the dynamical process below 900 hPa with a tendency respectively of –2 for sedimentation and –0.9 $g.kg^{-1}.day^{-1}$ for dynamical processes (**Figure 6b**). Above the ocean (**Figure 6d**), the large-scale scavenging effect redistributes dust between the surface and 950 hPa. The latter shows an important effect of the advection tendency in the SAL between 500 and 900 hPa (1 and 5 km) in agreement with the dust occurrence over the ocean in summer (**Figure 3d**) and the CALIOP observations (**Figure 3c**). Large particles are also transported far from the dust sources in the high altitudes between (500 and 800 hPa) in agreement with the observations from the Fennec campaign [27].

3.5 Control by deep convection

Our analysis is focused in this section on the mechanisms controlling the vertical distribution of CODU and FINE dust inside the ITCZ during summer over West Africa (**Figure 7**). Inside the grid-box selected in **Figure 7**, the dust is transported by advection in the upper part of the SAL (500 and 750 hPa) (**Figures 7a and 7b**) corresponding to the altitude between 2.5 and 5 km where the maximum DOF has been found with CALIOP (**Figure 3c**). This strong dust advection is shown by a positive value of the tendency with a maximum of 0.04 $g.kg^{-1}.day^{-1}$ in the south part of the African Easterly Jet (AEJ) (600 and 700 hPa above 3 km) (**Figure 7b**). At this altitude, the removal of dust by the combination of sedimentation, stratiform precipitation (600 and 950 hPa), and convective rainfall is less important than the advection. Between 750 and 900 hPa (1 and 3 km), the dust originates from the sedimentation effect (**Figure 7b**), convective transport and the re-evaporation of the unsaturated drafts (**Figure 7d**) is removed by the large-scale scavenging (**Figures 7b and 7d**). In western Africa, the model has a strong large-scale tendency to concentrate dust at lower levels between 950 hPa and surface (**Figure 7d**). However, the impact of the atmospheric boundary layer is very strong and brings dust up to 4 km (600 hPa) (**Figure 7b**). **Figure 7c** shows the same behavior in terms of convection and large-scale circulation but FINE is not affected by the sedimentation. **Figures 7c and 7d** show that the convective transport moves a part of dust from the SAL between 500–750 hPa (3 and 5 km) to high altitudes between 100 and 350 hPa (8 and 16 km) with a maximum contribution around of 200 hPa (12 km). However, the import of dust by convection is almost canceled: Dust is removed by the saturated updrafts combined with the effect of large-scale scavenging (**Figures 7c and 7d**). Strong activity of the convection removes a large part of dust contained in the side part of the AEJ between 500 and 900 hPa (1 and 5 km) but the unsaturated downdraft redistributes dust between 3 and 4 km (**Figure 7d**).

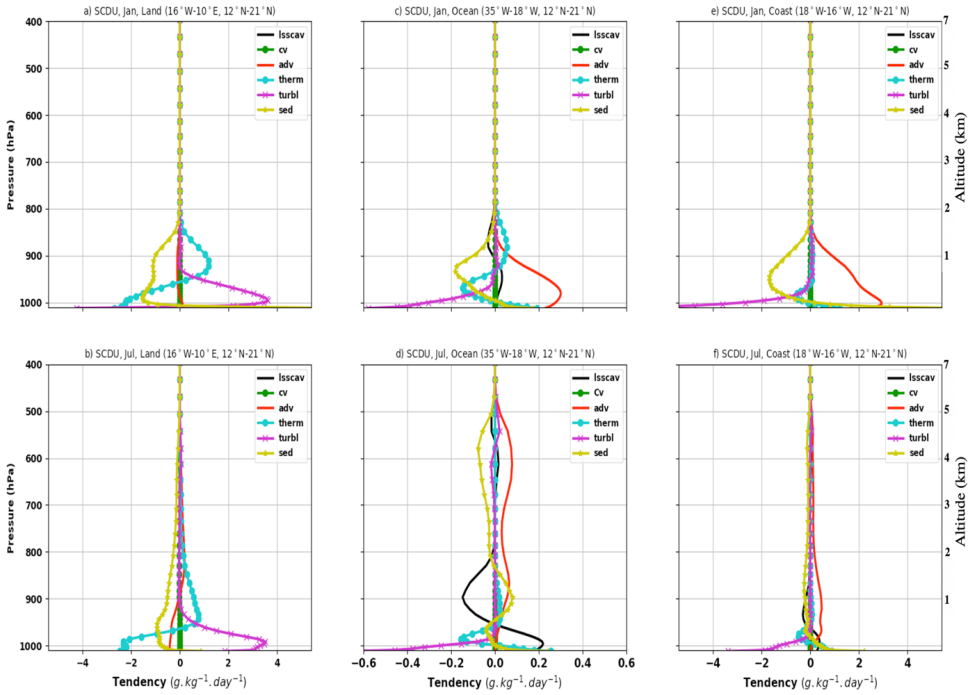

Figure 6. January (top) and July (bottom) vertical profiles of the different terms (g.kg^{-1}.day^{-1}) controlling the dust evolution in the SCAV LMDZ experiment averaged between 2006 and 2010 overland (a and b; 16°W–10°W), ocean (c and d; 35°W–20°W) and around the coast (e and f; 18°W–16°W). The large-scale scavenging (lsscav) corresponds to black solid lines, the convective scavenging combined with the vertical transport (cv) is shown by the green lines with dot markers, the advection (adv) is represented by the red lines, the thermal plume (therm) is shown by cyan solid lines with dot markers, the boundary layer turbulence diffusion (turbl) by magenta solid with markers, and the sedimentation (sed) in yellow with star markers.

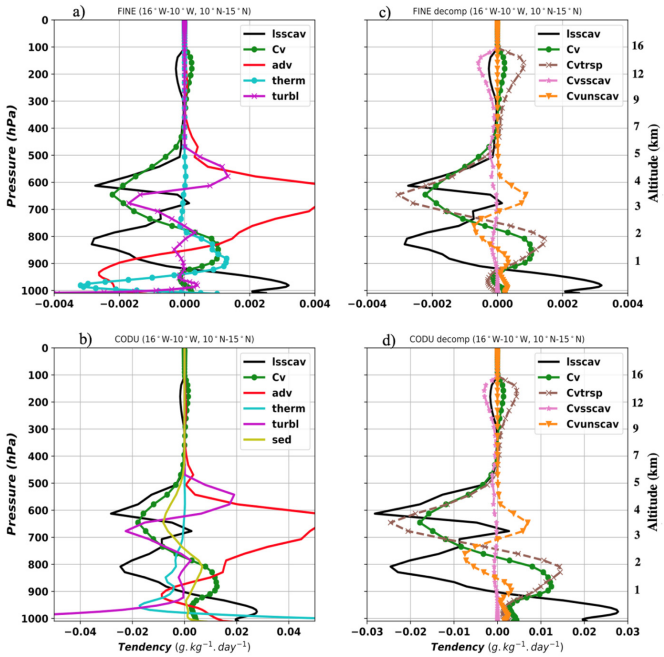

Figure 7. Simulated vertical tendencies of CODU (a) and FINE (b) in July 2006–2010. The plots are made in the convectively active domain (10°N-15°N) for zonal cross-sections (16°W–10°W). In panels (a), (b), the lsscav tendency is in black solid lines, the advection (adv) red solid lines, the Cv (green lines with dot markers), the term in cyan with dot markers, the turbl (magenta with star markers), and sed (yellow solid lines). Panels (c), (d) show the lsscav (black solid lines) and the total Cv of the simulation which is separated into three tendencies: Vertical transport (Cvtrsp) in dashed brown line with markers, the saturated updraft (Cvsscav) in dashed magenta lines with star markers, and unsaturated downdraft (Cvunscav) in orange with star markers.

4. Discussion

The comparison of two configurations of the LMDZ model with satellites and ground observations reveals a bias in the simulated AOD showing the importance of representing deep convective scavenging in models used for research on dust. This uncertainty is related to the accumulation of dust in the atmosphere during the boreal summer (**Figures 3c, 3d and 3e**). The combination of intense activity of the Saharan dust sources and the absence of precipitation in the model increases the AOD of dust. The overestimation of AOD with the SCAV simulation in Dakar is due to the strong dust emission of the model on the West African coast in agreement with Hourdin et al. (2015). The comparison of LMDZ's AOD in Escribano et al. (2016) [24] shows that the coastal dust sources are well represented in the model during the whole year. Our results are in accordance with previous studies [65,87]. Messager et al. (2010) have shown that intense surface heating from solar radiation (so-called heat low) controls dry convection processes which contribute about 35% of the global dust budget [24,88]. This study has also identified the processes involved in the control of the vertical distribution of mineral dust in West Africa. The advection in the SAL is reproduced by the model as shown by the vertical profile of dust over the ocean which slightly underestimates the vertical profile between the surface and around 1.5 km. The collocation of the maximum DOF in the SAL (**Figure 3d**) with a maximum wind speed (**Figures 7a and 7b**) by the model simulations near the West African coast is in agreement with the findings of Tsamalis et al. (2013) [68]. **Figures 6b–6d** and **Figures 7a and 7b** show a location of the AEJ above 3 km during summer in agreement with observed data [68]. The weak dry deposition of CODU and FINE between land and ocean could be related to their intrusion in the SAL. The removal effect of large-scale scavenging between 1 and 3 km (**Figures 7b and 7d**) and the good agreement of the model's AOD in the summer season (**Figure 1**) show that the underestimation of the DOF below 3 km (**Figure 5a**) for SCAV could be attributed to the negative effect of stratiform precipitation. The changes noticed in the dust occurrence for the model between land and ocean are essentially explained by the strong activity of the dynamical processes (advection) inside the SAL between 2 and 5 km for SCDU (**Figure 6d**) associated with the weak effect of the sedimentation for CODU (**Figure 7b**) and low precipitations (**Figure 6d**). This result is in agreement with the findings of Vuolo et al. (2009) [69]. Finally, it should be noted that our simulations are relatively short given the documented interannual and decadal variability in dust emissions and transport. However, we intend to perform a larger set of ensemble simulations over a longer period to overcome the limitations of a two short simulation study and to be able to improve vertical dust transport diagnostic and statistics.

5. Conclusions

The online implementation of the SPLA module coupled with the LMDZ GCM makes it possible to organize the dust size in three bins and to discriminate the different contributions of the physical processes as tendencies. This paper focuses on the vertical distribution of mineral dust and on the mechanisms impacting their redistribution in the troposphere in particular over Western-North Africa inside the (5°N–15°N; 16°W–10°W) domain, during the monsoon season, where deep convection was dominant. The results show that the LMDZ model has the skill to reproduce a clear seasonal cycle of AOD when all the physical processes listed are activated in the model. By deactivating scavenging, we show the importance of this specific process, as well as the importance of processed-based transport and scavenging in a deep convective parameterization on the dust seasonal cycle and vertical distribution of Saharan dust. Deep convection contributes to increasing atmospheric dust loading around 650 hPa (3.5 km) and 900 hPa (1 km). While scavenging processes are always considered as a sink for aerosols, it is shown here that convection can locally increase the dust concentration by the re-evaporation of the unsaturated downdraft. The effects of large-scale scavenging due to the re-evaporation of the strati-

form precipitation are seen mostly activated between the surface and 900 hPa. Above the dry convection region around 20°N, the intertropical discontinuity signal is clearly shown near the surface and explained by the convergence between Harmattan and monsoon flux. Moreover, the vertical distribution of dust is limited above the top dust layer by the large-scale subsidence of air masses due to the Hadley cell. Vertical transport of dust is clearly shown in North Africa around the latitude 10°N. The elevation of the dust layer on the eastern side of the Atlantic Ocean is mostly due to the marine boundary layer rather than the dynamic effects. Differences in the vertical profiles of dust occurrence frequency between the model and CALIPSO aerosol types show that the LMDZ model reproduces reasonably well the vertical transport and the advection but underestimates the dust mass concentration over North Africa below 3 km due to stratiform precipitation. The elevation of the SAL above the Atlantic Ocean starts at the transitional zone between land and ocean in the satellite observations and model simulations. This study brings to light that the elevation of dust near the western African coast, which previously has been only attributed to the dynamics of the monsoon flux, may be more affected by marine boundary layer processes. The large dust occurrence in the West Africa area during the summer season, due to the higher activity of the dust sources, is reproduced by model simulations. The study also points out a connection between the intertropical discontinuity (ITD) and the ITCZ overland in summer, inducing a vertical transport of mineral dust in the Sahara.

Conflict of Interest

There is no conflict of interest.

Acknowledgments

The authors wish to thank the Ecosystem Approach to the management of fisheries and the marine environment in the West African Waters (AWA) project. They also acknowledge support from the international joint laboratory ECLAIRS. The Laboratoire de Météorologie Dynamique (LMD) and the Global Challenges Research Fund (GCRF) African Science for Weather Information and Techniques (SWIFT) Programme. NASA, CNES, and ICARE are acknowledged for providing access to CALIOP and Sun photometer AERONET data.

References

[1] Washington, R., Todd, M.C., Engelstaedter, S., et al., 2006. Dust and the low-level circulation over the Bodélé Depression, Chad: Observations from BoDEx 2005. Journal of Geophysical Research: Atmospheres. 111(D3). DOI: https://doi.org/10.1029/2005JD006502

[2] Haustein, K., Pérez, C., Baldasano, J.M., et al., 2009. Regional dust model performance during SAMUM 2006. Geophysical Research Letters. 36(3). DOI: https://doi.org/10.1029/2008GL036463

[3] Kaufman, Y.J., Koren, I., Remer, L.A., et al., 2005. Dust transport and deposition observed from the Terra-Moderate Resolution Imaging Spectroradiometer (MODIS) spacecraft over the Atlantic Ocean. Journal of Geophysical Research: Atmospheres. 110(D10). DOI: https://doi.org/10.1029/2003JD004436

[4] Senghor, H., Roberts, A.J., Dieng, A.L., et al., 2021. Transport and deposition of Saharan dust observed from satellite images and ground measurements. Journal of Atmospheric Science Research. 4(2), 1–11. DOI: https://doi.org/10.30564/jasr.v4i2.3165

[5] Diokhane, A.M., Jenkins, G.S., Manga, N., et al., 2016. Linkages between observed, modeled Saharan dust loading and meningitis in Senegal during 2012 and 2013. International Journal of Biometeorology. 60, 557–575. DOI: https://doi.org/10.1007/s00484-015-1051-5

[6] Samoli, E., Stafoggia, M., Rodopoulou, S., et al., 2013. Associations between fine and coarse particles and mortality in Mediterranean cities: Results from the MED-PARTICLES project. Environmental Health Perspectives. 121(8), 932–938.

DOI: http://dx.doi.org/10.1289/ehp.1206124

[7] Yu, H., Tan, Q., Zhou, L., et al., 2021. Observation and modeling of the historic "Godzilla" African dust intrusion into the Caribbean Basin and the southern US in June 2020. Atmospheric Chemistry and Physics. 21(16), 12359–12383. DOI: https://doi.org/10.5194/acp-21-12359-2021

[8] Creamean, J.M., Suski, K.J., Rosenfeld, D., et al., 2013. Dust and biological aerosols from the Sahara and Asia influence precipitation in the western US. Science. 339(6127), 1572–1578.

[9] Sokolik, I.N., Toon, O.B., 1999. Incorporation of mineralogical composition into models of the radiative properties of mineral aerosol from UV to IR wavelengths. Journal of Geophysical Research: Atmospheres. 104(D8), 9423–9444. DOI: https://doi.org/10.1029/1998JD200048

[10] Balkanski, Y., Bonnet, R., Boucher, O., et al., 2021. Dust induced atmospheric absorption improves tropical precipitations in climate models. Atmospheric Chemistry and Physics Discussions. DOI: https://doi.org/10.5194/acp-2021-12

[11] Engelstaedter, S., Tegen, I., Washington, R., 2006. North African dust emissions and transport. Earth-Science Reviews. 79(1–2), 73–100. DOI: https://doi.org/10.1016/j.earscirev.2006.06.004

[12] Hourdin, F., Gueye, M., Diallo, B., et al., 2015. Parameterization of convective transport in the boundary layer and its impact on the representation of the diurnal cycle of wind and dust emissions. Atmospheric Chemistry and Physics. 15(12), 6775–6788. DOI: https://doi.org/10.5194/acp-15-6775-2015

[13] Allen, C.J., Washington, R., Engelstaedter, S., 2013. Dust emission and transport mechanisms in the central Sahara: Fennec ground-based observations from Bordj Badji Mokhtar, June 2011. Journal of Geophysical Research: Atmospheres. 118(12), 6212–6232. DOI: https://doi.org/10.1002/jgrd.50534

[14] Miller, S.D., Kuciauskas, A.P., Liu, M., et al., 2008. Haboob dust storms of the southern Arabian Peninsula. Journal of Geophysical Research: Atmospheres. 113(D1). DOI: https://doi.org/10.1029/2007JD008550

[15] Tost, H., Jöckel, P., Lelieveld, J., 2006. Influence of different convection parameterisations in a GCM. Atmospheric Chemistry and Physics. 6(12), 5475–5493. DOI: https://doi.org/10.5194/acp-6-5475-2006

[16] Tost, H., Lawrence, M.G., Brühl, C., et al., 2010. Uncertainties in atmospheric chemistry modelling due to convection parameterisations and subsequent scavenging. Atmospheric Chemistry and Physics. 10(4), 1931–1951. DOI: https://doi.org/10.5194/acp-10-1931-2010

[17] Pilon, R., Grandpeix, J.Y., Heinrich, P., 2015. Representation of transport and scavenging of trace particlesin the Emanuel moist convection scheme. Quarterly Journal of the Royal Meteorological Society. 141(689), 1244–1258. DOI: https://doi.org/10.1002/qj.2431

[18] Knippertz, P., Stuut, J.B.W., 2014. Introduction. Mineral dust. Springer: Dordrecht. pp. 1–14. DOI: https://doi.org/10.1007/978-94-017-8978-3_1

[19] Malavelle, F., Pont, V., Mallet, M., et al., 2011. Simulation of aerosol radiative effects over West Africa during DABEX and AMMA SOP-0. Journal of Geophysical Research: Atmospheres. 116(D8). DOI: https://doi.org/10.1029/2010JD014829

[20] Solmon, F., Elguindi, N., Mallet, M., 2012. Radiative and climatic effects of dust over West Africa, as simulated by a regional climate model. Climate Research. 52, 97–113. DOI: https://doi.org/10.3354/cr01039

[21] Ji, Z., Wang, G., Pal, J.S., et al., 2016. Potential climate effect of mineral aerosols over West Africa. Part I: model validation and contemporary climate evaluation. Climate Dynamics. 46, 1223–1239. DOI: https://doi.org/10.1007/s00382-015-2641-y

[22] Schmechtig, C., Marticorena, B., Chatenet, B., et al., 2011. Simulation of the mineral dust content over Western Africa from the event to

the annual scale with the CHIMERE-DUST model. Atmospheric Chemistry and Physics. 11(14), 7185–7207.
DOI: https://doi.org/10.5194/acp-11-7185-2011

[23] Pérez, C., Haustein, K., Janjic, Z., et al., 2011. Atmospheric dust modeling from meso to global scales with the online NMMB/BSC-Dust model—Part 1: Model description, annual simulations and evaluation. Atmospheric Chemistry and Physics. 11(24), 13001–13027.
DOI: https://doi.org/10.5194/acp-11-13001-2011

[24] Escribano, J., Boucher, O., Chevallier, F., et al., 2016. Subregional inversion of North African dust sources. Journal of Geophysical Research: Atmospheres. 121(14), 8549–8566.
DOI: https://doi.org/10.1002/2016JD025020

[25] Hu, Z., Huang, J., Zhao, C., et al., 2020. Modeling dust sources, transport, and radiative effects at different altitudes over the Tibetan Plateau. Atmospheric Chemistry and Physics. 20(3), 1507–1529.
DOI: https://doi.org/10.5194/acp-20-1507-2020

[26] Kallos, G., Papadopoulos, A., Katsafados, P., et al., 2006. Transatlantic Saharan dust transport: Model simulation and results. Journal of Geophysical Research: Atmospheres. 111(D9).
DOI: https://doi.org/10.1029/2005JD006207

[27] Ryder, C.L., Highwood, E.J., Lai, T.M., et al., 2013. Impact of atmospheric transport on the evolution of microphysical and optical properties of Saharan dust. Geophysical Research Letters. 40(10), 2433–2438.
DOI: https://doi.org/10.1002/grl.50482

[28] Gasteiger, J., Wiegner, M., Groß, S., et al., 2011. Modelling lidar-relevant optical properties of complex mineral dust aerosols. Tellus B. 63(4), 725–741.
DOI: https://doi.org/10.1111/j.1600-0889.2011.00559.x

[29] Adebiyi, A.A., Kok, J.F., Wang, Y., et al., 2020. Dust Constraints from joint Observational-Modelling-experiMental analysis (DustCOMM): Comparison with measurements and model simulations. Atmospheric Chemistry and Physics. 20(2), 829–863.
DOI: https://doi.org/10.5194/acp-20-829-2020

[30] Liu, H., Jacob, D.J., Bey, I., et al., 2001. Constraints from ^{210}Pb and ^{7}Be on wet deposition and transport in a global three-dimensional chemical tracer model driven by assimilated meteorological fields. Journal of Geophysical Research: Atmospheres. 106(D11), 12109–12128.
DOI: https://doi.org/10.1029/2000JD900839

[31] Heinrich, P., Jamelot, A., 2011. Atmospheric transport simulation of ^{210}Pb and ^{7}Be by the LMDz general circulation model and sensitivity to convection and scavenging parameterization. Atmospheric Research. 101(1–2), 54–66.
DOI: https://doi.org/10.1016/j.atmosres.2011.01.008

[32] Heinrich, P., Pilon, R., 2013. Simulation of ^{210}Pb and ^{7}Be scavenging in the tropics by the LMDz general circulation model. Atmospheric Research. 132, 490–505.
DOI: https://doi.org/10.1016/j.atmosres.2013.07.004

[33] Hourdin, F., Rio, C., Grandpeix, J.Y., et al., 2020. LMDZ6A: The atmospheric component of the IPSL climate model with improved and better tuned physics. Journal of Advances in Modeling Earth Systems. 12(7), e2019MS001892.
DOI: https://doi.org/10.1029/2019MS001892

[34] Grandpeix, J.Y., Phillips, V., Tailleux, R., 2004. Improved mixing representation in Emanuel's convection scheme. Quarterly Journal of the Royal Meteorological Society. 130(604), 3207–3222.
DOI: https://doi.org/10.1256/qj.03.144

[35] Emanuel, K.A., 1991. A scheme for representing cumulus convection in large-scale models. Journal of the Atmospheric Sciences. 48(21), 2313–2329.
DOI: https://doi.org/10.1175/1520-0469(1991)048<2313:ASFRCC>2.0.CO;2

[36] Grandpeix, J.Y., Lafore, J.P., 2010. A density current parameterization coupled with Eman-

uel's convection scheme. Part I: The models. Journal of the Atmospheric Sciences. 67(4), 881–897.
DOI: https://doi.org/10.1175/2009JAS3044.1

[37] Grandpeix, J.Y., Lafore, J.P., Cheruy, F., 2010. A density current parameterization coupled with Emanuel's convection scheme. Part II: 1D simulations. Journal of the Atmospheric Sciences. 67(4), 898–922.
DOI: https://doi.org/10.1175/2009JAS3045.1

[38] Rochetin, N., Couvreux, F., Grandpeix, J.Y., et al., 2014. Deep convection triggering by boundary layer thermals. Part I: LES analysis and stochastic triggering formulation. Journal of the Atmospheric Sciences. 71(2), 496–514.
DOI: https://doi.org/10.1175/JAS-D-12-0336.1

[39] Hourdin, F., Jam, A., Rio, C., et al., 2019. Unified parameterization of convective boundary layer transport and clouds with the thermal plume model. Journal of Advances in Modeling Earth Systems. 11(9), 2910–2933.
DOI: https://doi.org/10.1029/2019MS001666

[40] Le Trent, H., Li, Z.X., 1991. Sensitivity of an atmospheric general circulation model to prescribed SST changes: Feedback effects associated with the simulation of cloud optical properties. Climate Dynamics. 5, 175–187.

[41] Coindreau, O., Hourdin, F., Haeffelin, M., et al., 2007. Assessment of physical parameterizations using a global climate model with stretchable grid and nudging. Monthly Weather Review. 135(4), 1474–1489.
DOI: https://doi.org/10.1175/MWR3338.1

[42] Hourdin, F., Grandpeix, J.Y., Rio, C., et al., 2013. LMDZ5B: The atmospheric component of the IPSL climate model with revisited parameterizations for clouds and convection. Climate Dynamics. 40, 2193–2222.
DOI: https://doi.org/10.1007/s00382-012-1343-y

[43] Wang, F., Ducharne, A., Cheruy, F., et al., 2018. Impact of a shallow groundwater table on the global water cycle in the IPSL land–atmosphere coupled model. Climate Dynamics. 50, 3505–3522.
DOI: https://doi.org/10.1007/s00382-017-3820-9

[44] Krinner, G., Viovy, N., de Noblet-Ducoudré, N., et al., 2005. A dynamic global vegetation model for studies of the coupled atmosphere-biosphere system. Global Biogeochemical Cycles. 19(1).
DOI: https://doi.org/10.1029/2003GB002199

[45] Cheruy, F., Ducharne, A., Hourdin, F., et al., 2020. Improved near-surface continental climate in IPSL-CM6A-LR by combined evolutions of atmospheric and land surface physics. Journal of Advances in Modeling Earth Systems. 12(10), e2019MS002005.
DOI: https://doi.org/10.1029/2019MS002005

[46] Marticorena, B., Chatenet, B., Rajot, J.L., et al., 2010. Temporal variability of mineral dust concentrations over West Africa: Analyses of a pluriannual monitoring from the AMMA Sahelian Dust Transect. Atmospheric Chemistry and Physics. 10(18), 8899–8915.
DOI: https://doi.org/10.5194/acp-10-8899-2010

[47] Dee, D.P., Uppala, S.M., Simmons, A.J., et al., 2011. The ERA-Interim reanalysis: Configuration and performance of the data assimilation system. Quarterly Journal of the Royal Meteorological Society. 137(656), 553–597.
DOI: https://doi.org/10.1002/qj.828

[48] Hersbach, H., Bell, B., Berrisford, P., et al., 2020. The ERA5 global reanalysis. Quarterly Journal of the Royal Meteorological Society. 146(730), 1999–2049.
DOI: https://doi.org/10.1002/qj.3803

[49] Huneeus, N., Chevallier, F., Boucher, O., 2012. Estimating aerosol emissions by assimilating observed aerosol optical depth in a global aerosol model. Atmospheric Chemistry and Physics. 12(10), 4585–4606.
DOI: https://doi.org/10.5194/acp-12-4585-2012

[50] Menut, L., Pérez, C., Haustein, K., et al., 2013. Impact of surface roughness and soil texture on mineral dust emission fluxes modeling. Journal of Geophysical Research: Atmospheres. 118(12), 6505–6520.

DOI: https://doi.org/10.1002/jgrd.50313

[51] Marticorena, B., Bergametti, G., 1995. Modeling the atmospheric dust cycle: 1. Design of a soil-derived dust emission scheme. Journal of Geophysical Research: Atmospheres. 100(D8), 16415–16430.
DOI: https://doi.org/10.1029/95JD00690

[52] Alfaro, S.C., Gomes, L., 2001. Modeling mineral aerosol production by wind erosion: Emission intensities and aerosol size distributions in source areas. Journal of Geophysical Research: Atmospheres. 106(D16), 18075–18084.
DOI: https://doi.org/10.1029/2000JD900339

[53] Shao, Y., Lu, H., 2000. A simple expression for wind erosion threshold friction velocity. Journal of Geophysical Research: Atmospheres. 105(D17), 22437–22443.
DOI: https://doi.org/10.1029/2000JD900304

[54] Marticorena, B., Bergametti, G., Aumont, B., et al., 1997. Modeling the atmospheric dust cycle: 2. Simulation of Saharan dust sources. Journal of Geophysical Research: Atmospheres. 102(D4), 4387–4404.
DOI: https://doi.org/10.1029/96JD02964

[55] Huneeus, N., Boucher, O., Chevallier, F., 2009. Simplified aerosol modeling for variational data assimilation. Geoscientific Model Development. 2(2), 213–229.
DOI: https://doi.org/10.5194/gmd-2-213-2009

[56] Reddy, M.S., Boucher, O., 2004. A study of the global cycle of carbonaceous aerosols in the LMDZT general circulation model. Journal of Geophysical Research: Atmospheres. 109(D14).
DOI: https://doi.org/10.1029/2003JD004048

[57] Hourdin, F., Armengaud, A., 1999. The use of finite-volume methods for atmospheric advection of trace species. Part I: Test of various formulations in a general circulation model. Monthly Weather Review. 127(5), 822–837.
DOI: https://doi.org/10.1175/1520-0493(1999)127<0822:TUOFVM>2.0.CO;2

[58] Yamada, T., 1983. Simulations of nocturnal drainage flows by a q2l turbulence closure model. Journal of the Atmospheric Sciences. 40(1), 91–106.
DOI: https://doi.org/10.1175/1520-0469(1983)040<0091:SONDFB>2.0.CO;2

[59] Holben, B.N., Eck, T.F., Slutsker, I.A., et al., 1998. AERONET—A federated instrument network and data archive for aerosol characterization. Remote Sensing of Environment. 66(1), 1–16.
DOI: https://doi.org/10.1016/S0034-4257(98)00031-5

[60] Léon, J.F., Derimian, Y., Chiapello, I., et al., 2009. Aerosol vertical distribution and optical properties over M'Bour (16.96° W; 14.39° N), Senegal from 2006 to 2008. Atmospheric Chemistry and Physics. 9(23), 9249–9261.
DOI: https://doi.org/10.5194/acp-9-9249-2009

[61] Hunt, W.H., Winker, D.M., Vaughan, M.A., et al., 2009. CALIPSO lidar description and performance assessment. Journal of Atmospheric and Oceanic Technology. 26(7), 1214–1228.
DOI: https://doi.org/10.1175/2009JTECHA1223.1

[62] Winker, D.M., Hunt, W.H., McGill, M.J., 2007. Initial performance assessment of CALIOP. Geophysical Research Letters. 34(19).
DOI: https://doi.org/10.1029/2007GL030135

[63] Winker, D.M., Pelon, J.R., McCormick, M.P., 2003. CALIPSO mission: Spaceborne lidar for observation of aerosols and clouds. Lidar Remote Sensing for Industry and Environment Monitoring III. 4893, 1–11.
DOI: https://doi.org/10.1117/12.466539

[64] Liu, Z., Vaughan, M., Winker, D., et al., 2009. The CALIPSO lidar cloud and aerosol discrimination: Version 2 algorithm and initial assessment of performance. Journal of Atmospheric and Oceanic Technology. 26(7), 1198–1213.
DOI: https://doi.org/10.1175/2009JTECHA1229.1

[65] Senghor, H., Machu, É., Hourdin, F., et al., 2017. Seasonal cycle of desert aerosols in western Africa: Analysis of the coastal transition with passive and active sensors. Atmospheric Chemistry and Physics. 17(13), 8395–8410.

DOI: https://doi.org/10.5194/acp-17-8395-2017

[66] Adams, A.M., Prospero, J.M., Zhang, C., 2012. CALIPSO-derived three-dimensional structure of aerosol over the Atlantic Basin and adjacent continents. Journal of Climate. 25(19), 6862–6879.
DOI: https://doi.org/10.1175/JCLI-D-11-00672.1

[67] Schuster, G.L., Vaughan, M., MacDonnell, D., et al., 2012. Comparison of CALIPSO aerosol optical depth retrievals to AERONET measurements, and a climatology for the lidar ratio of dust. Atmospheric Chemistry and Physics. 12(16), 7431–7452.
DOI: https://doi.org/10.5194/acp-12-7431-2012

[68] Tsamalis, C., Chédin, A., Pelon, J., et al., 2013. The seasonal vertical distribution of the Saharan Air Layer and its modulation by the wind. Atmospheric Chemistry and Physics. 13(22), 11235–11257.
DOI: https://doi.org/10.5194/acp-13-11235-2013

[69] Vuolo, M.R., Chepfer, H., Menut, L., et al., 2009. Comparison of mineral dust layers vertical structures modeled with CHIMERE-DUST and observed with the CALIOP lidar. Journal of Geophysical Research: Atmospheres. 114(D9).
DOI: https://doi.org/10.1029/2008JD011219

[70] Wallace, J.M., Hobbs, P.V., 2006. Atmospheric science: An introductory survey (Vol. 92). Elsevier: Amsterdam.

[71] Weinzierl, B., Ansmann, A., Prospero, J.M., et al., 2017. The Saharan aerosol long-range transport and aerosol–cloud-interaction experiment: overview and selected highlights. Bulletin of the American Meteorological Society. 98(7), 1427–1451.
DOI: https://doi.org/10.1175/BAMS-D-15-00142.1

[72] Prospero, J.M., Ginoux, P., Torres, O., et al., 2002. Environmental characterization of global sources of atmospheric soil dust identified with the Nimbus 7 Total Ozone Mapping Spectrometer (TOMS) absorbing aerosol product. Reviews of Geophysics. 40(1), 21–31.
DOI: https://doi.org/10.1029/2000RG000095

[73] Cuesta, J., Marsham, J.H., Parker, D.J., et al., 2009. Dynamical mechanisms controlling the vertical redistribution of dust and the thermodynamic structure of the West Saharan atmospheric boundary layer during summer. Atmospheric Science Letters. 10(1), 34–42.
DOI: https://doi.org/10.1002/asl.207

[74] Ansmann, A., Petzold, A., Kandler, K., et al., 2011. Saharan mineral dust experiments SAMUM–1 and SAMUM–2: What have we learned? Tellus B. 63(4), 403–429.
DOI: https://doi.org/10.1111/j.1600-0889.2011.00555.x

[75] Hamilton, R.A., Archbold, J.W., Douglas, C.K.M., 1945. Meteorology of Nigeria and adjacent territory. Quarterly Journal of the Royal Meteorological Society. 71(309–310), 231–264.
DOI: https://doi.org/10.1002/qj.49707130905

[76] Stuut, J.B., Zabel, M., Ratmeyer, V., et al., 2005. Provenance of present-day eolian dust collected off NW Africa. Journal of Geophysical Research: Atmospheres. 110(D4).
DOI: https://doi.org/10.1029/2004JD005161

[77] Ozer, P., Laghdaf, M.B.O.M., Lemine, S.O.M., et al., 2007. Estimation of air quality degradation due to Saharan dust at Nouakchott, Mauritania, from horizontal visibility data. Water, Air, and Soil Pollution. 178, 79–87.
DOI: https://doi.org/10.1007/s11270-006-9152-8

[78] Yu, H., Chin, M., Yuan, T., et al., 2015. The fertilizing role of African dust in the Amazon rainforest: A first multiyear assessment based on data from Cloud-Aerosol Lidar and Infrared Pathfinder Satellite Observations. Geophysical Research Letters. 42(6), 1984–1991.
DOI: https://doi.org/10.1002/2015GL063040

[79] Goudie, A.S., Middleton, N.J., 2001. Saharan dust storms: Nature and consequences. Earth-Science Reviews. 56(1–4), 179–204.
DOI: https://doi.org/10.1016/S0012-8252(01)00067-8

[80] Bou Karam, D., Flamant, C., Knippertz, P., et al.,

2008. Dust emissions over the Sahel associated with the West African monsoon intertropical discontinuity region: A representative case-study. Quarterly Journal of the Royal Meteorological Society. 134(632), 621–634.
DOI: https://doi.org/10.1002/qj.244

[81] Knippertz, P., Todd, M.C., 2010. The central west Saharan dust hot spot and its relation to African easterly waves and extratropical disturbances. Journal of Geophysical Research: Atmospheres. 115(D12).
DOI: https://doi.org/10.1029/2009JD012819

[82] Tegen, I., Schepanski, K., Heinold, B., 2013. Comparing two years of Saharan dust source activation obtained by regional modelling and satellite observations. Atmospheric Chemistry and Physics. 13(5), 2381–2390.
DOI: https://doi.org/10.5194/acp-13-2381-2013

[83] Chiapello, I., Bergametti, G., Gomes, L., et al., 1995. An additional low layer transport of Sahelian and Saharan dust over the north-eastern tropical Atlantic. Geophysical Research Letters. 22(23), 3191–3194.
DOI: https://doi.org/10.1029/95GL03313

[84] Liu, D., Wang, Y., Wang, Z., et al., 2012. The three-dimensional structure of transatlantic African dust transport: A new perspective from CALIPSO LIDAR measurements. Advances in Meteorology. 850704.
DOI: https://doi.org/10.1155/2012/850704

[85] Friese, C.A., van der Does, M., Merkel, U., et al., 2016. Environmental factors controlling the seasonal variability in particle size distribution of modern Saharan dust deposited off Cape Blanc. Aeolian Research. 22, 165–179.
DOI: https://doi.org/10.1016/j.aeolia.2016.04.005

[86] Schepanski, K., Tegen, I., Laurent, B., et al., 2007. A new Saharan dust source activation frequency map derived from MSG-SEVIRI IR-channels. Geophysical Research Letters. 34(18).
DOI: https://doi.org/10.1029/2007GL030168

[87] Lavaysse, C., Flamant, C., Janicot, S., et al., 2009. Seasonal evolution of the West African heat low: A climatological perspective. Climate Dynamics. 33, 313–330.
DOI: https://doi.org/10.1007/s00382-009-0553-4

[88] Messager, C., Parker, D.J., Reitebuch, O., et al., 2010. Structure and dynamics of the Saharan atmospheric boundary layer during the West African monsoon onset: Observations and analyses from the research flights of 14 and 17 July 2006. Quarterly Journal of the Royal Meteorological Society. 136(S1), 107–124.
DOI: https://doi.org/10.1002/qj.469

BILINGUAL PUBLISHING GROUP

Journal of Atmospheric Science Research

https://journals.bilpubgroup.com/index.php/jasr/index

ARTICLE

Evaluation of the Mechanisms Acting on the Atlantic Meridional Overturning Circulation in CESM2 for the 1pctCO_2 Experiment

***Lívia Sancho*[1*], *Elisa Passos*[2,3], *Marcio Cataldi*[4,5*], *Luiz Paulo de Freitas Assad*[1,6], *Luiz Landau*[1]**

[1] *Laboratory of Computational Methods in Engineering, Civil Engineering Program, Alberto Luiz Coimbra Institute for Graduate Studies and Research in Engineering, Federal University of Rio de Janeiro, Rio de Janeiro, 21941-617, Brazil*

[2] *Civil Engineering Program, Alberto Luiz Coimbra Institute for Graduate Studies and Engineering Research, Federal University of Rio de Janeiro, Rio de Janeiro, 21941-617, Brazil*

[3] *Physical Oceanography Laboratory, Department of Physical Oceanography, Faculty of Oceanography, Rio de Janeiro State University, Rio de Janeiro, 20559-900, Brazil*

[4] *Climate System Monitoring and Modeling Laboratory, Water Resources and Environmental Engineering, Fluminense Federal University, 24020-140, Brazil*

[5] *Regional Atmospheric Modeling Group (MAR), Physics of the Earth, Department of Physics, Regional Campus of International Excellence (CEIR) "Campus Mare Nostrum", University of Murcia, Murcia, 30100, Spain*

[6] *Department of Meteorology, Institute of Geosciences, Federal University of Rio de Janeiro, Rio de Janeiro, 21941-617, Brazil*

ABSTRACT

The Atlantic Meridional Overturning Circulation (AMOC) is a crucial component of the Earth's climate system due to its fundamental role in heat distribution, carbon and oxygen transport, and the weather. Other climate components, such as the atmosphere and sea ice, influence the AMOC. Evaluating the physical mechanisms of those interactions is paramount to increasing knowledge about AMOC's functioning. In this study, the authors used outputs from the Community Earth System Model version 2 and observational data to investigate changes in the AMOC and the associated physical processes. Two DECK experiments were evaluated: piControl and 1pctCO_2, with an annual increase of 1% of atmospheric CO_2. The analysis revealed a significant decrease in the AMOC, associated with changes in mixed layer depth and buoyancy in high latitudes of the North Atlantic, resulting in the shutdown of deep convection and potentially affecting the formation of North Atlantic Deep Water and Antarctic Bottom Water. A vital aspect observed in this study is the association between increased runoff and reduced water evaporation, giving rise to a positive feedback process. Consequently, the rates of freshwater spreading have intensified during this period, which could lead to an accelerated disruption of the AMOC beyond the projections of existing models.

Keywords: AMOC; Meridional cell; Climate change; Deep circulation; CESM2 results; CMIP6

*CORRESPONDING AUTHOR:

Lívia Sancho, Laboratory of Computational Methods in Engineering, Civil Engineering Program, Alberto Luiz Coimbra Institute for Graduate Studies and Research in Engineering, Federal University of Rio de Janeiro, Rio de Janeiro, 21941-617, Brazil; Email: liviasancho@coppe.ufrj.br

Marcio Cataldi, Climate System Monitoring and Modeling Laboratory, Water Resources and Environmental Engineering, Fluminense Federal University, 24020-140, Brazil; Regional Atmospheric Modeling Group (MAR), Physics of the Earth, Department of Physics, Regional Campus of International Excellence (CEIR) "Campus Mare Nostrum", University of Murcia, Murcia, 30100, Spain; Email: marciocataldi@um.es

ARTICLE INFO

Received: 6 November 2023 | Revised: 3 January 2024 | Accepted: 10 January 2024 | Published Online: 18 January 2024

DOI: https://doi.org/10.30564/jasr.v7i1.6070

CITATION

Sancho, L., Passos, E., Cataldi, M., et al., 2024. Evaluation of the Mechanisms Acting on the Atlantic Meridional Overturning Circulation in CESM2 for the 1pctCO_2 Experiment. Journal of Atmospheric Science Research. 7(1): 40–58. DOI: https://doi.org/10.30564/jasr.v7i1.6070

1. Introduction

The Industrial Revolution of the 18th and 19th centuries led to a substantial increase in greenhouse gas (GHG) emissions, causing global climate change and rising temperatures [1,2]. These changes pose significant concerns for the scientific community, like the increase in frequency and intensity of weather extremes [3,4]. Central to the climate system is the Atlantic Meridional Overturning Circulation (AMOC), a complex system responsible for a net northward flow of warm water in the upper layers and a net southward flow of the North Atlantic Deep Water (NADW) [5–7], which is critical for the global climate system. It is responsible for alleviating the harsh winters in Europe, along with the westerlies of that region [8–10]. Furthermore, the AMOC plays a vital role in the uptake and distribution of essential tracers such as heat, carbon, and oxygen [8].

Recent models highlight a strong link between deepwater formation at high latitudes in the North Atlantic Ocean and the AMOC's intensity [11]. The AMOC's sensitivity to evaporation is limited unless the flow is reduced to values close to 0.03 Sv, and a freshwater build-up of 0.32 Sv in the Atlantic can lead to lower local density and shut off the deep convection [12]. Other studies estimate a freshwater build-up between 0.1 and 0.5 Sv, highlighting the critical role of freshwater input in modulating the AMOC strength and the potential for even small changes in this term to significantly impact the global climate system [13]. Freshwater input can result in changes to the northward heat transport and heat release in the North Atlantic region, with impacts beyond the Atlantic Ocean [14]. Therefore, understanding the AMOC is crucial for researchers and government decision-making [15,16]. The studies [17,18] demonstrated the potential for freshwater input to impact the AMOC and global climate system significantly.

This study aims to investigate the impact of increasing atmospheric concentrations of CO_2 on the AMOC and associated ocean, sea ice, and atmosphere interactions. Thus, a high-emission CO_2 experiment from the Community Earth System Model version 2, combined with observational data, was used. Our analysis seeks to identify changes in the AMOC and estimate different terms to gain insight into the evolution of the AMOC in the current climate and assess how close we are to crossing a critical climate breaking point.

The paper is structured as follows: In Section 2, we describe the data sources, the Earth System model, and experimental setup, as well as the methodology for implemented analysis. Section 3 presents and discusses our findings, focusing on RAPID data and Meridional Overturning, the mixed layer depth, and the freshwater input to the North Atlantic Ocean. Finally, we summarize our conclusions and offer some final remarks in Section 4.

2. Methodology

We used observational data and Earth System modeling results to evaluate the effects of atmospheric CO_2 on AMOC behavior. The following sections will describe the model outputs, the observational data, and the mathematical framework. This methodology provides a comprehensive approach to evaluate the impact of increasing atmospheric CO_2 on AMOC and related processes, which is essential for predicting the future of our climate and its potential impacts on global ecosystems.

2.1 Model description

This article analyzes the behavior of the AMOC patterns under a climate change scenario using the results of the state-of-the-art Earth System model Community Earth System Model version 2 (CESM2) [19]. CESM2 is the latest version of the National Center for Atmospheric Research (NCAR) Earth System model and the one used to perform simulations of the Coupled Model Intercomparison Project Phase 6 (CMIP6) [20]. Its design aims to simulate the physical, chemical, and human components that govern the climate system and the intrinsic feedback system on timescales of hundreds of years or more.

The CESM2 experiments used five components to represent various elements of the Earth system (atmosphere, ocean, land surface, sea ice, and river

runoff) in a nominal 1° horizontal resolution [20]. The various components of the Earth System and their interactions are modeled as follows: The Community Atmosphere Model version 6.0 (CAM6) [21] is used for the atmospheric component. This version includes aerosol-activated cloud droplet formation, and it models precipitation processes due to the size of condensation nuclei and the interaction between cloud particles in an explicit way.

The Community Land Model version 5 (CLM5) [22,23] is used for the land component. It quantifies the physical, chemical, and biological processes by which terrestrial ecosystems affect and are affected by climate across various spatial and temporal scales. The model consists of multiple components related to biogeophysics, hydrologic cycle, biogeochemistry, and ecosystem dynamics [24].

The Community Ice Code version 4 (CICE) [25] simulates the sea-ice interaction. It calculates local snow and ice growth rates due to radiative, conductive, and turbulent fluxes and ice dynamics [26,27], includes multiple scattering shortwave radiation treatment [28], and explicitly simulates the evolution of melt pools of ice (melt pond) and the deposition and cycling of dust aerosols and black carbon in the ice sheet [29]. The ice thickness distribution follows [30].

The Model for Scale Adaptive River Transport (MOSART) [31] accounts for river transport with the primary objective of providing freshwater input data to the ocean model. Surface runoff is routed across slopes and discharged along with subsurface runoff into a sub-grid before entering the main channel. Channel velocities and water depth in the channel varying in time are considered. River flow is determined by a kinematic wave method.

Although the results of the experiments were simulated using all five components, the oceanic outputs—ocean fields and fluxes from other components—were the focus of this study. The ocean component of CESM is version 2 of the Parallel Ocean Program model (POP2), developed by Los Alamos National Laboratory (LANL) [32]. POP2 is a general global ocean circulation model that solves primitive ocean dynamics equations in three dimensions using the hydrostatic and Boussinesq approximations [24,32]. The model is vertically discretized in z-coordinates [32,33] with 60 vertical levels. The ocean has a thickness of 10 m from the surface to 160 m. Below that depth, the thickness gradually increases to 250 m at 3500 m, which remains constant until the bottom (5500 m) [20].

2.2 Experimental setup

Results from two scientifically validated CMIP6 experiments were used to evaluate how the AMOC reacts to a greenhouse's worsening climate [20,34]. They are part of the CMIP6 Diagnostic, Evaluation, and Characterization of Klima (DECK) experiments. The piControl experiment represents the preindustrial period with non-evolving conditions, while the 1pctCO_2 experiment simulates an exponential annual 1% increase in atmospheric CO_2 concentration. GHG concentrations [35] were used for both experiments. The DECK experiments are crucial for understanding how the Earth's climate will respond to increasing greenhouse gas concentrations, and they have been used extensively in previous climate research [34]. Interested readers can find more technical details about these experiments in various sources [20,36–39] and others.

piControl experiment

The piControl experiment was designed to simulate the preindustrial period with non-evolving conditions, using 1850 as a reference year. This experiment aims to evaluate the coupled system and study the unforced variability of the climate system, serving as a baseline for other experiments that branch from it [34]. The assumptions made for the piControl are the following. There are no secular changes in forcing (concentrations of atmospheric constituents and land use are fixed), and the Earth's orbital characteristics are constant. That way, since there are no changes in forcing, natural or anthropogenic, the piControl is suited to study the internal variability of the climate system [34].

piControl simulation started after a spin-up for the model to come into balance with the forcing, and it was run for 1200 years, but we only used the first 500 years of it. The top-of-the-atmosphere global-

and time-mean heat fluxes were controlled through tuning, resulting in an average imbalance of +0.05 $W \cdot m^{-2}$ [20]. These adjustments remained fixed for the subsequent simulations from this experiment, such as the 1pctCO_2 experiment. The climatological state of piControl was validated by comparing it with observations, reanalysis, and descriptions in the literature, making it suitable for reference for the 1pctCO_2 experiment. Although piControl's validation is a necessary process, it is beyond the scope of this paper to discuss its results.

1pctCO_2 experiment

The 1pctCO_2 is an idealized climate change experiment designed to simulate the climate system's response to a gradual increase in atmospheric CO_2 concentrations [40]. This experiment was branched from year 501 of piControl and involves a yearly rise in 1% of atmospheric CO_2 concentration from the annual global mean value of 1850 (284.3 ppm) [34,35,40]. To ensure that the 1pctCO_2 is reliable, the simulation is run for at least 150 years beyond the quadrupling of CO_2 at year 140 [34].

To compare 1pctCO_2 experiment results to observations, we used Mauna Loa CO_2 emissions values during the RAPID 15-year period (382.09–414.24 ppm) and identified a similar emission period in the 1pctCO_2 experiment. Since 1pctCO_2 is an idealized experiment, CO_2 intervals between both products serve to evaluate the model performance. That way, the 1pctCO_2 experiment period was divided into three different periods. The period with an emissions interval similar to RAPID was called R-1pctCO_2 (model years 32–40) to represent the current climate. The remaining 1pctCO_2 period after R-1pctCO_2 is called F-1pctCO_2 (model years 41–150) and represents the future state of the climate. To facilitate analysis, we also defined L-1pctCO_2 (model years 141–150) as the last decade of the 1pctCO_2 experiment. The article uses piControl as a synonym for the past climate.

2.3 Observational data

RAPID data for the AMOC estimation

We evaluated the present AMOC using data from the Rapid Climate Change Meridian Overturning Circulation and Heatflux array (RAPID array) [41]. We then compared the results with the model outputs to validate them using CO_2 measurements from Mauna Loa. The RAPID array consists of a series of moorings along the 26.5°N parallel, spanning from Morocco to Florida, measuring temperature, salinity, and velocity of currents from near the surface to the bottom [42]. The goal of this array is to continuously monitor the strength and structure of the AMOC [43]. Further details on the RAPID moorings can be found [43,44].

We used horizontally integrated and monthly profiles from the RAPID array from 2005 to 2019. The RAPID profiles cover the surface until almost 6000 m, with an average vertical resolution of 19.59 m (19.33–19.87 m). We extracted time series as the maximum profile value at each time, and vertical equivalence to match and compare RAPID to the model output's vertical resolution was achieved through nearest-neighbor interpolation, degrading RAPID's vertical resolution.

Mauna Loa CO_2 measuring

The Mauna Loa Observatory in Hawaii (19.5°N, 155.6°W) has collected CO_2 measurements since 1958, making it the oldest site for such data [2]. CO_2 records were obtained from the National Oceanic and Atmospheric Administration (NOAA) website, the organization responsible for acquiring these data. The monthly measurements from November 1962 to October 2021 were used to estimate CO_2 emissions during the RAPID period and find a similar emission period in the model outputs.

2.4 Mathematical framework

The AMOC is a variable provided by POP2 as the Eulerian mean of the total transport for the Atlantic Ocean, Mediterranean Sea, Labrador Sea, GIN Sea, Arctic Ocean, and Hudson Bay. It is provided as a variable dependent on depth, latitude, and time. It was used to evaluate the meridional overturning at 26.5°N. The North Atlantic Ocean's total surface freshwater flux (FW) was calculated using Equations (1) and (2) to assess the region's freshwater changes. The green-shaded area in **Figure 1** shows the region

of interest for this analysis, which has also been used in previous studies [17,45,46]. Understanding freshwater inputs to the North Atlantic Ocean is important because they can impact ocean circulation and climate patterns.

$$FW = \frac{(P-E+R+M_{ice}+Salt+F_{ice})\cdot ocean\_area}{\rho} \quad (1)$$

$$F_{ice} = {}^{Q}/_{L_f} \quad (2)$$

where:

i. P is the precipitation flux (rain + snow) in $kgm^{-2}s^{-1}$.

ii. E is the evaporation flux in $kgm^{-2}s^{-1}$.

iii. R is the river runoff flux (liquid + frozen) in $kgm^{-2}s^{-1}$.

iv. M_{ice} is the melting of sea ice in $kgm^{-2}s^{-1}$.

v. *Salt* is the salt flux due to ice melt in $kgm^{-2}s^{-1}$.

vi. F_{ice} is the contribution of frazil ice formation.

vii. *ocean area* is the surface area of the ocean in m^2.

viii. ρ is the ocean density in kgm^{-3}.

ix. Q is the ocean heat flux due to ice formation in Wm^{-2}.

x. L_f is the latent heat of fusion in Jkg^{-1} ($W = Js^{-1}$).

To estimate buoyancy in the North Atlantic Ocean, we adopted the methodology [47] and applied Equation (3) to the red polygons depicted in **Figure 1**. These regions were selected based on the significant shallowing of the mixed layer depth in March, as discussed in the results section. Buoyancy is a critical term for comprehending ocean circulation and climate dynamics since it provides insight into the vertical stratification of the ocean.

$$B = \frac{g\alpha(Q_s - L_v E)}{c_p} - g\beta(E-P)S + gR \quad (3)$$

where:

i. g is the acceleration due to gravity of 9.81 ms^{-2}.

ii. α is the thermal expansion coefficient in K^{-1} ($-\rho^{-1}\partial\rho/\partial T$).

iii. Q_s is the heat flux due to radiation and conduction processes at the ocean-atmosphere interface in Wm^{-2}.

iv. L_v is the latent heat of evaporation of $25.01 \cdot 10^5$ Jkg^{-1}.

v. c_p is the specific heat at constant pressure in $Jkg^{-1}K^{-1}$.

vi. β is the saline contraction coefficient ($-\rho^{-1}\partial\rho/\partial S$).

vii. S is the salinity.

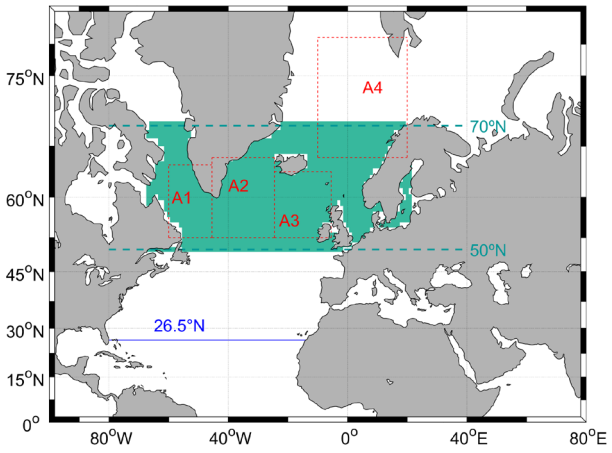

Figure 1. Regions evaluated in this work. The red polygons are areas where the depth of the mixed layer and the buoyancy associated with the vertical stratification of the ocean were analyzed. The green region assesses freshwater flux into the North Atlantic Ocean. The blue line is the section where the meridional overturning was evaluated.

Figure 1 was also used to assess the depth profile and time series of the meridional transport in the model results and RAPID using the blue transect and to estimate the mixed layer depth in the regions marked by the red polygons. The geographic boundaries of the areas in **Figure 1** are presented in **Table 1**. The mixed-layer depth is a crucial term that affects the exchange of heat and salt between the atmosphere and the ocean. The POP2 code uses the method [48] to estimate the mixed-layer depth. This method considers the effects of turbulent mixing on the vertical distribution of buoyancy and provides a reliable estimate of the mixed-layer depth.

We employed the Decision Tree method to analyze the importance of different forcing mechanisms on the freshwater flux to the North Atlantic throughout the

experiments [49–51]. This method is a nonlinear model that splits the data into a series of decision nodes, each representing a critical point for simulating the resultant freshwater flux. We used the average time series of freshwater flux in the green region of **Figure 1** as the dependent variable and the main terms, including frazil ice formation, evaporation flux, sea ice melting flux, precipitation flux, and river runoff flux, as the independent variables. The Decision Tree algorithm calculates the importance of each independent variable in conceiving the dependent one and provides statistical quantities, such as RMSE and R^2, to evaluate its accuracy [51].

Table 1. Geographic limits of the regions used in the analysis of **Figure 1**.

Region	Latitude	Longitude
Area 1	52.5°N–65°N	60°W–45.5°W
Area 2	52.5°N–66°N	45.5°W–24.5°W
Area 3	52.5°N–64°N	24.5°W–5.5°W
Area 4	66°N–78°N	10°W–20°E
26.5°N	26.5°N	80°W–14°W

Decision Tree Regressor is a powerful technique for environmental data since it can handle large amounts of values and a smaller number of variables [52]. The Decision Tree was implemented as a training set for the 500y of piControl, the 150y of 1pctCO_2, the 9y of R-1pctCO_2, the 110y of the F-1pctCO_2 and the 10y of L-1pctCO_2, with monthly frequency, to evaluate changes in the predictors of freshwater flux with six nodes.

Throughout the article, we used statistical quantities to analyze the relationships between variables. These included mean, median, variance, standard deviation, correlation, and R^2. All the correlations in this article are significant at the 95% confidence level, and we consider strong correlations above 0.70. The lag was estimated as the time of maximum correlation between both time series. These statistical quantities provide valuable insights into the system's behavior and the interplay between different terms.

3. Results and discussion

3.1 RAPID data and meridional overturning

Figure 2 displays the time series of the overturning transport, both integrated on the water column (panel a) and as a depth profile of the RAPID moorings in the 26.5°N parallel (panel b). The integrated overturning transport represents the total volume of water moved by the AMOC per unit time, which is generally positive, with a mean value of 16.91 Sv and a standard deviation of 4.59 Sv. However, we observe dips of approximately 26% in 2009/2010, 17% in 2012/2013, and 12% in 2018/2019, consistent with previous studies [44,53,54]. These dips are related to changes in ocean circulation, freshwater input, and atmospheric forcing.

The depth profile (**Figure 2b**) shows northward transport from the surface to deep depths and southward transport below them, reflecting the upper and lower branches of the AMOC cell. The transport inversion exhibits significant variability, with depths ranging from near the surface (59.60 m) to the bottom (5956.40 m) and an average inversion depth of 4230.92 m. At times, we also observe southward transports from near the surface to the bottom, as reflected by the dips in the time series (**Figure 2a**). The variability in the AMOC is primarily driven by high-frequency variability in zonal winds [53], and the RAPID measurements were taken during the warm (positive) phase of the Atlantic Multidecadal Variability.

The R-1pctCO_2 period, corresponding to model years 32 to 40, has been estimated to represent the RAPID dataset. Hence, the 15-year RAPID time series is equivalent to 9 years of an intensive emission experiment through CO_2 measurements, which allows us to observe the current high rate of CO_2 emissions. In the left panel of **Figure 3**, we present the statistics of the RAPID data and the experiments. The average value of the time series decreases from the past to the present and future, indicating a weakening of the AMOC. Although the present period has

an average value similar to RAPID, it has lower variability, possibly due to the model's non-eddy-permitting horizontal resolution, which fails to resolve mesoscale processes. This observation suggests that the model is more conservative in its representation. CMIP6 model biases in the mean climate have been identified, which can influence AMOC response to climate change [56].

In the future (F-1pctCO$_2$), the average flux is projected to decrease significantly, with the average dropping to approximately 10 Sv and a substantial increase in the standard deviation. Given the conservative behavior of the model, the future may be even more alarming than what is modeled. Moreover, on F-1pctCO$_2$, the median value is lower than the mean, indicating a time series with lower values and higher extremes. Finally, in the last decade, the AMOC overturning has been extremely low, reaching approximately 6 Sv. The mean and median values are similar, and the variations are reduced, characterizing a low, more uniformly distributed overturning.

To provide a detailed evaluation of the AMOC profile, we examine the meridional transport profile in **Figure 3b**. This figure shows all products' upper and lower branches of the AMOC. While the profile pattern of the present climate is similar to RAPID, there is a noticeable difference in the depth of the lower branch. Despite this discrepancy, **Figure 3c** displays a scatter plot between both products; the high R^2 value indicates good agreement between them. This difference is likely related to the time required for the deep ocean to stabilize numerically. Nevertheless, this study examines how the system responds to atmospheric forcing and the propagation of forcing through the ocean surface and does not require a stabilized deep ocean.

F-1pctCO$_2$ shows a significant reduction in the AMOC upper limb and a shallowing of the lower limb compared to RAPID, with L-1pctCO$_2$ intensifying this behavior. The upper limb retreats from its maximum value of 22.02 Sv at 928.04 m and 34°N to 13.51 Sv at 60.00 m and 12°N (not shown), resulting in less heat reaching high latitudes in the North Atlantic. This weakening may have responded to changes in the mixed layer depth and the shutdown of deep convection. Moreover, the meridional transport behavior in L-1pctCO$_2$ can be attributed to a decrease in NADW formation and an increase in AABW formation, possibly caused by changes in the salinity gradient of the sea surface between the Southern Ocean and the North Atlantic Ocean. This freshening is noticeable in the North Atlantic Ocean, as shown in **Figures 4c and 4e**. Strengthening AABW formation and decreasing NADW formation may have caused AABW to spread through the deep Atlantic further north. Additionally, the negative SST trends south of Greenland (**Figures 4d and 4f**), known as the 'warming hole', together with strong negative salinity trends in the same region, are consistent with an AMOC slowdown [57,58].

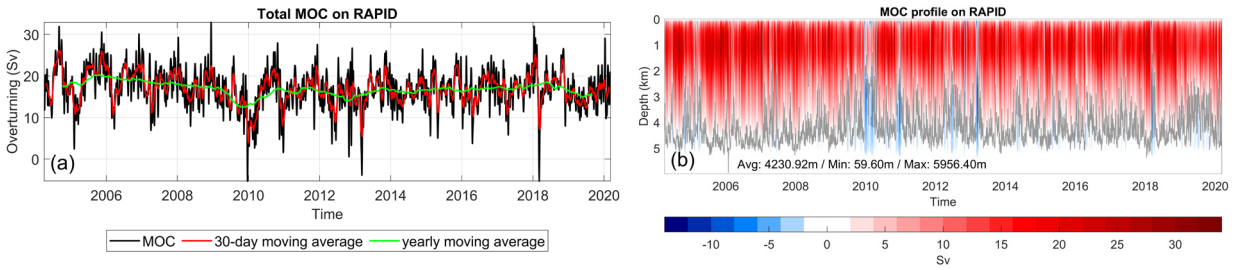

Figure 2. Zonally averaged meridional overturning circulation time series estimated by RAPID moorings along the 26.5°N parallel. (a) Vertically integrated, 30-day, and yearly moving average time series, and (b) Profile time series. Positive values (red) are associated with northward transport, and negative values (blue) are associated with southward transport [55]. The gray line marks the depth of transport inversion, and the values are the average, minimum, and maximum depths where the inversion occurs.

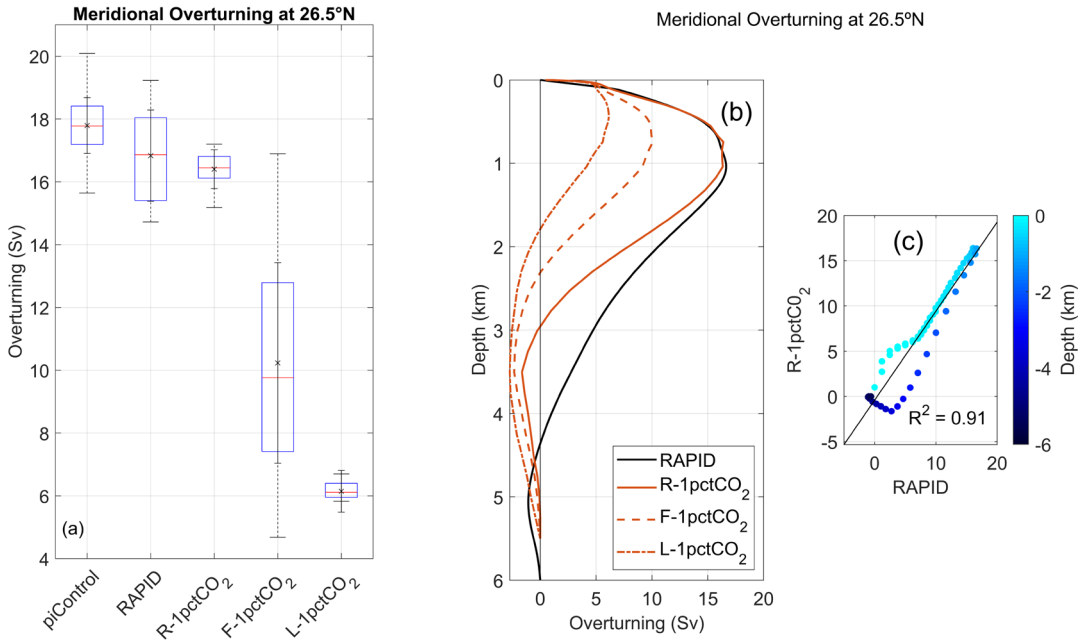

Figure 3. Meridional Overturning at 26.5°N. (a) Boxplot showing the distribution of Meridional Overturning (in Sv) across multiple CESM2 experiments and RAPID data. The black x represents the mean of each series, the red line represents the median, and the box corresponds to the data's 25th and 75th percentiles. The whiskers (solid and dashed) indicate the standard deviation and the range of the data, respectively. (b) Zonally integrated and time-averaged meridional transport profile in the Atlantic at 26.5°N. The y-axis shows the depth (in km), and the x-axis shows the overturning (in Sv). (c) Scatter plot showing the overturning (in Sv) and the colored depth values (in km) for the meridional transport at 26.5°N.

Figure 5 displays the zonally averaged distribution of vertically integrated global meridional heat transport. Positive (negative) values indicate transport northward (southward). The heat transport behaves as expected, transferring heat poleward in both hemispheres, consistent with the findings [59]. In the piControl simulation, the heat transport peaks at ~1.54 PW near 20°N in the Northern Hemisphere and ~1.16 PW near 11°S in the Southern Hemisphere. This difference in value and position is related to the South Atlantic Ocean advecting heat northward rather than poleward [60,61].

Moreover, the maximum value of 1.54 PW near 20°N agrees with the 1.30 PW reached by the AMOC upper limb around 24.5°N [62]. This similarity reinforces the significant influence of the AMOC on global meridional heat transport. In the L-1pctCO_2 simulation, the northward heat transport decreases by 0.50 PW or 32.61%. This decrease is linked to a weakening (38.64%) of the upper branch of the AMOC cell and its ability to advect heat northward. Conversely, the southward heat transport increases, which may be related to the strengthening of the lower AMOC cell.

3.2 The mixed layer depth

March is typically the month when the mixed layer of the North Atlantic is deepest [48,63,64] and is widely used in the literature as a benchmark for mixed layer depth analysis [63,65,66]. The evaluation of the mixed layer depth anomaly in March in the North Atlantic Ocean (not shown) revealed signals of mixed layer shallowing in crucial regions for the NADW formation [67,68] and hence the AMOC, mainly around the Labrador and Norwegian Seas, as well as southeast of Greenland. We have isolated the areas of mixed layer negative anomalies (red polygons in **Figure 1**) to better monitor them.

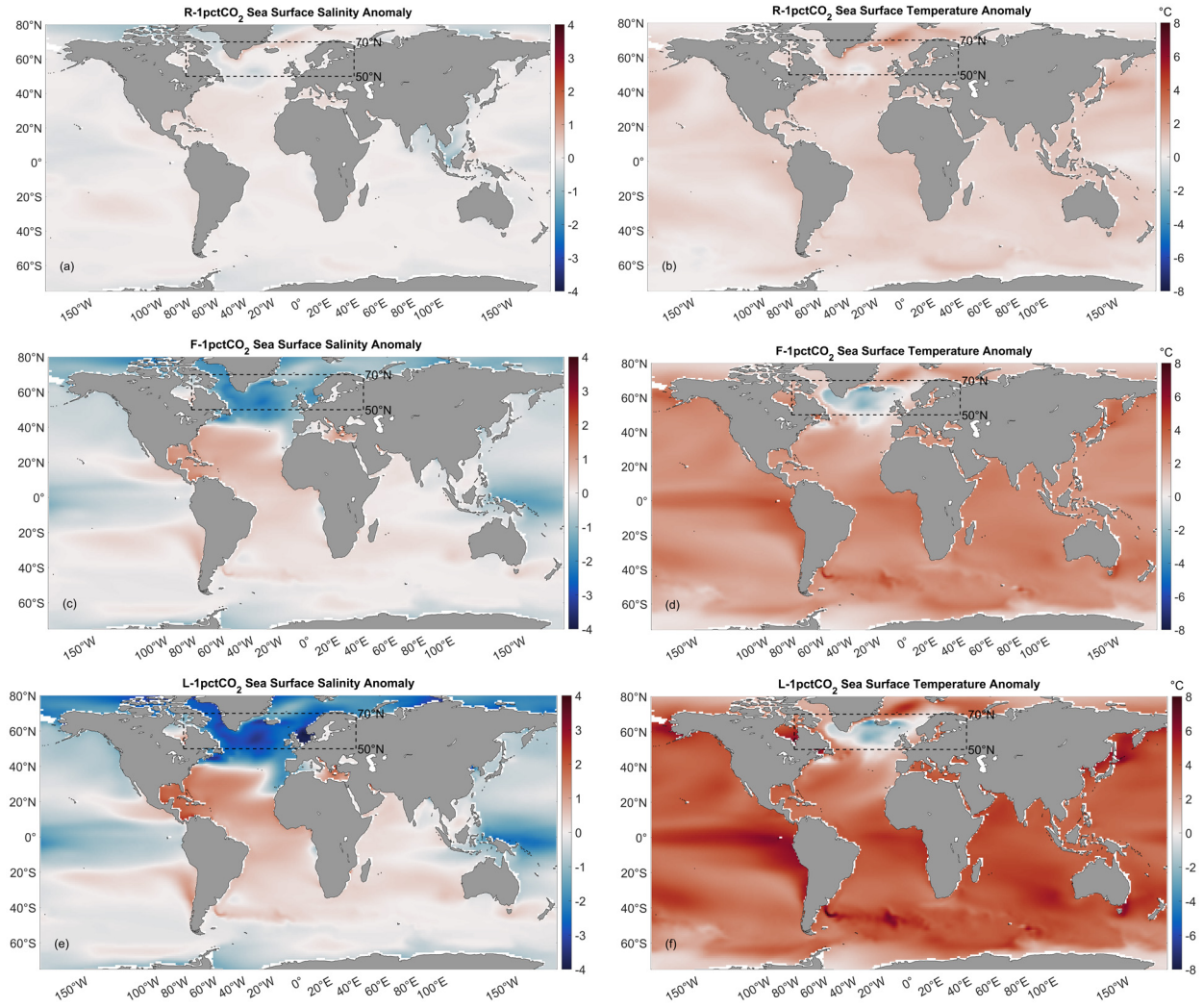

Figure 4. Anomalies of sea surface salinity (left panels) and sea surface temperature (right panels) in 1pctCO$_2$, compared to the time average of 500 years of piControl. The top panels show the anomalies for R-1pctCO$_2$, the middle panels show the anomalies for F-1pctCO$_2$, and the lower panels show the anomalies for L-1pctCO$_2$. Positive (negative) values indicate an increase (decrease) in the term relative to the average period of piControl. Additionally, the dashed region marks the area used to assess the freshwater flux between 50°N and 70°N.

The maximum mixed layer depth time series in March for each Area is shown in **Figure 6**. The piControl results indicate that all four Areas are relatively stable, and their values agree with those reported in previous studies [68,69]. However, in 1pctCO$_2$, all areas experience a strong shallowing at different times. Area 1 shows the earliest and most pronounced shallowing, followed by the others [70]. Furthermore, the percentage reduction in mixed layer depth decreases from Area 1 to Areas 2, 3, and 4, indicating a cascade effect process. Specifically, the lag between consecutive areas is 25 years between Areas 1 and 2, 19 years between Areas 2 and 3, and 17 years between Areas 3 and 4, with corresponding lag-adjusted correlation values of 0.91, 0.89, and 0.86, respectively. This reduction in lag time between the areas is likely related to the amplification of global warming. Additionally, the variability in mixed layer depth practically reduces to zero (not shown), indicating that deep convection is shut down.

The reduction of mixed layer depth due to warming can increase the water column's stratification. Increased surface buoyancy leads to a more stratified water column [47]. To assess this effect in the simulations, we computed the surface buoyancy for Areas 1–4 using Equation (3). **Figure 7** shows each area's

time series of buoyancy. In the piControl simulation, we observe variability throughout the series with no discernible trend. However, in the 1pctCO_2 simulation, we observe a clear increase in buoyancy in the first few decades for all areas, particularly for Areas 1 and 2, which has direct implications for the formation of NADW. Area 3 exhibits oscillations and a smaller increase in buoyancy in the last decade compared to the other areas, which other factors beyond the scope of this study may influence.

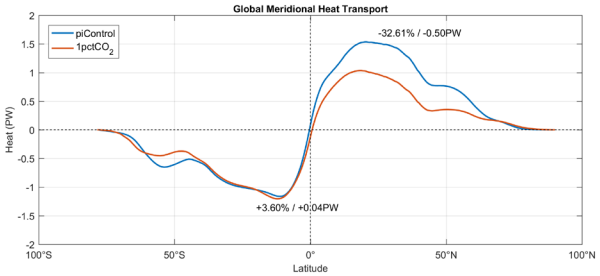

Figure 5. Latitudinal distribution of zonally averaged and depth-integrated heat transport (in petawatts, PW) for the time average of 500 years of piControl and L-1pctCO_2. Furthermore, the texts show the percentage and absolute increase (+) or decrease (–) in L-1pctCO_2 compared to the average of piControl. The black dashed lines mark zero transport and 0° latitude.

3.3 Freshwater input to the North Atlantic Ocean

Figure 8a shows the time-averaged distribution of the total surface freshwater flux to the North Atlantic in piControl, expressed in mSv. The results are consistent with previous studies [71,72]. Although some regions have negative freshwater flux, particularly near Ireland, most of the North Atlantic experiences a net gain of freshwater, which reduces surface salinity and the buoyancy of the water. The freshwater input is overall low (ranging from 0 to 0.1 mSv), with higher values concentrated around the east coast of North America, the coast of Europe, and the west and east sides of Greenland, reaching up to 0.44 mSv, 0.33 mSv, 0.15 mSv, and 0.46 mSv, respectively.

The pattern of freshwater anomalies consistently intensifies from present to future, with the most significant changes occurring in the last decade. Specifically, there is a noticeable decrease in freshwater on both sides of Greenland, in the north and northeast of Iceland and the eastern coast of North America, while the freshwater flux in the ocean interior increases. These changes could trigger modifications to the NADW formation, such as the weakening identified in this article and shown previously.

The average freshwater anomaly in L-1pctCO_2 (not shown) is $7.00 \cdot 10^{-3}$ mSv, lower than the amounts reported in previous studies [12,13,17,18]. However, even this amount of freshwater input can cause significant changes in the AMOC cell, as seen previously [73]. Overall, these findings highlight the critical role of freshwater input in the ocean's circulation and emphasize the potential impacts of even relatively small changes in this input.

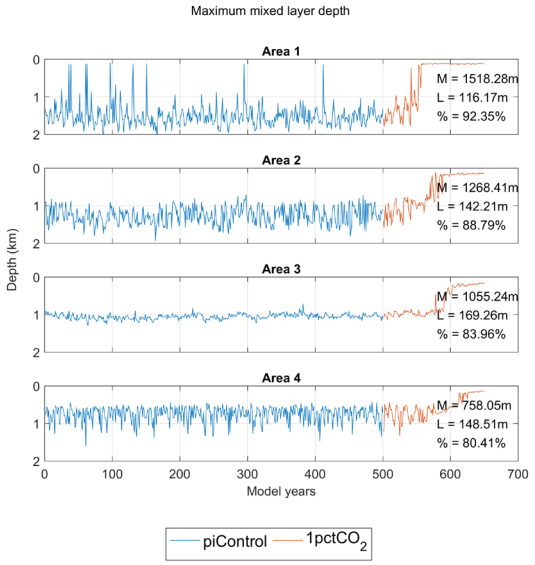

Figure 6. Time series of maximum mixed layer depth in March for each area (red polygons in **Figure 1**) in the piControl and 1pctCO_2 experiments. *M* represents the average piControl value, *L* is the average L-1pctCO_2 value, and % indicates the percentage of shallowing (decrease in mixed layer depth) in L-1pctCO_2 compared to the time average of 500 years of piControl. Shallowing refers to a reduction in the maximum depth of the mixed layer, which measures the depth of the layer in which temperature and salinity are relatively uniform.

Figure 9 illustrates the behavior of each term used to estimate freshwater flux over time. The salt flux is not included as it is directly correlated with the sea ice melting flux, which showed a reduction of 92.64% in L-1pctCO_2. Both sea ice terms exhibited reductions of over 85%, but their weak correlation

(0.55) indicates that different factors affect them. Meanwhile, the runoff flux increased throughout the experiment while the evaporation flux decreased. The precipitation flux exhibited fluctuations throughout the 150-year experiment, but the average value of L-1pctCO_2 was similar to the piControl mean.

It's worth noting that the variables related to sea ice showed high reductions, which is problematic because it is crucial for climate [74]. Diminished sea ice cover increases the surface area for atmospheric-ocean interaction and decreases the region's albedo, causing the ocean to absorb more heat, which leads to further melting. Reduced sea ice also increases the ocean's freshwater, which increases its buoyancy. Overall, these findings emphasize the importance of sea ice in regulating the Earth's climate and highlight the potential impacts of its reduction.

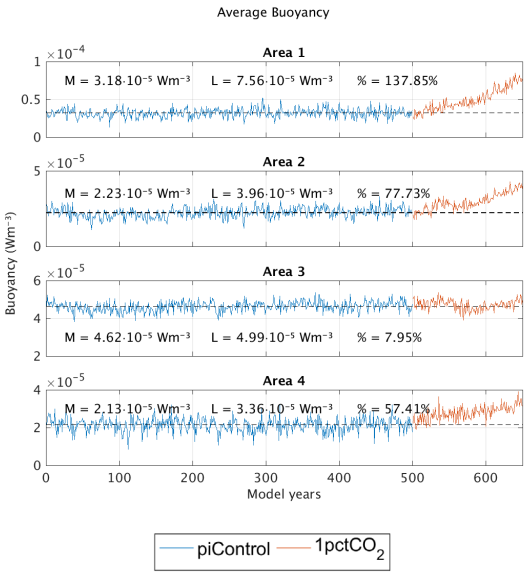

Figure 7. Buoyancy time series for each area (red polygons in **Figure 1**) in the piControl and 1pctCO_2 experiments. Buoyancy, a measure of the vertical stratification of the ocean, plays an important role in regulating ocean circulation and climate dynamics. The buoyancy was calculated using Equation (3). *M* represents the average piControl value, *L* is the L-1pctCO_2, and % indicates the percentage of increase in L-1pctCO_2 compared to the time average of 500 years of piControl.

The amount of freshwater flux into the ocean is affected by several factors, including sea ice melting, evaporation, runoff, and frazil ice formation. Changes in each term can either increase or decrease the freshwater flux, and the overall effect is complex and challenging to predict [57]. Our study found that the main factor driving changes in freshwater flux in L-1pctCO_2 was a decrease in evaporation flux, likely caused by colder SSTs in the North Atlantic. We observed that the evaporation flux and sea ice melting flux were strongly correlated, even though they had opposite effects on freshwater flux. This behavior suggests that climate stability may partly be due to the complex interplay between different factors affecting the ocean system.

A complex interplay of various factors determines the outcome of freshwater flux. We employed a decision tree algorithm to simulate the freshwater flux based on these factors, summarized in **Table 2**. The algorithm successfully obtained the freshwater flux with low RMSE and high R^2, with runoff being the most critical predictor across all scenarios. Evaporation was the second most important predictor for R-, F-, and L-1pctCO_2, followed by sea ice melting flux. For R- and L-1pctCO_2, precipitation, and frazil fluxes were also significant predictors, while for F-1pctCO_2, frazil and precipitation fluxes were significant.

In the past, we observed that runoff was the most critical factor limiting the total freshwater flux in the region. However, in the current climate, while the increasing tendency of runoff (**Figure 9**) still gives it a high score, it shares the importance with the evaporation flux, which is decreasing. This behavior is intensified on the L-1pctCO_2 with additional participation from the sea ice melting flux, which decreases drastically and justifies the higher score. At the end of 1pctCO_2, the hydric balance (E-P) becomes more important. With colder SST (**Figure 4f**), the evaporation flux decreases, creating more high-pressure air masses, increasing surface pressure, and inhibiting the convection process.

It is crucial to notice that MOSART, the river transport model used at CESM2, only simulates the runoff process to the river and, consequently, the sea. It does not simulate the processes of infiltration, percolation, water storage in the saturated region of the ground (aquifer), and, subsequently, the discharge

of the aquifer into the sea. In this way, the process of transporting freshwater to the sea from the melting may be underestimated in the vast majority of Earth System Models, which use the same or similar models for this process, which would indicate that a possible collapse of the AMOC could happen much earlier than is being predicted.

Overall, our findings suggest that the amount of freshwater flux into the ocean is affected by a complex interplay of factors and that small changes in one term can significantly affect the overall system. By understanding these relationships, we can gain insights into the stability of the climate system and improve our ability to predict future changes.

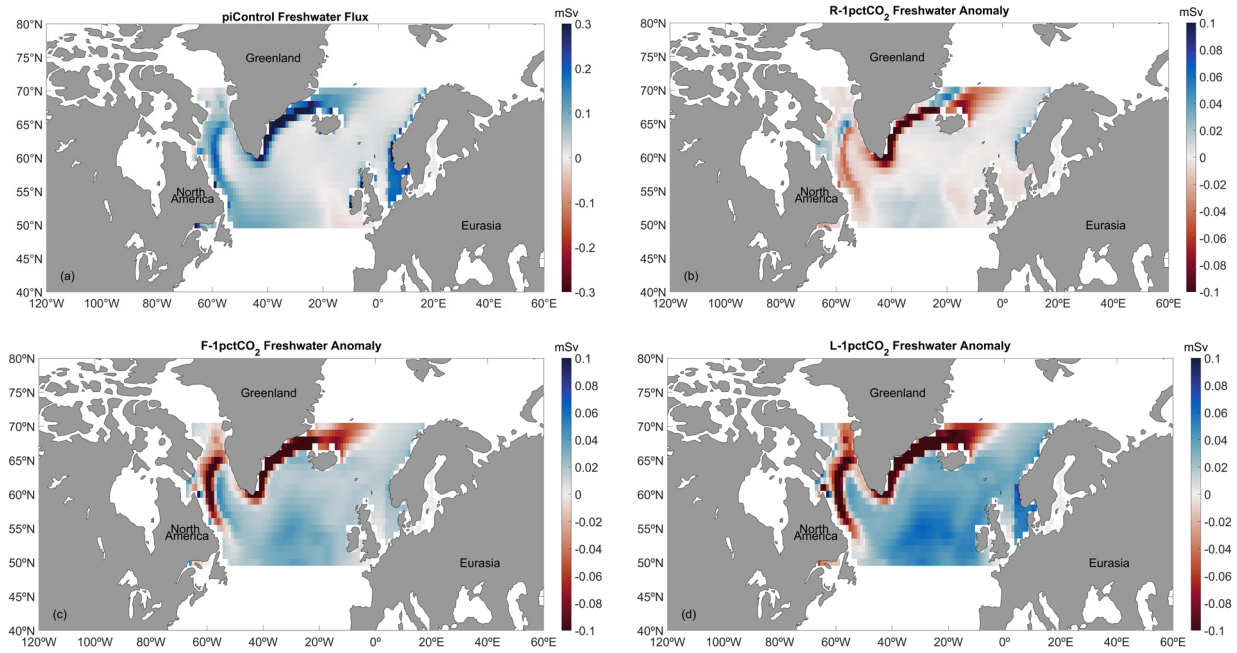

Figure 8. Freshwater flux to the North Atlantic Ocean, between 50°N and 70°N (the green region in **Figure 1**). (a) The time average of 500 years of piControl. (b) (c) and (d) represent R-1pctCO$_2$, F-1pctCO$_2$, and L-1pctCO$_2$ anomalies, respectively, compared to the time average of piControl. The color scale represents the freshwater flux anomaly (in miliSverdrups), and positive (negative) values indicate more (less) freshwater flux in 1pctCO$_2$ compared to piControl.

Table 2. The decision tree regressor is used to evaluate the most important components in the freshwater flux in monthly frequency. The top part of the table depicts statistical quantities (RMSE, R^2) of the ability of the algorithm to represent the freshwater flux (dependent variable). The bottom part of the table depicts the scores of the variables used to calculate the freshwater flux (independent variables) for the 500y of piControl, the 150y of 1pctCO$_2$, the 9y of R-1pctCO$_2$, the 110y of the F-1pctCO$_2$ and the 10y of L-1pctCO$_2$.

Metrics	**piControl**	**1pctCO$_2$**	**R-1pctCO$_2$**	**F-1pctCO$_2$**	**L-1pctCO$_2$**
RMSE (m^3s^{-1})	0.050	0.073	0.028	0.071	0.040
R^2	0.913	0.822	0.979	0.979	0.907
Scores	**piControl**	**1pctCO$_2$**	**R-1pctCO$_2$**	**F-1pctCO$_2$**	**L-1pctCO$_2$**
Sea ice melting flux	0.105	0.076	0.086	0.071	0.167
Frazil flux	0.001	0.041	0.017	0.070	0.022
Runoff flux	0.886	0.811	0.739	0.753	0.559
Precipitation flux	0.003	0.021	0.023	0.020	0.045
Evaporation flux	0.005	0.051	0.136	0.085	0.207

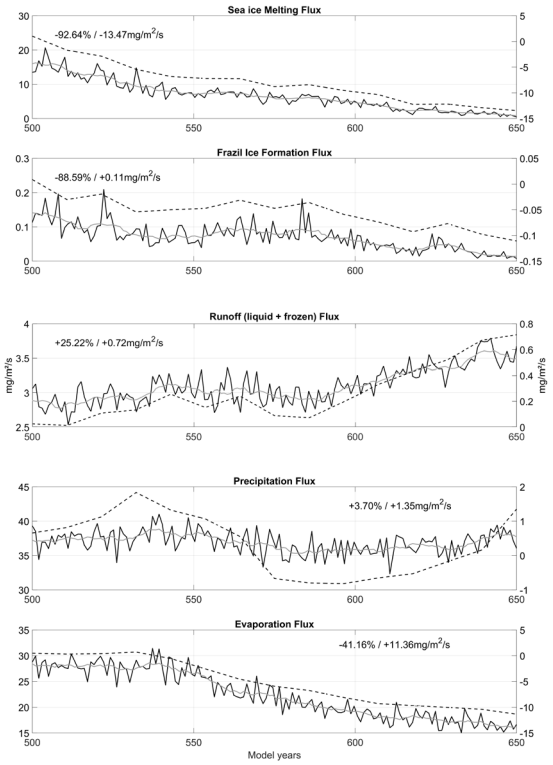

Figure 9. Annual mean series of terms used to calculate the 1pctCO_2 experiment freshwater (in mg/m^2/s). The left y-axis corresponds to the continuous black and gray lines, which show the flux and the 10-year moving average from each series, respectively. The right y-axis corresponds to the dashed black lines showing decadal anomalies. The green region in **Figure 1** represents the area considered for the calculation.

4. Conclusions

This study focused on the impacts of increased atmospheric CO_2 on the AMOC dynamics and related mechanisms between the ocean, sea ice, and atmosphere using Earth System model results with CO_2 forcing. The significant decrease in the time series of the overturning was due to the weakening and shallowing of the AMOC upper branch and the strengthening and stretching of the lower branch, which confined the upper branch to shallower waters.

The freshening in high latitudes of the North Atlantic led to a shallower mixed layer depth and reduced deep convection, resulting in a decrease in NADW formation and an increase in AABW formation and spread. These changes, in turn, weakened the upper branch of the AMOC, resulting in less heat reaching high latitudes in the North Atlantic, which was evident from the warming hole observed on the surface of the North Atlantic Ocean.

This work noted that the observed data showed that the AMOC weakening conditions were more pronounced than in the CESM2 simulations (R-1pctCO_2). This behavior may be associated with simulating the complex heat, mass, and momentum fluxes in the ocean-atmosphere and soil-ice-atmosphere interactions.

During the last decade of the experiment (L-1pct-CO_2), there was a significant drop in ocean evaporation and sea ice and an increase in river runoff. The lower SSTs in the warming hole area, caused by melted sea ice, resulted in reduced evaporation and surface salinity. At the same time, the increase in runoff led to more freshwater being sent to the ocean, creating a positive feedback loop. The model seems to underestimate the impact of this positive feedback loop, as observed in the current climate (RAPID vs. R-1pctCO_2). This underestimation could potentially lead to a faster disruption of the AMOC than what is being predicted by Earth System models.

While we have not yet reached a moment of a pattern change in the climate system, the increasing intensity and frequency of extreme events indicate the amplification of climate variability due to additional energy being added to the system. The probability of this process accelerating is closely linked to our socioeconomic model of unrestrained consumption, unclean energy production, and planned obsolescence. Future research could explore potential impacts on other aspects of the world's ocean and atmosphere, building on the findings presented here.

Author Contributions

All authors contributed to the conceptualization of the study. Lívia Sancho, Luiz Paulo Assad, and Luiz Landau were responsible for the resources. Lívia Sancho and Elisa Passos were responsible for the software, formal analysis, and manuscript writing. Lívia Sancho, Elisa Passos, Luiz Paulo de Freitas Assad, and Marcio Cataldi conceived and reviewed the manuscript. Luiz Paulo de Freitas Assad, Marcio Cataldi, and Luiz Landau edited the text.

Luiz Paulo Assad and Luiz Landau were responsible for the funding acquisition. All authors read and approved the final manuscript.

Conflict of Interest

The authors declare that the research was conducted without any commercial or financial relationship that could be construed as a potential conflict of interest.

Data Availability

CMIP6 outputs are available from the following websites: https://esgfnode.llnl.gov/search/cmip6/, https://esgf-node.ipsl.upmc.fr/search/cmip6-ipsl/, https://esgf-node.ipsl.upmc.fr/search/cmip6-ipsl/ and https://esgfindex1.ceda.ac.uk/search/cmip6-ceda/.

The Natural Environment Research Council funds data from the RAPID AMOC monitoring project (https://doi.org/10.5285/e91b10af-6f0a-7fa7-e053-6c86abc05a09) and are freely available from www.rapid.ac.uk/rapidmoc.

Mauna Loa CO_2 records (https://doi.org/10.6075/J0QJ7F7N) are also freely available from https://library.ucsd.edu/dc/object/bb90132731.

Funding

This work was possible through the financing of PEC-20480 Project between Royal Dutch Shell (Shell) and the *Laboratório de Métodos Computacionais em Engenharia* (LAMCE) and through the doctoral fellowship funding by CNPq for Elisa Passos Case number 141819/2016-2 and the postdoctoral fellowship funding by FAPERJ E 10/2020—*Edital Inteligência Artificial* Case Number E-26/203.327/2022—Enrollment No. Scholarship 2015.08297.7 for Lívia Sancho.

Acknowledgments

We gratefully acknowledge the *Universidade Federal do Rio de Janeiro* (UFRJ), the *Instituto Alberto Luiz Coimbra de Pós-Graduação e Pesquisa de Engenharia* (COPPE), the *Programa de Engenharia Civil*, the *Conselho Nacional de Desenvolvimento Científico e Tecnológico* (CNPq) and the *Fundação de Amparo à Pesquisa do Estado do Rio de Janeiro* (FAPERJ) for granting the opportunity to develop this work.

References

[1] Global Warming of 1.5 °C [Internet]. IPCC. Available from: https://www.ipcc.ch/site/assets/uploads/sites/2/2019/06/SR15_Full_Report_High_Res.pdf

[2] Costello, A., Abbas, M., Allen, A., et al., 2009. Managing the health effects of climate change: lancet and University College London Institute for Global Health Commission. The Lancet. 373(9676), 1693–1733.
DOI: https://doi.org/10.1016/S0140-6736(09)60935-1

[3] IPCC, 2013. Summary for policymakers. Cambridge University Press: Cambridge.
DOI: https://doi.org/10.1017/CBO9781107415324.004

[4] Sundquist, E.T., 2013. Geological perspectives on carbon dioxide and the carbon cycle. American Geophysical Union (AGU): Washington, D.C. pp. 5–60.
DOI: https://doi.org/10.1029/GM032p0005

[5] Broecker, W.S., 1987. Unpleasant surprises in the greenhouse? Nature. 328, 123–126.
DOI: https://doi.org/10.1038/328123a0

[6] Broecker, W.S., 1997. Thermohaline circulation, the Achilles heel of our climate system: Will man-made CO_2 upset the current balance? Science. 278(5343), 1582–1588.
DOI: https://doi.org/10.1126/science.278.5343.1582

[7] Jackson, L.C., Biastoch, A., Buckley, M.W., et al., 2022. The evolution of the North Atlantic meridional overturning circulation since 1980. Nature Reviews Earth & Environment. 3, 241–254.
DOI: https://doi.org/10.1038/s43017-022-00263-2

[8] Johnson, H.L., Cessi, P., Marshall, D.P., et al., 2019. Recent contributions of theory to our understanding of the Atlantic meridional overturning circulation. Journal of Geophysical Re-

search: Oceans. 124(8), 5376–5399.
DOI: https://doi.org/10.1029/2019JC015330

[9] Frajka-Williams, E., Foukal, N., Danabasoglu, G., 2023. Should AMOC observations continue: How and why?. Philosophical Transactions of the Royal Society A. 381(2262).
DOI: https://doi.org/10.1098/rsta.2022.0195

[10] Anthoff, D., Estrada, F., Tol, R.S., 2016. Shutting down the thermohaline circulation. American Economic Review. 106(5), 602–606.
DOI: https://doi.org/10.1257/aer.p20161102

[11] Danabasoglu, G., Yeager, S.G., Kim, W.M., et al., 2016. North Atlantic simulations in Coordinated Ocean-ice Reference Experiments phase II (CORE-II). Part II: Inter-annual to decadal variability. Ocean Modelling. 97, 65–90.
DOI: https://doi.org/https://doi.org/10.1016/j.ocemod.2015.11.007

[12] Stocker, T.F., Wright, D.G., 1991. Rapid transitions of the ocean's deep circulation induced by changes in surface water fluxes. Nature. 351, 729–732.
DOI: https://doi.org/10.1038/351729a0

[13] Lenton, T.M., Held, H., Kriegler, E., et al., 2008. Tipping elements in the Earth's climate system. Proceedings of the national Academy of Sciences. 105(6), 1786–1793.
DOI: https://doi.org/10.1073/pnas.0705414105

[14] Orihuela-Pinto, B., England, M.H., Taschetto, A.S., 2022. Interbasin and interhemispheric impacts of a collapsed Atlantic Overturning Circulation. Nature Climate Change. 12, 558–565.
DOI: https://doi.org/10.1038/s41558-022-01380-y

[15] Luo, Y., Tjiputra, J., Guo, C., et al., 2018. Atlantic deep water circulation during the last interglacial. Scientific Reports. 8, 4401.
DOI: https://doi.org/10.1038/s41598-018-22534-z

[16] Buckley, M.W., Marshall, J., 2016. Observations, inferences, and mechanisms of the Atlantic Meridional Overturning Circulation: A review. Reviews of Geophysics. 54(1), 5–63.
DOI: https://doi.org/10.1002/2015RG000493

[17] Manabe, S., Stouffer, R.J., 1999. The role of thermohaline circulation in climate. Tellus A: Dynamic Meteorology and Oceanography. 51(1), 91–109.

[18] Vellinga, M., Wood, R.A., 2002. Global climatic impacts of a collapse of the Atlantic thermohaline circulation. Climatic Change. 54, 251–267.
DOI: https://doi.org/10.1023/A:1016168827653

[19] Knutti, R., Masson, D., Gettelman, A., 2013. Climate model genealogy: Generation CMIP5 and how we got there. Geophysical Research Letters. 40(6), 1194–1199.
DOI: https://doi.org/10.1002/grl.50256

[20] Danabasoglu, G., Lamarque, J.F., Bacmeister, J., et al., 2020. The community earth system model version 2 (CESM2). Journal of Advances in Modeling Earth Systems. 12(2), e2019MS001916.
DOI: https://doi.org/10.1029/2019MS001916

[21] Cam6.3 User's Guide [Internet]. NCAR: National Center for Atmospheric Research [cited 2023 Dec 23]. Available from: https://doi.org/10.5065/Z953-ZC95

[22] Lawrence, D.M., Fisher, R.A., Koven, C.D., et al., 2019. The Community Land Model version 5: Description of new features, benchmarking, and impact of forcing uncertainty. Journal of Advances in Modeling Earth Systems. 11(12), 4245–4287.
DOI: https://doi.org/10.1029/2018MS001583

[23] Technical Description of Version 4.0 of the Community Land Model (CLM) [Internet]. NCAR: National Center for Atmospheric Research. Available from: https://opensky.ucar.edu/islandora/object/technotes%3A493/datastream/PDF/view

[24] Hurrell, J.W., Holland, M.M., Gent, P.R., et al., 2013. The community earth system model: A framework for collaborative research. Bulletin of the American Meteorological Society. 94(9), 1339–1360.
DOI: https://doi.org/10.1175/BAMS-D-12-00121.1

[25] CICE: The Los Alamos Sea Ice Model Docu-

mentation and Software User's Manual Version 4.1 LA-CC-06-012 [Internet]. Los Alamos National Laboratory. Available from: https://csdms.colorado.edu/w/images/CICE_documentation_and_software_user%27s_manual.pdf

[26] Hunke, E.C., Dukowicz, J.K., 2002. The elastic-viscous-plastic sea ice dynamics model in general orthogonal curvilinear coordinates on a sphere—Incorporation of metric terms. Monthly Weather Review. 130(7), 1848–1865. DOI: https://doi.org/10.1175/1520-0493(2002)130<1848:TEVPSI>2.0.CO;2

[27] Bitz, C.M., Lipscomb, W.H., 1999. An energy-conserving thermodynamic model of sea ice. Journal of Geophysical Research: Oceans. 104(C7), 15669–15677. DOI: https://doi.org/10.1029/1999JC900100

[28] A Delta-Eddington Mutiple Scattering Parameterization for Solar Radiation in the Sea Ice Component of the Community Climate System Model (No. NCAR/TN-472+STR) [Internet]. [cited 2023 Dec 23]. Available from: https://doi.org/10.5065/D6B27S71

[29] Holland, M.M., Bailey, D.A., Briegleb, B.P., et al., 2012. Improved sea ice shortwave radiation physics in CCSM4: The impact of melt ponds and aerosols on Arctic sea ice. Journal of Climate. 25(5), 1413–1430. DOI: https://doi.org/10.1175/JCLI-D-11-00078.1

[30] Thorndike, A.S., Rothrock, D.A., Maykut, G.A., et al., 1975. The thickness distribution of sea ice. Journal of Geophysical Research. 80(33), 4501–4513. DOI: https://doi.org/10.1029/JC080i033p04501

[31] Li, H., Wigmosta, M.S., Wu, H., et al., 2013. A physically based runoff routing model for land surface and earth system models. Journal of Hydrometeorology. 14(3), 808–828. DOI: https://doi.org/10.1175/JHM-D-12-015.1

[32] The Parallel Ocean Program (POP) Reference Manual: Ocean Component of the Community Climate System Model (CCSM) and Community Earth System Model (CESM) [Internet]. Los Alamos National Laboratory. Available from: https://opensky.ucar.edu/islandora/object/manuscripts%3A825/datastream/PDF/view

[33] Griffies, S.M., Böning, C., Bryan, F.O., et al., 2000. Developments in ocean climate modelling. Ocean Modelling. 2(3–4), 123–192. DOI: https://doi.org/10.1016/S1463-5003(00)00014-7

[34] Eyring, V., Bony, S., Meehl, G.A., et al., 2016. Overview of the Coupled Model Intercomparison Project Phase 6 (CMIP6) experimental design and organization. Geoscientific Model Development. 9(5), 1937–1958. DOI: https://doi.org/10.5194/gmd-9-1937-2016

[35] Meinshausen, M., Vogel, E., Nauels, A., et al., 2017. Historical greenhouse gas concentrations for climate modelling (CMIP6). Geoscientific Model Development. 10(5), 2057–2116. DOI: https://doi.org/10.5194/gmd-10-2057-2017

[36] Hoesly, R.M., Smith, S.J., Feng, L., et al., 2018. Historical (1750–2014) anthropogenic emissions of reactive gases and aerosols from the Community Emissions Data System (CEDS). Geoscientific Model Development. 11(1), 369–408. DOI: https://doi.org/10.5194/gmd-11-369-2018

[37] Van Marle, M.J., Kloster, S., Magi, B.I., et al., 2017. Historic global biomass burning emissions for CMIP6 (BB4CMIP) based on merging satellite observations with proxies and fire models (1750–2015). Geoscientific Model Development. 10(9), 3329–3357. DOI: https://doi.org/10.5194/gmd-10-3329-2017

[38] Kay, J.E., Deser, C., Phillips, A., et al., 2015. The Community Earth System Model (CESM) large ensemble project: A community resource for studying climate change in the presence of internal climate variability. Bulletin of the American Meteorological Society. 96(8), 1333–1349. DOI: https://doi.org/10.1175/BAMS-D-13-00255.1

[39] Steele, M., Morley, R., Ermold, W., 2001. PHC: A global ocean hydrography with a high-quality Arctic Ocean. Journal of Climate. 14(9), 2079–2087.
DOI: https://doi.org/10.1175/1520-0442(2001)014<2079:PAGOHW>2.0.CO;2

[40] Bacmeister, J.T., Hannay, C., Medeiros, B., et al., 2020. CO_2 increase experiments using the CESM: Relationship to climate sensitivity and comparison of CESM1 to CESM2. ESS Open Archive.
DOI: https://doi.org/10.1002/essoar.10502611.1

[41] Atlantic Meridional Overturning Circulation Observed by the RAPID-MOCHA-WBTS (Rapid-Meridional Overturning Circulation and Heatflux Array-Western Boundary Time Series) Array at 26N from 2004 to 2022 (v2022.1) [Internet]. British Oceanographic Data Centre. [cited 2023 Nov 11]. Available from: https://doi.org/10.5285/04c79ece-3186-349a-e063-6c86abc0158c

[42] Lozier, M.S., Bacon, S., Bower, A.S., et al., 2017. Overturning in the Subpolar North Atlantic Program: A new international ocean observing system. Bulletin of the American Meteorological Society. 98(4), 737–752.
DOI: https://doi.org/10.1175/BAMS-D-16-0057.1

[43] McCarthy, G.D., Smeed, D.A., Johns, W.E., et al., 2015. Measuring the Atlantic meridional overturning circulation at 26°N. Progress in Oceanography. 130, 91–111.
DOI: https://doi.org/10.1016/j.pocean.2014.10.006

[44] Frajka-Williams, E., Ansorge, I.J., Baehr, J., et al., 2019. Atlantic meridional overturning circulation: Observed transport and variability. Frontiers in Marine Science. 6, 260.
DOI: https://doi.org/10.3389/fmars.2019.00260

[45] Kim, S.K., Kim, H.J., Dijkstra, H.A., et al., 2022. Slow and soft passage through tipping point of the Atlantic Meridional Overturning Circulation in a changing climate. npj Climate and Atmospheric Science. 5, 13.
DOI: https://doi.org/10.1038/s41612-022-00236-8

[46] Manabe, S., Stouffer, R.J., 1997. Coupled ocean-atmosphere model response to freshwater input: Comparison to Younger Dryas event. Paleoceanography and Paleoclimatology. 12(2), 321–336.
DOI: https://doi.org/10.1029/96PA03932

[47] Castro, B.M., 2014. Summer/winter stratification variability in the central part of the South Brazil Bight. Continental Shelf Research. 89, 15–23.
DOI: https://doi.org/10.1016/j.csr.2013.12.002

[48] Large, W.G., Danabasoglu, G., Doney, S.C., et al., 1997. Sensitivity to surface forcing and boundary layer mixing in a global ocean model: Annual-mean climatology. Journal of Physical Oceanography. 27(11), 2418–2447.
DOI: https://doi.org/10.1175/1520-0485(1997)027<2418:STSFAB>2.0.CO;2

[49] Kadiyala, A., Kumar, A., 2017. Applications of Python to evaluate environmental data science problems. Environmental Progress & Sustainable Energy. 36(6), 1580–1586.
DOI: https://doi.org/10.1002/ep.12786

[50] Loh, W.Y., 2011. Classification and regression trees. Wiley Interdisciplinary Reviews: Data Mining and Knowledge Discovery. 1(1), 14–23.
DOI: https://doi.org/10.1002/widm.8

[51] Pedregosa, F., Varoquaux, G., Gramfort, A., et al., 2011. Scikit-learn: Machine learning in Python. The Journal of Machine Learning Research. 12, 2825–2830.

[52] De'ath, G., Fabricius, K.E., 2000. Classification and regression trees: A powerful yet simple technique for ecological data analysis. Ecology. 81(11), 3178–3192.
DOI: https://doi.org/10.1890/0012-9658(2000)081[3178:CARTAP]2.0.CO;2

[53] Moat, B.I., Smeed, D.A., Frajka-Williams, E., et al., 2020. Pending recovery in the strength of the meridional overturning circulation at 26°N. Ocean Science. 16(4), 863–874.
DOI: https://doi.org/10.5194/os-16-863-2020

[54] Smeed, D.A., Josey, S.A., Beaulieu, C., et al.,

2018. The North Atlantic Ocean is in a state of reduced overturning. Geophysical Research Letters. 45(3), 1527–1533.
DOI: https://doi.org/10.1002/2017GL076350

[55] Atlantic Meridional Overturning Circulation Observed by the RAPID-MOCHA-WBTS (RAPID-Meridional Overturning Circulation and Heatflux Array-Western Boundary Time Series) Array at 26N from 2004 to 2020 (v2020.1) [Internet]. National Oceanography Centre. Available from: https://doi.org/10.5285/cc1e34b3-3385-662b-e053-6c86abc03444

[56] Jackson, L.C., Hewitt, H.T., Bruciaferri, D., et al., 2023. Challenges simulating the AMOC in climate models. Philosophical Transactions of the Royal Society A. 381(2262), 20220187.
DOI: https://doi.org/10.1098/Rsta.2022.0187

[57] Swingedouw, D., Mignot, J., Braconnot, P., et al., 2009. Impact of freshwater release in the North Atlantic under different climate conditions in an OAGCM. Journal of Climate. 22(23), 6377–6403.
DOI: https://doi.org/10.1175/2009JCLI3028.1

[58] Boers, N., 2021. Observation-based early-warning signals for a collapse of the Atlantic Meridional Overturning Circulation. Nature Climate Change. 11(8), 680–688.
DOI: https://doi.org/10.1038/s41558-021-01097-4

[59] Stammer, D., Köhl, A., Vlasenko, A., et al., 2018. A pilot climate sensitivity study using the CEN coupled adjoint model (CESAM). Journal of Climate. 31(5), 2031–2056.
DOI: https://doi.org/10.1175/JCLI-D-17-0183.1

[60] Sancho, L.M.B., de Freitas Assad, L.P., Landau, L., 2015. Volume and heat transports analysis in the South Atlantic Basin related to climate change scenarios. Brazilian Journal of Geophysics. 33(2), 333–348.
DOI: http://dx.doi.org/10.22564/rbgf.v33i2.724

[61] Zhu, Y., Wei, Z., Wang, Y., et al., 2014. The annual mean sketches and climatological variability of the volume and heat transports through the inter-basin passages: A study based on 1400-year spin up of MOM4p1. Acta Oceanologica Sinica. 33, 12–24.
DOI: https://doi.org/10.1007/s13131-014-0513-7

[62] Srokosz, M., Baringer, M., Bryden, H., et al., 2012. Past, present, and future changes in the Atlantic meridional overturning circulation. Bulletin of the American Meteorological Society. 93(11), 1663–1676.
DOI: https://doi.org/10.1175/BAMS-D-11-00151.1

[63] Lique, C., Johnson, H.L., Plancherel, Y., 2018. Emergence of deep convection in the Arctic Ocean under a warming climate. Climate Dynamics. 50, 3833–3847.
DOI: https://doi.org/10.1007/s00382-017-3849-9

[64] Carton, J.A., Grodsky, S.A., Liu, H., 2008. Variability of the oceanic mixed layer, 1960–2004. Journal of Climate. 21(5), 1029–1047.
DOI: https://doi.org/10.1175/2007JCLI1798.1

[65] Lohmann, K., Drange, H., Bentsen, M., 2009. Response of the North Atlantic subpolar gyre to persistent North Atlantic oscillation like forcing. Climate Dynamics. 32, 273–285.
DOI: https://doi.org/10.1007/s00382-008-0467-6

[66] Mauritzen, C., Häkkinen, S., 1997. Influence of sea ice on the thermohaline circulation in the Arctic-North Atlantic Ocean. Geophysical Research Letters. 24(24), 3257–3260.
DOI: https://doi.org/10.1029/97GL03192

[67] Colling, A., 1989. Ocean circulation. Elsevier: Oxford.

[68] Talley, L., Pickard, G., Emery, W., et al., 2011. Descriptive physical oceanography: An introduction. Elsevier: Boston.

[69] Grassl, H., 2001. The ocean and climate: Climate and oceans. Ocean circulation and climate: Observing and modelling the global ocean. Academic Press: Cambridge. pp. 3–10.

[70] Muntjewerf, L., Sellevold, R., Vizcaino, M., et al., 2020. Accelerated Greenland ice sheet mass loss under high greenhouse gas forcing as simulated by the coupled CESM2. 1-CISM2. 1. Journal of Advances in Modeling Earth Sys-

tems. 12(10), e2019MS002031.
DOI: https://doi.org/10.1029/2019MS002031

[71] Forryan, A., Bacon, S., Tsubouchi, T., et al., 2019. Arctic freshwater fluxes: Sources, tracer budgets and inconsistencies. The Cryosphere. 13(8), 2111–2131.
DOI: https://doi.org/10.5194/tc-13-2111-2019

[72] McDonagh, E.L., King, B.A., Bryden, H.L., et al., 2015. Continuous estimate of Atlantic oceanic freshwater flux at 26.5°N. Journal of Climate. 28(22), 8888–8906.
DOI: https://doi.org/10.1175/JCLI-D-14-00519.1

[73] Rahmstorf, S., 1995. Climate drift in an ocean model coupled to a simple, perfectly matched atmosphere. Climate Dynamics. 11, 447–458.
DOI: https://doi.org/10.1007/BF00207194

[74] Bitz, C.M., Holland, M.M., Hunke, E.C., et al., 2005. Maintenance of the sea-ice edge. Journal of Climate. 18(15), 2903–2921.
DOI: https://doi.org/10.1175/JCLI3428.1

BILINGUAL PUBLISHING GROUP

Journal of Atmospheric Science Research

https://journals.bilpubgroup.com/index.php/jasr/index

ARTICLE

Assessment of the Intertropical Convergence Zone over the Atlantic Ocean through an Algorithm Based on Precipitation

Natan Chrysostomo de Oliveira Nogueira*, *Pedro Henrique Gomes Machado*, *Michelle Simões Reboita**, *André Luiz Reis

Natural Resources Institute, Federal University of Itajubá, Itajubá, Minas Gerais, 37500-903, Brazil

ABSTRACT

The Intertropical Convergence Zone (ITCZ) is a key atmospheric system on a global scale, primarily driven by trade wind convergence near the equator. The ITCZ plays a crucial role in modulating the climate of the borders of tropical continental areas. For instance, Northeastern Brazil experiences a climate influenced by the ITCZ over the Atlantic Ocean. In some periods, the ITCZ exhibits double bands, known as the double ITCZ. While the features of the ITCZ have been described using various approaches and atmospheric variables, there is still a lack of regional studies focusing on the ITCZ and double ITCZ in the Atlantic Ocean. In this context, the main goals of this study are (1) to describe a simple algorithm based on precipitation to identify the ITCZ and double ITCZ, (2) to present a climatology (1997–2022) of the position, width, and intensity of these two convective bands, and (3) to investigate variabilities in the ITCZ characteristics associated with anomalies of sea surface temperature (SST) in the tropical Pacific and Atlantic oceans. The double ITCZ typically occurs southward of the main cloud band, and between February and April, both bands are more distant (~4.5°). In the western sector of the Atlantic Ocean, the ITCZ and its double band extend to more southerly latitudes in austral autumn. Considering the entire Atlantic basin, the annual mean of the latitudinal position, width, and intensity of the ITCZ is 4.9°N, 4.2°, and 11 mm/day, respectively, while for the double ITCZ, it is 0.4°N, 2.6°, 10.3 mm/day, respectively. While the SST anomalies in the Pacific Ocean (El Niño and La Niña episodes) affect more the ITCZ width, the SST anomalies in the Tropical South Atlantic affect both its position and width.

Keywords: Double ITCZ; Precipitation; Latitudinal position; Northeastern Brazil; Atlantic Ocean; ENSO

*CORRESPONDING AUTHOR:
Michelle Simões Reboita, Natural Resources Institute, Federal University of Itajubá, Itajubá, Minas Gerais, 37500-903, Brazil;
Email: reboita@unifei.edu.br

ARTICLE INFO
Received: 30 December 2023 | Revised: 11 January 2024 | Accepted: 15 January 2024 | Published Online: 22 January 2024
DOI: https://doi.org/10.30564/jasr.v7i1.6188

CITATION
Nogueira, N.C.O., Machado, P.H.G., Reboita, M.S., et al., 2024. Assessment of the Intertropical Convergence Zone over the Atlantic Ocean through an Algorithm Based on Precipitation. Journal of Atmospheric Science Research. 7(1): 59–73. DOI: https://doi.org/10.30564/jasr.v7i1.6188

1. Introduction

The Intertropical Convergence Zone (ITCZ) is a large-scale atmospheric system originating from the ascending branch of the Hadley cell [1]. It manifests near the equator in various atmospheric fields as a band of trade wind convergence, minimum in atmospheric pressure, minimum in outgoing longwave radiation (OLR), deep convective clouds, and frequent intermittent rain events that transfer freshwater from the atmosphere to the ocean [2–11]. These characteristics do not necessarily occur simultaneously and/or in the same location [7,12]. The average annual position of the ITCZ globally is found slightly north of the equator due to the Atlantic Ocean's transport of energy northward across the equator, resulting in the Northern Hemisphere being warmer than the Southern Hemisphere [13]. However, throughout the seasons, the ITCZ exhibits spatial variability, migrating toward the summer hemisphere [1,3,14].

The cloudiness associated with the ITCZ plays a crucial role in the atmospheric energy balance by influencing albedo and releasing latent heat into the atmosphere [4,15]. Additionally, it significantly contributes to hydrological balances, accounting for 32% of global precipitation [16]. While the ITCZ is well-defined over oceans, its characterization over continental areas is more complex. Factors contributing to its complexity include the less homogenous nature of continental surfaces, and in some instances, the ITCZ is part of regional monsoons [12]. Therefore, considering continental areas, coastal regions are the most influenced by the ITCZ, as is the case with the coastline of Northeastern Brazil [17], which is influenced by the ITCZ over the Atlantic Ocean.

Globally the ITCZ has a wider extent in the Northern Hemisphere (200–600 km) than in the Southern Hemisphere (~ 300 km) [18,19]. Over the Atlantic Ocean, few studies are addressing the characteristics of the ITCZ. Some of them include: ITCZ is located farther north (~10°N), in September, and farther south (~4°S), between February and May [20–22]. Along the longitude of 27.5°W, the ITCZ exhibits maximum width (6°) between October and November and minimum width (3°) between January and March [22]. Observational longwave radiation data showed that the ITCZ is more intense in the central region of the Atlantic Ocean than near the coast of South America from July to December [23].

The ITCZ, over the Atlantic [24–26], Pacific [27–29] and Indian oceans [3], experiences episodes of double bands. In other words, there is a secondary band of the ITCZ that positions itself to the south of the main cloudy band. Over the Atlantic Ocean, in the climatology from 2010 to 2017 between December and April, these episodes are more frequent and last during the months of March and April [26]. Liu and Xie [25] suggest that the double ITCZ is caused by the deceleration of surface winds as they approach the cold upwelling water near the equator. Additionally, decreases in vertical mixing and increases in vertical wind shear in the atmospheric boundary layer may contribute to the deceleration of trade winds as they move from warmer to colder water. On the other hand, Talib et al. [31] mention that the controls of the location and intensity of the ITCZ remain a fundamental question in climate science. As the double ITCZ is associated with heavy rainfall and convection, its understanding is crucial for comprehending variations in rainfall distribution, particularly in proximity to continental areas.

The location and intensity of the ITCZ in the Atlantic Ocean can also be influenced by ocean-atmosphere interaction mechanisms such as the El Niño-Southern Oscillation (ENSO) phenomenon and sea surface temperature (SST) anomalies in the Tropical South Atlantic (TSA). Berry and Reeder [32] compared the global position of the ITCZ during El Niño (EN) and La Niña (LN) events. Over the Atlantic Ocean, the ITCZ is located southward during La Niña episodes compared to El Niño ones. A more regional study focusing on the north of Northeast Brazil by Xavier et al. [33] showed that during the rainy season in the region (February to May), the average position of the ITCZ in LN years is between 2°S and 4°S, which aligns with the climatological pattern. On the other hand, in EN years, the ITCZ migrates northward, approaching the equator. Therefore, the latitudinal migration of the ITCZ impacts rainfall in

the northern region of Northeast Brazil, so that very rainy years may be influenced by LN, and less rainy years by EN. However, Liu et al. [9] found little variability in the ITCZ in the Atlantic Ocean associated with different phases of the ENSO.

Some studies suggest that the variability of the ITCZ over the Atlantic Ocean, with its respective impact on the coast of Northeast Brazil, is more closely linked to SST anomalies in the TSA sector than with SST anomalies in the Pacific Ocean. More intense positive anomalies in the TSA than in the Tropical North Atlantic imply a southward migration of the ITCZ, contributing to rainfall on the coast of Northeast Brazil [34–36]. Other studies also emphasize that the combination of negative anomalies in the TSA concurrent with EN events affects the position of the ITCZ, leading to precipitation deficits in Northeast Brazil. On the other hand, positive anomalies occur when there are positive SST anomalies in the TSA and LN events occurring simultaneously [37].

Studies aiming to characterize the properties of the ITCZ such as its location, width, and intensity employ various approaches and atmospheric variables for system identification. For instance, Gadil and Guruprasad [38] utilized daily 2.5° data of OLR and albedo, applying thresholds: OLR < 185 W m^{-2} and albedo > 0.5. Grid points meeting these conditions were retained only if the conditions were satisfied by at least two of the eight neighboring grid points. Berry and Reeder [32] defined the ITCZ as the location where the magnitude of the horizontal gradient of divergence is zero, applying additional techniques to refine its location. Liu et al. [9] defined the ITCZ position based on the maximum zonal mean precipitation. The maximum zonal mean precipitation between 20°S–20°N is considered the ITCZ intensity, and the corresponding latitude is the ITCZ position. A similar methodology was used by Elsemüller [39], who quantified the latitudinal ITCZ mid-position based on the minimum convergence over longitudes. Samuel et al. [40] employed brightness temperature as a proxy for deep convective cloud cores, associating it with the ITCZ position. Carvalho and Oyama [22] characterized the properties of the ITCZ through pentad precipitation over a span of 10 years (1999 to 2008) with a data grid spacing of 1°. They used a threshold of approximately 7 mm/day to outline the region of ITCZ activity over the central Atlantic Ocean (27.5ºW).

Since the ITCZ over the Atlantic Ocean affects the weather and climate of the Northeastern region of Brazil, it is important to understand its main characteristics as well as the variability associated with some of the ocean-atmosphere interaction processes (teleconnection patterns). A more detailed description of the ITCZ over the Atlantic Ocean can also provide useful information for studies aimed at improving global and regional climate models. Hence, these are the motivations for this study.

Although there are studies about the ITCZ, most of them have a global perspective, which differs from the present study that focuses on a regional scale. Additionally, some methodologies for identifying the ITCZ are not very straightforward. Therefore, here we aim to develop a simple and efficient algorithm that can be adapted for any ocean basin (the same is available in a public database, see methodology) using one of the most widely observed variables globally, which is precipitation. Hence, the objectives of this study are (1) to describe the algorithm developed to record the position, width, and intensity of the ITCZ as well as its double band, (2) based on the application of the algorithm, to present the climatology of the basic characteristics of the ITCZ (position, width, and intensity) from 1997 to 2022, and (3) to investigate variabilities in the ITCZ characteristics associated with anomalies of SST in the tropical Pacific (EN and LN) and the Tropical South Atlantic.

2. Materials and methods

2.1 Study area

The study area comprises the region of the Tropical Atlantic Ocean situated between 10°S–18°N and 49°W–10°W, as defined previously [22] (blue box in **Figure 1**). **Figure 1** also shows two regions, Niño 3.4 (marked with a red box) and TSA (marked with

a green box), which are used to compute SST anomalies for analyzing their impact on ITCZ characteristics.

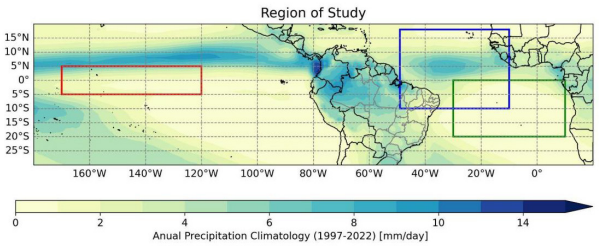

Figure 1. Study region (blue box), areas used to compute TSA (green box), and Niño 3.4 indices (red box). Global Precipitation Climatology Project (GPCP [41]) annual precipitation (mm/day) climatology from 1997 to 2022 is shown in shaded.

2.2 Data

Precipitation

Daily precipitation data from 1997 to 2022 used in this study were obtained from the Global Precipitation Climatology Project (GPCP) of the National Oceanic and Atmospheric Administration (NOAA) [41]. These data have a horizontal resolution of 1° × 1° and can be accessed at: https://www.ncei.noaa.gov/products/climate-data-records/precipitation-gpcp-daily.

Winds

Daily (0000 UTC) wind components (zonal, u, and meridional, v) at 10 meters above ground level were obtained from the ERA5 reanalysis [42]. ERA5 has a horizontal resolution of 0.25° × 0.25°, and data access is available through the Climate Data Store (CDS): https://cds.climate.copernicus.eu/cdsapp#!/dataset/reanalysis-era5-single-levels?tab=overview.

Climate indices

In this study, tree climate indices such as the Oceanic Niño Index (ONI) and TSA index. The different phases of ENSO were identified through the ONI, calculated monthly data from the NOAA within the Niño 3.4 region (**Figure 1**), and is available at: https://origin.cpc.ncep.noaa.gov/products/analysis_monitoring/ensostuff/ONI_v5.php. The TSA index, a monitoring index for the Tropical South Atlantic Ocean (**Figure 1**), was computed using NOAA Optimum Interpolation (OI) SST V2 (https://psl.noaa.gov/data/gridded/data.noaa.oisst.v2.html). This dataset has a horizontal resolution of 1° x 1°. The TSA index was obtained as follows: first, the monthly mean of SST and its anomaly is calculated in the box 30°W–10°E, 20°S–0° (**Figure 1**). Given the positive trend exhibited by this obtained time series, the trend is removed. This final result is the TSA index.

2.3 Methodology

Algorithm description for identifying the ITCZ

Although there are different ways to identify the ITCZ, we aimed for a simple methodology that would be easy to apply and use by other researchers interested in the subject. Thus, the algorithm described below is an adaptation of the methodology by Carvalho and Oyama [22], who identified the ITCZ in a single longitude band over the central Tropical Atlantic. Our algorithm is written in Python, uses only daily precipitation data converted into pentads, and is freely available on the GitHub platform: https://github.com/CATUnifei/ITCZ_code. The variable precipitation has one of the highest numbers of observations and estimates globally, and it is used in various studies for ITCZ identification [22,9].

General idea of the algorithm

1) The process begins by reading daily precipitation data in millimeters (mm) in NETCDF format and transforming the daily data into pentads (5-day averages). This allows the removal of high-frequency disturbances related to daily fluctuations [22].

2) The second step is to define the precipitation threshold that will be applied at each grid point to identify the ITCZ. Here, we defined the threshold as the average precipitation over the entire dataset period in the study area (**Figure 1**) plus one standard deviation (threshold = mean + one standard deviation). The values obtained were 3 mm/day for the average and 4 mm/day for the standard deviation, resulting in a threshold of 7 mm/day. It is a flexible threshold that the user can configure as a mean of a specific period, hence, being useful in climate change studies.

3) Grid points with precipitation greater than the

threshold (> 7 mm/day) are coded with the number 1 (true), otherwise, with 0 (false). This information is stored and will allow the identification of initial latitudes (Li) and final latitudes (Lf) (technical details are provided below).

4) Since the data are in grid points, a function is created to read their information at all latitudes. The data scan starts at the westernmost longitude and given latitudes from north to south; after scanning and identifying Li and Lf of the ITCZ band, the algorithm moves on to the next longitude. Two empty lists and three control variables are created, respectively, to store (a) Li and (b) Lf, and to have (c) a counter (cont), (d) a value accumulator (value), and (e) the ITCZ band number (n). This last information is because a double ITCZ band can also occur. To consider that there is an ITCZ band, it must have a minimum width of 2° latitude (2 grid points) where precipitation is above the threshold, meaning that for every two consecutive "1" in the column, the code records an ITCZ band.

This algorithm stands out by identifying both the primary and secondary bands of the ITCZ. Its steps are represented in **Figure 2**. Regarding the technical aspects of the code, a brief description is presented here.

Technical details of the algorithm

Initially, the variables cont, value, and n are set to zero; at the beginning of the process, 1 is added to cont, and the boolean (0 or 1) from the matrix is added to the value. After that, there are four situations:

1) If value = 1, Li is recorded, and the operation continues;

2) If value ≠ cont and value = 1, it indicates that there is no continuation of the ITCZ band because it lacks the prerequisite of 2 grid points, so cont and value are set to zero to proceed with the analysis;

3) If value ≠ cont and value = 0, it is verified that the ITCZ band, and cont and value are set to zero for the next analysis;

4) If value ≠ cont and value > 1, the previous latitude is recorded in Lf since the analysis stopped one latitude ahead, and "1" is added to n to indicate that the first ITCZ band has been found. Cont and value are reset to zero again in case the second ITCZ band can be found at the same longitude (column). The function then returns the values of Li and Lf to be stored in two arrays for the same ITCZ band number.

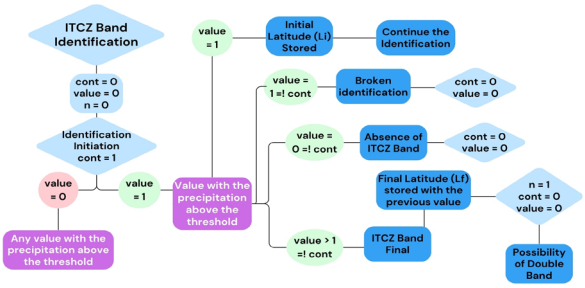

Figure 2. Flowchart of the algorithm steps for identifying the ITCZ bands.

As output, the algorithm provides, for each pentad and longitude, the initial latitude (Li) and final latitude (Lf) of the primary and secondary bands of the ITCZ, representing the position of the ITCZ. From this information, it is possible to obtain the width of each band in degrees (Lf-Li) and its mean position. The intensity of the ITCZ is calculated by averaging all grid points between Li and Lf for each longitude. Based on the algorithm output in pentads, monthly, seasonal, and annual climatologies can be calculated. In this study, the focus is the seasonal climatologies (position, width, and intensity of the ITCZ).

ITCZ variability

We also analyzed the characteristics of the ITCZ during EN and LN episodes and in different phases of the TSA index. The months with the occurrence of EN and LN events were selected in the time series of the ONI and separated by the season of the year. The ONI table provided by NOAA also includes the classification of the EN and LN periods. The next step was to calculate the average characteristics of the ITCZ during these seasonal periods with EN and LN occurrences and compare them with the climatology of the seasons. The same methodology was applied to analyze SST anomalies in the TSA region, except for the classification of the negative and positive phases of the TSA index. For this purpose, we first calculated the standard deviation of the time series. Then, we selected only the months with a TSA index

lower (higher) than one standard deviation for negative (positive index).

3. Results and discussion

3.1 Algorithm validation

Before applying the algorithm in any study, it is necessary to evaluate its performance. Validation was carried out by comparing the algorithm's results with the spatial map of precipitation, wind vectors at 10 meters height, and satellite images. One example is provided for the pentad from October 27 to October 31, 2022 (chosen aleatory) (**Figures 3 and 4**). As satellite images are not provided in pentads but at various times throughout the day, five images from the GOES-16 satellite in the visible channel were selected, one for each day of the pentad, and at 1200 UTC (**Figure 4**).

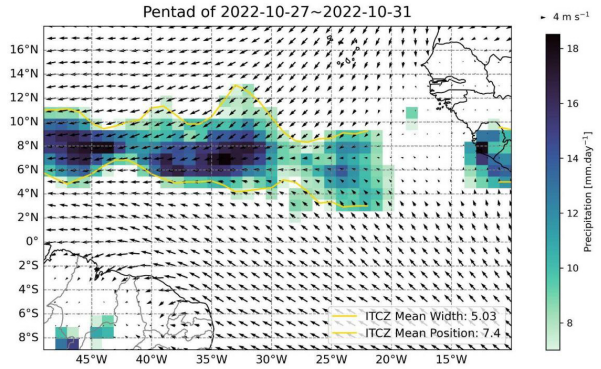

Figure 3. GPCP mean precipitation higher than 7 mm/day (shaded), wind intensity and direction at 10 m (m/s, black arrows), and the position of the ITCZ for the pentad from October 27th to October 31st, 2022. The initial (Li) and final (Lf) positions of the ITCZ are indicated by yellow lines. The mean position and width of the ITCZ are displayed at the bottom right of the panels.

In **Figure 3**, the band of precipitation > 7 mm/day is positioned approximately between 5° to 10°N and 50° to 20°W, which coincides with the region where the trade winds converge (arrows with larger size pointing south and meeting arrows with smaller size) and with the region of maximum cloudiness shown in the satellite images (**Figure 4**). The algorithm's result is represented by the two yellow lines delimiting the Li and Lf of the ITCZ (**Figure 3**). The algorithm captures the location of the rain well and does not show information between longitudes 20° to 13°W, where there is no precipitation and winds are weak (**Figure 3**). With Li and Lf, the width of the ITCZ can be estimated to be approximately 5° (500 km), consistent with satellite images and also with other studies [18,22].

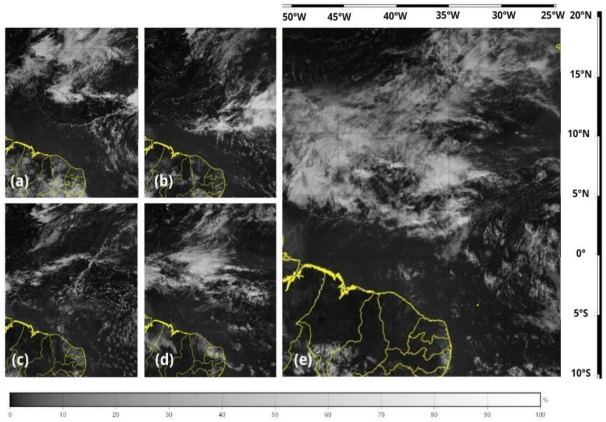

Figure 4. GOES-16 satellite image from visible channel 02 (0.64 microns) for October (a) 27, (b) 28, (c) 29, (d) 30, and (e) 31, 2022 at 1200 UTC.

Source: https://satelite.cptec.inpe.br

3.2 Seasonal climatology of the ITCZ

In this section, the seasonal climatology (**Figures 5 and 6**) of the position (Li, Lf and mean position), width, and intensity of the main band of the ITCZ (hereafter referred to as the ITCZ) and the secondary band (hereafter referred to as double ITCZ) are presented. **Figures 5 and 6** also show the spatial variability of these features.

In MAM, the ITCZ reaches its southernmost position in most of the Tropical Atlantic Ocean, with an average position of 1.4°N (**Figure 5b**). In this same season, in the western sector of the domain, the ITCZ is located between 2°N (Li) and 4°S (Lf), directly affecting the northern regions of North and Northeast Brazil. Meanwhile, in the center of the Tropical Atlantic (27.5°W), the mean position is around 1°N, consistent with Carvalho and Oyama [22]. The double ITCZ also occupies its southern position in MAM in the western sector of the domain (Li =

2°S, Lf = 5°S, and average = 3.5°S) (**Figure 5b**). The average width of the ITCZ and the double ITCZ is 4.14° and 2.44° (**Figures 6a and 6b**), respectively, and ITCZ is wider than in the other seasons west of 40°W. The intensity of the ITCZ and the double band is approximately 11.1 mm/day and 10.0 mm/day (average precipitation between Li and Lf, **Figures 6c and 6d**). Spatially, in MAM, precipitation shows higher volumes west of 30°W, near the North and Northeast regions of Brazil, which is in agreement with Kousky [23]. Additionally, these areas also exhibit higher standard deviation (**Figure 7b**).

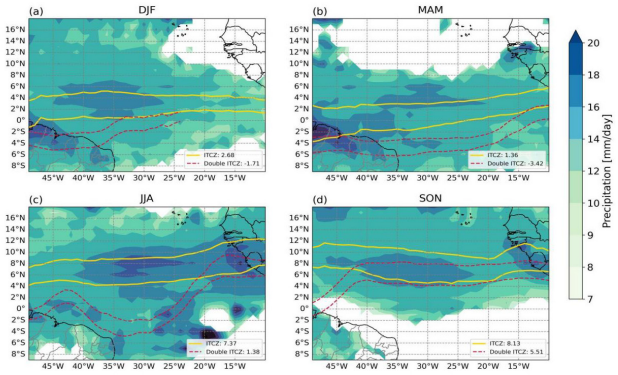

Figure 5. Seasonal climatology from 1997 to 2022 regarding the position of the ITCZ (yellow continuous lines) and double ITCZ (red dashed lines) for each longitude, as well as the spatial pattern of the precipitation > 7 mm/day (shaded): (a) DJF, (b) MAM, (c) JJA, (d) SON. The mean position of the ITCZ and the double ITCZ are displayed at the bottom right of the panels.

In JJA, the ITCZ migrates northward, positioning itself at an average of about 7.4° (**Figure 5c**). It is during this season that it reaches its northernmost position near the African continent (Li = 12°N and Lf = 6°N) and in the central Atlantic (Li = 9°N and Lf = 5°N), consistent with Carvalho et al. [22], who identified the northernmost position of the ITCZ to be approximately 8°N in August. The double ITCZ also migrates northward (average position of 1.4°N) but does not exhibit a zonal pattern like the ITCZ (**Figure 5c**). The average width of the ITCZ and the double ITCZ is approximately 4.4° and 2.6° (**Figures 6a and 6b**), respectively, while the average precipitation is 11.6 and 10.7 mm/day (**Figures 6c and 6d**). In JJA, the highest precipitation volumes and standard deviation occur in the central and eastern Atlantic within the latitude band of 4° to 8°N. Daily accumulations reach up to 13 mm/day (**Figures 5c and 6c**) with a standard deviation exceeding 6 mm/day (**Figure 7c**).

In SON, the ITCZ reaches its northernmost position in the western Atlantic (Li = 12°N and Lf = 8°N) and begins to migrate southward on the eastern side (Li = 10°N and Lf = 5°N). Its average position considering the entire Atlantic is 8°N (**Figure 5d**). In SON, the double ITCZ is also positioned further north (5.5°N). However, in the western sector of the Atlantic, the double ITCZ shows a southwestward tilt, affecting parts of the northern and northeastern regions of Brazil (**Figure 5d**). The average width of the ITCZ and the double ITCZ is approximately 4.6° and 3.2° (**Figures 6a and 6b**), respectively. At 27.5°W, the ITCZ has a width of 5° (~500 km), which is one degree smaller compared to Carvalho et al. [22]. This difference may be associated with the study period and different databases used in the works. The intensity of the ITCZ and the double ITCZ are 11.0 and 10.3 mm/day, respectively (**Figures 6c and 6d**). Analyzing the spatial distribution of precipitation, the highest accumulations and standard deviations are recorded between 40°W and 25°W and 4° and 8°N, with values of 11–12 mm/day (**Figures 5d**) and 6 mm/day, respectively (**Figure 7d**).

In DJF, the ITCZ and the double ITCZ begin to migrate southward, with average locations of 2.7°N and 1.7°S, respectively (**Figure 5a**). During this season, the double ITCZ is unable to configure itself to the east of 25°W (**Figure 5a**). The average width of the ITCZ and the double ITCZ is 3.5° and 2.2°, respectively (**Figures 6a and 6b**), while the intensity is 10.6 and 10.1 mm/day, respectively (**Figures 6c and 6d**). Additionally, in DJF, at 27.5°W, the width of the ITCZ of 3° aligns with the study [22]. Spatially, oceanic precipitation is maximum between 45° and 30°W and 0° and 7°N (**Figure 5a**), coinciding with the region of the highest standard deviation (> 6 mm/day, **Figure 7a**). Over the Brazilian coast, precipitation exhibits the highest volumes and standard deviation in MAM followed by DJF (**Figures 6 and**

7). This higher standard deviation may be associated with the variability of large-scale transient systems that affect the region, such as eastward wave disturbances, upper-level cyclonic vortices etc. [22,24,43–45].

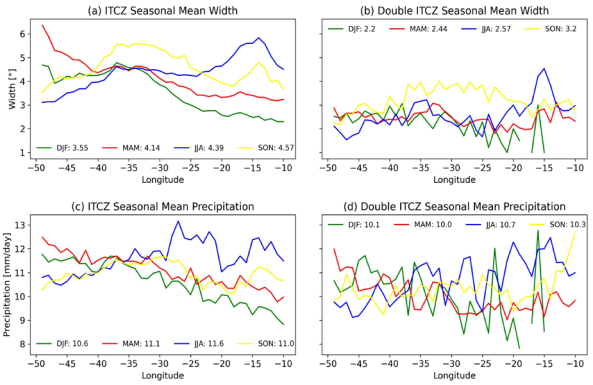

Figure 6. Seasonal climatology, from 1997 to 2022, of the width (degrees) of the (a) ITCZ and (b) double ITCZ for each longitude. The lines represent different seasons: DJF—green line, MAM—red line, JJA—blue line, and SON—yellow line). The mean width is also indicated in the panels.

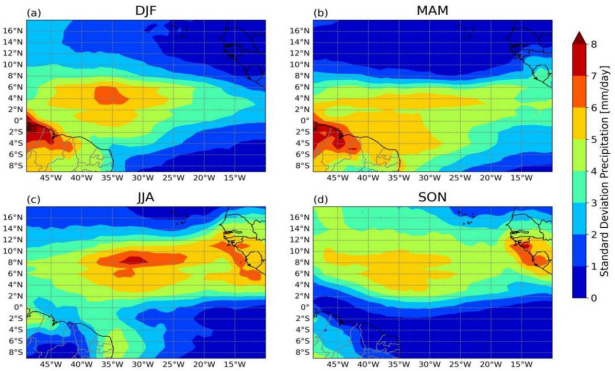

Figure 7. Seasonal standard deviation of the precipitation (mm/day) from 1997 to 2022: (a) DJF, (b) MAM, (c) JJA, (d) SON.

The seasonal frequency of the double ITCZ at various longitudes is depicted in **Figure 8**. Between 50°W and 42°W, the double ITCZ exhibits a similar higher frequency in both DJF and MAM, while to the east at 15°W, it is more frequent between JJA and SON. West of 30°W, on average, the double ITCZ occurs more frequently in MAM, agreeing with Teodoro et al. [26] (who focused on DJF and MAM only) and aligning with the practical knowledge of the third author in our study. When considering the entire Atlantic basin, events of the double ITCZ are slightly more prevalent in MAM (2 events) compared to other seasons.

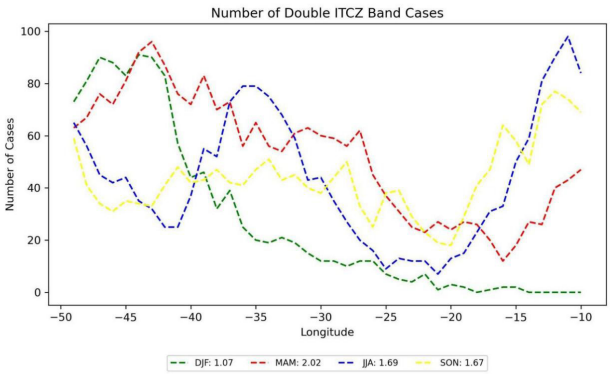

Figure 8. Seasonal frequency of the double ITCZ from 1997 to 2022 (DJF—green line, MAM—red line, JJA—blue line and SON—yellow line).

3.3 Monthly climatology of the ITCZ

To facilitate comparisons of the results with those from the literature, we also present monthly climatological values of the mean features (position, width, and intensity) for both the ITCZ and double ITCZ across the entire Tropical Atlantic basin (**Figure 9**). Additionally, **Figure 10** displays the monthly time series of the mean position for both the ITCZ and double ITCZ, aiming to identify any trends in these time series and emphasize the mean distance between the two bands.

Both the ITCZ and double ITCZ reach their northernmost position in September. The ITCZ shows Li at 12°N, Lf at 7.2°N, and a mean position of 9.6°N, while the double ITCZ has Li at 8.8°N, Lf at 5.5°N, and a mean position of 7.2°N (**Figure 9a**). Computing the difference between the mean positions of both bands, they are distant by 2.4°. When considering both Li and Lf, the southernmost position of the ITCZ occurs in March, with Li at around 2.1°N, Lf at approximately 1.6°S, and a mean position of about 0.24°N. However, when looking at only Lf, the most southern position occurs in both March and April. Applying the same criteria of Li and Lf, the double ITCZ has its southernmost position in February, with Li at approximately 3.3°S, Lf at around 5.2°S, and a mean position of 4.3°S (**Figure 9a**). But, considering only Lf, the most austral position occurs between February and April. During

this period of the year, both bands are distant by approximately 4.54°, aligning with the climatological value of 4° from December to May obtained by Teodoro et al. [26]. The annual cycle of the ITCZ position is consistent with some studies [20], which showed the ITCZ position in the west and east sectors of the Tropical Atlantic Ocean using various atmospheric variables.

The ITCZ has a greater width in August and September (~4.7°) and a smaller width in January (~3.4°), while the double ITCZ also exhibits a greater width in September (~3.3°) and a smaller width in February (~1.9°) (**Figure 9b**). The obtained values for the ITCZ are consistent with the global average for the Southern Hemisphere, which is approximately 3° (300 km) [18].

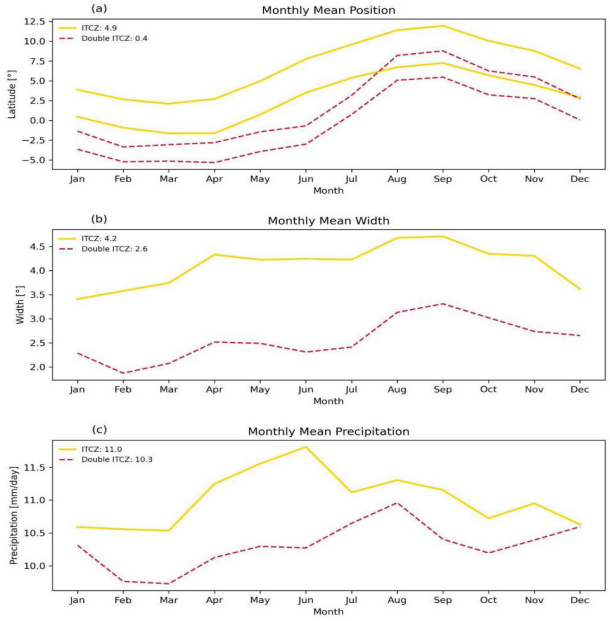

Figure 9. Annual cycle of the (a) position (degree latitude), (b) width (degree), and (c) intensity (mm/day) of ITCZ (yellow continuous lines) and double ITCZ (red dashed lines) from 1997 to 2022. Annual mean values are displayed in the upper left corner of the panels.

The ITCZ intensity is higher in June (~11.8 mm/day) and lower in March (~10.5 mm/day), while the double ITCZ exhibits its higher intensity in August (~11 mm/day) and lower intensity also in March (~9.7 mm/day) (**Figure 9c**). These results align with those for the central Tropical Atlantic obtained by Carvalho and Oyama [22]. According to these authors, the higher intensity of the ITCZ occurs between May and August (~13 mm/day), and the lower intensity between February and March (~10 mm/day). Xie et al. [6] also highlighted that in July-August, rainfall in the ITCZ is considerably stronger than in March-April, and this strengthening may be associated with the abundance of strong westward propagating easterly wave disturbances that help trigger convection over the ocean.

The time series of the monthly mean position of the ITCZ and double ITCZ exhibit a slightly southward trend, of –0.0036°/year and –0.02°/year, respectively, but without statistical significance (**Figure 10**). Liu et al. [9] depicted the annual time series of the ITCZ position in several locations globally. For the Atlantic Ocean (20°N–20°S and 49°W–9°W), **Figure 3d** also indicates a slightly negative trend between 1998 and 2018.

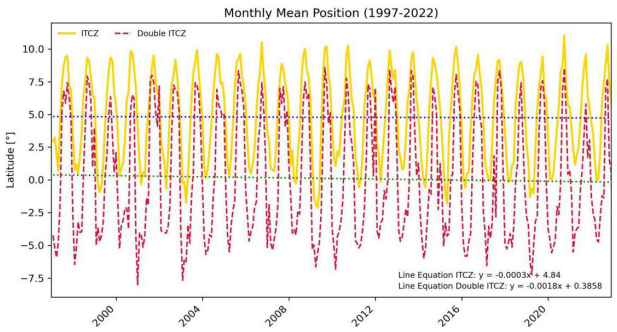

Figure 10. Monthly mean position (degree latitude) of the ITCZ (yellow continuous line) and double ITCZ (red dashed line) from 1997 to 2022. Linear trends are also depicted with dashed lines.

3.4 ITCZ interannual variability

ENSO

During the EN events, atmospheric convection intensifies in the central and eastern Tropical Pacific, leading to tropical tropospheric warming and anomalous subsidence over the tropical Atlantic, resulting in reduced precipitation [6]. On the other hand, during LN, it is expected that there will be more precipitation over the Tropical Atlantic. Indeed, **Figure 11** confirms the described pattern. In addition, it indicates that Northeast Brazil is more impacted by the ENSO phases in MAM (**Figures 11c and 11d**). To

verify if these spatial patterns of precipitation anomalies cause changes in the ITCZ position and width, **Figures 12 and 13** are presented.

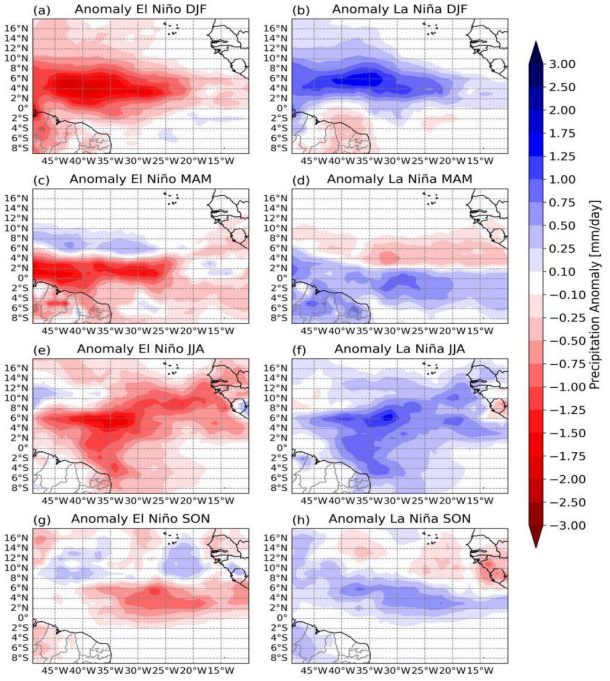

Figure 11. Seasonal precipitation anomaly (mm/day) in El Niño cases (left column) and La Niña cases (right column).

In periods with EN and LN, the mean position of the ITCZ is little affected, showing variations lower than 0.5° in comparison with the climatological value (**Figure 12**). On the other hand, when Li and Lf are individually analyzed, there are more variations, which affect the ITCZ width (**Figure 13**). During EN episodes in DJF, Li and Lf, west of 35°W, are displaced south compared to the climatological pattern (**Figure 12a**). In MAM, Lf, west of 35°W, is slightly retracted to the north (**Figure 12b**). In JJA and SON, Lf is also retracted to the north but over a larger extent in the central region of the oceanic basin (37.5°W to 17.5°W; **Figures 12c and 12d**). In SON, a difference is that Li, between 25°W and 17.5°W, is displaced to the north about climatology (**Figure 12d**). Considering LN episodes in DJF, west of 30°W, Li and Lf shift to the north about climatology (**Figure 12a**). In MAM, Lf moves south between 40°W and 20°W (**Figure 12b**). In the other seasons, Li and Lf have fewer differences about the climatological pattern. Our results partially support the findings [32], who emphasized that during the rainy season in the north of Northeast Brazil, the average position of the ITCZ in LN episodes aligns with the climatological pattern. However, they differ from those in EN episodes; during EN episodes, the ITCZ migrates northward, approaching the equator [32]. In our case, a higher change is observed in Lf rather than in both borders of the ITCZ.

In summary, during EN events, the ITCZ exhibits Lf slightly retracted to the north compared to the climatology. In LN events, both Li and Lf tend to be slightly more expanded than the climatology. These features impact the width of the ITCZ: during EN events, the ITCZ is narrower, whereas during LN events, the ITCZ is wider than in the climatology (**Figure 13**). The contraction of the ITCZ in EN events can reach up to 0.8° west of 35°W, except in SON. In JJA, the expansion of the ITCZ can reach 0.6° between 40°W and 30°W.

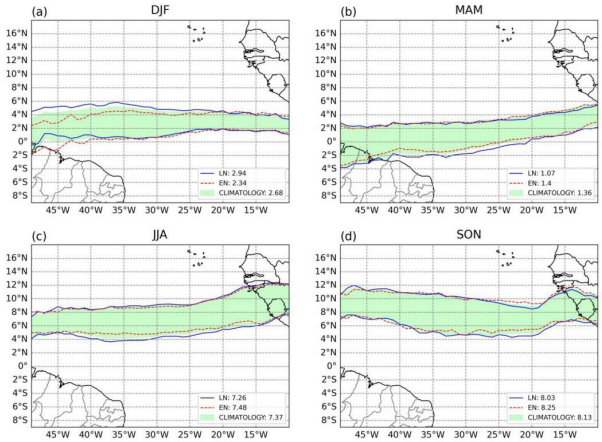

Figure 12. Climatological mean position (degrees) of the ITCZ (shaded), mean El Niño events (red dashed line), and during La Niña events (blue solid line). The mean position over the entire Atlantic is depicted in the bottom right of the panels.

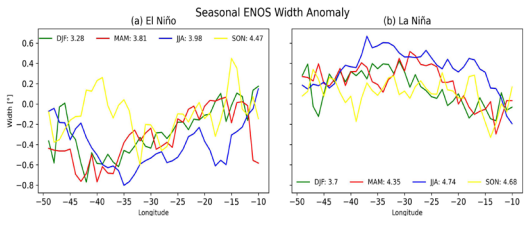

Figure 13. Seasonal anomaly of the mean width of the ITCZ in (a) El Niño (EN) and (b) La Niña (LN) events between 1997 and 2022. The mean width (degrees) of the ITCZ is also displayed in the panels.

TSA index

Figure 14 shows the spatial pattern of precipitation anomalies associated with different phases of the TSA index. Over the ocean, the ITCZ rainfall is intensified in its southern sector and weakened in its northern sector when a positive TSA index predominates (**Figures 14a, 14c, 14e, and 14g**). Conversely, precipitation anomalies of the opposite signal occur when a negative phase of the TSA index predominates (**Figures 14b, 14d, 14f, and 14h**). **Figure 14** also reveals that a great portion of the precipitation in the north and northeast sectors of Northeastern Brazil during MAM and JJA is influenced by SST anomalies in the TSA region.

A combined analysis of **Figures 11 and 14** corroborates the findings [36,37]. In other words, the negative (positive) phase of TSA and EN (LN) contribute to rainfall deficits (excess) in Northeastern Brazil.

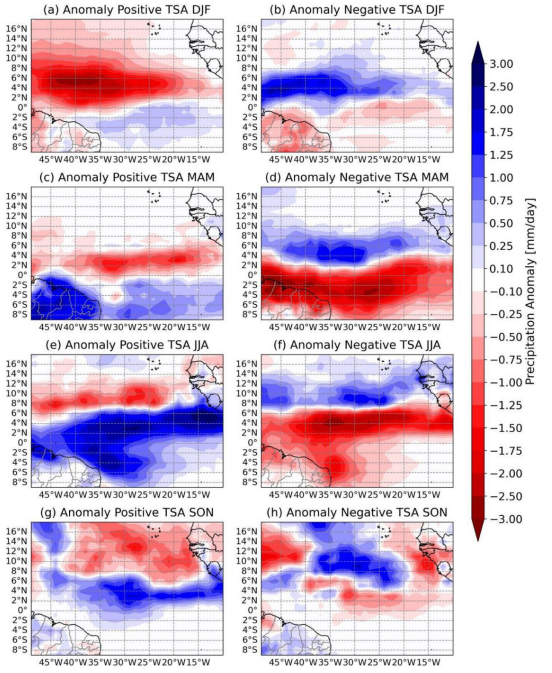

Figure 14. Seasonal precipitation anomaly (mm/day) in positive TSA index (left column) and negative TSA index (right column).

Figure 15 complements the results of **Figure 14** by showing the seasonal changes in the ITCZ position according to the dominant pattern of TSA anomalies. A positive TSA index is associated with the southward displacement of the ITCZ in all seasons. However, the mean position of the ITCZ is more southward displaced in DJF (0.97°), followed by JJA (0.72°), in relation to the climatology (**Figure 15**). The response of the ITCZ to a negative TSA index is a northward displacement, which, in terms of the mean position of the ITCZ, is higher in MAM (0.88°), followed by JJ (0.82°). SST anomalies also affect the width of the ITCZ. In the negative TSA index, generally, the ITCZ is narrower than the climatology except in SON between 40° and 30° W (**Figure 16b**). On the other hand, the width shows greater variability in the positive TSA index. The ITCZ is wider in JJA at all longitudes, and west of 40° W in MAM. Conversely, west of 25° W, the ITCZ is narrower than the climatology in DJF (**Figure 16a**).

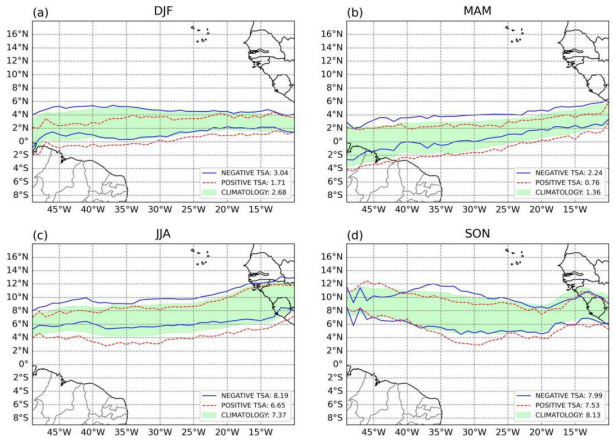

Figure 15. Climatological mean position (degrees) of the ITCZ (shaded), mean during positive TSA index (red dashed line), and negative TSA index (blue solid line). The mean position over the entire Atlantic is depicted in the bottom right of the panels.

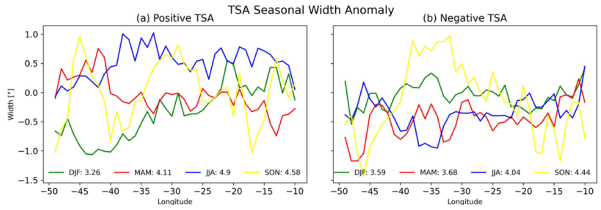

Figure 16. Seasonal anomaly of the mean width of the ITCZ in (a) positive TSA index and (b) negative TSA index between 1997 and 2022. The mean width (degrees) of the ITCZ is also displayed in the panels.

4. Conclusions

As the ITCZ is one of the large-scale precipitating systems that greatly influences the climate of

coastal tropical regions [17,46,47], the main objective of this study was to present an algorithm developed to locate both the primary and secondary bands (double ITCZ) of the ITCZ over the Atlantic basin. The algorithm identifies the initial (Li) and final (Lf) limits of the bands, providing information for the calculation of the average position, width, and intensity of the two bands. This algorithm is available on an open platform (https://github.com/CATUnifei/ITCZ_code) and can be easily adjusted for applications with other variables and in other oceanic basins. The study also aimed to present the climatology of the basic characteristics of the ITCZ and double ITCZ (position, width, and intensity) from 1997 to 2022 and to investigate variabilities in the ITCZ characteristics associated with anomalies of SST in the tropical Pacific (EN and LN) and the Tropical South Atlantic. The main findings are as follows:

Double ITCZ: It is located southward of the ITCZ with a mean distance reaching approximately 4.5° (computed considering the mean position of both bands) between February and April. West of 30°W, the double ITCZ occurs more frequently in MAM and has a mean position at 1°S, directly affecting the northern regions of North and Northeast Brazil. Considering the entire Tropical Atlantic Ocean, the double ITCZ shows a larger width (~3.3°) in September and a higher intensity (~11 mm/day) in August.

ITCZ: In MAM, the ITCZ reaches its southernmost position in most of the Tropical Atlantic Ocean, with an average position of 1.4°N. Considering the entire Tropical South Atlantic, the ITCZ shows a larger width (~4.7°) in August and September and a higher intensity (~11.8 mm/day) in June.

ITCZ interannual variability: Episodes of EN and LN affect the ITCZ width more, while SST anomalies in the TSA region affect both position and width. During EN and LN episodes, the mean position of the ITCZ is little affected, but changes in the limits of the ITCZ lead to alterations in width. Specifically, during EN events, the ITCZ is narrower, whereas during LN events, the ITCZ is generally wider than in the climatology. Considering the TSA index, a positive index is associated with the southward displacement of the ITCZ in all seasons, while a negative index indicates a northward displacement. Regarding the width, the ITCZ is generally narrower than the climatology during episodes of negative TSA index. On the other hand, the width exhibits greater variability during episodes of positive TSA index.

This study can serve as a guide for others, and we highlight that it is important to investigate the impact of other teleconnection mechanisms on the ITCZ and double ITCZ features.

Author Contributions

NCON: data collection, algorithm development, formal analysis and wrote the paper; PM: data collection, algorithm development, formal analysis and wrote the paper; MSR: conceived and designed the algorithm and analysis, wrote and reviewed the paper; ALR: algorithm development and reviewed the paper.

Conflict of Interest

The authors declare no conflict of interest.

Funding

This research was funded by Conselho Nacional de Pesquisas (CNPq), Fundação de Amparo à Pesquisa do Estado de Minas Gerais (FAPEMIG) and Coordenação de Aperfeiçoamento de Pessoal de Nível Superior (CAPES).

Acknowledgments

The authors thank all the meteorological centers that provided the datasets used in this study.

References

[1] Asnani, G.C., 1993. Tropical meteorology. Indian Institute of Tropical Meteorology: Pune.

[2] Waliser, D.E., Somerville, R.C.J., 1994. Preferred latitudes of the intertropical convergence zone. Journal of Atmospheric Sciences. 51(12),

1619–1639.
DOI: https://doi.org/10.1175/1520-0469(1994)051<1619:PLOTIC>2.0.CO;2

[3] Xie, S.P., Philander, S.G.H., 1994. A coupled ocean-atmosphere model of relevance to the ITCZ in the eastern Pacific. Tellus A. 46(4), 340–350.
DOI: https://doi.org/10.3402/tellusa.v46i4.15484

[4] Waliser, D.E., Gautier, C., 1993. A satellite-derived climatology of the ITCZ. Journal of Climate. 6(11), 2162–2174.
DOI: https://doi.org/10.1175/1520-0442(1993)006<2162:ASDCOT>2.0.CO;2

[5] Diaz, H.F., Bradley, R.S., 2004. The Hadley circulation: Present, past, and future. The Hadley circulation: Present, past and future. Advances in global change research. Springer: Dordrecht.
DOI: https://doi.org/10.1007/978-1-4020-2944-8_1

[6] Wang, C., Xie, S.P., Carton, J.A., 2004. Tropical Atlantic variability: Patterns, mechanisms, and impacts. Earth's Climate: The Ocean-Atmosphere Interaction. 147, 121–142.
DOI: https://doi.org/10.1029/147GM07

[7] Krishnamurti, T.N., Stefanova, L., Misra, V., 2013. Tropical meteorology—An introduction. Springer: New York.

[8] Aimola, L., Moura, M., 2016. The influence of the Atlantic Meridional overturning circulation in the definition of the mean position of the ITCZ north of the equator. A review. Revista Brasileira de Meteorologia. 31(4 suppl 1). (in Portuguese).
DOI: https://doi.org/10.1590/0102-778631231 4b20150059

[9] Liu, C., Liao, X., Qiu, J., et al., 2020. Observed variability of intertropical convergence zone over 1998–2018. Environmental Research Letters. 15(10), 104011.

[10] Iyer, S., Drushka, K., 2021. Turbulence within rain-formed fresh lenses during the SPURS-2 experiment. Journal of Physical Oceanography. 51(5), 1705–1721.
DOI: https://doi.org/10.1175/JPO-D-20-0303.1

[11] Windmiller, J.M., Stevens, B., 2023. The inner life of the Atlantic Intertropical Convergence Zone. Quarterly Journal of the Royal Meteorological Society.
DOI: https://doi.org/10.1002/qj.4610

[12] Misra, V., 2023. Intertropical Convergence Zone. An introduction to large-scale tropical meteorology. Springer: Cham. pp. 91–109.
DOI: https://doi.org/10.1007/978-3-031-12887-5_4

[13] Schneider, T., Bischoff, T., Haug, G., 2014. Migrations and dynamics of the intertropical convergence zone. Nature. 513, 45–53.
DOI: https://doi.org/10.1038/nature13636

[14] Philander, S.G.H., Gu, D., Lambert, G., et al., 1996. Why the ITCZ is mostly north of the equator. Journal of Climate. 9(12), 2958–2972.
DOI: https://doi.org/10.1175/1520-0442(1996)009<2958:WTIIMN>2.0.CO;2

[15] Bony, S., Stevens, B., Frierson, D.M.W., et al., 2015. Clouds, circulation and climate sensitivity. Nature Geoscience. 8, 261–268.
DOI: https://doi.org/10.1038/ngeo2398

[16] Kang, S.M., Shin, Y., Xie, S.P., 2018. Extratropical forcing and tropical rainfall distribution: Energetics framework and ocean Ekman advection. npj Climate and Atmospheric Science. 1, 20172.
DOI: https://doi.org/10.1038/s41612-017-0004-6

[17] Tomaziello, A.C.N., Carvalho, L.M.V., Gandu, A.W., 2016. Intraseasonal variability of the Atlantic Intertropical Convergence Zone during austral summer and winter. Climate Dynamics. 47, 1717–1733.
DOI: https://doi.org/10.1007/s00382-015-2929-y

[18] Khrgian, A., 1977. Physical meteorology. Summaries of scientific progress: Meteorology and climatology, Volume 2. G.K. Hall: Boston.

[19] Monsoons [Internet]. World Meteorological Organization (WMO); 1986. Available from: https://library.wmo.int/idurl/4/37019

[20] Hastenrath, S., 1991. Climate dynamics of the tropics. Kluwer Academic Publishers: Dordrecht.

[21] Mendonça, F., Danni-Oliveira, I.M., 2007. Climatology: Basic concepts and Brazilian climatates. Oficina de Textos Publisher: São Paulo. (in Portuguese).

[22] Carvalho, M.A.V., Oyama, M.D., 2013. Atlantic Intertropical Convergence Zone width and intensity variability: Observational aspects. Revista Brasileira de Meteorologia. 28(3), 305–316. (in Portuguese).
DOI: https://doi.org/10.1590/S0102-77862013000300007

[23] Kousky, V.E., 1988. Pentad outgoing longwave radiation climatology for the South American sector. Revista Brasileira de Meteorologia. 3(1), 217–231.

[24] Uvo, C. R. B., 1989. The Intertropical Convergence Zone (ITCZ) and its relationship with precipitation in the northern region of northeast Brazil. (in Portuguese).

[25] Liu, W.T., Xie, X., 2002. Double intertropical convergence zones—A new look using scatterometer. Geophysical Research Letters. 29(22), 291–294.
DOI: https://doi.org/10.1029/2002GL015431

[26] Teodoro, T.A., Reboita, M.S., Escobar, G.C.J., 2019. Characterization of the double band of the Intertropical Convergence Zone (ITCZ) over the Atlantic Ocean. Yearbook of the Institute of Geosciences. 42(2), 282–298. (in Portuguese).
DOI: https://doi.org/10.11137/2019_2_282_298

[27] Hubert, L.F., Krueger, A.F., Winston, J.S., 1969. The double intertropical convergence zone-fact or fiction? Journal of the Atmospheric Sciences. 26(4), 771–773.
DOI: https://doi.org/10.1175/1520-0469(1969)026<0771:TDICZF>2.0.CO;2

[28] Zhang, C., 2001. Double ITCZs. Journal of Geophysical Research: Atmospheres. 106(D11), 11785–11792.
DOI: https://doi.org/10.1029/2001JD900046

[29] Henke, D., Smyth, P., Haffke, C., et al., 2012. Automated analysis of the temporal behavior of the double Intertropical Convergence Zone over the east Pacific. Remote Sensing of Environment. 123, 418–433.
DOI: https://doi.org/10.1016/j.rse.2012.03.022

[30] Meenu, S., Rajeev, K., Parameswaran, K., et al., 2007. Characteristics of the double intertropical convergence zone over the tropical Indian Ocean. Journal of Geophysical Research: Atmospheres. 112(D11).
DOI: https://doi.org/10.1029/2006JD007950

[31] Talib, J., Woolnough, S.J., Klingaman, N.P., et al., 2018. The role of the cloud radiative effect in the sensitivity of the intertropical convergence zone to convective mixing. Journal of Climate. 31(17), 6821–6838.
DOI: https://doi.org/10.1175/JCLI-D-17-0794.1

[32] Berry, G., Reeder, M.J., 2014. Objective identification of the intertropical convergence zone: Climatology and trends from the ERA-Interim. Journal of Climate. 27(5), 1894–1909.
DOI: https://doi.org/10.1175/JCLI-D-13-00339.1

[33] Teresinha de Maria Bezerra, X., Tércio, A., Maria Elisa S, S., 2017. Applications of models and techniques in the detection of climate variability and extremes. Bank of Northeast Brazil. (in Portuguese).

[34] Hastenrath, S., Greischar, L., 1993. Circulation mechanisms related to northeast Brazil rainfall anomalies. Journal of Geophysical Research: Atmospheres. 98(D3), 5093–5102.
DOI: https://doi.org/10.1029/92JD02646

[35] Reboita, M.S., Santos, I.A., 2014. Teleconnection influences in some precipitation standards. Brazilian Journal of Climatology. 15, 28–48. (in Portuguese).
DOI: https://doi.org/10.5380/abclima.v15i0.37686

[36] Reboita, M.S., Ambrizzi, T., Crespo, N.M., et al., 2021. Impacts of teleconnection patterns on South America climate. Annals of the New

York Academy of Sciences. 1504(1), 116–153. DOI: https://doi.org/10.1111/nyas.14592

[37] Pezzi, L., Cavalcanti, I., 2001. The relative importance of ENSO and tropical Atlantic sea surface temperature anomalies for seasonal precipitation over South America: A numerical study. Climate Dynamics. 17, 205–212. DOI: https://doi.org/10.1007/s003820000104

[38] Gadgil, S., Guruprasad, A., 1990. An objective method for the identification of the intertropical convergence zone. Journal of Climate. 3(5), 558–567. DOI: https://doi.org/10.1175/1520-0442(1990)003<0558:AOMFTI>2.0.CO;2

[39] Elsemüller, L., 2021. Quantifying the Intertropical Convergence Zone using wind convergences [Master's thesis]. Tübingen: Eberhard Karls Universität Tübingen.

[40] Samuel, S., Mathew, N., Sathiyamoorthy, V., 2023. Characterization of intertropical convergence zone using SAPHIR/Megha-Tropiques satellite brightness temperature data. Climate Dynamics. 60, 3765–3783. DOI: https://doi.org/10.1007/s00382-022-06549-x

[41] Adler, R.F., Gu, G., Sapiano, M., et al., 2017. Global precipitation: Means, variations and trends during the satellite era (1979–2014). Surveys in Geophysics. 38, 679–699. DOI: https://doi.org/10.1007/s10712-017-9416-4

[42] Hersbach, H., Bell, B., Berrisford, P., et al., 2020. The ERA5 global reanalysis. Quarterly Journal of the Royal Meteorological Society. 146(730), 1999–2049. DOI: https://doi.org/10.1002/qj.3803

[43] Study of the vertical and horizontal structure of precipitation and atmospheric circulation in the region of the ITCZ, 2002. (in Portuguese).

[44] Gomes, H.B., Ambrizzi, T., Pontes da Silva, B.F., et al., 2019. Climatology of easterly wave disturbances over the tropical South Atlantic. Climate Dynamics. 53, 1393–1411. DOI: https://doi.org/10.1007/s00382-019-04667-7

[45] Ferreira, G.W.S., Reboita, M.S., da Rocha, R.P., 2020. Upper level cyclonic vortices in the vicinity of Northeast Brazil: Climatology and analysis of the isentropic potential vorticity. Yearbook of the Institute of Geosciences. 42(3), 568–585. (in Portuguese). DOI: https://doi.org/10.11137/2019_3_568_585

[46] Jafari, M., Lashkari, H., 2020. Study of the relationship between the intertropical convergence zone expansion and the precipitation in the southern half of Iran. Journal of Atmospheric and Solar-Terrestrial Physics. 210, 105439. DOI: https://doi.org/10.1016/j.jastp.2020.105439

[47] Lashkari, H., Jafari, M., 2021. Annual displacement and appropriate index to determine ITCZ position in East Africa and the Indian Ocean regions. Meteorology and Atmospheric Physics. 133, 1111–1126. DOI: https://doi.org/10.1007/s00703-021-00797-y

BILINGUAL PUBLISHING GROUP

Journal of Atmospheric Science Research

https://journals.bilpubgroup.com/index.php/jasr/index

ARTICLE

Analysis of Extreme Temperature Variability in Rwanda

***Protais Seshaba*[1], *Edouard Singirankabo*[2*], *Donat Nsabimana*[3]**

[1] *Department of Science and Humanities, Protestant Institute of Arts and Social Sciences, P O Box 619, Huye, Rwanda*

[2] *Department of Mathematics, Science and Physical Education, University of Rwanda, College of Education, P O Box 55, Rukara, Rwanda*

[3] *Department of Forestry, University of Rwanda, College of Science and Technology, P O Box 55, Huye, Rwanda*

ABSTRACT

The temperature is one of the most important factors in weather and climate forecasting. Studying its behaviour is crucial to understanding climate variability, which could vary spatially and temporally at local, regional, and global scales. Several recent studies on air temperature findings show that the Earth's near surface air temperature increased between 0.6 °C and 0.8 °C throughout the twentieth century. Using temperature records from ten meteorological stations, this study examined climate variability in Rwanda from the 1930s to 2014. The air temperature data were collected from Meteo Rwanda. Before making the analysis, the authors used software, such as Excel 2007 and INSTAT to control the quality of the raw data. The analysis of maxima and minima indicated that the trends of maximum air temperature were positive and significant at height meteorological stations, whereas the trends for minimum air temperature were found to be at 10 meteorological stations. For all parameters analysed, Kigali Airport meteorological station indicated the higher significance of the trends. The majority of meteorological stations showed an increase in both hot days and nights, confirming Rwanda's warming over time. The analysis of average seasonal air temperature showed almost similar trends even though not all were significant. This similarity in trends could be attributed to the fact that Rwanda's short and long dry seasons coincide with rainy seasons.

Keywords: Climate variability; Air temperature; Solar radiation; Meteorological station

*CORRESPONDING AUTHOR:

Portain Seshaba, Department of Science and Humanities, Protestant Institute of Arts and Social Sciences, P O Box 619, Huye, Rwanda; Email: nkabo12edus@gmail.com

ARTICLE INFO

Received: 27 November 2023 | Revised: 15 January 2024 | Accepted: 22 January 2024 | Published Online: 26 January 2024

DOI: https://doi.org/10.30564/jasr.v7i1.6107

CITATION

Seshaba, P., Singirankabo, E., Nsabimana, D., 2024. Analysis of Extreme Temperature Variability in Rwanda. Journal of Atmospheric Science Research. 7(1): 74–89. DOI: https://doi.org/10.30564/jasr.v7i1.6107

1. Introduction

One of the elements in weather control is temperature, which is measured for a variety of purposes. Apart from the temperature variation such as ground, soil, and sea water temperature, air temperature is the most common variable measured at various heights. WMO defined air temperature as "*the temperature indicated by a thermometer exposed to the air in a place sheltered from direct solar radiation*" [1]. Thermometers that indicate the prevailing temperature are often known as ordinary thermometers, while those that indicate extreme temperatures over a period of time are called maximum or minimum thermometers. Enz et al. [2] indicated that the measured air temperature around the Earth's surface originates from the sun and emits its radiation of high temperature (5,727 °C or 10,341 °F) which consists of very short wavelengths that carry large amounts of energy. The Earth, after being heated by the sun radiation, becomes a radiating body and it radiates energy to the atmosphere in long waveforms that carry only small amounts of energy, compared with that carried by solar radiation.

Normally, land accumulates the temperature during the daytime and as the sun sets the temperature falls rapidly and continues to fall until it reaches its minimum as the Earth's surface keeps emitting the energy received in the daytime than it receives [2,3]. The WMO [1] showed that air temperature distribution varies at any place due to factors like the latitude of the place, the longitude of the place, the air mass circulation, the presence of warm and cold ocean currents and local aspects.

IPCC [4] reported that the signs of warming of the climate system are clear and prevailing, as it is now evident from observations of increases in global average air and ocean temperatures, widespread melting of snow and ice and rising global average sea level. The average global surface air temperature has warmed 0.8 °C in the past century and 0.6 °C in the past three decades [5], due to different human activities [6]. However, Katz and Brown [7] argued that this warming was not spatially or temporally uniform. The IPCC [8] has projected that greenhouse gas emissions lead to the cause of climate change and contribute to the tremendous rise of temperature, which influences global warming hence the world temperature should increase by 1.4–5.8 °C by the end of the 21st century.

Observational records show that during the 20th century, the continent of Africa has been warming at a rate of about 0.05 °C per decade, with slightly larger warming in the June–November seasons than in December–May [9]. By 2000, the five warmest years in Africa had all occurred since 1988, where the years 1988 and 1995 are the two warmest years [10]. Warming projections under medium scenarios indicate that extensive areas of Africa exceeded 2 °C during the last 2 decades of this century relative to the late 20th century means annual temperature and all of Africa under high emission scenarios [11].

DFID [12] indicated that countries of Eastern Africa are exposed to extreme climatic events such as droughts. For instance, during the 1970s and 1980s, droughts caused widespread famine and economic hardships in many countries of the sub-Saharan region, which is in agreement with the study of Nash and Ngabitsinze [13].

Numerous studies on long-term climate fluctuations in various parts of the world show that it is likely that the effects of climate change will challenge and even reverse the advancements made in many African countries' socio-economic well-being [14]. It was indeed shown that Rwanda has experienced temperature increases higher than the global average (1.4 °C since 1970), accompanied by air temperature extremes that generated negative impacts throughout the country [15]. Hence, the current study aimed at the analysis of patterns of climate variability in Rwanda as indicated by air temperature records (maximum and minimum) and determined related impacts on the socio-economic sector.

In Rwanda, different research on climate variability has been conducted, but they mainly referred to Kigali meteorological station [16]. However, this represents a lack of information from all representative climatic zones in Rwanda. For example, Safari [17] analysed the mean annual temperatures during the

last 52 years in Rwanda using only five meteorological stations, such as Kigali, Gitarama, Rubona, Kibuye and Gisenyi. Additionally, Habiyaremye [18] has also studied precipitation, temperature, and humidity variability in Rwanda for 30 years using only data from Kigali Aero meteorological station. The study of (Edouard Singirankabo E. I., 2023) [19] looked at the modelling of maximum extreme temperature in Rwanda using extreme value analysis. They argued that the temperature in Rwanda will continue to rise in the future.

It is observed that these studies did not cover the whole climatic zones of Rwanda which would contribute to showing the real image of climate variability of the country. In addition, the mean annual temperature variability studied by Safari (2012) [17] does not reflect the impact that could be caused by temperatures below or above fixed thresholds on biodiversity such as high drought that could cause plants to dry, low temperatures that could cause crop injury through the hail process and impacts on human health especially high temperatures that could cause death to people and animals. The main objective of the current study is to evaluate and analyse climatic variability in terms of temperature records over the past 83 years. We analyse the trends of minimum and maximum air temperature and discuss the impacts of climate variability in Rwanda. The rest of this paper is organized as follows: Section 2 represents materials and methods; Section 3 describes numerical results and discussion; Section 4 shows conclusions and recommendations.

2. Materials and methods

2.1 Description of the study area

Rwanda is a small, landlocked country in equatorial East Africa covering 26,338 km^2, located at 02°00 Latitude South and 30°00 Longitude East. As indicated on the below political map of Rwanda (**Figure 1**), the country is bordered by the Democratic Republic of Congo (DRC), Burundi, Uganda and Tanzania respectively Western, Southern, Northern and Eastern parts. Rwanda is known as the "*land of a thousand hills*" as its topography is characterized by steep slopes and green hills, upon which its predominantly rural population survives on subsistence agriculture [16]. The average temperature of Rwanda is around 20 °C and varies topographically (**Figure 2**), with a short dry season happening in January–February and a long dry season occurring in June–August [17].

Figure 1. Political map of Rwanda.

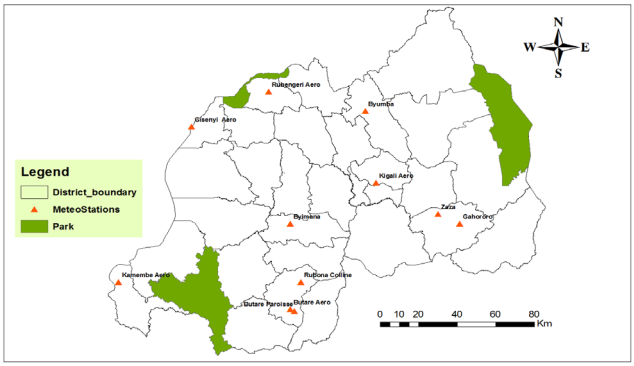

Figure 2. Geographical location of meteorological stations.

Table 1 below lists the meteorological stations whose temperature records were considered in this study.

2.2 Research design

Data source and data collection techniques

This research is both qualitative and quantitative. The data used in this study are collected from the National Meteorological Service, and the time-series of temperature records were collected from Meteo Rwanda based in Kigali. Quality control was per-

formed on raw data before analysis in Excel 2007 and INSTAT Software. The analysis was based on daily minimum and maximum temperature data series.

Sampling techniques

Until today, the total number of meteorological stations that existed plus those still functioning in Rwanda is about 183. The 1990–1994 Tutsi genocide and the war in Rwanda destroyed more than 80% of meteorological infrastructure and a few of them reopened afterwards [20]. During the sampling process, meteorological stations for the current study were purposively selected, based on the availability of daily minimum and maximum temperature data, period of record and fair distribution of the stations across Rwanda [21,22]. The most important criterion in consideration was to select the meteorological station that presents at least 20 years of observation period.

The data of Butare Paroisse and Butare Aero meteorological stations were combined not only because they are located at the same elevation (1760 m, ASL), but also because Butare Paroisse meteorological station stopped working in 1967 and was shifted to Butare Aerodrome in 1971, and the distance between the two locations is less than 1 km. The meteorological stations in Rwanda were not established in the same period and not all are still functioning. Hence, a sub-period-based analysis of air temperature consists of selecting meteorological stations that present the complete temperature datasets at the same subperiod in order to make a realistic comparison of air temperature trends.

2.3 Extreme temperature and thresholds

Changes in annual frequencies of the amount of days and nights with maximum and minimum temperatures in defined categories have been investigated based on some of the indices developed by Collins [23] (see **Table 2**), but also it is important to keep in mind that climate seems to be complex; i.e., temperature can vary differently throughout different places depending on various factors. However, for our study, it was important to consider the temperature categories employed by the forecasting section of Meteo Rwanda, for which temperature thresholds are defined for forecasting purposes (**Table 3**), e.g., when a day or night is defined as hot or cold.

Table 1. List of meteorological stations used in this study.

Meteo-Station	Longitude	Latitude	Elevation (m)	District	Province	Period
Butare Paroisse	29.73	–2.61	1760	Huye	South	1935–1967
Butare Aerodrome	29.71	–2.6	1760	Huye	South	1971–1993
Rubona Colline	29.76	–2.46	1706	Huye	South	1958–2012
Byimana	29.71	–2.16	1750	Ruhango	South	1960–2014
Kamembe Aerodrome	28.91	–2.46	1591	Rusizi	West	1957–2014
Gisenyi Aerodrome	29.25	–1.66	1554	Rubavu	West	1975–2014
Ruhengeri Aerodrome	29.61	–1.48	1878	Musanze	North	1977–2014
Byumba Pref	30.06	–1.58	2235	Gicumbi	North	1945–2011
Kigali Aero	30.11	–1.95	1490	Gasabo	Kigali City	1971–2014
Zaza	30.4	–2.11	1515	Ngoma	East	1945–1994
Gahororo	30.5	–2.16	1607	Ngoma	East	1960–1993

Table 2. Temperature indices used in the analysis of extreme temperatures developed by Collins et al., 2000.

Maximum Temperature Extreme Indices	Minimum Temperature Extreme Indices
Very hot days: $T_x \geq 35$ °C	Hot nights: $T_n \geq 20$ °C
Hot days: 30 °C ≤ T_x < 35 °C	Warm nights: 15 °C ≤ T_n < 20 °C
Cold days: $T_x \leq 15$ °C	Very cold nights: $T_n \leq 0$ °C
Cool days: 15 °C < $T_x \leq 19$ °C	Cold nights: 0 °C < $T_n \leq 5$ °C

Note: T_x: maximum temperature; T_n: minimum temperature.

Table 3. Temperature indices used in the analysis of extreme temperatures developed by Meteo Rwanda.

Maximum Temperature Extreme Indices	Minimum Temperature Extreme Indices
Hot days: Tx ≥ 28 °C	Hot nights: Tn ≥ 18 °C
Cold days: Tx ≤ 25 °C	Cold nights: 0 ºC < Tn ≤ 16 °C

Note: T_x: maximum temperature; T_n: minimum temperature.

3. Numerical results and interpretations

3.1 Monthly maxima and minima in air temperature

Figure 3 indicates trends of monthly maxima and minima air temperatures measured at the 10 meteorological stations in Rwanda. Major stations indicate that minimum temperatures rapidly occurred compared to maximum temperatures as indicated by the regression coefficients. The analysis of 10 meteorological stations (**Figure 3**) showed that 8 of the 10 stations indicated positive trends for the maximum of maximum air temperature, whereas all 10 meteorological stations showed positive trends for the minimum of minimum air temperature.

The results showed the trends of maximum air temperature. Seven out of the ten weather stations showed noteworthy upward trends which is significant. Butare, Gahororo, and Ruhengeri Aero are the three remaining meteo-stations that displayed negative trends and insignificant. Kigali meteorological station presented a greater increase in temperature ($R^2 = 0.2013$, $p = 0.000$). All 10 meteorological stations showed positive and significant trends for the minimum and minimum air temperature, with Kigali presenting again a higher value of R-squared and a highly significant trend ($R^2 = 0.3702$, p = 0.000) as indicated in **Table 4**.

It was reported by various authors that the minimum air temperature increased faster than the maximum air temperature because of different factors. Folland [24] showed that the minimum air temperatures increased about twice as fast as the maximum temperatures over global land areas since 1950, resulting in a broad decline in the diurnal temperature range (DTR: difference of maximum and minimum air temperature). Among the factors that could affect the minimum air temperature, we note changes in cloud cover, precipitation, soil moisture, and atmospheric circulation likely accounted for much of the trend differential during a given period for example [25–28]. Changes in land use also impacted the difference in maximum and minimum air temperature in some areas [29–32].

As indicated by Christy [29], there are differences between *Tx* and *Tn* trends, especially recently, as they may reflect a response to complex changes in the boundary layer dynamics. They added that the *Tx* represents the significantly greater daytime vertical connection to the deep atmosphere, whereas *Tn* represents only a shallow layer whose air temperature is more dependent on the turbulent state than on the temperature in the upper atmosphere and this turbulent state in the stable boundary layer is highly dependent on local land use and perhaps locally produced aerosols, and the significant human development of the surface may be responsible for the rising *Tn* while having little impact on *Tx*. Byamukama [16] indicated that land use change in Rwanda (forest, grass, and wetlands conversion to arable land) is also the contributors to GHGs (Green House Gas) emissions. This may affect the real and natural patterns of air temperature trends in Rwanda, especially minimum air temperature. For both monthly maxima and minima of air temperature analysed, it was noticeable that the air temperature trends for Kigali Aero meteorological station indicated positive and significant trends with a greater coefficient of determination (R^2). This may be related to the level at which urbanization involves artificial changes to the land surface and increases energy consumption.

It indicated that urbanization affects the surface energy budget and land-atmosphere interaction, resulting in the 'urban heat island' effect (UHI) [23,33]. Parker [34] argued that urbanization usually induces a warming trend in the observed surface air temperature series, in a way similar to that of the increasing concentration of atmospheric greenhouse gases, however, the effect of urbanization has become a matter of concern in the field of climate change detection. Some authors highlighted that the urban influence on the global air temperature series is negligible [24,34], but the urbanization-induced warming in local (or regional) air temperature observations could be considerable [35,36]. For example, Portman [37] showed that urban meteorological stations in North China experienced an urban-induced warming trend of 0.15–0.26 °C/30 years during 1954–1983.

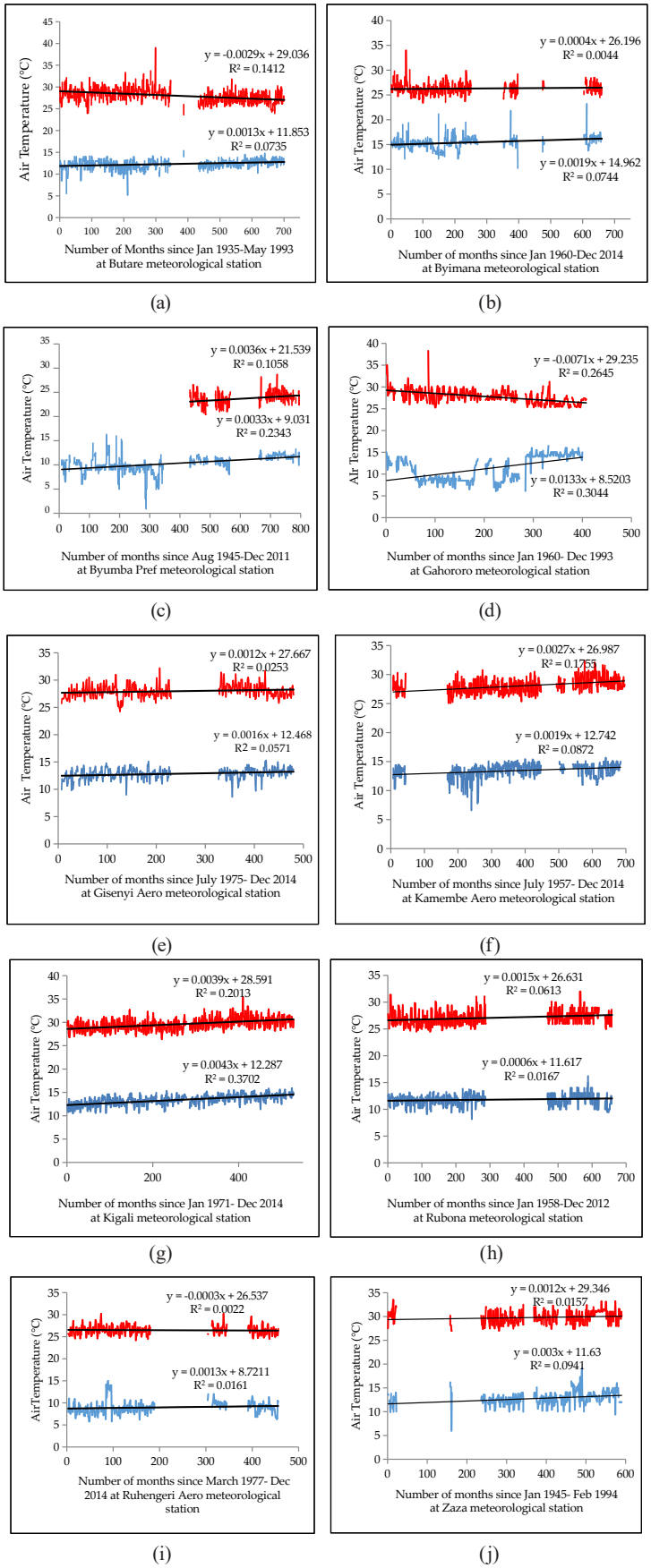

Figure 3. Trends of monthly maxima and minima in air temperature at 10 meteorological stations.

Although Safari [17] worked on annual mean air temperature in Rwanda, his findings in the 19-year sub-period (1958–1977) showed that Kigali Aero meteorological station (capital city of Rwanda) has a positive trend with a very high coefficient of determination (R^2 = 0.67). He also concluded that the observed warming is most likely explained by the growing population accompanied by the increasing emission of greenhouse gases, and the growing urbanization and industrialization the country has experienced, especially the city of Kigali, during some last decades.

Table 4 clearly indicates the aspect, regression coefficients and the significance of trends for both maximum and minimum air temperature. At each meteorological station, the hottest and coldest days and nights have been summarized according to the periods of observation.

Table 4 shows that half of the meteorological stations presented their highest extremes of monthly maximum air temperature in the year 2005. In fact, as noted by Byamukama [16], the year 2005 was among the hottest years in Rwanda, such as 1999, 2000, and 2006. This high level of recorded air temperature created severe droughts in some regions of the country, particularly in the east (Bugesera, Umutara, and Mayaga regions), where agricultural production has been undermined. Nash and Ngabitsinze [13], also noted that the year 2005 was marked with severe drought in Rwanda. The studies show that the period 2001–2010 was the warmest decade on record since modern meteorological records began around the year 1850 [38,39]. The report indicates that the year 2005 was hotter above the land in the southern hemisphere whereas it was hotter above the ocean in the northern hemisphere.

The analysis of minimum air temperature indicated that Byumba Pref meteorological station showed the lowest extremes of monthly minimum air temperature. This may be due to the fact that Byumba Pref (Byumba Province) meteorological station is located in the region with the highest altitude (2235 m, ASL) considering other meteorological stations used in this study.

Table 4. Regression analysis of monthly extreme air temperature at 10 meteorological stations.

Meteo-Station	Extremes of Air Temperature	Trend	R-Square	P-Value	Remark
Butare	Minimum of minimum	*Positive*	0.07	0.000	Significant
	Maximum of maximum	*Negative*	0.14	0.000	Significant
Byimana	Minimum of minimum	*Positive*	0.07	0.000	Significant
	Maximum of maximum	*Positive*	0.00	0.215	Non-Significant
Byumba pref	Minimum of minimum	*Positive*	0.23	0.000	Significant
	Maximum of maximum	*Positive*	0.11	0.000	Significant
Gahororo	Minimum of minimum	*Positive*	0.30	0.000	Significant
	Maximum of maximum	*Negative*	0.26	0.000	Significant
Gisenyi Aero	Minimum of minimum	*Positive*	0.06	0.000	Significant
	Maximum of maximum	*Positive*	0.03	0.002	Significant
Kamembe Aero	Minimum of minimum	*Positive*	0.09	0.000	Significant
	Maximum of maximum	*Positive*	0.18	0.000	Significant
Kigali Aero	Minimum of minimum	*Positive*	0.37	0.000	Significant
	Maximum of maximum	*Positive*	0.20	0.000	Significant
Rubona	Minimum of minimum	*Positive*	0.02	0.005	Significant
	Maximum of maximum	*Positive*	0.06	0.000	Significant
Ruhengeri Aero	Minimum of minimum	*Positive*	0.02	0.032	Significant
	Maximum of maximum	*Negative*	0.00	0.432	Non-Significant
Zaza	Minimum of minimum	*Positive*	0.09	0.000	Significant
	Maximum of maximum	*Positive*	0.02	0.022	Significant

Table 5 indicates that 5 of 10 meteorological stations (Rubona, Kamembe Aero, Kigali Aero, Byumba Pref and Ruhengeri Aero) presented their maximum air temperature in 2005, whereas the remaining 5 meteorological stations their maximum air temperatures were distributed in various years. The month of February hosted a large number of maxima throughout various years but mostly in 2005 for Rubona, Kamembe Aero, Kigali Aero, Byumba Pref (Byumba Prefecture) and Ruhengeri Aero whereas for Gahororo it was in 1967 and lastly Zaza in 1946. The highest maximum of maximum air temperature that has been ever measured at the 10 meteorological stations was 39 °C, recorded at Butare parish meteorological station in November 1959. The minimum of maximum temperatures has been varying in different years and months with the lowest value of 12.8 °C recorded at Byumba Pref meteorological station in April 2000.

The minimum of minimum air temperature also showed a varying pattern with air temperature ranging between 10.5 °C and 1 °C. This lowest value was measured at Byumba Pref meteorological station in December 1968. Generally, the month of December 1968 at Byumba Pref meteorological station indicated lower air temperature values compared to other months for air temperature measurements.

3.2 Variability in hot and cold days and nights

The analysis of 10 meteorological stations showed that there was variability in trends of hot days (HD), cold days (CD), hot nights (HN) and cold nights (CN) as well.

As it is visible in **Figure 4**, the trends of daily and night extreme air temperatures were displayed in the following way: Gahororo meteo-station presented negative trends for cold days and nights as well as for hot days and nights. Butare meteo-station showed only a positive trend for cold days whereas a positive trend was noticed for hot days at Byumba meteo-station. On the other hand, at Gisenyi Aero, Kamembe Aero, Kigali Aero, Rubona, and Zaza meteorological stations, the number of hot days and nights was increasing contrary to cold days and nights.

Table 6 gives more details about the trends and significance of daily and night extreme air temperatures at the 10 meteorological stations under study.

Table 5. The hottest and coldest days and nights as indices of extreme air temperatures.

Meteorological Stations	Maximum of Maximum air Temperature		Minimum of Maximum Air Temperature		Maximum of Minimum Air Temperature		Minimum of Minimum Air Temperature	
	Value (°C)	Month and Year	Value (°C)	Month and Year	Value (°C)	Month and Year	Value (°C)	Month and Year
Butare (Parish)	39	Nov. 1959	15	Apr. 1950	20.5	Jul. 1935	5.2	Nov. 1936
Rubona	32	Feb. 2005	16	Mar. 2005	16.6	Aug. 1967	8.2	Jul. 1978
Byimana	34	Dec. 1963	12.9	Dec. 1963	23.1	Jan. 2011	4.7	Jul. 1973
Kamembe Aero	32.3	Feb. 2005	16.3	Aug. 1978	19.9	Nov. 2007	7	Jan. 1977
Gisenyi Aero	32.2	Mar. 1992	16.1	Dec. 2014	19.2	Mar. 1992	9	Aug.1986
Kigali Aero	35.4	Feb. 2005	17	Sep. 2014	20.5	Jan. 2013	10.5	Feb. 1972
Gahororo	38.3	Feb.1967	14	Nov. 1963	27; 26.5	Feb. 1960; Nov. 1961	6.1; 6.3	Aug.; Nov. 1978
Zaza	33.5	Feb. 1946	15	Oct. 1959	23.2	May 1983	6	May 1958
Byumba Pref	28.7	Feb. 2005	12.8	Apr. 2000	20.5	Apr. 1964	1	Dec. 1968
Ruhengeri Aero	30.2	Feb. 1983; 2005	15.8	Sep. 2014	19.2	Dec. 1987	5.8	Jan. 1985

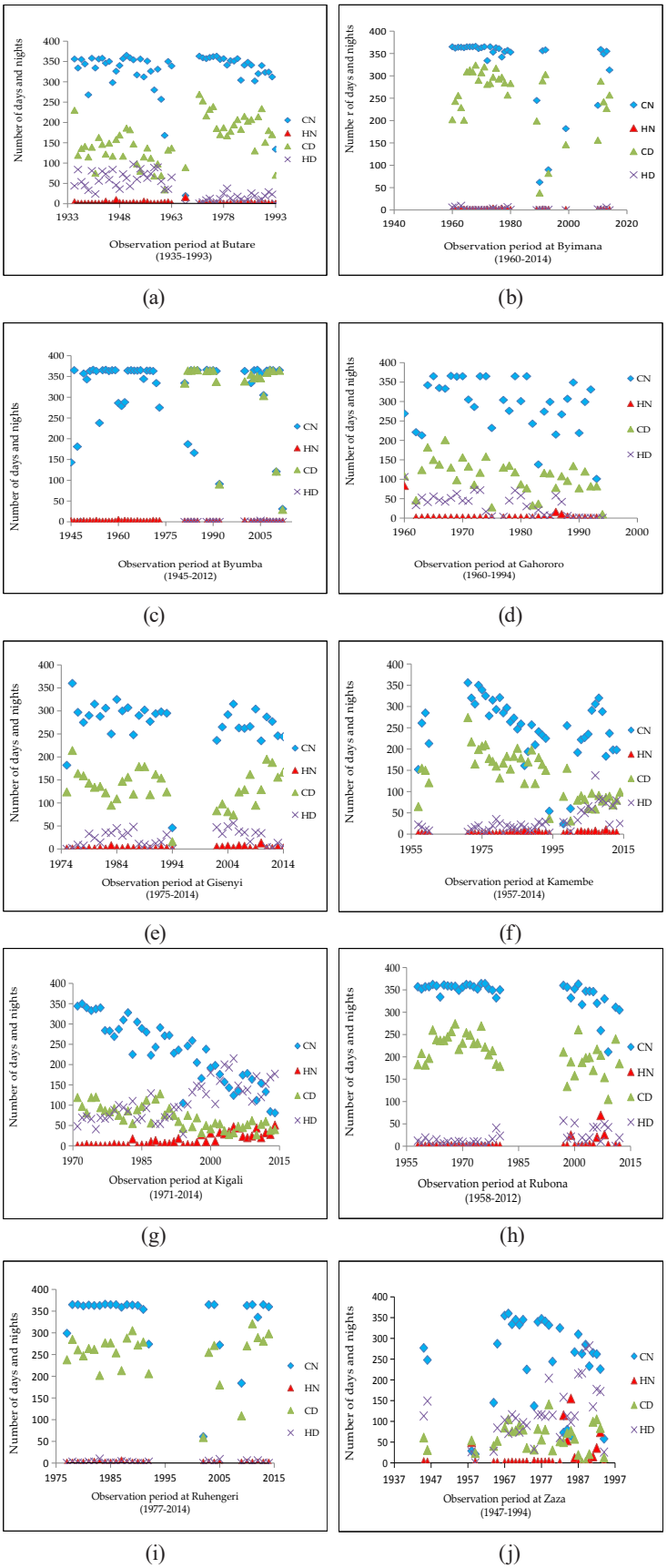

Figure 4. Trends of daily and night extreme air temperatures at 10 meteorological stations.

Table 6. Regression analysis of daily and night extreme air temperature at 10 meteorological stations.

Meteo Station		Trend	R-Square	P-Value	Remark
Butare	CN	*Negative*	0.015	0.374	Non-Significant
	HN	*Negative*	0.014	0.405	Non-Significant
	CD	*Positive*	0.157	0.003	Significant
	HD	*Negative*	0.495	0.000	Significant
Byimana	CN	*Negative*	0.160	0.023	Significant
	HN	*Negative*	0.007	0.639	Non-Significant
	CD	*Negative*	0.120	0.052	Significant
	HD	*Negative*	0.029	0.348	Non-Significant
Byumba pref	CN	*Negative*	0.000	0.931	Non-Significant
	HN	*Negative*	0.063	0.075	Non-Significant
	CD	*Negative*	0.095	0.163	Non-Significant
	HD	*Positive*	0.029	0.452	Non-Significant
Gahororo	CN	*Negative*	0.089	0.097	Non-Significant
	HN	*Negative*	0.065	0.159	Non-Significant
	CD	*Negative*	0.186	0.012	Significant
	HD	*Negative*	0.457	0.000	Significant
Gisenyi Aero	CN	*Negative*	0.030	0.333	Non-Significant
	HN	*Positive*	0.213	0.007	Significant
	CD	*Negative*	0.009	0.608	Non-Significant
	HD	*Positive*	0.021	0.416	Non-Significant
Kamembe Aero	CN	*Negative*	0.092	0.048	Significant
	HN	*Positive*	0.209	0.002	Significant
	CD	*Negative*	0.354	0.000	Significant
	HD	*Positive*	0.410	0.000	Significant
Kigali Aero	CN	*Negative*	0.833	0.000	Significant
	HN	*Positive*	0.646	0.000	Significant
	CD	*Negative*	0.570	0.000	Significant
	HD	*Positive*	0.573	0.000	Significant
Rubona	CN	*Negative*	0.330	0.000	Significant
	HN	*Positive*	0.158	0.014	Significant
	CD	*Negative*	0.234	0.002	Significant
	HD	*Positive*	0.264	0.001	Significant
Ruhengeri Aero	CN	*Negative*	0.064	0.212	Non-Significant
	HN	*Negative*	0.041	0.321	Non-Significant
	CD	*Negative*	0.007	0.687	Non-Significant
	HD	*Positive*	0.005	0.735	Non-Significant
Zaza	CN	*Negative*	0.001	0.882	Non-Significant
	HN	*Positive*	0.069	0.145	Non-Significant
	CD	*Negative*	0.001	0.875	Non-Significant
	HD	*Positive*	0.207	0.009	Significant

The trends of daily and night extreme air temperatures were obtained in a varying pattern, where HD represents hot days, CD stands for cold days, HN represents hot nights and CN represents cold nights. The majority of the trends showed an increasing number of hot days and nights but not always significant (**Table 6**). Regardless of the non-significance of trends in hot days and nights, on the other hand, they show a picture of the warming that has been occurring in Rwanda over time.

3.3 Change in average seasonal air temperature

The analysis assessed the similarity and difference in air temperature trends for one month belonging to a short dry season (February) and another belonging to a long dry season (August). As indicated in **Figure 5**, except Butare which showed a negative trend for the short dry season, other meteorological stations presented an increase in trends of monthly mean air temperature for both short dry and long dry seasons.

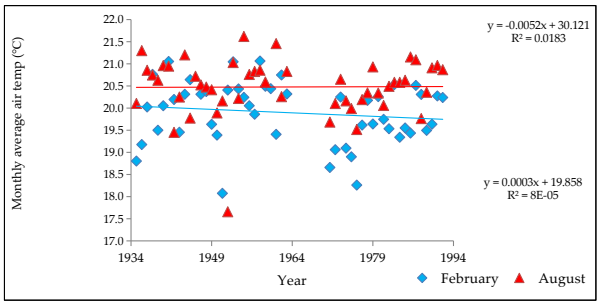

(a) Air temperature trends at Butare Aero meteorological station.

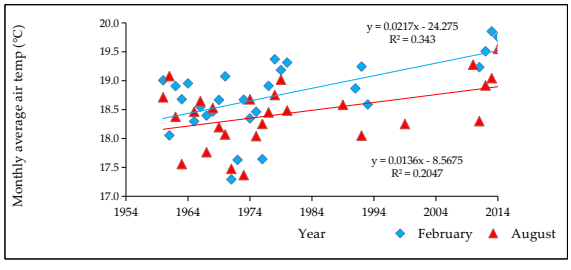

(b) Air temperature trends at Byimana meteorological station.

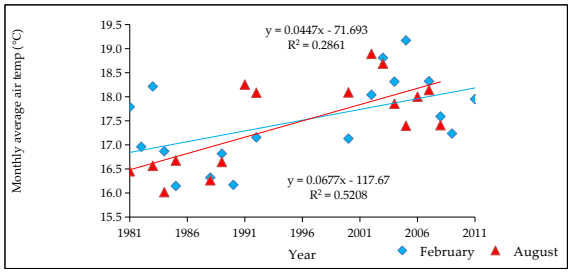

(c) Air temperature trends at Byumba pref meteorological station.

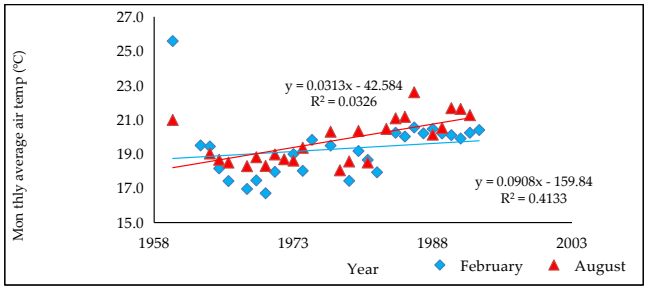

(d) Air temperature trends at Gahororo meteorological station.

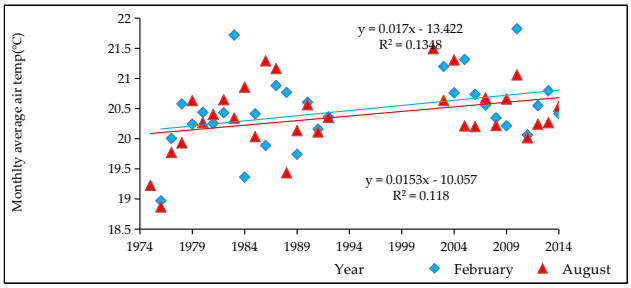

(e) Air temperature trends at Gisenyi Aero meteorological station.

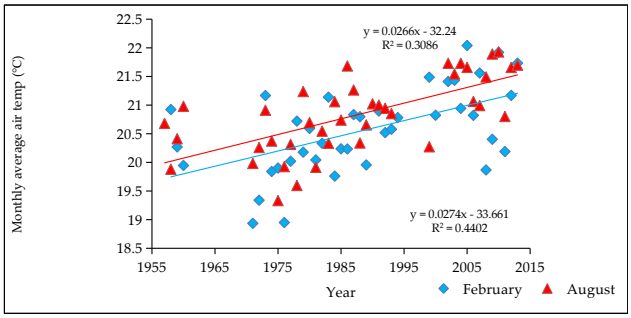

(f) Air temperature trends at Kamembe Aero meteorological station.

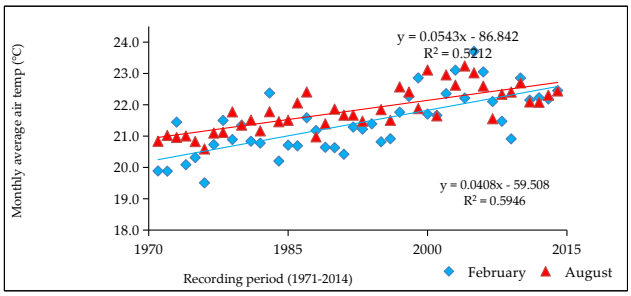

(g) Air temperature trends at Kigali Aero meteorological station.

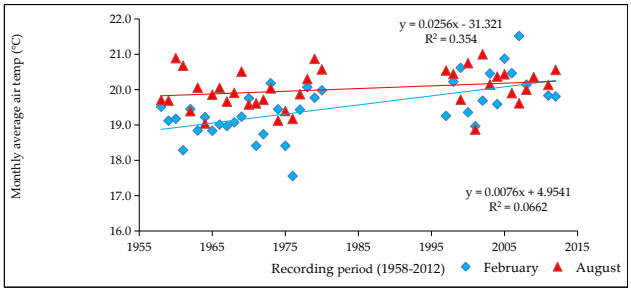

(h) Air temperature trends at Rubona meteorological station.

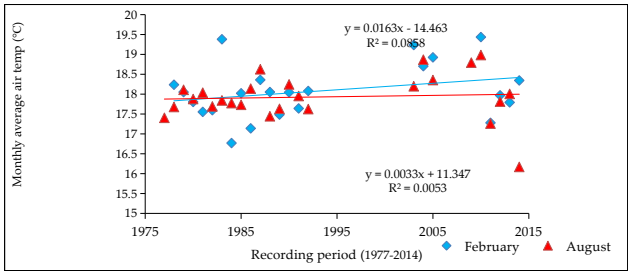

(i) Air temperature trends at Ruhengeri Aero meteorological station.

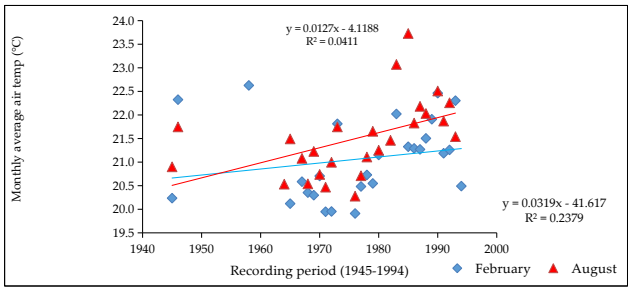

(j) Air temperature trends at Ruhengeri Aero meteorological station.

Figure 5. Trends of monthly average air temperature in February and August at 10 meteorological stations.

The output of regression analysis for the 10 meteorological stations showed that the trend of seasonal air temperature was much positive and highly significant at Kigali Aero meteorological station compared to the remaining meteo-stations (**Table 7**). According to the same results the trends for both short and long dry seasons at Ruhengeri meteo-station were in no case significant even though they were positive. The trends of seasonal air temperature were negative for the short dry season and positive for the long dry season but both were not significant.

The analysis of average seasonal air temperature showed almost similar trends even though not all were significant (**Table 7**). For the trends of short and long dry seasons at the 10 meteorological stations, only Butare presented a negative and non-significant trend for the short dry season. Most of the trends were statistically significant and very few were not. The similarity of these trends described above is due to the fact that the months of February and August belong to the periods that intersect with rainfall time in Rwanda.

3.4 Impacts of observed warming in Rwanda

A number of studies conducted recently in Rwanda have recognized that climate variability and change were happening and were coupled with significant impacts on the country's natural resources including agriculture, which is the main source of livelihood in rural areas [38]. It was indicated that the climate variability in Rwanda was expressed in the occurrence of higher changes in frequency, intensity, and persistence of extremes such as drought [40]. For example, MINITERE [41] reported that the eastern region of the country has been experiencing severe rainfall deficits over the last decades with the high vulnerability of the population in the region. It also noted that the observation made from 1961 to 2005 showed that the period between 1991 and 2000 has been the driest since 1961. These observations showed a marked prolonged drought in 1992, 1993, 1996, 1999, and 2000. Similar results were obtained by Nash and Ngabitsinze [13] and included the years 2005 and 2006 on the list of years with severe droughts in Rwanda. They indicated that these temperature extremes seriously affected Bugesera, Umutara and Mayaga regions. In addition, REMA [42] reported that the eastern province especially Bugesera region experienced severe droughts in 1999, 2006, and 2008. The length and intensity of land degradation have also weakened the lands' resilience; and when it comes to be combined with overgrazing and poor cultivation practices, drought has led to deterioration in pasture and arable land to the point where they have been abandoned. In the report, it was indicated that a decline in food crop production because of low moisture content was no doubt associated with changing climatic conditions in Rwanda.

Table 7. Regression analysis for seasonal air temperature.

Meteo-Station	Season	Trend	R-Square	P-Value	Remark
Butare	Short dry	*Negative*	0.018	0.349	Non-Significant
	Long dry	*Positive*	0.000	0.950	Non-Significant
Byimana	Short dry	*Positive*	0.343	0.001	Significant
	Long dry	*Positive*	0.205	0.018	Significant
Byumba	Short dry	*Positive*	0.286	0.022	Significant
	Long dry	*Positive*	0.521	0.002	Significant
Gahororo	Short dry	*Positive*	0.033	0.367	Non-Significant
	Long dry	*Positive*	0.413	0.001	Significant
Gisenyi Aero	Short dry	*Positive*	0.135	0.050	Significant
	Long dry	*Positive*	0.118	0.058	Non-Significant
Kamembe Aero	Short dry	*Positive*	0.309	0.000	Significant
	Long dry	*Positive*	0.440	0.000	Significant
Kigali Aero	Short dry	*Positive*	0.521	0.000	Significant
	Long dry	*Positive*	0.595	0.000	Significant
Rubona	Short dry	*Positive*	0.354	0.000	Significant
	Long dry	*Positive*	0.066	0.119	Non-Significant
Ruhengeri Aero	Short dry	*Positive*	0.086	0.175	Non-Significant
	Long dry	*Positive*	0.005	0.730	Non-Significant
Zaza	Short dry	*Positive*	0.041	0.311	Non-Significant
	Long dry	*Positive*	0.238	0.011	Significant

4. Conclusions and recommendations

This study shows that generally, the analysis of both daily maximum and minimum air temperatures indicated visible patterns of climate variability in Rwanda. The analysis of monthly extreme air temperatures showed that the year 2005 hosted a higher number of hottest days mostly observed in February. On the other hand, the minima (coldest days) in air temperature were recorded in Byumba, a region with higher altitude compared to the locations of meteorological stations used for this study. Throughout this study, it was noticed that the number of hot days and nights increased for the majority of analysed meteorological stations and consequently the reduction in the number of cold days and nights. The trends of seasonal air temperatures were not far different, and this is due to the short and long dry seasons intercepted with rainfall in Rwanda. Impacts of warming have been observed in Rwanda since a long time ago. Various researchers argued that these impacts expressed in the form of severe droughts were observed especially in the eastern part of the country affecting massive people who had to rely on external supply because of the failure in crop production. This past climate variability, which has been accompanied by various catastrophic impacts in Rwanda, should trigger further and deeper researches for forecasting purposes. The development of early meteorological warning systems will help Rwandan people, especially farmers, and policy makers to change the way things used to be and cope with this changing climate.

Author Contributions

Protais Seshaba: Conceptualization (lead); data curation (equal); formal analysis (equal); investigation (lead); methodology (equal); project administration (lead); resources (equal); software (lead); supervision (equal); validation (equal); visualization (equal); writing the original draft (lead), writing, review and editing (lead).

Edouard Singirankabo: Conceptualization

(supporting); data curation (equal); formal analysis (equal); investigation (supporting); methodology (equal); project administration (supporting); resources (supporting); supervision (equal); validation (equal); visualization (equal); writing the original draft (supporting), writing, review and editing (supporting).

Donat Nsabimana: Conceptualization (supporting); data curation (equal); formal analysis (equal); investigation (supporting); methodology (supporting); project administration (equal); resources (supporting); supervision (lead); validation (lead); visualization (equal); writing the original draft (equal), writing, review and editing (equal).

Conflict of Interest

There is no conflict of interest.

Funding

No funding.

Acknowledgments

We are grateful to Meteo Rwanda for allowing us to have access to its meteorological dataset for responding to the questions of the current research.

References

[1] World Meteorological Organization, 1992. Measurement of temperature and humidity (Technical Note No. 194). WMO: Geneva.

[2] Enz, J.W., Hofman, V., Thostenson, A., 2014. Air temperature inversions causes, characteristics and potential effects on pesticide spray drift. NDSU Extension Service.

[3] Lobell, D.B., Schlenker, W., Costa-Roberts, J., 2011. Climate trends and global crop production since 1980. Science. 333(6042), 616–620. DOI: https://doi.org/10.1126/science.1204531

[4] IPCC, 2007. Climate change 2007: Impacts, adaptation and vulnerability. Cambridge University Press: Cambridge.

[5] GISS surface temperature analysis. NASA Goddard Institute for Space Studies and Columbia University Earth Institute: New York.

[6] IPCC, 2007. Climate change 2007: The physical scientific basis. Cambridge University Press: Cambridge.

[7] Katz, R.W., Brown, B.G., 1992. Extreme events in a changing climate: variability is more important than averages. Climatic Change. 21, 289–302. DOI: https://doi.org/10.1007/BF00139728

[8] Nicholson, S.E., Kim, J., 1997. The relationship of the El Niño—Southern oscillation to African rainfall. International Journal of Climatology. 17(2), 117–135. DOI: https://doi.org/10.1002/(SICI)1097-0088(199702)17:2<117::AID-JOC84>3.0.CO;2-O

[9] Hulme, M., Doherty, R., Ngara, T., et al., 2001. African climate change: 1900–2100. Climate Research. 17(2), 145–168. DOI: https://doi.org/10.3354/cr017145

[10] IPCC, 2001. Climate change 2001: The scientific basis. Cambridge University Press: Cambridge.

[11] Niang, I., Ruppel, O.C., Abdrabo, M.A., et al., 2014. Africa. Climate change 2014: Impacts, adaptation, and vulnerability. Cambridge University Press: Cambridge. pp. 1199–1265.

[12] DFID, 2009. Economic impacts of climate change: Kenya, Rwanda, and Burundi. Oxford Office: Oxford.

[13] Nash, E., Ngabitsinze, J.C., 2013. Low-carbon resilient development in Rwanda. International Institute for Environment and Development (IIED): London.

[14] WWF, 2006. Climate change impacts on East Africa. World Wide Fund: Gland.

[15] Fischlin, A., Midgley, G.F., Price, J.T., et al., 2007. Ecosystems, their properties, goods, and services. Climate change 2007: Impacts, adaptation and vulnerability. Cambridge University Press: Cambridge. pp. 211–272.

[16] Byamukama, B., Carey, C., Cole, M., et al., 2011. National strategy on climate change and low carbon development for Rwanda. Univer-

sity of Oxford: Oxford.

[17] Safari, B., 2012. Trend analysis of the mean annual temperature in Rwanda during the last 52 years. Journal of Environmental Protection. 3(6), 20077.
DOI: https://doi.org/10.4236/jep.2012.36065

[18] Habiyaremye, G., Jairu, N.D., de la Paix Mupenzi, J., et al., 2012. Statistical analysis of climatic variables and prediction outlook in Rwanda. East African Journal of Science and Technology. 1(1), 27–34.

[19] Singirankabo, E., Iyamuremye, E., Habineza, A., et al., 2023. Statistical modelling of maximum temperature in Rwanda using extreme value analysis. Open Journal of Mathematical Sciences. 7, 180–195.
DOI: https://doi.org/10.30538/oms2023.0206

[20] Mutabazi, A., 2010. Assessment of operational framework related to climate change in Rwanda. REMA: Kigali.

[21] Downing, T., Watkiss, P., Dyszynski, J., et al., 2009. Economics of Climate change in Rwanda. Stockholm Environment Institute: UK Oxford Office.

[22] Stott, P.A., Gillett, N.P., Hegerl, G.C., et al., 2010. Detection and attribution of climate change: A regional perspective. Wiley Interdisciplinary Reviews: Climate Change. 1(2), 192–211.
DOI: https://doi.org/10.1002/wcc.34

[23] Collier, C.G., 2006. The impact of urban areas on weather. Quarterly Journal of the Royal Meteorological Society. 132(614), 1–25.
DOI: https://doi.org/10.1256/qj.05.199

[24] Folland, C.K., Vose R.S., Easterling D.R., et al., 2001. Observed climate variability and change. Climate change 2001: The scientific basis. Cambridge University Press: Cambridge. pp. 108–109.

[25] Przybylak, R., 2000. Diurnal temperature range in the Arctic and its relation to hemispheric and Arctic circulation patterns. International Journal of Climatology. 20(3), 231–253.
DOI: https://doi.org/10.1002/(SICI)1097-0088(20000315)20:3<231::AID-JOC468>3.0.CO;2-U

[26] Braganza, K., Karoly, D.J., Arblaster, J.M., 2004. Diurnal temperature range as an index of global climate change during the twentieth century. Geophysical Research Letters. 31(13).
DOI: https://doi.org/10.1029/2004GL019998

[27] Flannigan, M.D., Stocks, B.J., Wotton, B.M., 2000. Climate change and forest fires. Science of the Total Environment. 262(3), 221–229.
DOI: https://doi.org/10.1016/S0048-9697(00)00524-6

[28] Foden, W., Mace, G., Vié, J.C., et al., 2008. Species susceptibility to climate change impacts. IUCN: Gland, Switzerland.

[29] Balling Jr, R.C., Klopatek, J.M., Hildebrandt, M.L., et al., 1998. Impacts of land degradation on historical temperature records from the Sonoran Desert. Climatic Change. 40, 669–681.
DOI: https://doi.org/10.1023/A:1005370115396

[30] Bonan, G.B., 2001. Observational evidence for reduction of daily maximum temperature by croplands in the Midwest United States. Journal of Climate. 14(11), 2430–2442.
DOI: https://doi.org/10.1175/1520-0442(2001)014<2430:OEFROD>2.0.CO;2

[31] Small, E.E., Sloan, L.C., Nychka, D., 2001. Changes in surface air temperature caused by desiccation of the Aral Sea. Journal of Climate. 14(3), 284–299.
DOI: https://doi.org/10.1175/1520-0442(2001)014<0284:CISATC>2.0.CO;2

[32] Stott, P.A., Jones, G.S., Christidis, N., et al., 2011. Single-step attribution of increasing frequencies of very warm regional temperatures to human influence. Atmospheric Science Letters. 12(2), 220–227.
DOI: https://doi.org/10.1002/asl.315

[33] Arnfield, A.J., 2003. Two decades of urban climate research: A review of turbulence, exchanges of energy and water, and the urban heat island. International Journal of Climatology. 23(1), 1–26.
DOI: https://doi.org/10.1002/joc.859

[34] Parker, D.E., 2010. Urban heat island effects on estimates of observed climate change. Wiley Interdisciplinary Reviews: Climate Change. 1(1), 123–133.
DOI: https://doi.org/10.1002/wcc.21

[35] Lin, X.C., Yu, S.Q., 2005. Interdecadal changes of temperature in the Beijing region and its heat island effect. Chinese Journal of Geophysics. 48(1), 47–54.
DOI: https://doi.org/10.1002/cjg2.624

[36] Yan, Z., Li, Z., Li, Q., et al., 2010. Effects of site change and urbanisation in the Beijing temperature series 1977–2006. International Journal of Climatology. 30(8), 1226–1234.
DOI: https://doi.org/10.1002/joc.1971

[37] Portman, D.A., 1993. Identifying and correcting urban bias in regional time series: Surface temperature in China's northern plains. Journal of Climate. 6(12), 2298–2308.
DOI: https://doi.org/10.1175/1520-0442(1993)006<2298:IACUBI>2.0.CO;2

[38] WFP/FEWS-NET, 2003. Rwanda vulnerability baseline report. World Food Programme of the United Nations (WFP)/Famine Early Warning Systems Network (FEWS-NET): Kigali.

[39] World Meteorological Organization, 2013. The global climate 2001–2010: A decade of climate extremes. World Meteorological Organization: Geneva.

[40] Climate Risk Country Profile: Rwanda [Internet]. World Bank Group; 2021. Available from: https://climateknowledgeportal.worldbank.org/sites/default/files/2021-09/15970-WB_Rwanda%20Country%20Profile-WEB.pdf

[41] MINITERE, 2006. National adaptation programmes of action (NAPA) to climate change. Ministry of Lands, Environment, Forestry, Water and Mines (MINITERE): Kigali.

[42] REMA, 2007. Pilot integrated ecosystem assessment of Bugesera. United Nations Development Programme (UNDP), United Nations Environment Programme (UNEP) and Rwanda Environment Management Authority (REMA): Kigali.

BILINGUAL PUBLISHING GROUP

Journal of Atmospheric Science Research

https://journals.bilpubgroup.com/index.php/jasr/index

ARTICLE

Multi-decadal Changes of the Impact of El Niño Events on Tibetan Plateau Summer Precipitation

***Weinan Jiang*[1,2,3], *Ning Cao*[1,2,3,4*], *Riga Aze*[1,2,3], *Jianjun Xu*[2,3,4]**

[1] *College of Ocean and Meteorology, Guangdong Ocean University, Zhanjiang, Guangdong, 524088, China*

[2] *CMA-GDOU Joint Laboratory for Marine Meteorology, Guangdong Ocean University, Zhanjiang, Guangdong, 524088, China*

[3] *South China Institute of Marine Meteorology (SIMM), Guangdong Ocean University, Zhanjiang, Guangdong, 524088, China*

[4] *Shenzhen Institute of Guangdong Ocean University, Shenzhen, Guangdong, 518108, China*

ABSTRACT

Precipitation on the Tibetan Plateau (TP) has an important effect on the water supply and demand of the downstream population. Involving recent climate change, the multi-decadal variations of the impact of El Niño-Southern Oscillation (ENSO) events on regional climate were observed. In this work, the authors investigated the changes in summer precipitation over TP during 1950–2019. At the multi-decadal scale, the authors found that the inhabiting impact of El Niño events on the TP summer precipitation has strengthened since the late 1970s. The main factor contributing to this phenomenon is the significant amplification in the decadal amplitude of El Niño during 1978–2019 accompanied by a discernible escalation in the frequency of El Niño events. This phenomenon induces anomalous perturbations in sea surface temperatures (SST) within the tropical Indo-Pacific region, consequently weakening the atmospheric vapor transport from the western Pacific to the TP. Additionally, conspicuous anomalies in subsidence motion are observed longitudinally and latitudinally across the TP which significantly contributes to a curtailed supply of atmospheric moisture. These results bear profound implications for the multi-decadal prediction of the TP climate.

Keywords: Tibetan plateau; Summer precipitation; ENSO; Multi-decadal changes; Climate variability

*CORRESPONDING AUTHOR:

Ning Cao, College of Ocean and Meteorology, Guangdong Ocean University, Zhanjiang, Guangdong, 524088, China; CMA-GDOU Joint Laboratory for Marine Meteorology, Guangdong Ocean University, Zhanjiang, Guangdong, 524088, China; South China Institute of Marine Meteorology (SIMM), Guangdong Ocean University, Zhanjiang, Guangdong, 524088, China; Shenzhen Institute of Guangdong Ocean University, Shenzhen, Guangdong, 518108, China; Email: ncao@gdou.edu.cn

ARTICLE INFO

Received: 27 December 2023 | Revised: 24 January 2024 | Accepted: 26 January 2024 | Published Online: 31 January 2024

DOI: https://doi.org/10.30564/jasr.v7i1.6180

CITATION

Jiang, W.N., Cao, N., Aze, R., et al., 2024. Multi-decadal Changes of the Impact of El Niño Events on Tibetan Plateau Summer Precipitation. Journal of Atmospheric Science Research. 7(1): 90–105. DOI: https://doi.org/10.30564/jasr.v7i1.6180

1. Introduction

The Tibetan Plateau (TP) lies between 25°N and 45°N, 65°E and 105°E. It constitutes the world's largest Plateau, covering an area of 2.5 million square kilometers that extends from the Pamir Plateau in the west to the Hengduan Mountains in the east; and from the Kunlun Mountains and Qilian Mountains in the north to the Himalaya Mountains in the south [1]. The Tibetan Plateau also includes the highest land mass, with an average elevation of over 4500 meters. It forms one of the major drivers of global climate, referred as the Earth's "third pole" [2]. The TP area is recognized as the "Asia Water Tower" due to its location within Asia, where it plays a vital role in supplying water to numerous river networks [3]. Precipitation patterns in the region have been considered to be affected by climate change, with further impacts on the ecological environment and human society [4]. For example, changes in precipitation patterns not only influence vegetation distribution, consequently shaping the ecological environment [5], but also induce modifications in river flow, thereby exerting effects on downstream agriculture [3]. The latent heat released during precipitation can drive atmospheric circulation and further affect the climate of East Asia [6–8]. Summer precipitation over the TP accounts for more than 60% of the total annual precipitation [9]. Therefore, it is important for water resource variations and people's life to investigate the summer precipitation over the TP.

The primary factor influencing precipitation variations on the TP is the large-scale atmospheric circulation, the interaction between the westerlies and monsoons stands out as a key mechanism affecting water vapor transport and precipitation distribution in the TP region [10,11]. The westerlies transport moisture from the Mediterranean-Iran Plateau region to the TP and the moisture in the southern TP primarily comes from monsoons [12], changes in the westerlies and monsoons inevitably lead to variations in the TP climate. Alongside global climate warming and changes in the atmospheric circulation model, the precipitation on the Tibetan Plateau has also changed. Of course, there are many factors that affect precipitation on the TP [13–15], and changes in sea surface temperature (SST) are one of them. As the strongest signal in the air-sea interaction system, the influence of El Niño-Southern Oscillation (ENSO) on precipitation cannot be ignored.

During El Niño, SST significantly rises in the eastern Pacific, while in La Niña the opposite occurs. The influence of El Niño on TP precipitation is usually indirect, El Niño induces changes of SST in other ocean basins and atmospheric circulation to affect TP precipitation. For example, El Niño can induce SST anomalies in the Indian Ocean and North Atlantic [16–20], which affect TP summer precipitation through the Indo-western Pacific Ocean capacitor [17,21] effect and atmospheric circulation. To elaborate, during the 3–6 months following the peak of El Niño, the SST in the Indian Ocean and the tropical North Atlantic Ocean become warmer than normal [16], and the land-sea thermal contrast between the Eurasian continent and the Indian Ocean weakens. Furthermore, El Niño induced Indian Ocean SST anomaly and led to an anti-symmetric pattern of atmospheric anomalies in the tropical north Indian Ocean [22], which delayed the onset of the Indian monsoon and reduced early summer precipitation in the TP [23]. As El Niño decays during the summer, the Indo-western Pacific Ocean capacitor effect sustains the warming of SST in the tropical North Indian Ocean [21], thus maintaining the impact of ENSO on TP summer precipitation. With regard to the North Atlantic SST, El Niño can trigger a tripolar SST pattern in the North Atlantic, a phenomenon that often persists into the summer [24]. This tripolar pattern exerts a remote influence on the summer precipitation in the Tibetan Plateau through teleconnections [25]. These mechanisms determine that the impact of El Niño's effects persist not only during the development year of ENSO but even in the year following its peak [26].

Many studies have shown that the developing phase of El Niño can weaken TP summer precipitation [27–29]. In recent decades, the structure of

ENSO has experienced interdecadal changes [30,31], with frequent Central-Pacific El Niño events and increasing intensity [32–34], the duration of SST anomalies in the Central Pacific caused by El Niño is also longer than in the past [35]. This means that the regional climate system related to ENSO is undergoing interdecadal changes [19,36–38], including TP summer precipitation. Then the question arises: What decadal changes have occurred in the relationship between El Niño and TP summer precipitation? The objective of the present study is to reveal the TP summer responses to the interdecadal change of ENSO, and to feature corresponding changes of water vapor transport over TP and the surrounding plateau-monsoon regions.

2. Materials and methods

The global land surface precipitation data used in this work are from version 4.05 of the CRU TS monthly high-resolution gridded climate dataset [39], produced by the UK's National Centre for Atmospheric Science (NCAS) at the University of East Anglia's Climatic Research Unit (CRU). It has a horizontal resolution of 0.5° × 0.5°, covering the period 1901–2020. The CRU-TS4.05 data comprises monthly gridded fields based on monthly observational data calculated from daily or sub-daily data by National Meteorological Services and other external agents.

In contrast, total precipitation data from the reanalysis dataset ERA5 are also used to validate the results derived from CRU-TS4.05 data. The vertical integral of water vapor flux, total column water vapor, and vertical velocity data are all from the ERA5 product, downloaded from the Climate Data Store (CDS). ERA5 is the fifth-generation ECMWF reanalysis for global climate and weather, with a horizontal resolution of 0.25° × 0.25° and 37 levels in the vertical direction for atmosphere reanalysis. It is available from 1940 [40], with a large number of observations assimilated into the numerical weather forecasting model to obtain a consistent dataset constrained by the laws of physics [41]. In this work, we use the ERA5 product for the period 1950 to 2019.

The SST used in this work is from the Hadley Centre Sea Ice and Sea Surface Temperature dataset (HadISST) [42]. The monthly index of ENSO is specified as the area-averaged SST from the Niño-3.4 region (5°S–5°N and 170–120°W, anomaly with the 1981–2010 mean removed) using the HadISST1 dataset, hereafter the Niño-3.4 index. The study period is denoted as 1950–2019 according to the time ranges of these datasets. If not specifically specified, the seasonal mean is defined as March-April-May mean for spring, June-July-August mean for summer, September-October-November mean for autumn, and December-January-February mean for winter, according to the boreal season cycle. Additionally, we use (0) to denote the year of TP summer we focused on, (–1) to denote the former year, and (1) to denote the following year. ENSO is phase-locked to the annual cycle. Typically, eastern Pacific (Niño-3.4) SST anomalies begin to develop in JJA(0), peak in D(0)JF(1), and decay rapidly in MAM (1). The developing stage denotes JJA(0) to D(0)JF(1), while the decaying stage denotes D(0)JF(1) to MAM(1).

Using the Pearson R statistical test, we analyze the correlation between ENSO and summer precipitation on the plateau. Additionally, we observe its variations through a 21-year sliding correlation analysis (comprising the preceding 10 years, the current year, and the subsequent 10 years). As we investigate the interdecadal to multi-decadal change in the interannual relationship, all data are linearly detrended. The statistical significance is tested via the two-tailed Student's *t* test.

3. Results

3.1 TP summer precipitation and its changes

Using monthly precipitation data from the observation-determined product of the global land surface precipitation dataset CRU-TS4.05 and the widely used ERA5 products from the fifth-generation ECMWF reanalysis system, we present the 70-year mean summer precipitation (1950–2019) in **Figures 1a–1b**. In both datasets, patterns of "wet in southeast TP and dry in north and west TP" are observed. It

is evident that summer precipitation mainly occurs in the south and southeast parts of TP for multi-year means, with an average daily precipitation of 5–8 mm at the southern edge of the plateau. The summer precipitation in northern and western TP is less than 2 mm/day. A magenta rectangle in (a, b) was drawn to denote the area of southeast TP (SETP, 85°–105°E, 25°–35°N). Based on the CRU data for 1950–2019, summer precipitation over the SETP region accounts for about 70% of that over the entire TP region. For the regional mean, SETP has 4.0 mm/day precipitation averaged in summer, which is nearly twice the TP mean summer precipitation (2.4 mm/day). The time series of TP and SETP mean summer precipitation are shown in **Figures 1c–1d**.

The TP mean summer precipitation is associated with ENSO, with the correlation coefficient reaching –0.40 and –0.31 between the summer Niño-3.4 index (bars in the figure) and the TP mean series for CRU-TS4.05 and ERA5, respectively (**Figure 1c**), exceeding a 99% confidence level. The SETP mean summer precipitation also correlates with the summer Niño-3.4 index with coefficients of –0.30 and –0.14 for CRU-TS4.05 and ERA5 (**Figure 1d**), but only the CRU result exceeds the 98% confidence level, while the ERA5 result is less than 80%. In fact, although precipitation over the SETP region accounts for about 70% of that over the entire TP region, the dominant significant negative correlations lie in the region of south and south-west of TP, rather than the rectangle region of SETP, as is shown in **Figure 3** with the patterns of correlation coefficients. Therefore, we designate the time series of TP mean summer precipitation as an index to represent the changes in TP precipitation in the following correlation and regression analyses.

3.2 TP summer precipitation and its changes

To highlight the relationship between TP summer precipitation and ENSO, we present the lead-lag correlation coefficients of TP mean summer precipitation (shown in **Figure 1c**) and the monthly Niño-3.4 index in a 3-year cycle during 1950–2019, using CRU-TS4.05 and ERA5 precipitation data in **Figure 2a**. At a 95% confidence level, both datasets show that TP mean summer precipitation negatively correlates with the Niño-3.4 index from spring(0) to spring(1), indicating that the variability of TP summer(0) precipitation is consistent with the variabilities of ENSO during its life-cycle from onset in spring(0) to dying out in spring(1).

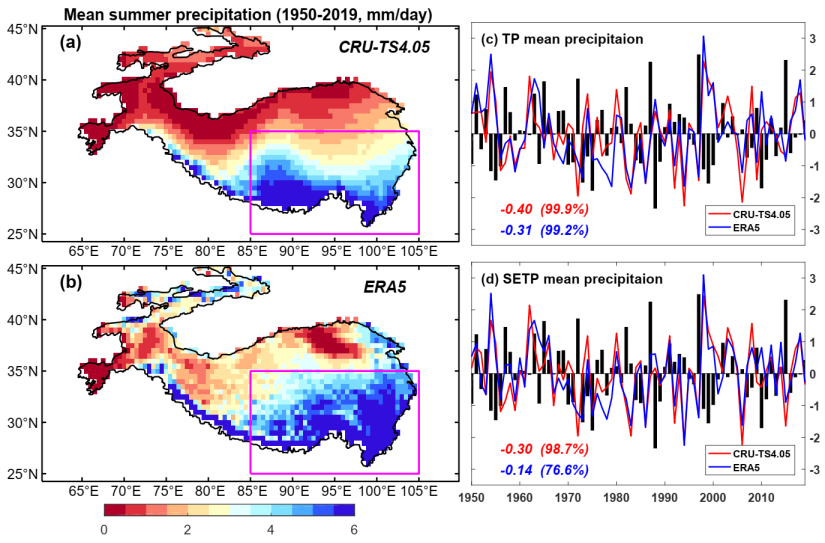

Figure 1. Mean summer precipitation over Tibetan Plateau during 1950–2019 using data from (a) CRU TS4.05 and (b) ERA5 products, and the time series of the normalized (c) TP mean and (d) SETP mean summer precipitation derived by CRU-TS4.05 (red line) and ERA5 (blue line) products and the normalized concurrent summer Niño-3.4 index (bars). The magenta rectangle in (a, b) denotes the area SETP. The correlation coefficients between the precipitation time series and the Niño-3.4 index are shown on the bottom with the confidence levels in parentheses. All time series have been linearly detrended.

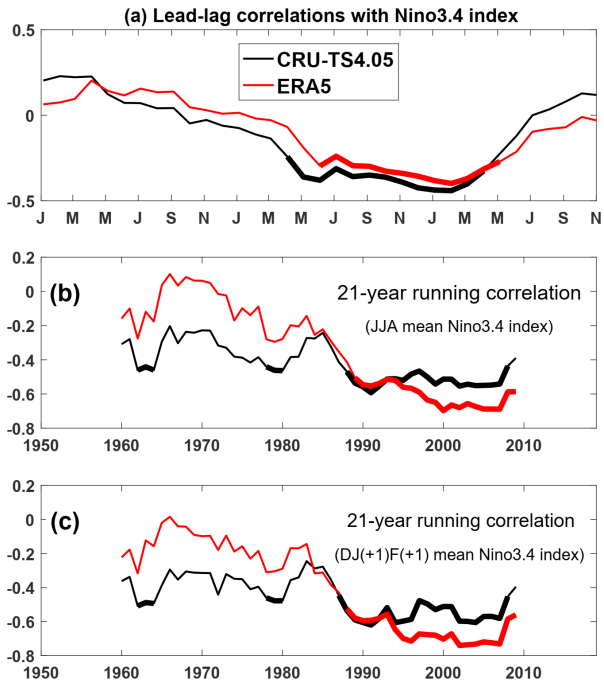

Figure 2. (a) Lead-lag correlation coefficients of TP mean summer precipitation and the monthly Niño-3.4 index in 3-year cycle during 1950–2019; (b) The 21-year running correlation of TP mean summer precipitation and the JJA mean Niño-3.4 index; (c) Same as (b), but for the DJ(+1)F(+1) mean Niño-3.4 index. The notation (+1) denotes the year after the ENSO event. Results of CRU-TS4.05 and ERA5 data are shown in black and red lines. The correlation is shown at the center year of the 21-year window. Bold lines indicate correlation coefficients exceeding 95% confidence level.

Based on this result, we focused our attention on the impact of ENSO on TP summer climate in the developing stage and examined the interdecadal change in the relationship between the two series. Here we introduce a method of running correlations with a 21-year window. **Figures 2b–2c** present the results of a 21-year running correlation between the normalized TP mean summer precipitation and Niño-3.4 index for JJA(0) mean and D(0)JF(1) mean, respectively. It is evident that the relationship between them has experienced an interdecadal change since the late 1980s, precisely since 1988 for CRU and since 1989 for ERA5, at the 95% confidence level. As the correlation is shown at the center year of the 21-year window, taking 1989 as an example, it represents the relations of the two for the 1979–1999 period. So if the transition from insignificant to significant occurred since 1989, it means that any 21-year period after the year 1979 will show a significant correlation.

Both the concurrent summer Niño-3.4 index and the mature phase winter Niño-3.4 index show consistent results, and the two precipitation datasets also support each other. As the 21-year running correlation coefficient was statistically significant since 1988/1989 (the result for the period of 1978–1998/1979–1999), we can conclude that relations between TP summer precipitation and ENSO have exhibited an interdecadal abrupt change and become statistically significant in recent decades, suggesting a strengthened relationship between TP mean summer precipitation and ENSO since the late 1970s. Thus, we choose 1950–1978 (P1) and 1979–2019 (P2) as the two sub-periods in the following correlation and regression analyses to understand the different relationships between TP summer rainfall and tropical Indo-Pacific SST variabilities. Obviously, the two sub-periods respectively represent insignificant and significant correlations between TP summer precipitation and ENSO in its developing stage.

Figure 3 presents patterns of correlation coefficients of TP summer precipitation derived from CRU and ERA5 data with the summer mean Niño-3.4 series for the whole period 1950–2019 and the divided sub-periods of 1950–1978 (P1) and 1979–2019 (P2). It is evident that the most significant correlation coefficient center is located in southwest TP, consistent with a previous study [28], but the patterns for the two sub-periods show some remarkable differences. During 1950–1978, the patterns mainly show negative correlations at southwest TP (significant) and positive at north-central-southeast parts (mostly insignificant). The impact of ENSO on southwest TP can be considered a part of the Indian summer monsoon system, indicating that El Niño events in their developing years will significantly weaken the summer monsoon and bring less precipitation in the Indian subcontinent, while La Niña event effects are the opposite. However, during 1979–2019, the location of negative correlations

expands eastward, making a dramatic decrease in the positive correlations at north-central-southeast TP. As stated above, for the 1950–2019 climatology, SETP accounts for about 70% of the entire TP summer precipitation. In 1950–1978, although the positive correlations at north-central-southeast TP are not statistically significant, they can generally offset the negative correlations at SWTP, causing insignificant correlations between entire TP mean summer precipitation and ENSO (**Figure 2b**). In contrast, during 1979–2019, the positive correlations at north-central-southeast TP have greatly weakened and even become negative. Meanwhile, the significant negative correlations have expanded to central-southeast TP, causing significant correlations between the entire TP mean summer precipitation and ENSO (**Figure 2b**). By investigating the ENSO-related summer precipitation over a larger region (known as monsoon Asia), in the former period, ENSO mainly impacts the north of the Indian subcontinent and southwest of TP negatively, while the correlation is relatively weak and insignificant in the south of India and central and east China. In contrast, for the later period, ENSO negatively correlates with summer precipitation in south India, south-central TP, east TP, and central China at a 90% confidence level. The comparisons led us to confirm that ENSO's impact on summer precipitation in central-southeast TP has significantly strengthened after 1979.

4. Possible mechanisms for interdecadal change

As shown above, the relationship between ENSO and TP summer precipitation has experienced an interdecadal change since the late 1970s. In this section, we further investigate the possible mechanisms for this interdecadal change by starting with a further contrast of the correlation of TP summer precipitation with SST before and after the late 1970s. There seems to be no distinct interdecadal change in the annual variation of TP mean summer precipitation in the 1970s, either for mean summer precipitation over the entire TP or for that over SETP (**Figures 1c–1d**). Therefore, the possible reasons for such interdecadal change in their correlations probably lie in the following two factors: the change of ENSO intensity or the pattern change of the contemporaneous SST in the tropical Indo-Pacific domain.

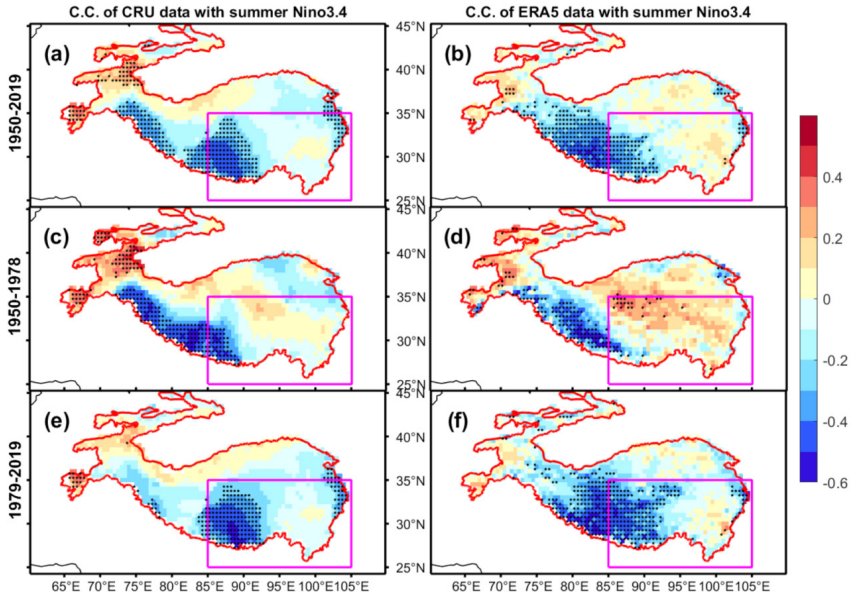

Figure 3. Patterns of correlation coefficients (C.C.) of summer precipitation derived from CRU (a, c, e) and ERA5 (b, d, f) data with summer Niño-3.4 series, for (a, b) the whole period 1950–2019, and the divided periods of (c, d) 1950–1978, (e, f) 1979–2019. The dotted areas indicate correlation coefficients exceed 90% confidence level. All data has been detrended to remove the effect of global warming.

4.1 Interdecadal change in relations between TP summer precipitation and ENSO

Firstly, the change of ENSO intensity is considered. Since the Niño-3.4 index captures the SST anomalies averaged generally over the maximum SST anomalies region, and the variations of SST are well phase-locked with the annual cycle, we can assign the D(0)JF(1) mean Niño-3.4 index as the amplitude of ENSO events, and the standard deviation of Niño3.4 index can be used to denote the intensity of ENSO. By using a 21-year sliding analysis method, the running standard deviation (STD) of the D(0)JF(1) mean Niño-3.4 index is shown in **Figure 4**, along with the running correlation series, similar to **Figure 2c**. With correlation coefficients of –0.61 and –0.54, both CRU and ERA5 data show significant negative correlations (exceeding a 95% confidence level) of changes in 21-year running STD and 21-year running correlations between ENSO and TP summer precipitation. These results show that the interdecadal change in the relationship between ENSO and summer TP precipitation can be determined by the strengthening of ENSO amplitude since the late 1970s, as the running STDs of the D(0)JF(1) mean Niño-3.4 index experienced a distinct increase at about the same time (mid-1970s) when the running correlation series jumped from negatively insignificant to negatively significant (late 1970s).

This interdecadal change in ENSO intensity may be considered as a result of modulation by the Atlantic multi-decadal oscillation (AMO) [43]. The AMO was in its negative phase from the 1970s through 2000, causing strengthened ENSO variability. It is worth noting that the AMO has changed to a positive phase since the 2000s, and the related ENSO amplitude may be weakened during the 2010s according to this theory. Whether it indicates a forthcoming interdecadal change in relations between ENSO and TP summer precipitation is a question that needs further investigation, as shown in **Figures 2 and 4**, where the 21-year running correlations also show that it will change from significant to insignificant.

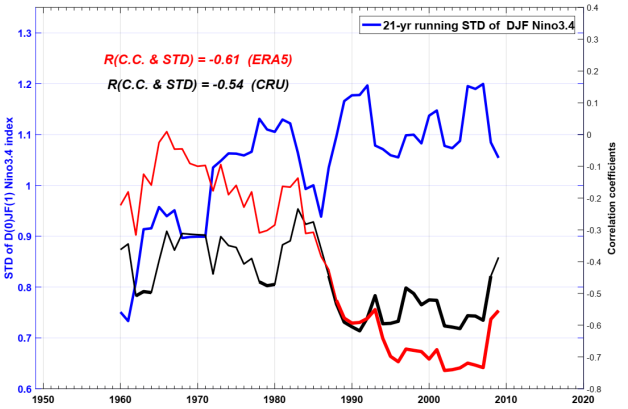

Figure 4. The 21-year running standard deviation of D(0)JF(1) mean Niño-3.4 index (STD, blue line), and the 21-year running correlation series same as **Figure 2c** (black and red lines). Bold black and red lines indicate correlation coefficients exceeding 95% confidence level.

4.2 Changes in ENSO patterns

Secondly, the pattern changes of the contemporaneous SST in the tropical Indo-Pacific domain are also examined by performing regression of tropical SST anomalies on the TP mean summer (JJA(0)) precipitation. The lead-lag regressions of seasonal mean SST onto TP mean summer precipitation, which show the results of seasonal evolution in the tropical Indo-Pacific oceans, are shown in **Figure 5**, from MAM(0)/spring to D(0)JF(1)/winter for two sub-periods.

Apparently, the SST anomalies related to TP summer precipitation in the tropical Indo-Pacific region are quite different between the two sub-periods. They generally show La Niña-like SST gradients for both sub-periods during an annual cycle, but the TP summer precipitation-related SST changes are much stronger in the later period than in the former period. In spring, the significantly related region includes the west Pacific (positive) and eastern equatorial Pacific (negative) in the former period, while in the later period as a contrast, the positive SST anomalies in the western Pacific greatly extend to the subtropical south and north Pacific, and the negative SST anomalies appear in central and northeastern equatorial Pacific. Over time, in the former period, the negative SST anomalies have

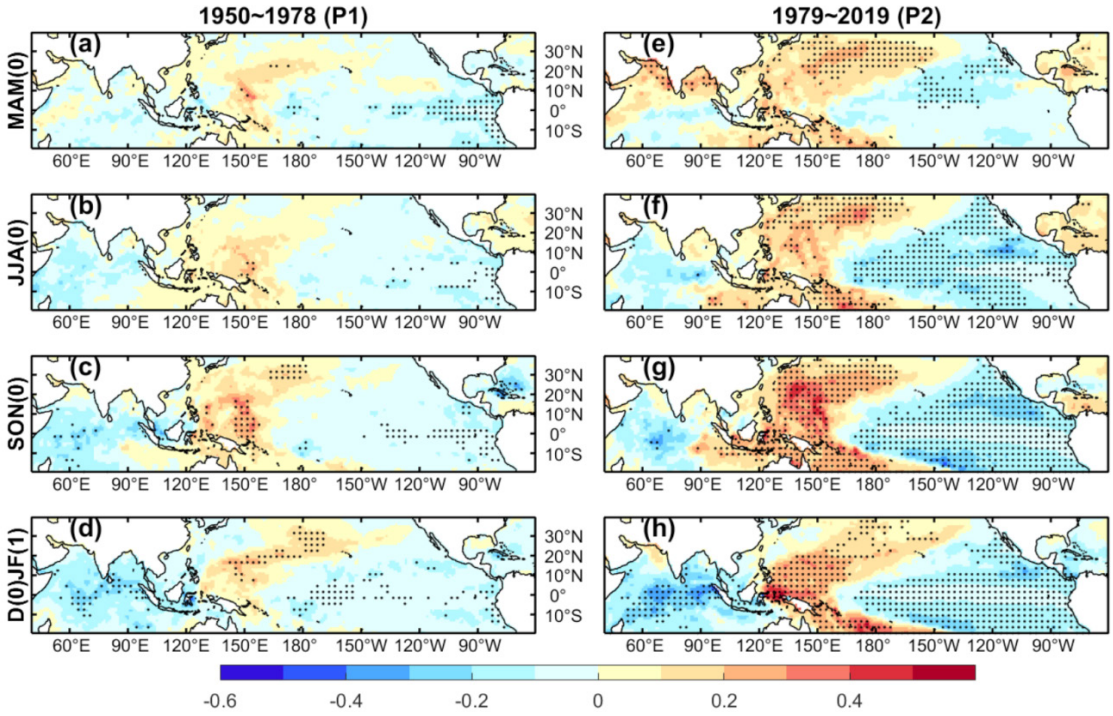

Figure 5. Lead-lag regressions of seasonal mean SST onto the TP mean summer precipitation for (a)–(d) period of 1950–1978 and (e)–(h) period of 1979–2019. Seasonal mean SSTA is for MAM(0), JJA(0), SON(0), and D(0)JF(1), respectively. Numerals 0 and 1 denote the simultaneous year and 1-year lag. The dots denote values exceeding the 95% confidence level. The SST data is derived from HadISST product and has been detrended.

greatly weakened in the eastern equatorial Pacific while the positive anomalies do not change much. By contrast, in the later period, the negative SST anomalies have greatly strengthened from spring to winter, with extraordinary positive-negative (or west-east) contrast covering almost the entire Pacific. The differences in TP summer precipitation-related SST anomalies patterns indicate that the relationship between TP summer precipitation and eastern equatorial Pacific SST anomalies has greatly strengthened in the later period relative to the former period.

Vastly different SST anomalies are also seen in the tropical Indian Ocean, which is considered to exhibit a season-dependent characteristic [44], that is, the SST anomaly is controlled by the Indian Ocean Dipole (IOD) mode during JJA and SON, and by Indian Ocean Basin wide (IOB) mode in DJF and MAM. The TP summer precipitation-related SST anomalies in the former period show no distinct IOD or IOB mode. However, in the later period, the related SST anomalies show a distinct IOD mode during JJA and SON, and IOB mode during MAM and DJF, which agrees pretty well with the season-dependent characteristic.

To investigate the differences in how the El Niño event impacts TP summer precipitation by affecting the water vapor transport during two sub-periods, a composite analysis is conducted. Here, we select the years of the El Niño developing stage and list them in **Table 1**. It was simply classified as an El Niño event if the D(0)JF(1) mean Niño-3.4 index exceeded half a standard deviation during the 1950–2019 period. There are 8 years in the period of 1950–1978, and 14 years in the period of 1979–2019 being selected as developing years of El Niño events.

Table 1. Selected years of El Niño developing stage for the divided two sub-periods.

Periods	Developing Years of El Niño Events
1950–1978 (P1)	1957 1963 1965 1968 1969 1972 1976 1977
1979–2019 (P2)	1979 1982 1986 1987 1991 1994 1997 2002 2004 2006 2009 2014 2015 2018

Composite results of seasonal evolution mean SST anomalies for El Niño developing years over the tropical Indo-Pacific Ocean for periods of 1950–1978 and 1980–2019 are presented in **Figure 6**, from MAM(0)/spring to D(0)JF(1)/winter. Moreover, it should be noted that there were three super strong El Niño events in the later period, which occurred in 1982–1983, 1997–1998, and 2014–2016. To remove the influence of strong El Niño events, we delete these two years when using composite analysis in this figure. In the period of 1950–1978, the positive SST anomalies in the tropical Pacific developed from spring to autumn, featuring a maximum warming center located in the eastern region (**Figures 6a–6d**). In the later period 1979–2019, the warm SST anomalies in the tropical Pacific developed in summer and turned stronger in autumn, featuring a maximum warming center located in the central region (**Figures 6e–6h**). Such distinct differences suggest that the impacts of El Niño on the Asian summer climate during the two sub-periods are different.

4.3 Changes in water vapor transport

Summer precipitation on the TP has been largely determined by moisture supply from the oceans, including the Indian Ocean, and western Pacific, and even by the cross-equatorial flow from the southern hemisphere [45]. The differences in atmospheric water vapor transport in the two sub-periods may tell us how the strengthened ENSO impacts the precipitation in TP and surrounding plateau-monsoon regions.

As a contrast, **Figure 7** shows the composite of MAM(0), JJA(0), SON(0), D(0)JF(1) mean sea surface temperature anomalies (shaded) and vertical integral of vapor flux anomalies (vector) for El Niño developing years over the tropical Indo-Pacific Ocean for periods of 1950–1978 and 1979–2018 without removing the super 1982–1983, 1997–1998, 2014–2016 events. It is evident that the three super events make the composite SST anomalies pattern in the later period fairly stronger. The result that the amplitude of the anomalous SST during a life-cycle of El Niño event in the later period is larger than that in the former period indicates the amplitude of El Niño events has increased since the 1970s. Meanwhile, the anomalous eastward water vapor fluxes during a life-cycle of El Niño event are also stronger in the later period. El Niño events in the former period show the maximum SST anomalies appearing in the equatorial eastern Pacific, with anomalous equatorial eastward vapor flux over

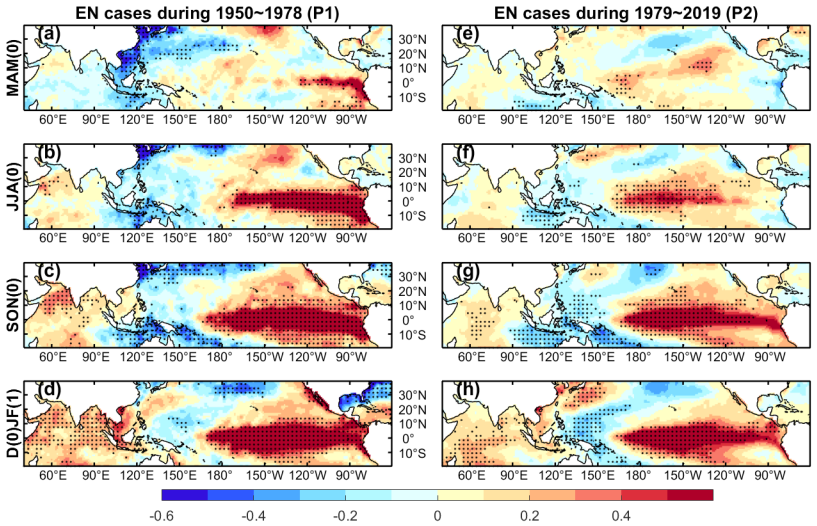

Figure 6. Composite of MAM(0), JJA(0), SON(0), D(0)JF(1) mean sea surface temperature anomalies for El Niño developing years (1982–1983, 1997–1998, 2014–2016 events are removed) during periods of 1950–1978 (left panel) and 1979–2019 (right panel). The dotted areas indicate composite mean SST anomalies exceed 95% confidence level. The SSTA data are derived from HadISST product and has been detrended.

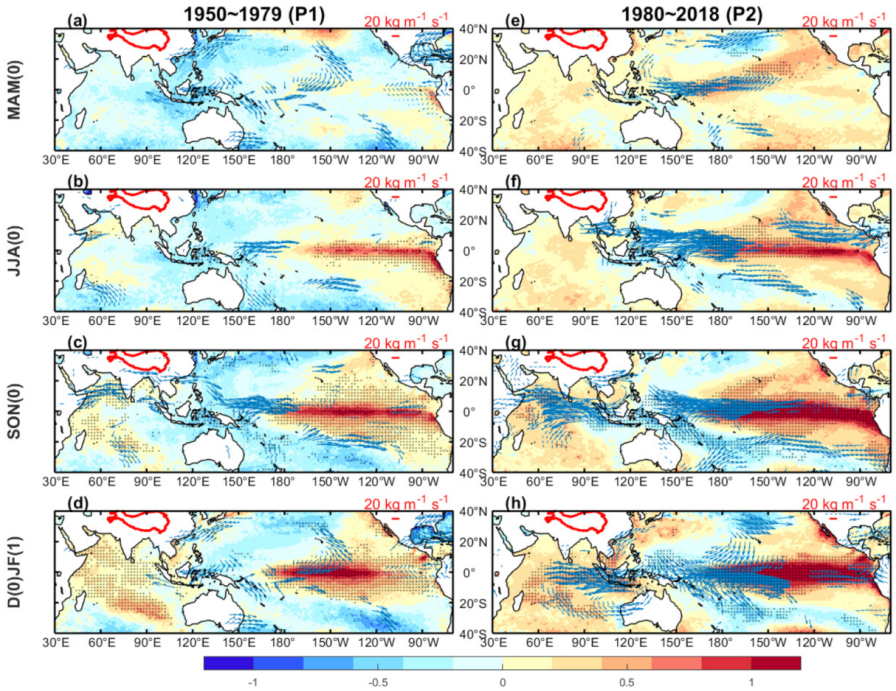

Figure 7. Same as **Figure 6**, but for composition including 1982–1983, 1997–1998, 2014–2016 events, and the concurrent vapor transport anomalies are shown.

the longitude range of 150°E–180°. In the later period, El Niño events show the initial maximum SST anomalies in spring appearing in the central Pacific and extra-equatorial of eastern Pacific and extending to central and eastern Pacific, with much stronger equatorial eastward anomalous vapor flux from 130°E to 150°W. The quantitative analysis on the detailed impact of three super El Niño events of 1982–1983, 1997–1998, and 2014–2016 events should be further investigated.

Considering the monsoon Asia region covering the TP and surrounding plateau-monsoon regions, **Figure 8** shows the composite anomalies of JJA(0) mean total column water vapor and vertical integral of vapor flux for El Niño developing years in the Large Triangular Sector of the plateau-monsoon region (TP-LTS) for the two sub-periods. In the former period, the significant anomalous water vapor flux appears in the northwest of the Indian Peninsula, with an anomalous anticyclone and strong anomalous vapor transport taking water vapor from the Indian Peninsula and Arab Sea to Africa. In the later period, significant anomalous water vapor flux appears in the Asia-Pacific region, with large amounts of water vapor being taken from the south and east of Asia, including the TP surrounding regions, to the tropical Pacific. An anomalous cyclone forms over the region surrounding Bengal, gathering much vapor over the Indo-China Peninsula. Meanwhile, the southward flow from north China to Beibu Gulf meets the eastward flow over the South China Sea, bringing large amounts of water vapor to southern China. This can well explain the correlation pattern shown in **Figure 3** and is consistent with the previous study.

4.4 Changes in vertical motion of air

Except for the horizontal transport of water vapor, the large-scale topography force can also reflect the vapor transport into or out of TP. So we examine the vertical structure of air motion during El Niño developing summer using ERA5 vertical velocity data. The negative (positive) values of vertical velocity indicate upward/ascent (downward/subsidence) air motion in the ERA5 dataset.

Figure 9 shows the latitude-pressure profiles of composite anomalies of JJA(0) mean vertical velocity for El Niño developing years averaged in

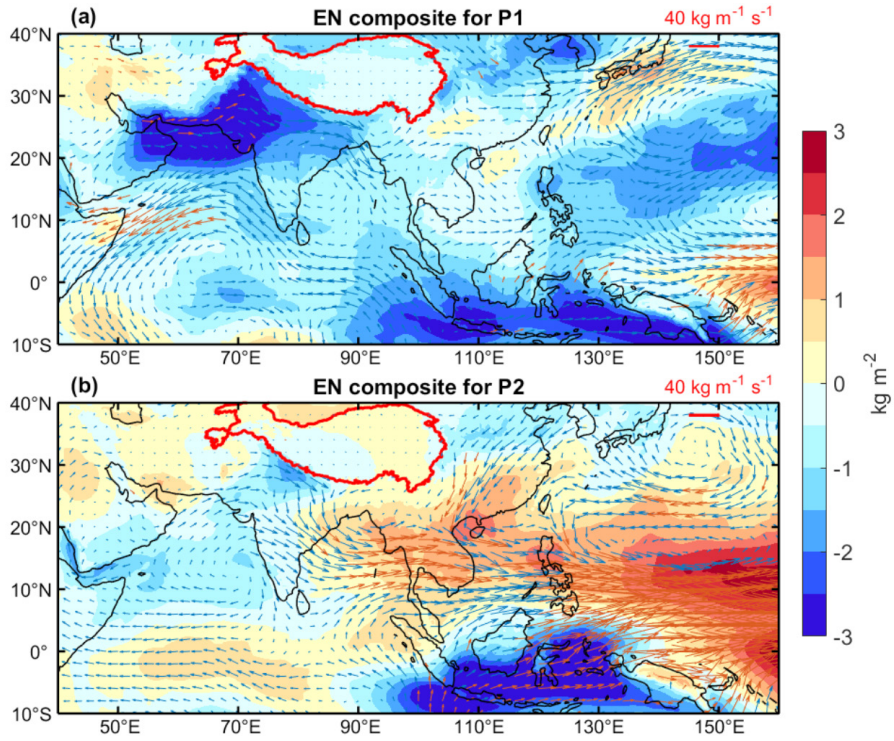

Figure 8. Composite of JJA(0) total column water vapor (shaded) and vertical integral of vapor flux (vector) anomalies for El Niño developing years including 1982–1983, 1997–1998, 2014–2016 events in the plateau monsoon region for the two periods. Significant water vapor flux anomalies at 90% confidence level are shown in red vectors.

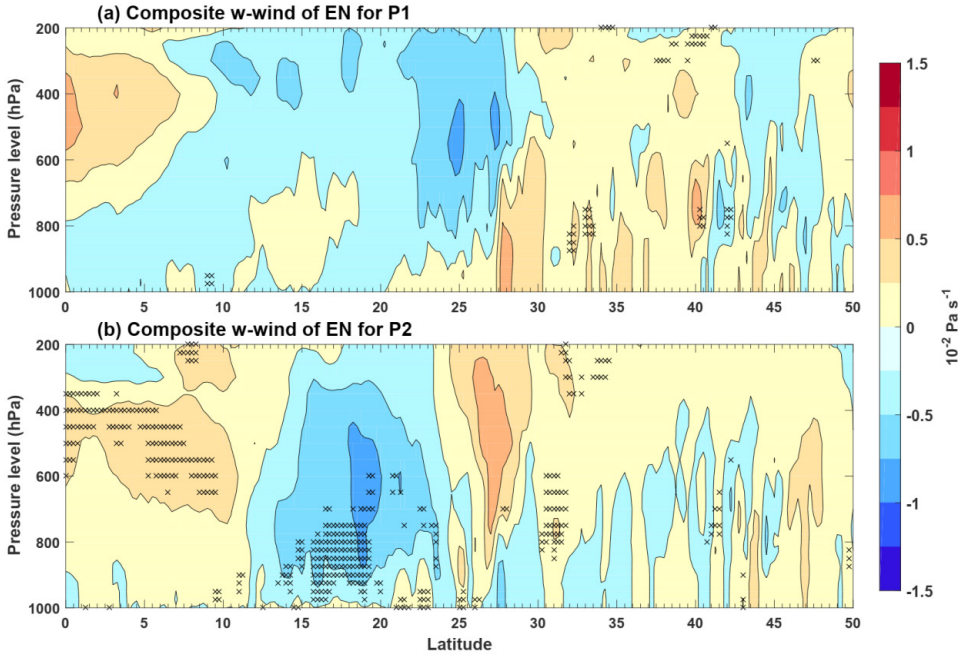

Figure 9. Latitude-pressure profile of composite JJA(0) vertical velocity (shaded) anomalies for El Niño developing years averaged in the longitude range of 80°–110°E for two sub-periods. The 'x' marked areas indicate composite vertical velocity anomalies exceed 90% confidence level. The negative values of vertical velocity indicate upward/ascent air motion, while the positive values indicate downward/subsidence motion.

the longitude range of 80°–110°E (from west to east of TP) for the two sub-periods, with latitude range from the equator to 50°N. There is no significant vertical motion at the south edge of TP (25°–30°N) in the former period, with anomalous upward motion at the south side of TP. In the later period, significant strong and deep anomalous upward motion can be seen at 15°–23°N, and, by contrast, anomalous subsidence motion appears at the south side of TP.

For changes on the longitude dimension, **Figure 10** shows the longitude-pressure profiles of composite anomalies of JJA(0) mean vertical velocity for El Niño developing years averaged in the latitude range of 27.5°–35°N (from south to north of TP) for the two sub-periods, with a longitude range of 60°–140°E. Distinct strong and deep downward motions can be seen at the western side (about 80°E) and eastern side (about 110°E) in the later period, indicating weakening of the water vapor flow climbing up to TP at both eastern and western.

5. Discussion and conclusions

In this study, we investigated the relationship between the variability of Tibetan Plateau summer precipitation and ENSO during the 1950–2019 period. The TP mean summer precipitation is significantly associated with the Niño-3.4 index, showing negative correlation coefficients from spring in the developing year to spring in the following year. However, such relations are unstable. Using a 21-year running correlation method, it is evident that the relation between the normalized TP mean summer precipitation and Niño-3.4 index has experienced an interdecadal change since the late 1980s, indicating that, for any 21-year window period after the late 1970s, the TP mean summer precipitation and Niño-3.4 index significantly correlate with each other. Both the CRU and ERA5 datasets support this point, and the mature phase winter Niño-3.4 index shows consistent results. Thus, we choose 1950–1978 (the

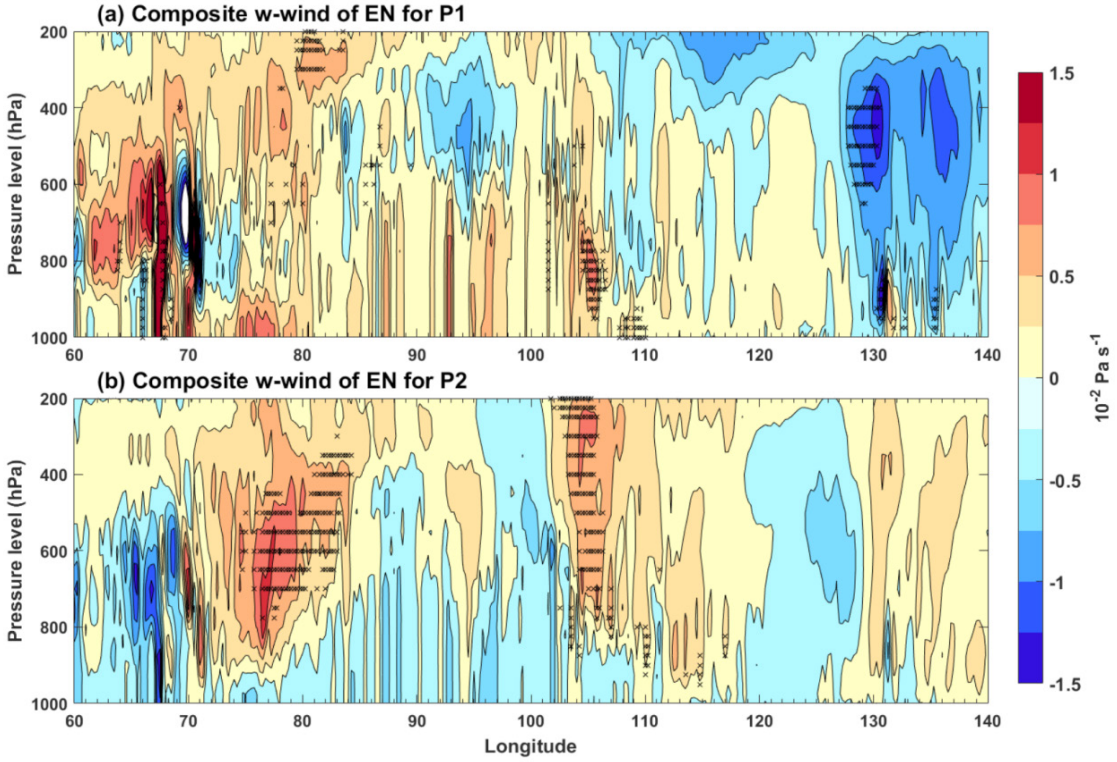

Figure 10. Same as **Figure 9**, but for the longitude-pressure profile averaged in the latitude range of 27.5°–35°N.

former period) and 1979–2019 (the latter period) as the two sub-periods to understand the different relationships between TP summer rainfall and tropical Indo-Pacific SST variabilities.

By analyzing the changes in ENSO intensity, ENSO pattern, moisture transport, and vertical motion in the two sub-periods, we discuss the possible mechanisms for the interdecadal change in the relationship between TP mean summer precipitation and Niño-3.4 index. Results show that, in the later period of 1979–2019, both the interdecadal strengthening of ENSO intensity and the SSTA patterns have an impact on the ENSO-induced TP summer precipitation anomalies. In the later period, significant anomalous water vapor flux appears in the Asia-Pacific region, with large amounts of water vapor being taken from the south and east of Asia, including the TP surrounding regions, to the tropical Pacific. Meanwhile, anomalous subsidence motion appears on the south side of TP. Distinct strong and deep downward anomalies can be seen at the western side and eastern side in the later period, indicating a weakening of the water vapor flow to TP.

For research on the Third Pole, this work is preliminary. We mainly present a result that the relations between TP summer precipitation and ENSO have experienced an interdecadal change since the late 1970s. How the strengthened ENSO amplitude influences the TP climate, and what role the central Pacific type of El Niño plays in modulating the climate over TP and the surrounding regions, needs further investigation. Another point is the role of the Indian Ocean during the El Niño developing stage [46]. Strong anomalous westward vapor fluxes can be seen in the Indian Ocean for the later period, and the season-dependent characteristic of SST anomalies in the Indian Ocean is not stable among the two sub-periods. In addition, the impact of local evaporation and evapotranspiration changes over TP on summer precipitation should also be investigated.

Author Contributions

All authors contributed to the study's conception and design. Material preparation, data collection and analysis were performed by Ning Cao, and Weinan Jiang. The first draft of the manuscript was written by Weinan Jiang and Ning Cao. Riga Aze and Jianjun Xu conceived and reviewed the manuscript and edited the text. Ning Cao and Jianjun Xu were responsible for the funding acquisition. All authors read and approved the final manuscript.

Conflict of Interest

The authors declare no conflict of interest.

Funding

This research was funded by the Second Tibetan Plateau Scientific Expedition and Research (STEP) program (2019QZKK0105), the Shenzhen Science and Technology Program (JCYJ20210324131810029), the National Natural Science Foundation of China (72293604, 42275017), the Guangdong Provincial College Innovation Team Project (060313452101), the Program for scientific research start-up funds of Guangdong Ocean University (R17056).

Acknowledgments

The authors acknowledge the teams from the University of East Anglia's Climatic Research Unit (CRU), the ECMWF, and the Hadley Centre for providing their data products. We extend our sincere thanks to the anonymous reviewers for their valuable constructive comments and suggestions, which have improved the quality of the manuscript.

References

[1] Yao, T., Liu, Y., Zhao, H., et al., 2011. Tibetan plateau. Encyclopedia of snow, ice and glaciers. Springer: Dordrecht. pp. 1172–1175. DOI: https://doi.org/10.1007/978-90-481-2642-2_578

[2] Qiu, J., 2008. China: The third pole. Nature. 454, 393–396. DOI: https://doi.org/10.1038/454393a

[3] Immerzeel, W.W., Van Beek, L.P.H., Bierkens, M.F.P., 2010. Climate change will affect the Asian Water Towers. Science. 328(5984), 1382–1385.
DOI: https://doi.org/10.1126/science.1183188

[4] Yao, T., Bolch, T., Chen, D., et al., 2022. The imbalance of the Asian water tower. Nature Reviews Earth & Environment. 3, 618–632.
DOI: https://doi.org/10.1038/s43017-022-00299-4

[5] Chen, F., Zhang, J., Liu, J., et al., 2020. Climate change, vegetation history, and landscape responses on the Tibetan Plateau during the Holocene: A comprehensive review. Quaternary Science Reviews. 243, 106444.
DOI: https://doi.org/10.1016/j.quascirev.2020.106444

[6] Jiang, X., Li, Y., Yang, S., et al., 2016. Interannual variation of summer atmospheric heat source over the Tibetan Plateau and the role of convection around the western maritime continent. Journal of Climate. 29(1), 121–138.
DOI: https://doi.org/10.1175/JCLI-D-15-0181.1

[7] He, C., Wang, Z., Zhou, T., et al., 2019. Enhanced latent heating over the Tibetan Plateau as a key to the enhanced East Asian summer monsoon circulation under a warming climate. Journal of Climate. 32(11), 3373–3388.
DOI: https://doi.org/10.1175/JCLI-D-18-0427.1

[8] Luo, X., Xu, J., Li, K., 2019. A review of atmospheric heat sources over Tibetan Plateau. Guangdong Ocean University. 39, 130–136. (in Chinese).

[9] Wang, X., Pang, G., Yang, M., 2018. Precipitation over the Tibetan Plateau during recent decades: A review based on observations and simulations. International Journal of Climatology. 38(3), 1116–1131.
DOI: https://doi.org/10.1002/joc.5246

[10] Joswiak, D.R., Yao, T., Wu, G., et al., 2013. Ice-core evidence of westerly and monsoon moisture contributions in the central Tibetan Plateau. Journal of Glaciology. 59(213), 56–66.
DOI: https://doi.org/10.3189/2013JoG12J035

[11] Yao, T., Masson-Delmotte, V., Gao, J., et al., 2013. A review of climatic controls on $\delta^{18}O$ in precipitation over the Tibetan Plateau: Observations and simulations. Reviews of Geophysics. 51(4), 525–548.
DOI: https://doi.org/10.1002/rog.20023

[12] Yao, T., Piao, S., Shen, M., et al., 2017. Chained impacts on modern environment of interaction between Westerlies and Indian monsoon on Tibetan Plateau. Bulletin of Chinese Academy of Sciences. 32(9), 976–984. (in Chinese).
DOI: https://doi.org/10.16418/j.issn.1000-3045.2017.09.007

[13] Li, G., Chen, H., Xu, M., et al., 2022. Impacts of topographic complexity on modeling moisture transport and precipitation over the Tibetan plateau in summer. Advances in Atmospheric Sciences. 39, 1151–1166.
DOI: https://doi.org/10.1007/s00376-022-1409-7

[14] Dong, N., Xu, X., Cai, W., et al., 2022. Comprehensive effects of interdecadal change of sea surface temperature increase in the Indo-Pacific Ocean on the warming-wetting of the Qinghai-Tibet Plateau. Scientific Reports. 12, 22306.
DOI: https://doi.org/10.1038/s41598-022-26465-8

[15] Jiang, X., F. Cai, Z. Li, et al., 2023. The westerly winds control the zonal migration of rainy season over the Tibetan Plateau. Communications Earth & Environment. 4, 363.
DOI: https://doi.org/10.1038/s43247-023-01035-6

[16] Klein, S.A., Soden, B.J., Lau, N., 1999. Remote sea surface temperature variations during ENSO: Evidence for a tropical atmospheric bridge. Journal of Climate. 12(4), 917–932.
DOI: https://doi.org/10.1175/1520-0442(1999)012<0917:RSSTVD>2.0.CO;2

[17] Xie, S., Kosaka, Y., Du, Y., et al., 2016. Indo-western Pacific Ocean capacitor and coherent climate anomalies in post-ENSO summer: A review. Advances in Atmospheric Sciences.

33, 411–432.
DOI: https://doi.org/10.1007/s00376-015-5192-6

[18] He, S., Yu, J., Yang, S., et al., 2020. ENSO's impacts on the tropical Indian and Atlantic Oceans via tropical atmospheric processes: Observations versus CMIP5 simulations. Climate Dynamics. 54, 4627–4640.
DOI: https://doi.org/10.1007/s00382-020-05247-w

[19] Wu, R., Zhu, P., 2021. Interdecadal change in the relationship of Indochina Peninsula May precipitation to ENSO. International Journal of Climatology. 41(4), 2441–2455.
DOI: https://doi.org/10.1002/joc.6968

[20] Ren, Q., Jiang, X., Shi, R., 2023. The enhanced relationship between summer rainfall over the eastern Tibetan Plateau and sea surface temperature in the tropical Indo-Pacific Ocean. Climate Dynamics. 60, 4017–4031.
DOI: https://doi.org/10.1007/s00382-022-06509-5

[21] Xie, S., Hu, K., Hafner, J., et al., 2009. Indian ocean capacitor effect on Indo-Western Pacific climate during the summer following El Niño. Journal of Climate. 22(3), 730–747.
DOI: https://doi.org/10.1175/2008JCLI2544.1

[22] Du, Y., Xie, S.P., Huang, G., et al., 2009. Role of air-sea interaction in the long persistence of El Niño-induced north Indian Ocean warming. Journal of Climate. 22(8), 2023–2038.
DOI: https://doi.org/10.1175/2008JCLI2590.1

[23] Chen, X., You, Q., 2017. Effect of Indian Ocean SST on Tibetan Plateau precipitation in the early rainy season. Journal of Climate. 30(22), 8973–8985.
DOI: https://doi.org/10.1175/JCLI-D-16-0814.1

[24] Park, J., Kug, J., Yang, Y., et al., 2023. Distinct decadal modulation of Atlantic-Niño influence on ENSO. npj Climate and Atmospheric Science. 6, 105.
DOI: https://doi.org/10.1038/s41612-023-00429-9

[25] Si, Y., Jin, F., Yang, W., et al., 2023. Change and teleconnections of climate on the Tibetan Plateau. Stochastic Environmental Research and Risk Assessment. 37, 4013–4027.
DOI: https://doi.org/10.1007/s00477-023-02492-3

[26] Nagura, M., Konda, M., 2007. The seasonal development of an SST anomaly in the Indian ocean and its relationship to ENSO. Journal of Climate. 20(1), 38–52.
DOI: https://doi.org/10.1175/JCLI3986.1

[27] Lei, Y., Zhu, Y., Wang, B., et al., 2019. Extreme lake level changes on the Tibetan Plateau associated with the2015/2016 El Niño. Geophysical Research Letters. 46(11), 5889–5898.
DOI: https://doi.org/10.1029/2019GL081946

[28] Hu, S., Zhou, T., Wu, B., 2021. Impact of developing ENSO on Tibetan plateau summer rainfall. Journal of Climate. 34(9), 3385–3400.
DOI: https://doi.org/10.1175/JCLI-D-20-0612.1

[29] Liu, M., Ren, H.L., Wang, R., et al., 2023. Distinct impacts of two types of developing El Niño-Southern oscillations on Tibetan plateau summer precipitation. Remote Sensing. 15(16), 4030.
DOI: https://doi.org/10.3390/rs15164030

[30] Ashok, K., Behera, S.K., Rao, S., et al., 2007. El Niño Modoki and its possible teleconnection. Journal of Geophysical Research. 112(C11).
DOI: https://doi.org/10.1029/2006JC003798

[31] Yeh, S., Kug, J., Dewitte, B., et al., 2009. El Niño in a changing climate. Nature. 461, 511–514.
DOI: https://doi.org/10.1038/nature08316

[32] Lee, T., McPhaden, M.J., 2010. Increasing intensity of El Niño in the central-equatorial Pacific. Geophysical Research Letters. 37(14).
DOI: https://doi.org/10.1029/2010GL044007

[33] Liu, Y., Cobb, K., Song, H., et al., 2017. Recent enhancement of central Pacific El Niño variability relative to last eight centuries. Nature Communications. 8, 15386.
DOI: https://doi.org/10.1038/ncomms15386

[34] Freund, M.B., Henley, B.J., Karoly, D.J., et al., 2019. Higher frequency of Central Pacific El Niño events in recent decades relative to past centuries. Nature Geoscience. 12, 450–455.

DOI: https://doi.org/10.1038/s41561-019-0353-3

[35] Li, G., Gao, C., Xu, B., et al., 2021. Strengthening influence of El Niño on the following spring precipitation over the Indochina Peninsula. Journal of Climate. 34(14), 5971–5984.
DOI: https://doi.org/10.1175/JCLI-D-20-0940.1

[36] Gao, C., Li, G., Chen, H., et al., 2020. Interdecadal change in the effect of spring soil moisture over the Indo-China Peninsula on the following summer precipitation over the Yangtze River Basin. Journal of Climate. 33(16), 7063–7082.
DOI: https://doi.org/10.1175/JCLI-D-19-0754.1

[37] Chen, L., Li, G., 2022. Interdecadal change in the relationship between El Niño in the decaying stage and the central China summer precipitation. Climate Dynamics. 59, 1981–1996.
DOI: https://doi.org/10.1007/s00382-022-06192-6

[38] Li, G., Gao, C., Lu, B., et al., 2021. Inter-annual variability of spring precipitation over the Indo-China Peninsula and its asymmetric relationship with El Niño-Southern Oscillation. Climate Dynamics. 56, 2651–2665.
DOI: https://doi.org/10.1007/s00382-020-05609-4

[39] Harris, I., Osborn, T.J., Jones, P., et al., 2020. Version 4 of the CRU TS monthly high-resolution gridded multivariate climate dataset. Scientific Data. 7, 109.
DOI: https://doi.org/10.1038/s41597-020-0453-3

[40] Hersbach, H., Bell, B., Berrisford, P., et al., 2023. ERA5 monthly averaged data on pressure levels from 1940 to present. Copernicus Climate Change Service (C3S) Climate Data Store (CDS).
DOI: https://doi.org/0.24381/cds.6860a573

[41] Hersbach, H., Bell, B., Berrisford, P., et al., 2020. The ERA5 global reanalysis. Quarterly Journal of the Royal Meteorological Society. 146(730), 1999–2049.
DOI: https://doi.org/10.1002/qj.3803

[42] Rayner, N.A., Parker, D.E., Horton, E.B., et al., 2003. Global analyses of sea surface temperature, sea ice, and night marine air temperature since the late nineteenth century. Journal of Geophysical Research. 108(D14).
DOI: https://doi.org/10.1029/2002JD002670

[43] Gong, Y., Li, T., Chen, L., 2020. Interdecadal modulation of ENSO amplitude by the Atlantic multi-decadal oscillation (AMO). Climate Dynamics. 55, 2689–2702.
DOI: https://doi.org/10.1007/s00382-020-05408-x

[44] Hong, C., Li, T., Ho, L., et al., 2010. Asymmetry of the Indian Ocean Basinwide SST Anomalies: Roles of ENSO and IOD. Journal of Climate. 23(13), 3563–3576.
DOI: https://doi.org/10.1175/2010JCLI3320.1

[45] Xu, X.D., Dong, L.L., Zhao, Y., et al., 2019. Effect of the Asian Water Tower over the Qinghai-Tibet Plateau and the characteristics of atmospheric water circulation. Chinese Science Bulletin. 64(27), 2830–2841. (in Chinese).

[46] Wu, X., Li, G., Jiang, W., et al., 2021. Asymmetric relationship between ENSO and the tropical Indian Ocean summer SST anomalies. Journal of Climate. 34(14), 5955–5969.
DOI: https://doi.org/10.1175/JCLI-D-20-0546.1

BILINGUAL PUBLISHING GROUP

Journal of Atmospheric Science Research

https://journals.bilpubgroup.com/index.php/jasr/index

ARTICLE

Seasonal Variability of Rainfall and Thunderstorm Patterns in Kenya

Mary Kurgat**, **Wilson Gitau

Department of Earth and Climate Sciences, University of Nairobi, Nairobi, 00100-30197, Kenya

ABSTRACT

This paper presents an analysis of spatial and temporal variation of rainfall and thunderstorm occurrence over Kenya from January 1987 to December 2017. The meteorological data used were obtained from the Kenya Meteorological Department (KMD) for the same period. This included the monthly thunderstorm occurrences and rainfall amounts of 26 synoptic stations across the country. The characteristics of monthly, seasonal and annual frequency results were presented on spatial maps while Time series graphs were used to display the pattern for annual cycle, seasonal variations and the inter-annual variability of rainfall amounts and thunderstorm occurrences. A well-known non-parametric statistical method Mann Kendall (MK) trend test was used to determine and compare the statistical significance of the trends. Thunderstorm frequencies over the Eastern, Central and Coast regions of the country showed a bimodal pattern with high frequencies coinciding with March-April-May (MAM) and October-November-December (OND) rainy seasons. Very few thunderstorm days were detected over June-July-August (JJA) season. The areas to the western part of the country, near Lake Victoria, had the highest thunderstorm frequencies in the country over the three seasons: MAM, JJAS and OND. The annual frequency showed a quasi-unimodal pattern. These places near Lake Victoria showed significantly increasing thunderstorm trends during the MAM and OND seasons irrespective of the rainfall trends. This shows the effects of Lake Victoria over these areas, and it acts as a continuous source of moisture for thunderstorm formation. However, most stations across the country showed a reducing trend of thunderstorm frequency during MAM and JJA seasons. The importance of these findings is that they could support various policy makers, and users of climate information, especially in the agriculture and aviation industries.

Keywords: Rainfall; Thunderstorm; Lake Victoria; Kenya; Mann Kendall

*CORRESPONDING AUTHOR:

Mary Kurgat, Department of Earth and Climate Sciences, University of Nairobi, Nairobi, 00100-30197, Kenya; Email: mcrotich2000@yahoo.com

ARTICLE INFO

Received: 11 December 2023 | Revised: 15 January 2024 | Accepted: 28 January 2024 | Published Online: 29 January 2024

DOI: https://doi.org/10.30564/jasr.v7i1.6144

CITATION

Kurgat, M., Gitau, W., 2024. Seasonal Variability of Rainfall and Thunderstorm Patterns in Kenya. Journal of Atmospheric Science Research. 7(1): 106–117. DOI: https://doi.org/10.30564/jasr.v7i1.6144

1. Introduction

Thunderstorms are usually associated with deep convective clouds in Kenya [1]. Virtually, these thunderstorm clouds can occur in any month due to the large water bodies and the position of the country on the equator. Close to the equator, there are light winds, intense heating and low-level convergence. The rising warm air causes instability in the atmosphere. It cools, condenses and produces clouds. Deep convective clouds cause thunderstorms to develop due to the release of big quantities of latent heat into the atmosphere. Audible thunder is a sequence of degenerated shock waves formed by the massive expansion of air on the intensively heated lightning channel, during a lightning flash [2].

A thunderstorm day is defined as a day on which thunder is heard at an observing station [3,4]. It is recorded as such regardless of the actual number of thunderstorms heard on that day and therefore the records do not give information on the frequency of occurrence of individual thunderstorms or their time of occurrence. It should however be noted that lightning without thunder is not recorded as a thunderstorm day, this is because light travels faster than sound at a speed of 2.998×10^8 m/s and sound at 3.43×10^2 m/s. It is possible to observe lighting outside the station radius. The condition that thunder must be heard restricts the covered area to a circle with a maximum radius of about 20 km by each observing point [5]. It is also possible for two neighboring stations to hear and report the same thunderstorm if they are within a 35 km distance apart.

Changnon et al. (1984) [6] investigated the temporal distribution of global thunder days from 90 stations in Northern America and 131 stations across the world. The results suggested that the variations in thunder days' frequencies are due to a major shift in large-scale circulation oscillations. Enno et al. (2014) [7] in a study of the long-term changes thunder days frequency over the Baltic countries noted that a long-term reduction in the Thunderstorm Days frequency goes with an augmented frequency of northerly Circulation Weather Types (CWTs) that are negative for thunderstorm development. Meanwhile, the frequency of southerly and easterly CWTs that are positive to thunderstorm formation decreased.

In the central United States, the study of contrails showed that there was an upsurge in cloudiness and a reduction in sunshine from the 1930s at times and areas where thunderstorm frequencies seemingly reduced. Such variations in cloudiness and their causes may be pertinent and connected to the reduction in thunderstorms because high cloudiness should, on average, deter convective activity and thunderstorm growth [6,8]. This current study needs to investigate the variations of thunderstorms during seasons of cloudiness and sunshine.

In a study on the distribution of monthly and annual frequency of thunderstorm days over East Africa. Chaggar (1977) [5] reported that in March-April-May there is a slight northward movement in the patterns of the frequency of thunderstorm days but the maximum frequency is in the area east and north of Lake Victoria into Western Kenya. There is a decrease in May over most of Kenya except the western areas. A general reduction in most parts is in June and July. The study was done over 40 years ago using sparse data observed only during daylight.

While forecasting thunderstorms and detection of convective features in their early stages is important, it is still difficult to forecast thunderstorms without Meteorological tracking and detection systems. One of the objectives of Sendai Framework 2015–2030 is to mainstream and integrate Disaster Risk Reduction (DRR) within and across all sectors for sustainable development. A thunderstorm is the most common weather-related hazard, and its impact causes death, damage to property and loss of revenue especially to the airlines. Weather-related delays interfere with the organization of flight schedules and cause additional operational costs to the airlines [9]. It also causes inconvenience to travelers.

Understanding where and when thunderstorms are likely to occur is crucial in issuing early warnings, to avoid disaster. An achievement of relatively higher skill and accuracy in issuing meteorological forecasts and advisories to stakeholders results in better short and long term planning. Proper forecast-

ing with lead time is an important factor in preventing local calamities from saving people [10].

Maloba (2015) [11] carried out a study on temporal and spatial characteristics of thunderstorms over the region east of Lake Victoria Basin in Kenya over the period 2000 to 2013 and established that the year 2016 MAM season recorded the highest frequency of thunderstorm occurrence during the study period while the lowest occurrence was 2007 for both MAM and September-October-November (SON) seasons.

Ayugi et al. (2016) [12] analysed the monthly, seasonal and annual scales of rainfall variations over Kenya data from 1971 to 2010. In agreement with Ongoma and Chen (2017) [13], the findings showed that among the two seasons, there was a noticeable decrease in rainfall over the MAM season and a slight increase over the OND season. Further results showed an overall significant decrease in annual rainfall over Kenya. Later studies have shown that there were some increasing trends over the short rainfall season (OND) and these were credited to Sea Surface Temperatures (SST) warming in the western Indian Ocean [14].

A thunderstorm is made up of two or more thunderstorm cells and each cell has three stages of development, namely, the cumulus stage, the mature stage and the dissipation stage [15]. An average thunderstorm has a horizontal diameter of about 24 kilometers and depending on the conditions present may take about 30 minutes to complete the life cycle from development to decay.

Local circulations such as Lake Victoria, mountains and strong solar insolation cause steep temperature gradients between the water surface and the surrounding high grounds as a result of the overhead sun. These give rise to strong mesoscale circulations over the region. Deep convective systems are initiated around 0700 UTC in the morning to 1000 UTC in the afternoon and peak during the late afternoon and evening times around 1200 UTC to 1600 UTC [16].

Eastern Africa exhibits bimodal rainfall consisting of long rains (March–May) and short rains (October–December) and this is observed in Kenya as a country in East Africa. Remote teleconnections, namely the El Niño—Southern Oscillation and the Indian Ocean Dipole, exert a dominant influence on interannual variability [17]. The number, duration and timing of these rainfall seasons vary, driven principally by the movement of the intertropical convergence zone (ITCZ) [18].

The core objective of this study is to evaluate the recent thunderstorm climatology over Kenya, determine the trends and compare it with rainfall occurrence. The results obtained confirmed that higher concentrations of thunderstorms are to the West and over the highland parts of the country and thunderstorm days' occurrence can be broadly classified as either bi-modal or quasi-uni-modal in Kenya. Besides enhancement of the existing knowledge, the evaluation of thunderstorm climatology in Kenya aims to give a better understanding of where, when and how thunderstorms are likely to occur and their possible impacts. This will possibly result in a policy shift towards the improvement in the forecasting experience and exchange of information. Improved accuracy in meteorological forecasts and weather advisories, therefore, leads to reduced costs of operations, enhanced profit, safety and customer satisfaction in the aviation industry.

2. Materials and methods

2.1 The study area

The study was carried out in Kenya. The country lies between 5° north and 4° south and between longitude 32° and 42° east. **Figure 1** shows the spatial distribution of the stations which were used in the analysis.

2.2 Data

The thunderstorm data and observed monthly rainfall amounts used were obtained from the Kenya Meteorological Department (KMD). It included each month of the year from January 1987 to December 2017 for the 26 synoptic stations across the country. The stations were selected according to the availability of data from the source.

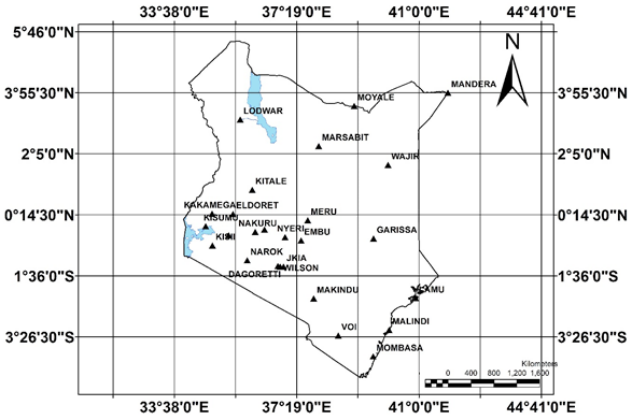

Figure 1. A map showing the location of the stations used in the study.

2.3 Estimation of missing data and homogeneity test

The arithmetic mean method (Equation (1)) was used to calculate the long-term mean, which was then used to fill the missing gaps. All the stations used in this study had missing data which was less than 10% for thunderstorm days while rainfall data had no missing data.

$$\overline{X} = \frac{1}{n}\sum x_i \tag{1}$$

where,

$\overline{X}$ = long term mean of thunderstorm days in a month;

n = number of years;

X_i = thunderstorm days in a month.

This is a technique recommended by the World Meteorological Organization (WMO) for estimating missing monthly, seasonal or annual meteorological data provided the percentage of the missing data does not exceed 10% of the total [3].

The next test was for data consistency or homogeneity test. It also checks the accuracy of data by identifying outliers or deviations from other related parameters or neighboring stations. This study adopted the Single Mass curves to assess the quality of the data. The total seasonal thunderstorm frequencies for each station were accumulated and plotted against the years. An almost straight line shows the data are homogeneous and the opposite is true [19].

2.4 Trend analysis of the thunderstorm days and rainfall

Using Mann Kendall's non-parametric trend test method [20,21], the assessment of whether there was a significant trend (at 95% confidence level) during MAM, JJA, and OND seasons, was determined for both rainfall and thunderstorm occurrences.

The MK test is used to determine statistically the significance of the decreasing and increasing trends in long-term temporal data [22]. The test is based on two hypotheses: when one is null (H_o) and the alternative which is (H_a) hypothesis. Mann-Kendall trend test interpretation was [23]:

H_o: There is no trend in the series.

H_a: There is a trend in the series.

If the computed p-value is greater than the significance level alpha = 0.05, one cannot reject the null hypothesis H_o because p > 0.05The MK formula is provided by the following Equation (2):

$$S = \sum_{i=1}^{n=1}\sum_{j=i+1}^{n} sign(x_j - x_i),\ sign(x_j - x_i) = \begin{cases} +1\ (x_j - x_i) > 0 \\ 0\ (x_j - x_i) = 0 \\ -1\ (x_j - x_i) < 0 \end{cases} \tag{2}$$

where n is the number of data points, X_j and X_i are annual values in years j and i, j. 1 and sign ($X_j - X_i$) are calculated using the equation: A positive S value indicates an upward trend, while a negative value indicates a downward trend.

The variance of the rainfall is calculated to obtain the Z value. The normal Z test statistic is calculated by Equation (3). This equation uses S–1 if S > 0, S+1 if S < 0 and Z is 0 if S = 0. A positive value of Z indicates an increasing trend. Otherwise, it indicates a downward trend.

$$Z_{MK} = \frac{S-1}{\sqrt{VAR(S)}} if S > 0$$
$$0\ if S = 0$$
$$\frac{S+1}{\sqrt{VAR(S)}} if S < 0 \tag{3}$$

The Sen's slope estimator is a test recommended by the World Meteorological Organization as part of trend detection in rainfall data F [24]. The trend is assumed to be linear and shows the quantification

of the time change and the test is not affected by the number of outliers and data errors when compared with the linear regression test. The Sen's Slope Equation (4) for a number of N data sample pairs is expressed as follows:

$$Q_i = \frac{(x_j - x_i)}{j-i}, i = 1,2,3, \ldots, N \quad (4)$$

x_j and x_i are data values at time j and i (j > i), respectively. If there are n values of x_j in the time series, there will be N = n(n-1)/2 slope estimates. The N value of Q_i is sorted from smallest to largest, then Sen's Slope used median Q_i (Qmed). A two-tailed test estimated the value of Qmed at a confidence interval of 90% and 95%, which is calculated as demonstrated in Equation (5).

$$Q_{med} = \begin{cases} Q_{\left[\frac{N+1}{2}\right]} & if\ N=odd \\ \frac{Q_{\left[\frac{N}{2}\right]} + Q_{\left[\frac{N+1}{2}\right]}}{2} & if\ N = even \end{cases} \quad (5)$$

3. Results and discussions

Out of the 36 stations of which thunderstorm datasets were considered, 26 stations had more complete sets and only 10 of them had more than 10% missing data and were therefore discarded. The rainfall data used for the same stations had no missing data and was good for comparison purposes.

The spatial distribution of thunderstorms in the country showed that higher concentrations are to the West and over the Highlands, as shown in **Figure 2**. The results in the current study are consistent with those [5,11,25,26] which showed that Western Kenya was the most thundery place.

3.1 Annual cycle

The annual cycle of the thunderstorm days showed that they can be broadly classified as either bi-modal or quasi-uni-modal. The bi-modal thunderstorm occurrence pattern was mainly observed over the North Eastern, Central and Coast regions of the country. There are two peaks: in April and November, as shown for Moyale station in **Figure 3**. This frequency coincides with the March-April-May (MAM) commonly referred to as the long rainfall season and October-November-December (OND) which is often referred to as the short rainfall season.

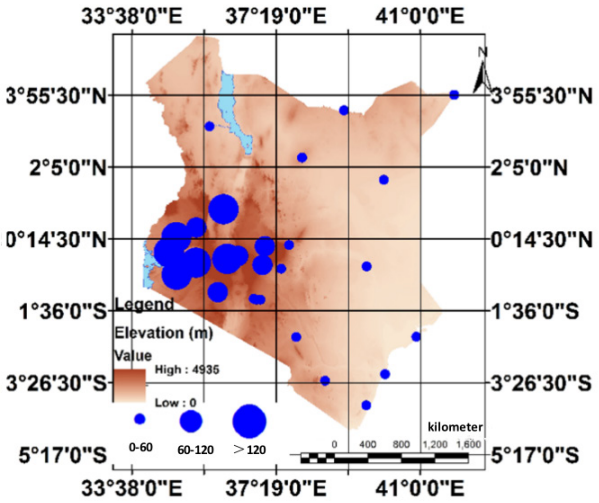

Figure 2. A map showing the spatial distribution of thunderstorms over Kenya.

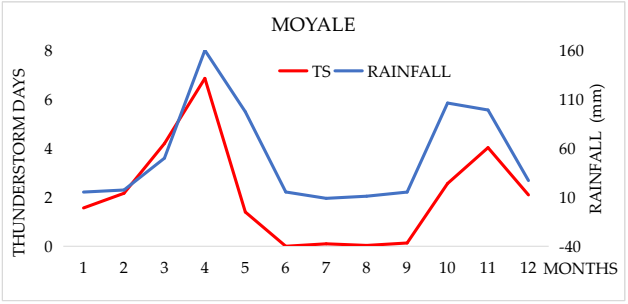

Figure 3. Annual cycle of rainfall and thunderstorms over Moyale in North-Eastern Kenya.

The quasi-uni-modal thunderstorm occurrence pattern has only one peak month but the timing of this peak varies from one location to another. This pattern was observed over the highland West of Rift Valley and the Lake Victoria region as shown in **Figure 4**. These areas to the western part of the country near Lake Victoria reported almost equal number of thunderstorms days over the three seasons: MAM, JJA and OND. The current study agrees with previous studies [5] on the maximum frequency of thunderstorm occurring over MAM in these areas. However, the previous study did not capture the varying peak months from one location to another over these areas.

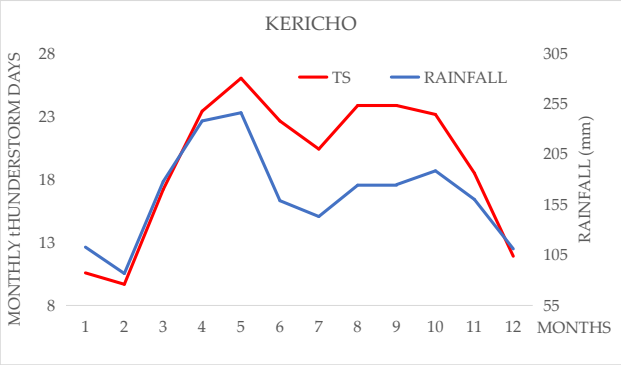

Figure 4. Annual cycle of rainfall and thunderstorms over Kericho in Highland West of Rift Valley.

3.2 Seasonal variability of rainfall and thunderstorms

During MAM season rainfall activities were reported throughout the country in varying amounts. The rainfall amounts increased towards the western parts of the country, as shown in **Figure 5**. With the availability of moisture from the long rain season, the high ground areas over the western parts of the country recorded high frequencies of thunderstorms. The terrain of an area affects thunderstorm formation, moisture tends to rush up the mountain. This is explained by **Figure 6** where the frequencies over Meru station are higher than the frequencies over Marsabit over MAM season. Meru station is influenced by Mount Kenya, and lies on the windward side of the mountain.

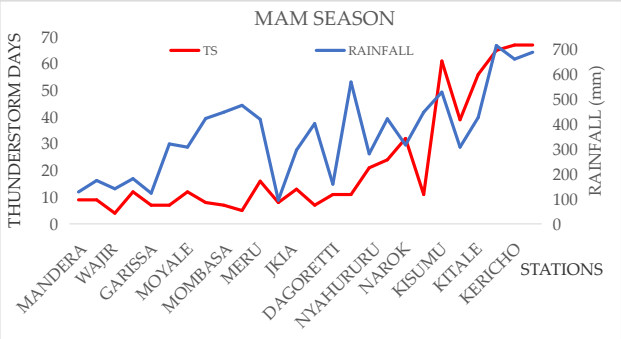

Figure 5. Seasonal variation of rainfall and thunderstorms over various stations during MAM over Kenya.

Over the June-July-August (JJA) season negligible number of thunderstorm days were reported over the Highland East of Rift Valley, North Eastern and the Coast of Kenya, as shown in **Figure 6**. Higher frequencies were observed over the highland west of Rift Valley [27]. Nakamara (1968) in the study of equatorial westerlies over East Africa showed that frequent incursions of these winds resulted in heavy thunderstorms over the Highlands of Kenya but a lee effect was evident in the regions east of the highlands.

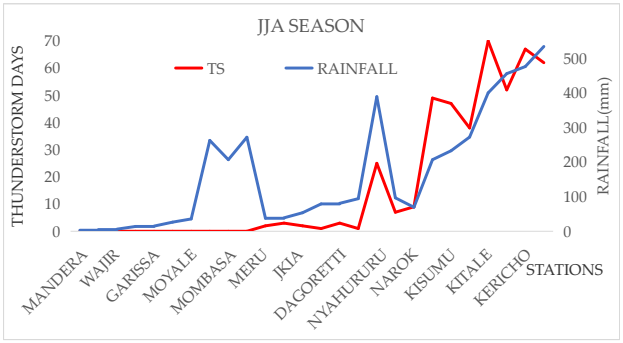

Figure 6. Seasonal variation of rainfall and thunderstorms over various stations during JJA over Kenya.

During the short rainy season (OND) the eastern half of the country reported low frequencies of Thunderstorms whereas there was a notable peak over the western part of the country. The western part of the country has a high influence from the Lake Victoria basin as its source of moisture and therefore, the latent heat over these areas is higher than the highlands in Central Kenya. The triggering mechanisms also include the orographic upslope. Even though there were peaks of rainfall frequencies over Central Kenya (Meru, Embu, Nyeri) thunderstorm frequencies were minimal, as shown in **Figure 7**.

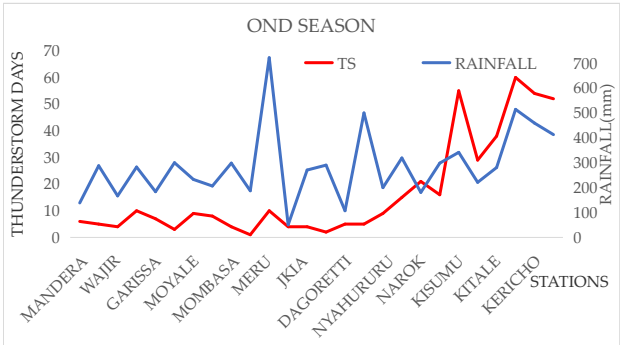

Figure 7. Seasonal variation of rainfall and thunderstorms during OND over Kenya.

3.3 Inter-annual variability of rainfall and thunderstorm

The observed thunderstorms and rainfall changed both in space and time over the study area during the period of study.

Over the North Eastern parts of the country, the thunderstorm days were mainly observed during MAM and OND rainfall seasons with slightly higher frequencies during the OND season. It also appeared to be a consistent tendency for peaks and troughs in thunderstorm frequency to coincide with the El Nino events (1987, 1991, 1992, 1994, 1997, 2002, 2004, 2006, 2009 and 2015) or La Nina events (1988, 1995, 1998, 1999, 2000, 2005, 2007, 2010, 2011, 2016 and 2017) during OND season in the northeastern parts of the country, as shown in **Figure 8**.

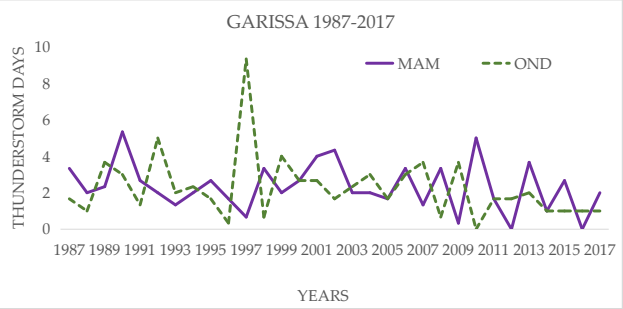

Figure 8. Inter-annual variability of thunderstorms over Garissa.

The coastal areas had a similar pattern as that of the northeastern parts but the MAM season had higher frequencies of thunderstorms than OND, as shown in **Figure 9**.

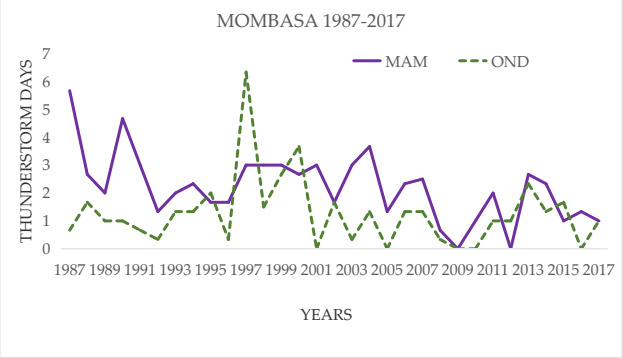

Figure 9. Inter-annual variability of thunderstorms over Mombasa.

The comparison of thunderstorm and rainfall frequencies over the coast confirms the coinciding peaks and troughs as shown in **Figure 10**.

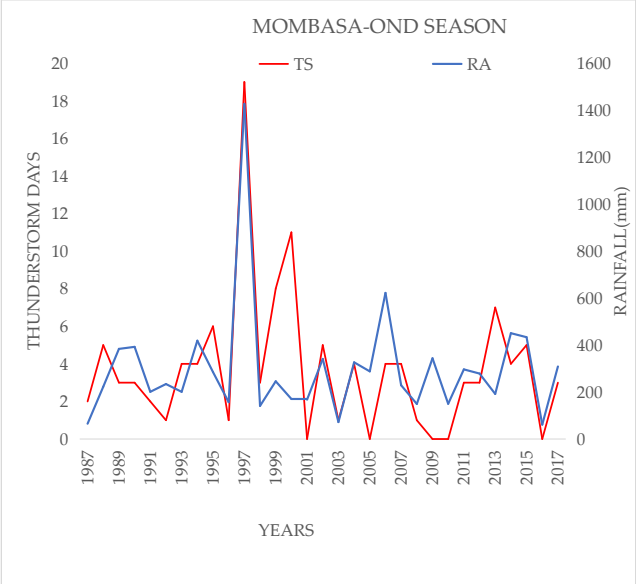

Figure 10. Inter-annual variability of thunderstorms and rainfall over Mombasa.

The analysis of thunderstorm data in areas around Lake Victoria showed that thunderstorm frequency did not vary significantly over MAM, JJA and OND rainfall seasons as shown in **Figure 11**. There were almost equal frequencies. These stations Kericho, Kakamega, Kisumu and Kisii are highly influenced by Lake Victoria which acts as a constant source of moisture.

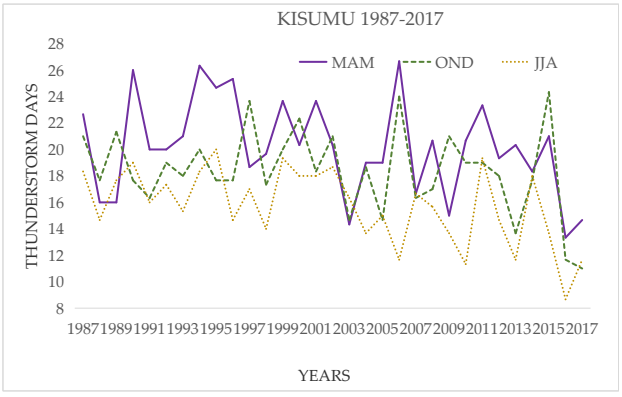

Figure 11. Inter-annual variability of thunderstorms over Kisumu.

The comparison of thunderstorm and rainfall frequencies over the same areas during the same period depicts the same pattern as shown in **Figure 12**.

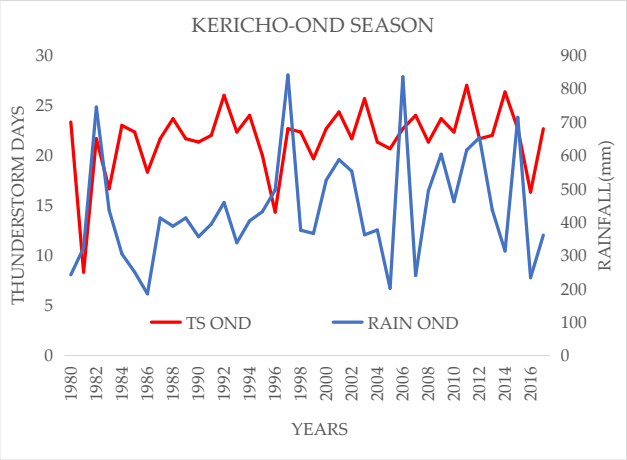

Figure 12. Inter-annual variability of thunderstorms and rainfall over Kericho.

3.4 Results of trend analysis for thunderstorms and rainfall

During the study period, thunderstorms and rainfall trends varied over different regions of the country in each season. The findings of the study confirmed previous studies that there was a noticeable decrease in rainfall over MAM and a slight increase over the OND season [13,14] as shown in **Table 1**.

During the MAM season, stations near the Lake Victoria Basin, Central and the Highland East of the Rift Valley had a non-significant reducing trend of rainfall but an increasingly significant and non-significant trend of thunderstorms. Over Northeastern and the Coastal regions, the reducing significant trends of thunderstorms agreed with the reducing non-significant trends of rainfall.

During the JJA season, areas that had a non-significant increasing trend were near Lake Victoria. The coast and the North Eastern region had a significant decreasing trend of rainfall and a non-significant trend for thunderstorms. Some stations had insignificant trends for both rainfall and thunderstorms. This was mainly observed during the JJA season over the North Eastern parts of the country and the Coastal Region.

During the OND season, western Kenya had a significantly increasing trend of thunderstorms while rainfall was increasing insignificantly. Areas where convergence occurs experience upward motion of air resulting in cloud formation. This leads to the formation of thunderstorms/precipitation if there is enough moisture and condensation nuclei [28]. Rather than the availability of moisture, the physical features (elevation) of a location contributed to thunderstorm occurrences. Though the findings of the current study on the rainfall trends over MAM and OND were agreed with the previous studies [14,29], the significance level differed, there were non-significant trends for the reducing MAM and the increasing OND rainfall trends. These are shown on the various maps (**Figure 13**).

4. Conclusions

The results obtained confirm that higher concentrations of thunderstorms are to the West and over the Highland parts of the country; areas around Lake Victoria which act as a source of moisture for thunderstorm formation. The Coastal and North Eastern regions reported the lowest frequencies of thunderstorms, this is because of the lack of moisture over the North Eastern region and the low elevation for the formation of deep convective clouds over the Coast region.

Thunderstorm days' occurrence can be broadly classified as either bi-modal or quasi-uni-modal in Kenya. The bi-modal thunderstorm occurrence pattern was mainly observed over the Eastern, Central and Coast regions and mostly coincides with the March-April-May (MAM) and October-November-December (OND) rainfall seasons. The quasi-unimodal thunderstorm occurrence pattern was observed over the Highland West of Rift Valley and the Lake Victoria region. These areas reported almost equal numbers of thunderstorm days from March to December.

Both significant and non-significant thunderstorm and rainfall trends were observed during all three seasons. For rainfall, both MAM and JJA seasons had decreasing trends over most stations. However, the decrease for the MAM season was not statistically significant. OND season showed an increasing trend over most stations, though it was not signifi-

Table 1. Thunderstorms trend values and their corresponding statistics.

	MAM						JJA				OND			
	Lat	**Lon**	**Trend**	**p value**	**Tau**	**Gradient**	**Trend**	**p value**	**Tau**	**Gradient**	**Trend**	**p value**	**Tau**	**Gradient**
Dagoretti corner	**–1.30**	**36.75**	▲	0.078	0.23	0.063	▲	0.063	0.253	0.021	▲	0.115	0.208	0.04
Jkia	**–1.32**	**36.92**	▼	0.102	–0.211	–0.083	▼	0.005	–0.379	–0.028	▼	0.031	–0.288	–0.037
Eldoret	**0.27**	**35.40**	▲	0.079	0.228	0.128	▼	0.932	0.013	0.000	▲	0.002	0.409	0.133
Wilson	**–1.32**	**36.82**	▼	0.959	–0.009	0.000	▼	0.453	–0.107	0.000	▲	0.888	–0.022	0.000
Embu	**–0.53**	**37.45**	▼	0.056	–0.248	–0.100	▼	0.655	–0.069	0.000	▼	0.572	–0.076	0.000
Meru	**0.08**	**37.65**	▲	0.798	0.035	0.000	▲	0.936	–0.014	0.000	▼	0.645	–0.062	–0.013
Nyeri	**–0.43**	**36.97**	▲	0.015	0.315	0.104	▲	0.111	0.210	0.037	▲	0.081	0.230	0.067
Nyahururu	**–0.20**	**36.35**	▲	0.932	0.013	0.011	▼	0.529	–0.083	–0.058	▲	0.124	0.202	0.044
Garissa	**–0.47**	**39.63**	▼	0.192	–0.173	–0.033		0.968	0.012	0.000	▼	0.136	–0.197	–0.039
Mandera	**3.93**	**41.87**	▼	0.000	–0.464	–0.146	▼	0.099	–0.256	0.000	▼	0.265	–0.148	–0.021
Marsabit	**2.32**	**37.98**	▼	0.003	–0.394	–0.080	▼	0.358	–0.126	0.000	•			
Moyale	**3.53**	**39.05**	▼	0.054	–0.251	–0.095	▼	0.920	-0.020	0.000	▼	0.109	–0.209	–0.058
Wajir	**1.75**	**40.07**	▲	0.361	0.123	0.012	•				▼	0.668	0.059	0.000
Makindu	**–2.28**	**37.83**	▼	0.026	–0.291	–0.078	•	1.000	0.004	0.000	▼	0.337	–0.128	–0.019
Malindi	**–3.23**	**40.10**	▼	0.001	–0.436	–0.083	▲	0.810	0.042	0.000	▼	0.311	–0.150	0.000
Mombasa	**–4.03**	**39.62**	▼	0.006	–0.364	–0.061	▼	0.240	–0.186	0.000	▼	0.503	–0.091	0.000
Kakamega	**0.28**	**34.77**	▲	0.658	0.059	0.024	▼	0.798	–0.035	0.000	▲	0.022	0.296	0.188
Voi	**–3.40**	**38.57**	▼	0.150	–0.190	–0.053	•				▲	0.645	0.062	0.012
Lodwar	**3.12**	**35.62**	▼	0.036	–0.274	–0.067	▲	0.205	0.172	0.013	▲	0.208	0.169	0.019
Lamu	**–2.27**	**40.90**	▼	0.009	–0.337	–0.111	▼	0.443	–0.120	0.000	▼	0.384	–0.114	–0.033
Kitale	**1.00**	**35.98**	▲	0.066	0.239	0.093	▼	0.932	–0.013	0.000	▲	0.102	0.212	0.104
Kisumu	**-0.10**	**34.58**	▲	0.941	–0.008	0.000	▼	0.037	–0.214	–0.074	▲	0.116	0.162	0.065
Kisii	**-0.68**	**34.78**	▼	0.540	0.081	0.002	▼	0.366	–0.119	–0.062	▲	0.071	0.234	0.083
Kericho	**–0.37**	**35.27**	▲	0.000	0.363	0.133	▲	0.001	0.333	0.117	▲	< 0.0001	0.488	0.247
Nakuru	**–0.27**	**36.07**	▼	0.508	–0.068	–0.028	▼	0.032	–0.221	–0.062	▲	0.139	0.153	0.049
Narok	**–1.13**	**35.83**	▲	0.762	0.032	0.009	▼	0.613	–0.053	0.000	▼	0.927	–0.010	0.000

▲: Increasing trend
▼:Decreasing trend
▲:Significant increasing trend
▼: Significant decreasing trend
●: No trend

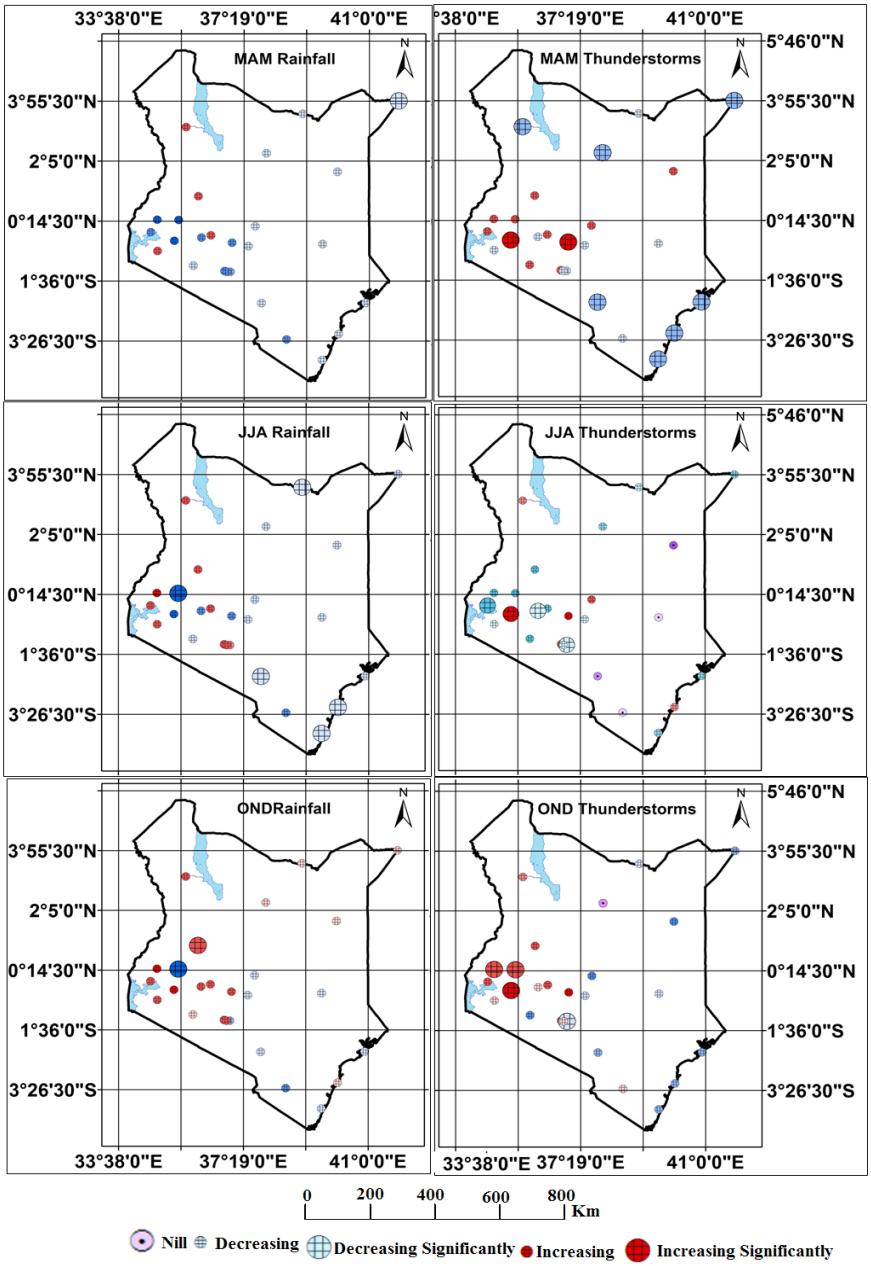

Figure 13. Comparison of trend results for thunderstorms and rainfall at seasonal time-scale over Kenya.

cant. For thunderstorms, a reducing significant trend was observed over most stations during the MAM season. In JJA season, most stations over the eastern half of the country observed nil thunderstorms while the western half had to reduce significant trends. During the OND season, most stations had increasing significant trends. In contrast, the stations around the Lake Victoria region mainly had an increasing trend during the MAM and OND seasons. In summary, the results indicated that the increasing/reducing trends of rainfall over the seasons were not converting to increasing/reducing trends of thunderstorms. The importance of these findings is that they could support various policy makers, and users of climate information, especially in the agriculture and aviation industries.

This study focused on thunderstorm frequencies and trends. It also analysed the same for rainfall in comparison to thunderstorms. The results were interesting, thus there is a need, to replicate this research to the other related parameters like temperature and establish the relationship between thunderstorms

and temperatures in Kenya. Thunderstorm days' data were used to analyse the frequencies, it will be important also to look at the daily frequencies to determine the intensity and duration of a thunderstorm in a given area.

Conflict of Interest

The author declares that there is no conflict of interest.

Acknowledgments

This research article is part of the Master of Science (MSc.) dissertation presented to the University of Nairobi by the lead author. The lead author thanks the Department of Meteorology of the University of Nairobi (UON), and Kenya Meteorological Department (KMD) especially, the Data Management Division, climatological, National Meteorological Centre (NMC) and Moi Airbase Meteorological Office, for the provision of data and guidance in data analysis.

Special appreciation goes to my thesis supervisors the late Prof. Joseph Mwalichi Ininda and Dr. Wilson Gitau. Thank you for your excellent guidance and support. I am grateful to Dr. Victor Ongoma of Mohammed VI Polytechnic University, Morocco for the motivation and guidance in the preparation of this paper.

References

[1] Okoola, R.E., 2005. Transition from the Southern to the Northern Hemisphere summer of zones of active convection over the Congo Basin. Meteorology and Atmospheric Physics. 84, 255–265.
DOI: https://doi.org/10.1007/s00703-003-0002-6

[2] Yuhua, O., Ping, Y., 2012. Audible thunder characteristic and the relation between peak frequency and lightning parameters. Journal of Earth System Science. 121, 211–220.
DOI: https://doi.org/10.1007/s12040-012-0147-0

[3] World Meteorological Organization (WMO), 1992. International meteorological vocabulary. World Meteorological Organization: Geneva.

[4] Lavigne, T., Liu, C., Liu, N., 2019. How does the trend in thunder days relate to the variation of lightning flash density? Journal of Geophysical Research: Atmospheres. 124(9), 4955–4974.
DOI: https://doi.org/10.1029/2018JD029920

[5] Chaggar, T.S., 1977. Geographical distribution of monthly and annual mean frequency of thunderstorm days over Eastern Africa. EAMD Technical Memorandum No.26.

[6] Temporal Distributions of Global Thunder Days [Internet]. Illinois Department of Energy and Natural Resources. Available from: https://www.isws.illinois.edu/pubdoc/cr/iswscr-337.pdf

[7] Enno, S.E., Piia, P., Agrita, B., et al., 2014. Long-term changes in the frequency of thunder days in the Baltic countries. Boreal Environmental Research. 19, 452–466.

[8] Changnon, S.A., 1981. Possible effects of contrail generated cirrus on mid-western cloud and sunshine. Journal of Applied Meteorology. 20(8).

[9] Wu, C., 2005. Inherent delays and operational reliability of airline schedule. Journal of Air Transport Management. 11(4), 273–282.
DOI: https://doi.org/10.1016/j.jairtraman.2005.01.005

[10] Bhattacharya, S., Bhattacharyya, H.C., 2023. A comparative study of severe thunderstorm among statistical and ANN methodologies. Scientific Reports. 13, 12038.
DOI: https://doi.org/10.1038/s41598-023-38736-z

[11] Maloba, S., 2015. Spatial and temporal characteristics of thunderstorms over the eastern region of Lake Victoria Basin in Kenya [Master's thesis]. Nairobi: University of Nairobi.

[12] Ayugi, B.O., Wang, W., Chepkemoi, D., 2016. Analysis for spatial and temporal patterns of rainfall variations over Kenya. Journal of Environmental and Earth Science. 6(11), 69–83.

[13] Ongoma, V., Chen, H., 2017. Temporal and spatial variability of temperature and precip-

itation over East Africa from 1951 to 2010. Meteorology and Atmospheric Physics. 129, 131–144.
DOI: https://doi.org/10.1007/s00703-016-0462-0

[14] Gitau, W., Camberlin, P., Ogallo, L., et al., 2018. Trends of intraseasonal descriptors of wet and dry spells over Equatorial eastern Africa. International Journal of Climatology. 38(3), 1189–1200.
DOI: https://doi.org/10.1002/joc.5234

[15] The Thunderstorm. Report of the Thunderstorm Project [Internet]. U.S. Government Printing Office. Available from: https://onlinebooks.library.upenn.edu/webbin/book/lookupid?key=ha007160453

[16] Koros, D., 2014. Determining convective precipitation using cold cloud top temperatures and its impact on aviation industry over western Kenya [Master's thesis]. Nairobi: University of Nairobi.

[17] Gamoyo, M., Reason, C., Obura, D., 2015. Rainfall variability over the East African coast. Theoretical and Applied Climatology. 120, 311–322.
DOI: https://doi.org/10.1007/s00704-014-1171-6

[18] Palmer, P.I., Wainwright, C.M., Dong, B., et al., 2023. Drivers and impacts of Eastern African rainfall variability. Nature Reviews Earth & Environment. 4, 254–270.
DOI: https://doi.org/10.1038/s43017-023-00397-x

[19] Pinzari, L., Mazumdar, S., Girosi, F., 2018. A framework for the identification and classification of homogeneous socioeconomic areas in the analysis of health care variation. International Journal of Health Geographics. 17, 42.
DOI: https://doi.org/10.1186/s12942-018-0162-8

[20] Mann, H.B., 1945. Nonparametric tests against trend. Econometrica. 13(3), 245–259.
DOI: https://doi.org/10.2307/1907187

[21] Kendall, M.G., 1975. Rank correlation methods. Charles Griffin: London..

[22] Mallick, J., Talukdar, S., Alsubih, M., 2021. Analysing the trend of rainfall in Asir region of Saudi Arabia using the family of Mann-Kendall tests, innovative trend analysis, and detrended fluctuation analysis. Theoretical and Applied Climatology. 143, 823–841.
DOI: https://doi.org/10.1007/s00704-020-03448-1

[23] Gadedjisso-Tossou, A., Adjegan, K.I., Kablan, A.K.M., 2021. Rainfall and temperature trend analysis by Mann-Kendall test and significance for Rainfed Cereal Yields in Northern Togo. Sci. 3(1), 17.
DOI: https://doi.org/10.3390/sci3010017

[24] Aditya, F., Gusmayanti, E., Sudrajat, J., 2021. Rainfall trend analysis using Mann-Kendall and Sen's slope estimator test in West Kalimantan. IOP Conference Series: Earth and Environmental Science. 893. 012006.
DOI: https://doi.org/10.1088/1755-1315/893/1/012006

[25] Asnani, G.C., 2005. Tropical meteorology: Special features of tropical meteorology; Climatology of the tropics; Climatic change; Physics and dynamics of monsoon.

[26] Obiero, K., 2013. Thunderstorm hazards and their impact in the Lake Victoria basin of Kenya [Master's thesis]. Nairobi: Kenyatta University.

[27] Nakamara, K., 1968. Equatorial Westerlies over East Africa and their climatological significance. Geographical Review of Japan. 41(6), 359–373.

[28] Okoola, R.E., 1999. Mid-tropospheric circulation patterns associated with extreme dry and wet episodes over equatorial Eastern Africa during the northern hemisphere spring. Journal of Applied Meteorology and Climatology. 38(8), 1161–1169.
DOI: https://doi.org/10.1175/1520-0450(1999)038<1161:MCPAWE>2.0.CO;2

[29] Liebmann, B., Hoerling, M.P., Funk, C., et al., 2014. Understanding recent eastern horn of Africa rainfall variability and change. Journal of Climate. 27(23), 8630–8645.
DOI: https://doi.org/10.1175/JCLI-D-13-00714.1

BILINGUAL PUBLISHING GROUP
Tel:+65 65881289
E-mail: contact@bilpublishing.com
Website:https://journals.bilpubgroup.com

2630-5119 01
9 772630 511249